The University of Manchester

Photoluminescent properties of novel colloidal quantum dots

A thesis submitted to The University of Manchester for the degree of Doctor of Philosophy in the Faculty of Engineering and Physical Sciences.

2015

Daniel Espinobarro Velazquez

The Photon Science Institute

School of Physics and Astronomy

Contents

Word count: 44,270

List of Figures

List of Tables

List of abbreviations

ADC ..... Analogue to Digital Converter

AgBr ..... Silver bromide

C ..... Chopper

CB ..... Conduction band

CBM ..... Common beam mask

CCT ..... Correlated colour temperature

CFD ..... Constant Fraction Discriminators

CFL ..... Compact fluorescent lamps

CQDs ..... Colloidal quantum dots

CRI ..... Colour rendering index

DEL ..... electrical delays

DL ..... deuterium lamp

DP ..... depolarizing

EIA ..... Energy Information Administration

FW ..... Filter-wheel

GaN ..... Gallium-Nitrade

GB ..... Green/Blue

HAADF ..... high angle annular dark field

HL ..... halogen lamp

InGaAs ..... Indium gallium arsenide

kWh ..... Kilowatt-hours

LED ..... Light Emitting Diodes

LER ..... Luminous efficiency of radiation

MBE ..... molecular beam epitaxy

MEG ..... Multiple exciton generation

MEM ..... Digital memory

MOCVD ..... Metalorganic vapour phase epitaxy

ND ..... Neutral density

NIR ..... near-infrared

PbS ..... Lead sulfide

PL ..... Photoluminescence

PLQY ..... Photoluminescence quantum yield

QDs ..... Quantum dots

R ..... Reference beam

S ..... Sample beam

SA ..... Slit assembly

SBA ..... Sample beam

TA ..... Transient absorption

TAC ..... Time-to-Amplitude Converter

TCSPC ..... Time correlated single photon counting

TDA ..... Tetradecylphosphonic acid

TDPA ..... Tetradecylphosphonic

TOF ..... Time of flight measurements

TOP ..... Trioctylphosphine

TRPL ..... Time-resolved PL

UV ..... Ultraviolet

VB ..... Valence band

Vis ..... Visible

XRD ..... X-ray powder diffraction

Δ_{xx} ..... Exciton-exciton interaction energy

Abstract

The work presented in this thesis was submitted to The University of Manchester for the degree of Doctor of Philosophy in April 2015 by Daniel Espinobarro Velazquez and is entitled “Photoluminescent properties of novel colloidal quantum dots”.

In this thesis type II colloidal quantum dots (CQDs) with zinc blende crystal structure were investigated. The optical properties were characterized by steady state absorption and photoluminescence (PL) spectroscopy for all the samples, and the PL quantum yield was measured for selected samples by using both absolute and relative methods. Exciton dynamics and interactions were investigated by time-resolved PL (TRPL).

The exciton-exciton interaction energy for CdSe, CdSe/CdTe and CdSe/CdTe/CdS CQDs was investigated using TRPL spectroscopy, an established method. The TRPL results were compared with previous results from ultrafast transient absorption (TA) measurements and theoretical predictions. The discrepancies between the TRPL and TA results and the theoretical calculations suggest that TRPL data has been misinterpreted in the literature.

The single exciton recombination dynamics for CdSe, CdSe/CdTe and CdSe/CdTe/CdS CQDs were investigated. The effects of non-radiative recombination were identified from the PL transients by using a theoretically-calculated radiative lifetime as a fitting parameter. The combined rate of the non-radiative processes thus found was consistent with the localisation of holes into shallow traps by an Auger-mediated process. A rate equation analysis also showed how shallow trapping can give rise to the tri-exponential PL dynamics observed experimentally.

Chloride passivation of CdTe CQDs resulted in a near-complete suppression of surface traps, producing a significant enhancement of the optical properties. PL quantum yield (PLQY) and PL lifetime in particular benefit from the chloride treatment. The radiative recombination rate that now could be extracted from PL transients for chloride treated samples was used to calculate the non-radiative recombination rate for the untreated samples. In addition, a study of the effects of air exposure on the PL, observed for both treated and untreated samples was undertaken and revealed the importance of the influence of the dielectric environment surrounding the traps states on recombination dynamics.

Declaration

No portion of the work referred to in the thesis has been submitted in support of an application for another degree or qualification of this or any other university or other institute of learning;

Copyright statement

Acknowledgments

I would like to thank Prof Phil Dawson and Dr. David Binks for the opportunity to study for this PhD over the past years. I would like to thank especially my supervisor Dr. David Binks for his guidance, feedback, tremendous patience and support. I would like to thank Prof Phil Dawson and his group for their patience, time and help with my technical issues, especially to Prof Phil Dawson, Dr. Tom Badcock, Dr. Matt Davies, Dr. Simon Hammersley and Dr. Catherine Othick. I would also like to acknowledge the Binks group and collaborators: Stuart, Ali, Musa, Charles, Claire, Chris and Marina for their support and suggestions. I would like to express thanks to Dr Chris Page for making all the quantum dots I characterised. I would like to thank the people in Photon Science Institute for their contributions.

I would like to acknowledge Dr. Teresa Alonso Rasgado for the support and help during this process, and the CONACyT for the scholarship.

I would like to thank all my friends who are part of my family, a big thank to you: Chloe, Matt, James, Jimbo, Filip, Xander, Callum, Fernando, Gerardo, Luis, Daniel, Javier and Jesus who always make my life happier and enjoyable. I would like to especially thank Chloe for the emotional support during last year and staying with me during the ups and downs.

I would like to show gratitude to the families who always treat me like I was part of them; Othick's, Stott's, Aquino's, Olle's, Avalos and Labastidas.

Finally, I would like to express all my gratitude to my Parents and my uncle Francisco, for the support, encouragement and opportunity to accomplish this step. I would not be the person I am, without them. I would like to thanks my brother wherever he is now.

I am grateful to all at the above for have your love and friendship.

Dedication

To my parents and family, in memory of my brother.

Publications and presentations

Journal articles

Espinobarro-Velazquez, D., Leontiadou, M. A., Page, R. C., Califano, M., O'Brien, P. and Binks, D. J. (2015), Effect of Chloride Passivation on Recombination Dynamics in CdTe Colloidal Quantum Dots. ChemPhysChem. doi: 10.1002/cphc.201402753

Page, R. C., Espinobarro-Velazquez, D., Leontiadou, M. A., Smith, C., Lewis, E. A., Haigh, S. J., Li, C., Radtke, H., Pengpad, A., Bondino, F., Magnano, E., Pis, I., Flavell, Wendy. R., O'Brien, P. and Binks, D. J. (2015), Photoluminescence: Near-Unity Quantum Yields from Chloride Treated CdTe Colloidal Quantum Dots (Small 13/2015). Small, 11: 1482. doi: 10.1002/smll.201570074

McElroy, N., Page, R.C., Espinbarro-Valazquez, D., Lewis, E., Haigh, S., O'Brien, P., Binks, D.J., Comparison of solar cells sensitised by CdTe/CdSe and CdSe/CdTe core/shell colloidal quantum dots with and without a CdS outer layer, Thin Solid Films, Volume 560, 2 June 2014, Pages 65-70, ISSN 0040-6090, http://dx.doi.org/10.1016/j.tsf.2013.10.085.

Conference presentation

Espinobarro-Velazquez, D., Binks, D., “Propiedades Fotoluminiscentes de Nuevas Nanoestructuras Coloidales”, II Simposio de becarios CONACyT, European Parliament Strasbourg, France (29th 30th Nov 2012)

Conference posters

R C Page, D Espinbarro-Velazquez, M Leontiadou, E Lewis, S J Haigh, H Radtke, A Pengpad, F Bondino, E Magnano, I Pis, W R Flavell, P O’Brien, C Lydon, and D J Binks,

“Mild cadmium chloride treatment of CdTe quantum dots producing near unity quantum yields”, Colloidal Quantum Dots and Nanocrystals, Chancellors Hotel and Conference Centre, Manchester, UK (14–15 July 2014)

D. Espinbarro-Velazquez, R. C. Page, M Cadirci, P. O’Brien & D Binks, “Photoluminescence behaviour of CdSe/CdTe/CdS Type- II Colloidal Quantum Dots” XI Symposium, University of Sheffield (11th – 13th of June, 2013).

M. Cadirci, D. Espinobarro-Velazquez, R. C. Page, P. O’Brien, E. Lewis, S. Haigh, D. Binks, “Attractive Biexciton Interaction Energies in CdSe/CdTe/CdS and CdTe/CdSe/CdS Type II Colloidal Dots” E-MRS 2013 Spring Meeting, Strasbourg, France, (28-30 May).

Chapter 1. Introduction.

1.1. Introduction

Understanding how to generate light efficiently and effectively has always been an essential need for humanity. The continuing importance and impact of light-generating technology was recognised with the award of last year's award of the Nobel Prize in Physics for the development of light-emitting diodes (LED's) based on gallium-nitride (GaN) [1]. We are currently at the beginning of a lighting revolution based on the use of GaN LED's [2], which can be more than ten times as efficient as incandescent lighting and twice as efficient as fluorescent lights. The savings associated with this increased efficiency has the potential to have a huge global impact. The International Energy Agency states that the global lighting represents ~20% of the total energy consumed. In the U.S, the Energy Information Administration (EIA) estimates 412 billion kilowatt-hours (kWh) of electricity were used for lighting in the US. This was 15% of the total electricity consumed by residential and commercial sector and about 11% of total U.S. electricity consumption[3]. The reduction in energy consumption produced by more efficient lighting could consequently reduce the generation of greenhouse gas emissions by roughly 180 million of tons of CO_2 [2]

However, GaN LEDs only emit blue light efficiently so in order to produce different colours phosphors are used which absorb some of the blue light and emit light at longer wavelengths. The combination of the blue-emitting LED and the phosphor leads to a white light if appropriately balanced, or to red and green emission as required, for example, in display technology.

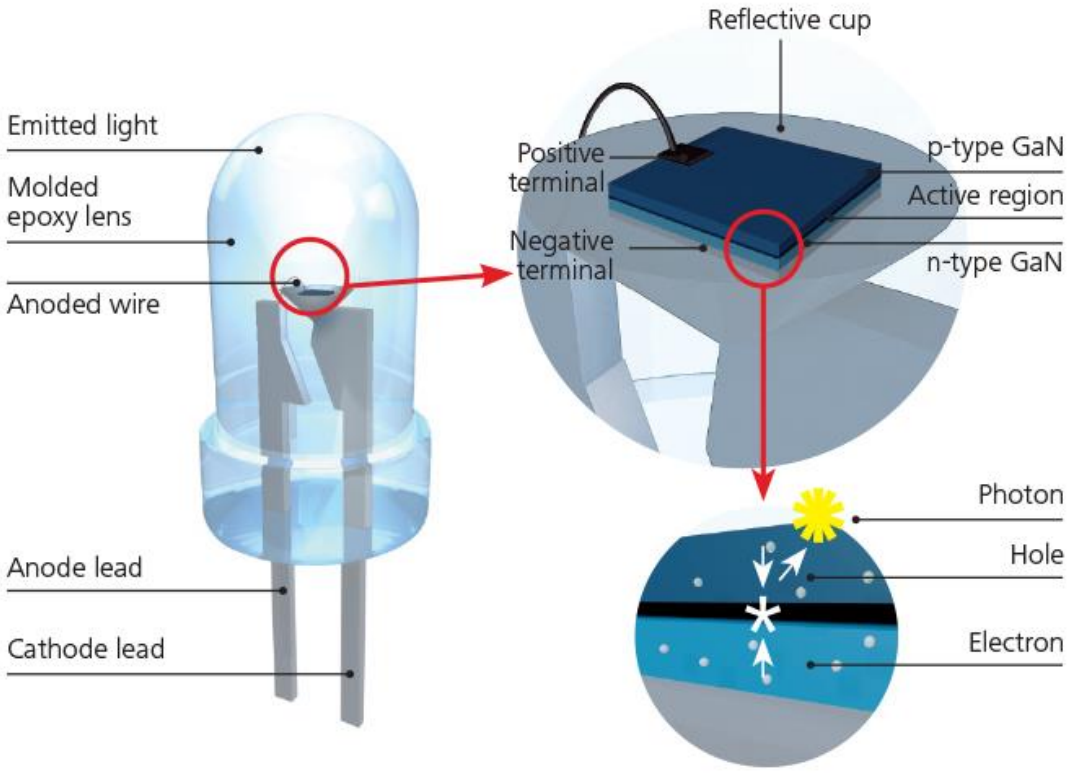

Figure 1. 1 Schematics of LEDs and principle (Taken from[4])

Figure 1. 1shows the parts of an LED and its functional principle, in which a n-type and p-type GaN semiconductors are connected to the anode and cathode. When a potential is applied electrons and holes are injected and then recombine, releasing photons. These photons will have energy and thus wavelength determined by the properties of the material.

The quality of the phosphors is a key factor, determining the spectral output and contributing to the overall luminous efficiency. Nowadays, there is great interest in nano-sized material as quantum wells, quantum wires and especially quantum dots (QDs) because their optical properties are readily tuned by control of their size, structure and composition. In particular, QDs can be used as an alternative to the phosphors currently used in LED technology, such as YAG:Ce^{3+}; other alternative phosphors include organic molecules [5].

Colloidal quantum dots (CQDs) have been researched for over three decades and more than ~14 000 journal articles have been pusblished since then [6]. This number is continuously increasing as the underlying fundamental physics and chemistry are still not fully understood. The widespread research of CQDs is driven by their clear benefits (i.e. easy tunability of the band gap through synthesis, low-cost fabrication, photostability and application potential). The optical properties such as photoluminescence (PL) spectrum, quantum yield, PL lifetime and absorption are important factors to take into consideration for applications using solutions based on CQDs.

The purpose of this thesis is to study and understand the factors, particularly surface and shell effects, affecting the PL properties of CdSe, CdSe/CdTe, CdSe/CdTe/CdS, CdTe and CdTe/Cl CQDs with type I and type II structures. By understanding how the recombination mechanisms work and behave, the design of highly efficient CQDs to improve the quality and efficacy of solid state lighting is enabled.

1.2. Thesis outline

The overall structure of this study of the photoluminescent properties of novel colloidal quantum dots takes the form of seven chapters including this one.

The background and theory of CQDs is described in Chapter 2, in which some key research is highlighted due its significant contribution to the QD field, including a description of QD system and the synthetic methods used to grow the QDs. The theory section discusses the size effects, spherical model, and also a brief description of band structure. A description is also given of excitons in QDs, including dark excitons, types of effect such as Auger recombination and Auger mediated trapping.

The techniques and procedures used to characterise the CQDs are explained in Chapter 3. The absorption and PL spectrometers used in these experiments are described in detail. A home-built system was used for the time-domain measurements; the system

description and the instrument response function are described. Two different methods were used for the measurement of photoluminescence quantum yield (PLQY), the comparative and absolute techniques, and these are described and compared.

The results for CdSe, CdSe/CdTe and CdSe/CdTe/CdS CQDs are presented in Chapter 4 and Chapter 5. In Chapter 4, exciton-exciton interactions were analysed using spectral data from the time-resolved PL system. This data was compared to results acquired in previous studies using the same technique and also to measurements of exciton-exciton interaction in the samples made using different techniques. To reconcile all these results, an alternative interpretation of the data based on hot emission is discussed.

The recombination dynamics for single excitons was analysed and discussed in Chapter 5. A novel description of the recombination rates was reported by comparing theoretical calculations and experimental results.

A study based on the effects of chloride ions on the surface of CdTe CQDs was reported in Chapter 6. This included the effect of the chloride ions on PLQY and on the degradation of PLQY by air exposure. In addition, the synthesis and structural characterisation is detailed, and a comparison made between the recombination dynamics for chloride treated and untreated samples. Further, a spectrally-dependent study of recombination dynamics is made as a function of the pump pulse power.

A summary of the results and conclusions is presented in Chapter 7, as well as a discussion of the further work that might proceed from this study.

References

1. HeberJoerg, *Nobel Prize 2014: Akasaki, Amano & Nakamura.* Nat Phys, 2014. 10(11): p. 791-791.
2. Pust, P., P.J. Schmidt, and W. Schnick, *A revolution in lighting.* Nature Materials, 2015. 14(5): p. 454-458.
3. (EIA), E.I.A., *ANNUAL ENERGY OUTLOOK 2015.* http://www.eia.gov/forecasts/aeo/tables_ref.cfm, 2015.
4. Lighting, O. *LED ACADEMY*. http://www.ledacademy.net/.
5. Reineke, S., *Complementary LED technologies.* Nature Materials, 2015. 14(5): p. 459-462.
6. Kim, J.Y., O. Voznyy, D. Zhitomirsky, and E.H. Sargent, *25th Anniversary Article: Colloidal Quantum Dot Materials and Devices: A Quarter-Century of Advances.* Advanced Materials, 2013. 25(36): p. 4986-5010.

Chapter 2. Background and Theory.

2.1. Background

The study of the size-dependence of optical material properties has a long history. In 1856, Faraday reported the first study of how material properties can vary with size (describing the optical properties of nanoparticles of gold and other materials) [1]. More than a century later in 1967, [2] Berry reported the absorption coefficient of a molecule of AgBr is reduced in comparison to bulk AgBr. However, it was not until the 1980s that the field changed from one of occasional reports to one of significant, ongoing activity, with the development of a theory to describe electronic structures in colloidal nanocrystals by Brus [3], and the new techniques in synthetic procedures were developed by Steigerwald *et al* [4] and Brennan *et al* [5]. Both helped to increase the knowledge and interest in nanomaterials.

The past two decades have seen the rapid development of novel methods to grow nanocrystals with various shapes and properties, with these systems anticipated to have novel application, such as for efficient lights, quantum dot lasers, spectral tags in biological imaging, commercial and military applications, and so on [6].

2.1.1. Semiconductor

A semiconductor is a crystalline or amorphous solid whose electrical conductivity is typically intermediate between that of metal and that of an insulator [6]. The width of the energy gap which separates the conduction band (CB) from the valence band (VB) is an important parameter. This bandgap energy (Eg) can determine the electrical and optical properties of the material. Semiconductor materials are usually characterized by bandgaps between 0.5 and 3 eV, which makes them ideal for many electronic and optical applications [7]. Compound semiconductors belong to three families depending on the

group of the Periodic Table: II-IV, III-V and III-IV. In these materials some electrons that are very weakly linked to their atoms can become conduction electrons. They can be n-type or p-type; with holes in the latter being the majority charge carrier and electrons performing this role in the former.

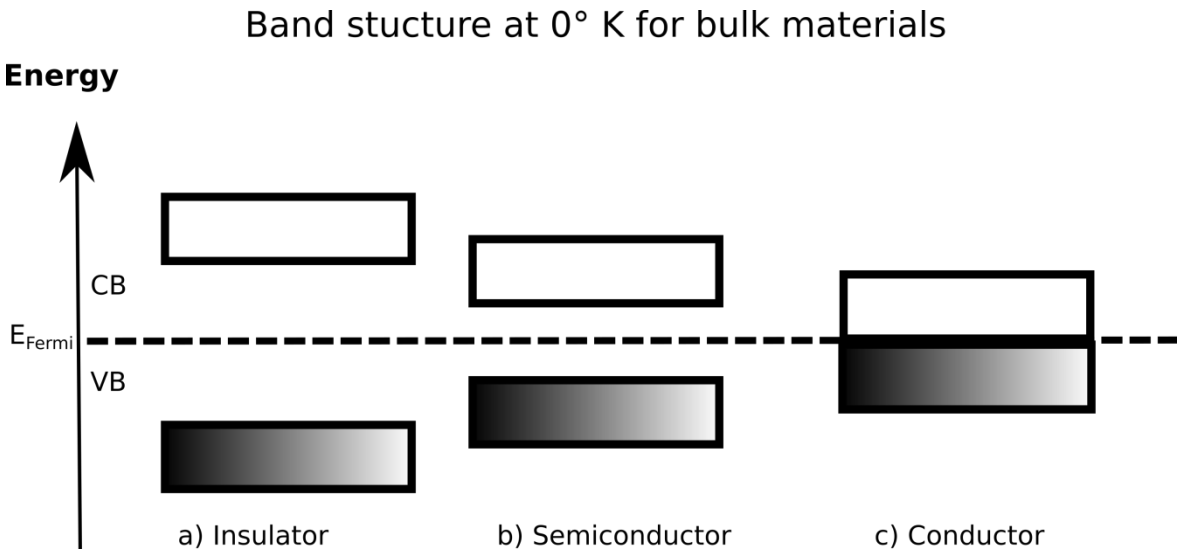

Figure 2. 1 Schematic of the band structure for bulk a) insulators, b) semiconductors, and c) conductors at 0° K

Figure 2. 1 shows schematic diagrams of the band structure for three classes of material. Insulators have a large band gap, typically greater than 4 eV, which prevents thermal excitation to the conduction band. Semiconductors have a reduced band gap, across which electrons can be thermally excited. Conductors are materials, generally metals, where their energy levels are partly filled or fully unoccupied with similar energies. The probability that a particular energy level is occupied by an electron is characterized by the Fermi energy (E_{Fermi}), which corresponds to the energy with a 50% occupation probability.

2.1.2. Cadmium – group VI semiconductors

The II-VI semiconductors are wide-bandgap compounds, and they have been used in optoelectronics devices and in solid state lighting (SSL). These semiconductors have a direct gap and bandgap energies suitable for different applications such as: optoelectronic

devices, light emitting diode (LED), laser diodes, solar cells, sensors, surface acoustic wave (SAW) devices, SAW filters, SAW oscillators, low threshold optical gain media, high-power electronic devices , field-effect transistors, substrate transparent electrodes, self-compensating gas sensors, pyroelectric and piezoelectric devices [59].

The properties of the Cadmium –group VI semiconductors are based on the arrangement of the atoms i.e. lattice structure. For CdSe, CdTe and CdS the lattice structure can be wurtzite (hexagonal symmetry) or zinc blende (cubic symmetry), See Figure 2. 2. The wurtzite structure consists of mixture of two hexagonal closed packed (HCP) sub-lattices, one of atom A and the other atom B, with a displacement of ⅜c from each other along c-axis where c is the lattice constant in this direction. The zinc blende consist of mixing two face centred cubic (FFC) sub-lattices, one of atom A and the other B, with a displacement from each other along the diagonal body by $a/4$, a is the lattice constant. The crystal structure affects the band gap for each compound (see Table 2. 1).

Table 2. 1 The energy band gap for a wurtzite and zinc blende [60]

Compounds	Band gap (eV)	
	Zinc blende	Wurtzite
CdSe	1.90	1.83
CdTe	1.60	1.60
CdS	2.55	2.58

The optical properties in a quantum dot are given by the band gap to size relation (sizing curve). For CdSe CQDs with wurtzite and zinc blende crystal structure, the sizing curve and the extinction coefficient are similar for both. However, for each crystal structure the strong confinement is described by different Hamiltonian [61].

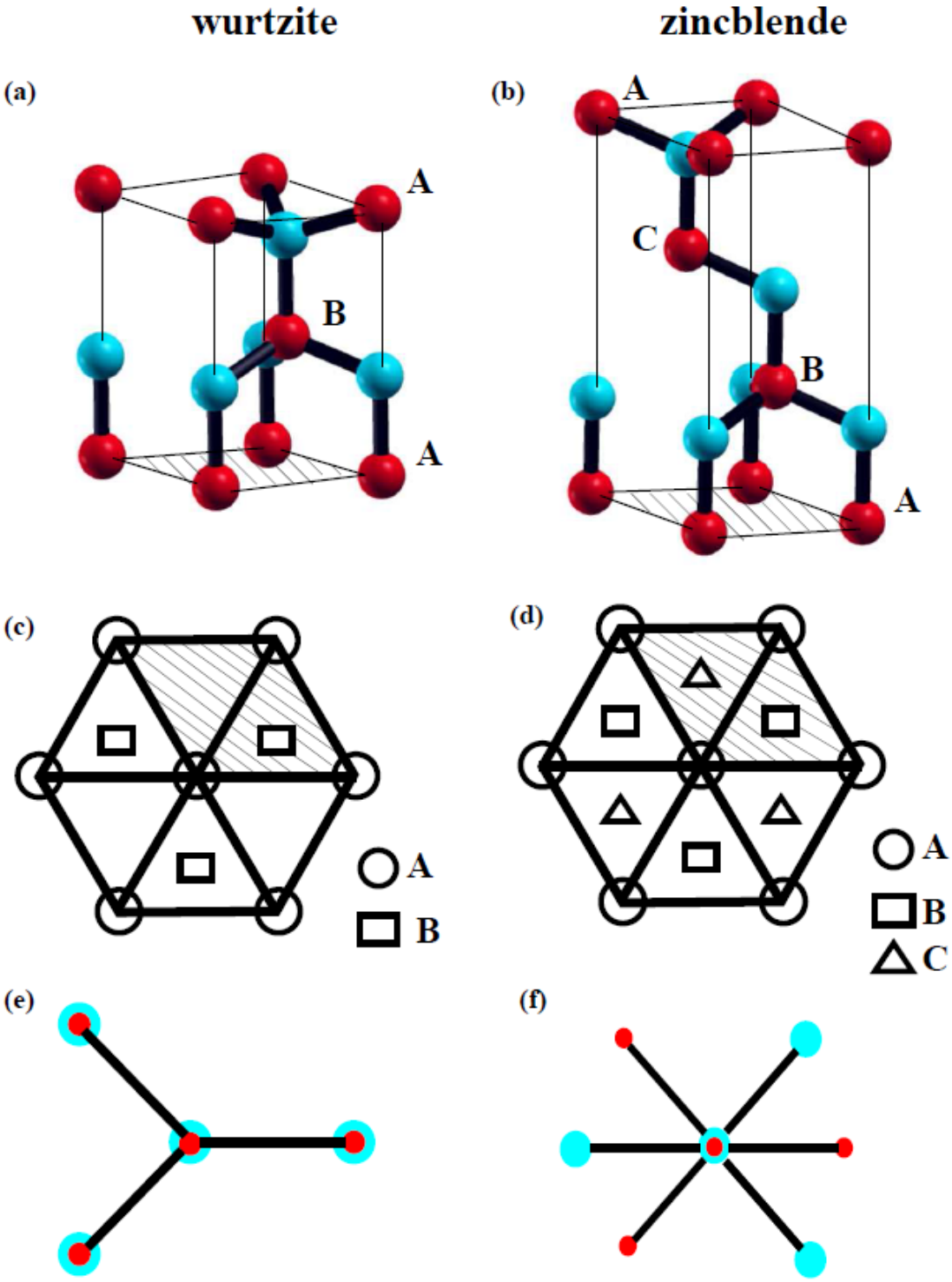

Figure 2. 2 The wurtzite (a) and zinc blende (b) crystal structure. The red colour represent atoms of Cd, and the blue atoms of X(X= Se,Te and S). Wurtzite crystal structure showing ABAB lattice (c) and (d) ABCABC lattice for zinc blende. The plane (111) is shown in (e) and (b), where the atoms are eclipsed and staggered (Taken from [60])

2.2. Quantum Dots

Modern semiconductor processing techniques allows the artificial creation of quantum confinement of a few or single electrons in three dimensions [8]. The resulting structures are called Quantum Dots (QDs) but are also known as nanocrystals, quantum boxes and artificial atoms. Their sizes are typically from 1 nm to 10 nm, but can extend to several μm [6]. The classification of quantum dots can be based on the fabrication method used, yielding the following types: electrostatic quantum dots, self-assembled quantum dots and colloidal quantum dots.

Electrostatic QDs are fabricated by restricting a two dimensional electron gas in a semiconductor heterostructure laterally by electrostatic gates, or vertically by etching techniques [8, 9].

Self-assembled QDs are obtained in hetero-epitaxial systems with different lattice constants. During the growth of a layer of one material on top of another, the formation of nanoscale islands take place [10]. Molecular beam epitaxy (MBE) and metalorganic chemical vapour deposition (MOCVD) are the most common technique used to grow this type of QD .[11, 12]

Colloidal quantum dots (CQDs), the subject of this thesis, are single solvent chemistry-synthesized crystals of the size of a few nanometres [13]. The temperature, duration and ligand molecules used in the synthesis of QDs control their shape and size [14]. A layer of other semiconductor can be grown around a colloidal QD, forming what is known as a core-shell system. Depending on the bandgaps and the relative position of electronic energy levels of the involved semiconductors, the core and shell can have different function in colloidal QDs[15, 16].

In a type I structure QD (see Figure 2. 3a), the shell is used to passivate the surface of the core, improving its optical properties. The shell of the QD physically separates the surface of the optically active core from the medium which coats it [15, 17]. This reduces the

interaction of free carries with the surface dangling bonds that can act as trap states for charge carries.

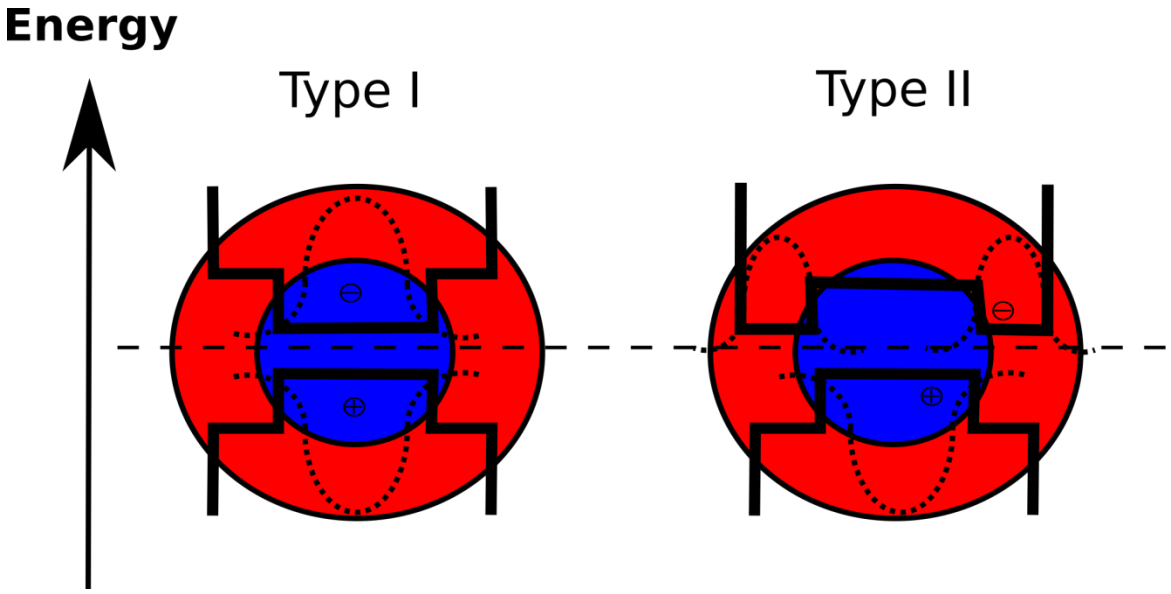

Figure 2. 3 QDs with type I and type II structures

In a type II structure QD (see Figure 2. 3b), the shell growth aims to red shift the emission wavelength. The staggered band alignment leads to a smaller effective bandgap. [15, 18]. In contrast to Type I systems, the photoluminescence (PL) decay time also lasts longer in type II structures due to the lower overlap of the electron and hole wave functions in this type of structure [15, 16, 18].

2.2.1. Synthesis CQDs

In general there are two main approaches to synthesising QDs: the colloidal and epitaxial methods. The QDs investigated in this thesis were grown using colloidal synthesis. This approach actually dates back to the Roman culture in the 4th century, but the process was not recognized until 1857 [1], and it was not until more than a century later, in 1980, that the synthesis of size-tuned CQDs was first understood. The process of synthesis has two main stages: nucleation and growth. Nucleation is the process where the seed is produced; this can be homogeneously or heterogeneously. Nucleation and growth can be understood via the LaMer principle [19], where there are three stages. First there is a rapid increase in monomer liberation, and then the concentration reaches a critical point which is saturation. The last stage is the nanoparticle growth. The hot injection method is a synthetic method which attracts attention due to it consistency of the precipitation reaction. This method offers stability at high temperatures up to 300°C, and thus allows the control over the QD particle size by increasing the temperature.

The CQDs studied in this thesis were produced by the hot injection method using two precursors for the core, with the shell grown by a slow layer by layer process [20]. This method offers the possibility to grow different sizes of QD by varying the temperature and the reaction time. The CQDs studied had a zinc blende (cubic) crystal structure which, since it is isotropic, facilitates uniform growth of the shell.

2.3. Theory

Despite the fact that the band gap of a bulk semiconductor is not easily altered, the bandgap of semiconductor nanocrystals can be readily adjusted. This is because in the regime of quantum confinement changes in the particle size alters the energy spectra [12, 13, 21]. This phenomenon is known as the quantum size effect. QDs are discrete particles whose size is such that they confine the wave functions of the electron and hole. This quantum confinement can occur in the low dimensional structures, known as quantum well for 2-D structures; a 1-D structure is called quantum wire. For quantum dot the confinement of the charge carrier is in 3-D, yielding a quasi “zero dimensional” structure.

The potential barrier represented by the limit of the dot will confine the charge carriers if its size approaches the natural length scale of the electron hole pair or exciton, termed the Bohr radius. The quantum dot crystal structure remains the same as for the bulk semiconductor yet this quantum size effect changes the continuous conduction and valence bands found in bulk into discrete atomic-like states (see Figure 2. 3). For this reason semiconductor nanocrystals have been dubbed artificial atoms, but unlike atoms the degree of quantization is a direct result of the size of the particle and therefore these states can be tuned by varying the nanocrystal size [22].

In the Figure 2.4 a bulk semiconductor has a constant conduction and valence bands separated by a fixed energy gap, but a QD is characterized by discrete states. (Taken from [12])

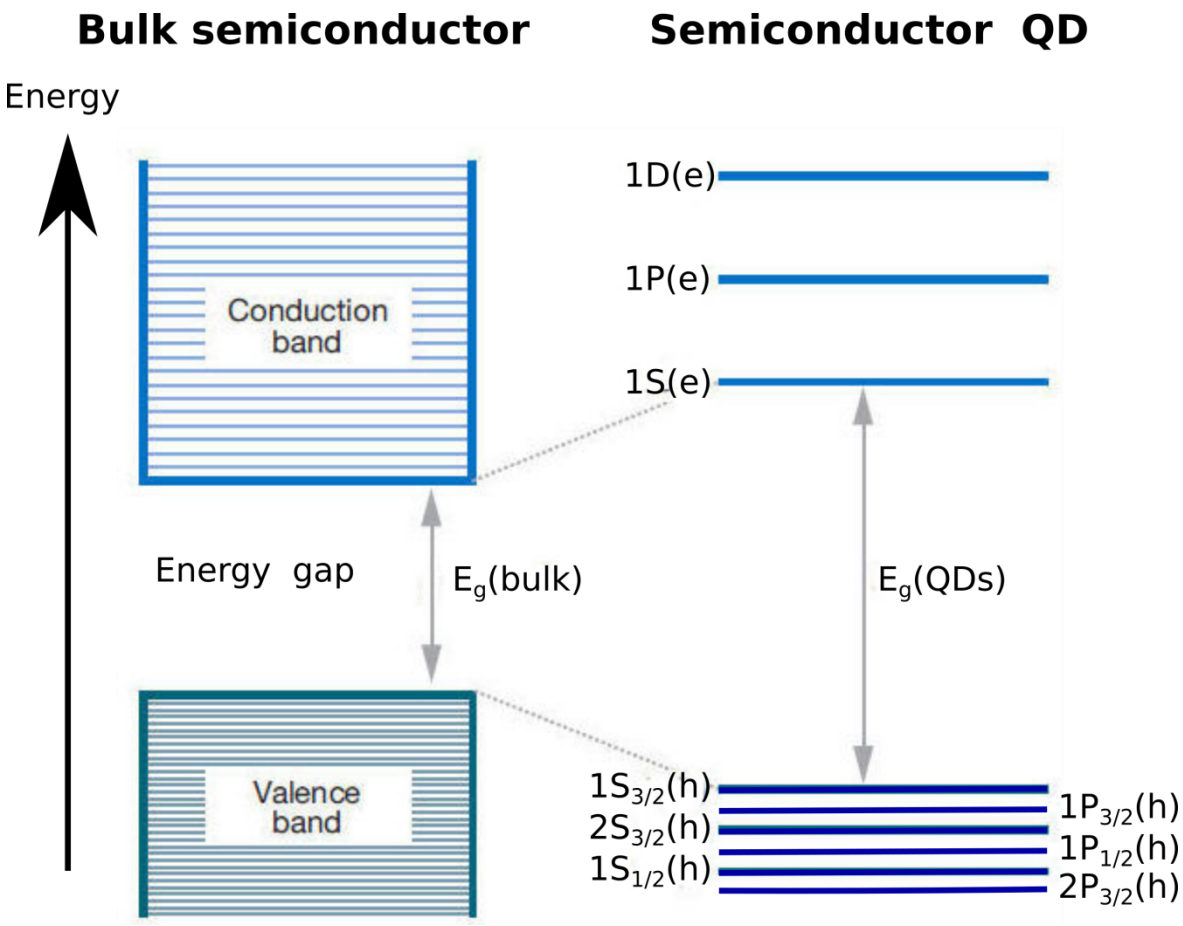

Figure 2.4 Comparison between Bulk semiconductor and QDs energy band (Modify from [23])

2.3.1. Size effects in QDs

The quantum size effect was first observed by Berry [2, 24] and Brus [3]; there is an inverse variation between energy gap and the QD size. The size of the nanoparticle relative to the Bohr Radii of the electron, hole and exciton determines the size regime it is said to occupy. It is possible to calculate the electron and hole Bohr radii using the relationship $a_b = \varepsilon_r \hbar / m_{e,h} e^2$ where ε_r is the relative dielectric constant, $\hbar$ is the reduced plank constant, $m_{e,h}$ is the electron or hole effective mass, and e is the elementary charge. The Bohr radius of the exciton can be found from the equation

$$\mathbf{a_b = \varepsilon_r \frac{m_0}{m^*} a_0},$$

(2. 1)

where m^* is the reduced effective mass of the electron hole pair, m_0 is the rest mass of the electron and a_0 is the Bohr radius of the hydrogen atom.

Three size regimes can be defined and are known as the strong, intermediate and weak confinement regimes. The size regime of a nanoparticle has an influence on the energy level of the electron and hole as well as the dynamics of the charge carriers [25]. Quantum dots in the weak confinement regime will only confine the centre of mass motion of the exciton and correspond to the situation when the radius of the nanocrystal, a, is larger than the Bohr radii of the electron (a_e) and hole (a_h) but is smaller than that of the exciton (a_{exc}) (i.e. $a_e, a_h < a < a_{exc}$). Features in the optical spectra of this regime are therefore due to the quantisation of the exciton centre of mass motion as the exciton binding energy will be greater than the energy quantisation of the electron and hole. When the radius of the nanocrystal is larger than the Bohr radii of the hole but smaller than that of the electron and exciton ($a_h < a < a_{exc}, a_e$) as found in materials where the electron and hole effective masses differ greatly, the QD is said to be in the intermediate confinement regime. In this case the hole will be strongly confined to the centre of the dot and the energy levels will mainly be determined by the quantisation of the electron motion. The strong confinement regime is found when the radius of the nanocrystal is smaller than the Bohr radii of the electron, hole and exciton. Here the charge carriers are strongly confined within the nanocrystal and the separation between the quantum size levels of both carriers is now of the order $m_{e,h}e^2$ which is large compared with the coulomb interaction between the electron and hole.

2.4. Spherical model

A sphere represents the thermodynamically lowest energy shape for a materials with a relatively isotropic underlying crystal structure [12]. Materials with a relatively anisotropic underlying crystal structure will often form nearly spherical nanoparticles. Crystal shape and growth direction can be largely controlled by influencing both kinetic and thermodynamic parameters. The precursor concentration in the reaction mixture is an important factor to control the kinetic growth conditions. High precursor concentrations will promote a fast kinetic growth, leading to a more anisotropic growth, especially in systems where the underlying crystal structure is anisotropic. A second important parameter is the ability of specific surfactant molecules to bind with different affinities to certain NC facets, controlling the relative reactivity of the surface facet [26]. Surface energy and binding energy calculations of the various facets of CdSe show a difference in reactivity and affinity of the different facets of wurtzite CdSe towards monomers and surfactants.

A relatively simple model of a spherical QD was formulated in the work by Efros and Brus [27, 28].This model was used by Norris [12] where it considered a particle of mass $m_0$within a spherical potential well of radius a, that is 0 within the well and infinite outside the well.

$$V(r)=\begin{cases}\mathbf{0} & \mathbf{r} \le \mathbf{a} \\ \infty & \mathbf{r} > \boldsymbol{a}\end{cases}$$

(2. 2)

The Schrodinger equation can be solved and separated into an angular part and a radial part where the angular solutions are the spherical harmonics known from the model of the hydrogen atom and the radial function can be described by Bessel functions [12] yielding

$$\boldsymbol{\Psi_{n,l,m}}(\mathbf{r},\boldsymbol{\theta},\boldsymbol{\phi}) = \mathbf{C}\frac{\mathbf{j_l}(\mathbf{k_{n,l}r})\mathbf{Y_l^m}(\boldsymbol{\theta},\boldsymbol{\phi})}{\mathbf{r}}$$

(2. 3)

where $j_l(k_{n,l}r)$ is the l^{th} order spherical Bessel function, Y_l^m Is a spherical harmonic and C is a normalization factor. Due to the boundary conditions the wave number, *k*, cannot take any value and so is determined by

$$\mathbf{k_{n,l}} = \frac{\boldsymbol{\alpha_{n,l}}}{\mathbf{a}} \tag{2. 4}$$

where $\alpha_{n,l}$ is the n^{th} zero of j_l The energy of the particles is given by

$$\mathbf{E_{n,l}} = \frac{\hbar^2 \mathbf{k_{n,l}^2}}{\mathbf{2m_0}} = \frac{\hbar^2 \boldsymbol{\alpha_{n,l}^2}}{\mathbf{2m_0 a^2}} \tag{2. 5}$$

The electron and hole levels can be labelled by the quantum numbers n (1,2,3,..), *l* (s,p,d,..). This general model reveals the strong energy dependence on nanocrystal size observed is a result of the $1/a^2$ term seen here.

In a bulk crystal with a periodic lattice the electron wave functions can be described as plane waves or Bloch functions that are modified by the influence of the periodic potential of the crystal lattice. Bloch functions are written according to Bloch's theorem as [12]

$$\boldsymbol{\Psi_{nk}}\,(\vec{\boldsymbol{r}}\,) = \boldsymbol{u_{nk}}\,(\vec{\boldsymbol{r}}\,)\;\boldsymbol{exp}(\boldsymbol{i}\,\vec{\boldsymbol{k}}\,\vec{\boldsymbol{r}}\,) \tag{2. 6}$$

where u_{nk} is a function accounting for the periodicity of the lattice and *n* is an index describing the particular band with wave vector $\vec{k}$. Also, under the effective mass approximation the bands described by the energy of these wave functions as a function of k are assumed to have a simple parabolic from. CdSe is a direct gap semiconductor for example with the valence band maximum and conduction band minimum occurring at k=0. See Figure 2.5

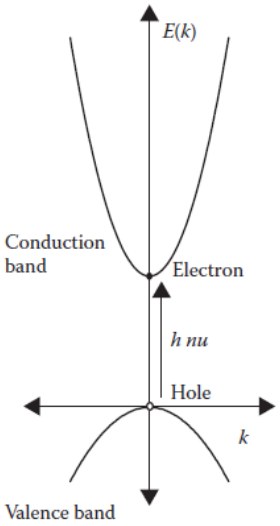

Figure 2.5 Band diagram for a simple two band model for direct gap semiconductor (Taken from[12])

In a QD, the energy of the conduction and valence states are given by

$$E_k^c = \frac{\hbar^2 k^2}{2m_{eff}^c} + E_g \quad \textbf{(2. 7)}$$

$$E_k^v = \frac{-\hbar^2 k^2}{2m_{eff}^v} \quad \textbf{(2. 8)}$$

where E_g is the direct semiconductor band gap and the energies are relative to the valence band maxima. See Figure 2.6

When the nanocrystal diameter is much larger than the lattice constant of the material, the single particle wave function can be expressed as a linear combination of Bloch functions:

$$\Psi_{SP} = (\vec{r}) = \sum_k C_{nk} u_{nk}(\vec{r}) exp(\vec{k} \cdot \vec{r}) \quad \textbf{(2. 9)}$$

where the coefficients C_{nk} ensure that the function takes into account the spherical boundary condition of the nanocrystal [12]. Taking the assumption that u_{nk} functions have a weak *k* dependence, then

$$\boldsymbol{\Psi_{SP}} = (\vec{\boldsymbol{r}}) = \boldsymbol{u_{n0}}(\vec{\boldsymbol{r}}) \sum_{\boldsymbol{k}} \boldsymbol{C_{nk}}\left(\boldsymbol{i}\vec{\boldsymbol{k}} \cdot \vec{\boldsymbol{r}}\right) = \boldsymbol{u_{n0}}(\vec{\boldsymbol{r}})\, \boldsymbol{f_{sp}}(\vec{\boldsymbol{r}}) \quad \textbf{(2. 10)}$$

where $f_{sp}(\vec{r})$ is the single particle *envelope function* and u_{n0} can be determined from the tight binding approximation.

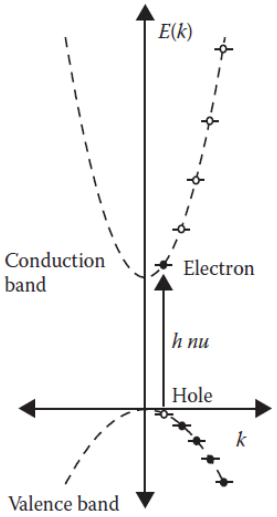

Figure 2.6 Optical transition in finite size semiconductor are discrete to the quantization of the bulk bands (Taken from[12])

Using Equations (2. 3) and (2. 5), the electron-hole (e-h) pair state in nanocrystals has energies are written as

$$\boldsymbol{E_{ehp}}(\boldsymbol{n_h L_h n_e L_e}) = \boldsymbol{E_g} + \frac{\hbar^2}{\boldsymbol{2a^2}}\left\{\frac{\boldsymbol{\alpha^2_{n_h,L_h}}}{\boldsymbol{m^v_{eff}}} + \frac{\boldsymbol{\alpha^2_{n_e,L_e}}}{\boldsymbol{m^c_{eff}}}\right\} - \boldsymbol{E_c} \quad \textbf{(2. 11)}$$

The states are labelled by quantum numbers $n_h L_h n_e L_e$.For pair states with the electron in the $1S_e$ level, the first order Coulomb correction,E_c, is $1.8e^2/\varepsilon a$, the second term taking

into the account the quantum energy of localization and the third term is incorporated as a result of the Coulomb attraction.

2.4.1. Band structure

The real band structure of II-VI semiconductors is typically more complicated. While the conduction band in CdSe is fairly well described within the effective mass approximation, the valence band is not [12]. The valence band arises from 4p atomic orbitals and is sixfold degenerate at k=0, including spin. This sixfold degeneracy leads to valence band substructure that modifies the results of the particle in sphere model. To incorporate this structure, CdSe is often approximated as having an ideal diamond like structure (see Figure 2.7), so, while the bands are still assumed to be parabolic, due to strong spin-orbit coupling the valence band degeneracy is lifted. When considering the valence band the quantum number J, which is the total angular momentum, is used to describe the sub-bands that result from the strong spin-orbit coupling. This is defined as $J = |L \pm S|$, where L (= 1 for p orbitals) are the orbital contributions to the angular momentum and S (=1/2 for electron) is the spin contribution to the angular momentum.

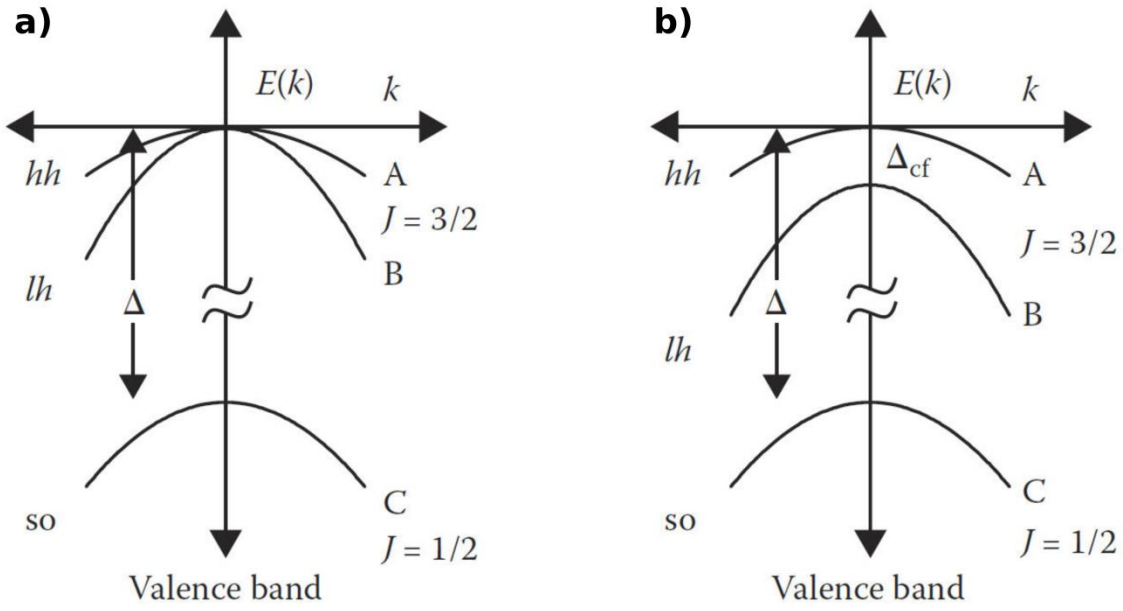

Figure 2.7 a) ideal diamond like band structure and b) Wurtzite CdSe near K =0. (Taken form [12])

Figure 2.7 shows the valence band structure for a) zinc-blende structure lattice and b) wurtzite structure lattice. The resultant crystal field of the hexagonal lattice causes the a and b bands to split [12]

The three subbands are referred to as the heavy-hole (*hh*), light-hole (*lh*), and split-off-hole (*so*) subbands, andare shown in Figure 2.6. At k= 0 the J =3/2 band is degenerate with different curvatures corresponding to different effective masses, hence the names light hole and heavy hole. For many semiconductors, the diamond like band structure is a good approximation but there are two different effects that contribute to split the *hh* and *lh* sub-bands. Firstly, the structure leads to a slightly prolate NQD shape resulting in a crystal field and secondly there is no longer inversion symmetry in the crystal which will further split the A and B bands. As these terms can be relatively small, they are often neglected in calculating the energy levels in QDs [22].

2.4.2. Exciton

If it is assumed that QDs have a spherical shape and a cubic crystal lattice, then each of the electron-hole pair states is highly degenerate. However, in reality QDs can deviate from this model, which breaks this degeneracy. Firstly, as mentioned earlier, CdSe QDs can have a unixial crystal lattice (wurtzite), which leads to a splitting of the valence subbands [29]. Secondly, electron microscopy experiments show that CdSe nanocrystals are not spherical, but rather slightly prolate [30]. This shape anisotropy will split the electron-hole pair states [31]. Finally, the electron–hole exchange interaction, which is negligible in bulk CdSe, can lead to level splitting in nanocrystals due to enhanced overlap between the electron and hole [32-35]. Therefore, when all of these effects are considered, the initially eightfold degenerate band-edge exciton is split into five sublevels [12, 36].

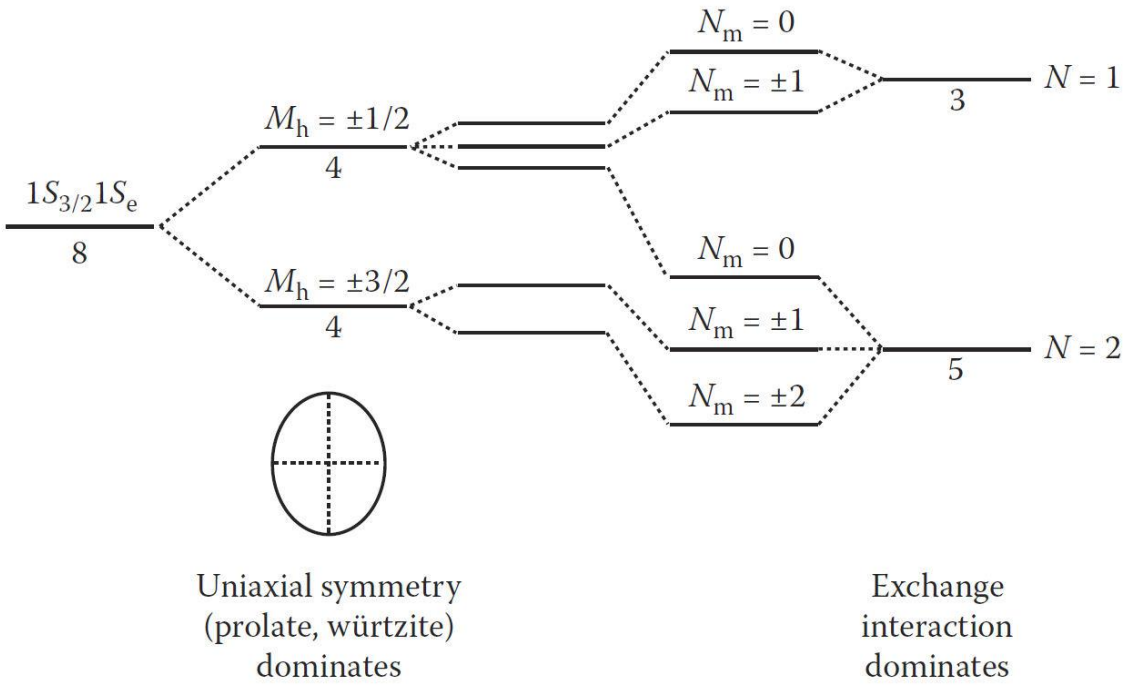

Figure 2.8 Exciton fine structure

To describe the structure (Figure 2.5 taken from [12]), two limits are considered. On the left side of Figure 2.5 the effect of the anisotropy of the crystal lattice or the nonpherical shape of the crystallite dominates[12].The right side represents the small nanocrystal limit where the exchange interaction dominates. When both effects are included, the good quantum number is the projection of N along the unique crystal axis N_m [12]. To include these effects into theory, the anisotropy and exchange terms can be added as perturbations to the spherical model [36].

2.4.3. The Dark exciton

The splitting described above helped to explain a long-standing question in the emission behaviour of CdSe nanocrystal. While exciton recombination in bulk II-VI semiconductors occurs with a ~1ns lifetime, CdSe dots can exhibit a ~1µs life time at 10K [12]. This effect could perhaps be rationalized in early samples, which were of poor quality and emitted weakly via deep trap fluorescence. However, even high-quality samples, which emit strongly at the band edge, have long radiative lifetimes. To explain this behaviour, the emission had been rationalized by many researchers as a surface effect [12]. Once the carriers are localized in surface traps, the decrease in carrier overlap increases the recombination time. This surface model could then explain the long radiative lifetimes, luminescence polarization results, and even the unexpectedly high LO Phonon coupling observed in emission [12].

The presence of exciton fine structure provides an alternative explanation for the anomalous emission behaviour. Emission from the lowest band edge state, $|N_m| = 2$, is optically forbidden in the electric dipole approximation. Relaxation of the electron–hole pair into this state, referred to as the dark exciton, can explain the long radiative lifetimes observed in CdSe QDs. Because two units of angular momentum are required to return to the ground state from the $|N_m| = 2$ sublevel, this transition is one-photon forbidden. However, less efficient, phonon-assisted transitions can occur, explaining the stronger LO-phonon coupling of the emitting state[12].

2.5. Auger recombination

Auger recombination occurs due to the strong spatial confinement of the electronic wave function in QDs, which increases the probability that an electron-hole pair recombines in a non-radiative way. Instead of releasing the energy as photon, the energy is transferred to another particle which could be an electron or a hole. This third particle is excited to a higher energy level without leaving the energy band. After the third particle is excited, the

relaxation of this particle is via vibrational processes [37]. Auger recombination is significantly more efficient in nanostructures than in bulk materials due to this strong carrier wavefunction overlap, especially QDs type I structures [38]. For the type II structure Auger recombination is somewhat reduced by the spatial separation of the carriers into different regions. Figure 2. 9 illustrate the Auger recombination process, and how it contributes to the average (i.e. observed) lifetime.

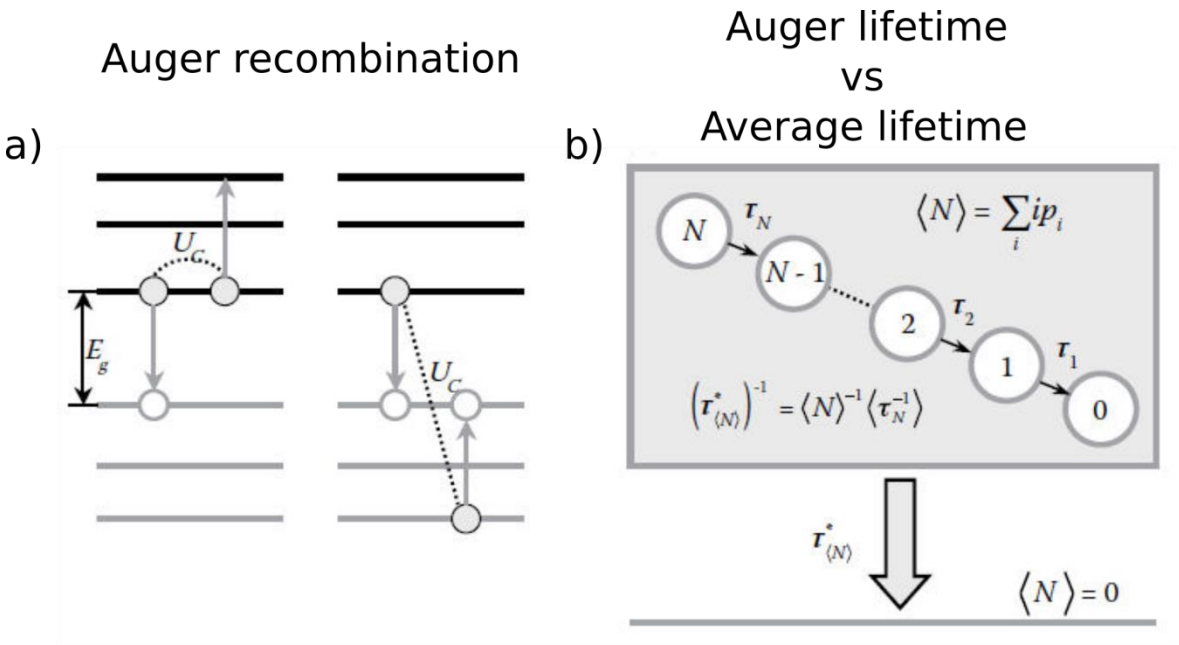

Figure 2. 9 a) Transitions in Auger recombination: the energy of recombination, U_C, is given either to an electron or hole so that it moves to a higher energy state in the CB or VB, respectively. b) An *N* exciton state undergoes Auger recombination with a lifetime τ_N to form a *N-1* exciton state that then undergoes Auger recombination with a lifetime τ_{N-1} to form a *N-2* exciton state and so on until a single exciton state is produced, which cannot under Auger recombination. This process produces a measured decay transient characterized by an average lifetime $\tau^*_{\langle N \rangle}$ which depends on τ_N and the average number of excitons per QD $\langle N \rangle = \sum_i ip_i$, where the probability of a QD containing i excitons, p_i, is determined by Poisson statistics (Modified from [37])

As shown in Figure 2. 9 a), the Auger recombination process always involves three particles, either two electrons and a hole, as shown on the left side, or one electron and two holes, as shown on the right. It cannot, therefore, occur for a single exciton. Auger recombination is an efficient process with typical lifetimes of 10-100 ps, i.e. significantly shorter than radiative lifetimes. Hence, in the absence of trap-related processes, i.e. for

well-passivated samples, Auger recombination is thus the dominant mechanism for multi-excitons, with radiative recombination only becoming significant for single exciton states.

2.6. Auger mediate trapping

The Auger mediate trapping (AMT) mechanism explains how holes become trapped on the surface of QDs. The traps on the surface are related to the unsaturated bonds on the QD surface caused by incomplete passivation. AMT is a non-radiative process which was used first to explain the PL intermittency [39] in QDs. In the AMT model, the electron receives the energy lost by the hole as it is trapped via an Auger interaction, and is thereby excited to higher lever in the conduction band – see Figure 2.9.

AMT rates have been calculated for a number of different CQD types using a semiempirical pseudopotential method [40]. AMT rates are calculated with eq (2. 12)

$$(\tau_{AMT})_i^{-1} = \frac{\Gamma}{\hbar} \sum_n \frac{|\langle i|\Delta H|f_n\rangle|^2}{\left(E_{f_n} - E_i\right)^2 + \left({}^{\Gamma}/_{2}\right)^2} \qquad \textbf{(2. 12)}$$

where $|i\rangle$ and $|f_n\rangle$ are the initial (delocalized) and final (trapped) excitonic states (see Figure 2. 10), E_i and E_{f_n} are their energies , ΔH is the Coulomb interaction and $\Gamma/\hbar$ is the lifetime of the final states. In eq (2. 12) the top expression, ($|\langle i|\Delta H|f_n\rangle|^2$), depends on the degree of wave function overlap and the bottom expression, ($\left(E_{f_n} - E_i\right)^2 + \left({}^{\Gamma}/_{2}\right)^2$), describes how close to resonance are the transition energies of the hole going into the trap and the electron going to a higher energy state.

The energy of the trap levels can also by calculated by the same method, and reveal that there exist hole transitions to trap levels that are sufficiently close to the valance band to allow thermal liberation back to the valance band; this is termed ‘shallow’ trapping. For instance, the energy of the traps states on the surface of CdTe QDs fall into two groups

which have energies of about $E_{VBM}^{Bulk} + 0.450\, eV$ and $E_{VBM}^{Bulk} + 0.050\, eV$.[41]. The second group of states are sufficiently close to the VBM for thermal escape and thus can act as shallow traps.Thus holes can populate these shallow traps and from there either escape back to the valence band using thermal energy [41] or recombine with the electron in the conduction band.

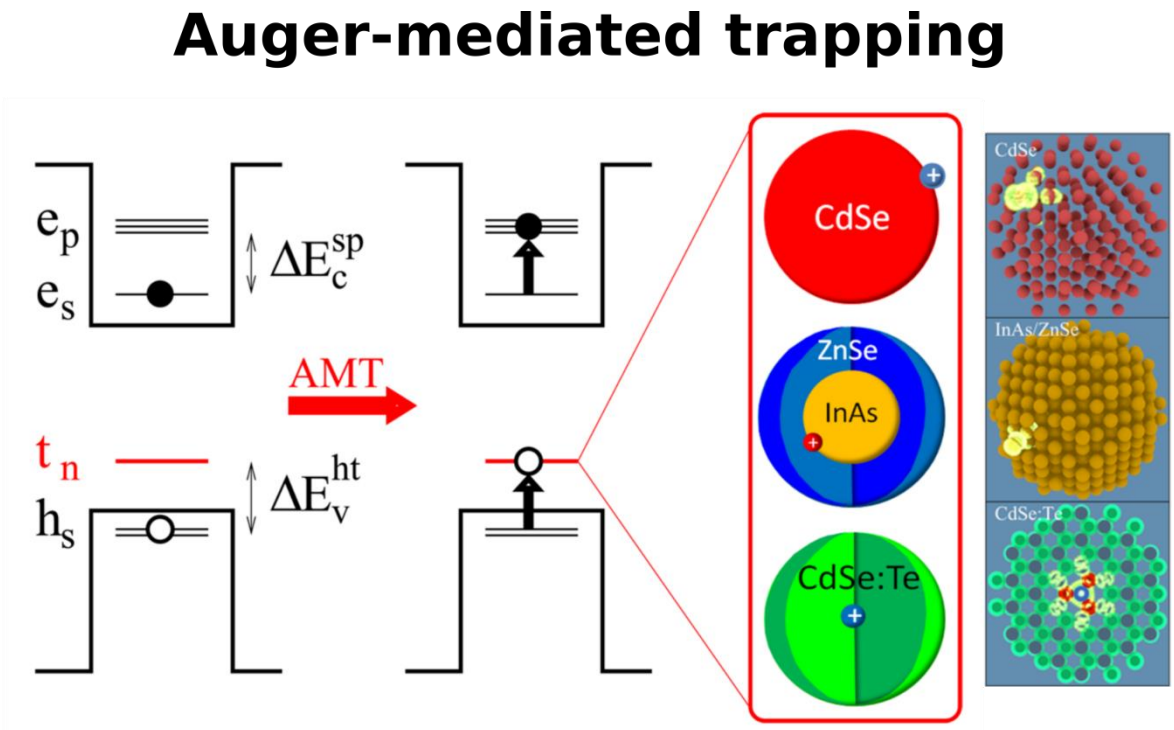

Figure 2. 10 Schematic of the Auger-mediated trapping mechanism (Modified from [40]). ΔE_v^{ht} is the energy of the valance band to hole trap transition. This energy is transferred non-radiatively to the electron which is excited to states higher in energy by ΔE_c^{sp}.)

2.7. Applications

CQDs have a great potential for different applications due to their electronic and optical properties which can be tuned by the relationship of the core size and shell thickness. In recent years, CQDs have gained popularity in optoelectronic device research for a wide range of application is due to this versatility. At the moment the CQDs have been used in photovoltaic devices [42], light emitting diodes [43], biomedical sensors (tagging)[44], photodetectors[45] and lasing[46]. These applications are discussed in more detail below. However, their potential is still to be fully realised because the underlying physics is not yet fully understood.

2.7.1. Photovoltaic devices

QDs have been used in photovoltaics devices due to their low cost and their optical properties. QDs allow the absorption edge to be selected for optimum cell efficiency and, in addition, offer the possibility to exceed the Shockley-Queisser limit for solar cell efficiency [47] by the process of multiple exciton generation (MEG), also known as carrier multiplication. The most common solar cells currently are those based on silicon and gallium arsenide, which have efficiencies upto 24.5% [48], and are called ‘first generation’ devices. The second generation is based on organic thin films, for which affordability is better but the performance is compromised [49]. Solar cells based on QDs may have the advantage of carrier multiplication to increase the efficiency; this occurs when a single absorbed photon produces more than one electron excited from the valence band to the conduction band.

2.7.2. Solid state lighting

Solid state lighting is based on light emitting diodes (LEDs). For over three decades LEDs have been used in industrial and home applications, but were not sufficiently efficient or had the spectral range to compete as a source of lighting. However, in recent years, the lighting market has evolved dramatically, not just in term of consumption or the efficiency

of the devices used, but also in terms of the purity in colour, device size and lifetime, directionality and the response period to switching. Figure 2. 11a) compares the efficiency between lighting systems, with the maximum efficiency is predicted to be more than 250 lm/W [50]. However, efficiency is not the sole factor, with other considerations such as packing, junction temperature, optical loses, etc. also being important. Figure 2. 11b) illustrates the progress of lighting in human history, where the most primitive way to produce light is with fire, which include gas lamps; in 1800's the incandescent light bulbs appeared and revolutionized the way of living, since then different types of lamp have been around, i.e. halogen lamp, metal-halide lamp, mercury lamp, and compact fluorescent lamp (CFL). However, it is not until 90's when LEDs based on quantum wells and QDs that the LEDs started to appear in every possible application due to their efficiency and low power consumption. In Figure 2. 11c) compares the size of a LED to a light bulb and fluorescent tubes (T8 and T5).

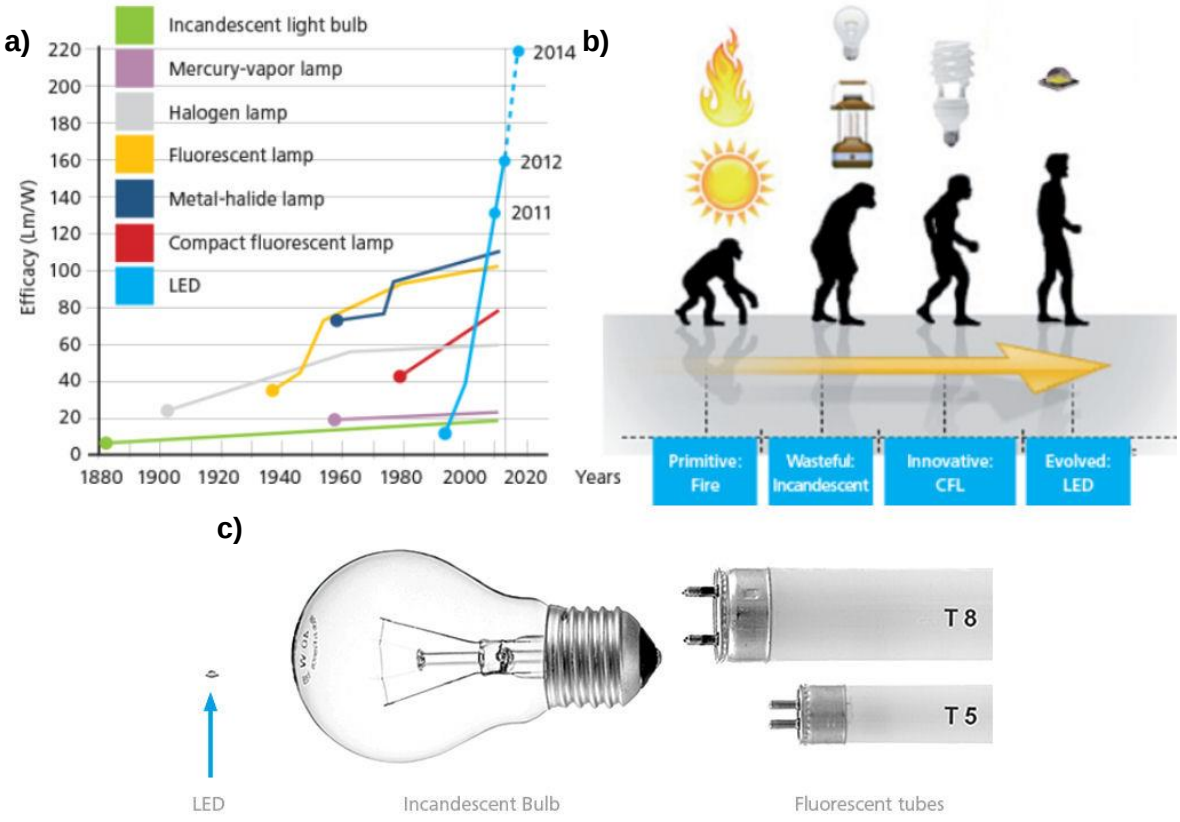

Figure 2. 11 Evolution of the lighting and size comparison of the LED (modify from [51])

2.7.2.1. Phosphor for white light emitting diodes

LEDs produce quasi–monochromatic light rather than the white light required for general illumination. There are two approaches to get white light from a LED based device. The first one is to combine three or more LEDs emitting in different parts of the visible spectrum (ideally one each of red, green and blue LEDs) with fixed power ratios in order to achieve the desired balance of the colours. The result of this is a white light with a specific colour temperature. The other approach is a single LED combined with one or more phosphor materials that absorb some of the LED light and re-emit at longer wavelengths [52]. Currently most commercial LEDs use the combination of a blue LED and a YAG:Ce^{3+} phosphor [52, 53], although UV emitting LEDs are also used [52, 54]. Figure 2.6 shows these three different approaches for obtaining white light (Figure 2.6 taken from [55])

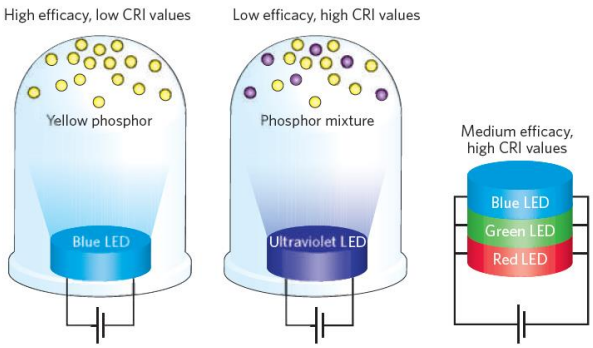

Figure 2. 12 Three dominant ways to produce white light based on LEDs

The luminous efficiency of radiation (LER) is a key performance parameter for lighting, describing how bright the radiation is perceived by the human eye, with units of lumen per watt. It can be calculated by

$$\boldsymbol{LER(lm) = 683\ lm/w \cdot \frac{\int_{360nm}^{830nm} I(\lambda)V(\lambda)d\lambda}{\int_{360nm}^{830nm} I(\lambda)d\lambda}} \quad \textbf{(2. 13)}$$

where $V(\lambda)$ is the eye sensitivity curve, and $I(\lambda)$ is the emission spectrum. As the eye sensitivity peaks at 555 nm, - see Figure 2.12 - the highest possible LER (683 lm/W) is obtained from monochromatic radiation at 555 nm. Therefore, 683 lm/W is the highest possible efficiency that can ever be obtained from a light source i.e. when 100% of the electrical power is converted to light at a wavelength of 555 nm, the efficiency of the light source is 683 lm/W [22, 52, 56].

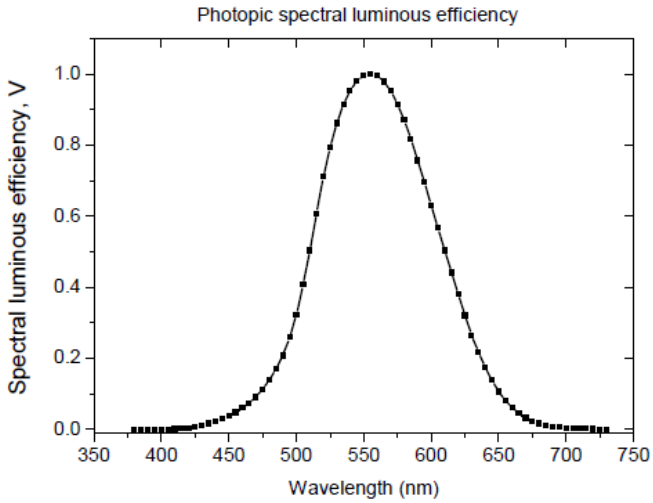

Figure 2. 13 $V(\lambda)$ the eye sensitivity curve - taken form [22]

The effect of the balance of colours obtained from a light source can be quantified by the colour rendering index (CRI). The CRI can be understood as a measure of the perceived colour of an object when illuminated by the light source. The CRI is found by comparing the colour of test objects when illuminated by the light source under test, to the colours of the object illuminated by a reference source, such as daylight [52]. The emission spectrum from a lighting device can also be quantified by its correlated colour temperature (CCT). Here, the spectrum of the test source is compared to that of a black body radiator, and the temperature of the black body that most closely matches the spectrum of the test source is the CCT of the device [52, 57]. Figure 2.13 compares the CRI and CCT of a blue LED plus yellow phosphor and a UV LED plus amixture of red, green and blue GB phosphors to sunlight. It is also clear from Figure 2.13 that the overall shape of the

spectra from these devices differs signficantly from the ideal, i.e. most natural, spectrum of sunlight. This deviation comes about largely from the broad emission about fixed wavelengths of the commonly used phosphors. The appeal of QDs for this application rests largely on the fact that their emission is tunable and much narrower in bandwidth, which enables a much better match with sunlight to be potentially achieved. However, to compete with established phosphors, QDs must also have a similar photoluminesence quantum yield, which approaches unity for the best phosphors [58]. This greater flexibility in colours also means that QDs are strong candidates for the emitting species in other diverse applications, such as TVs, traffic signals, and automobile applications.

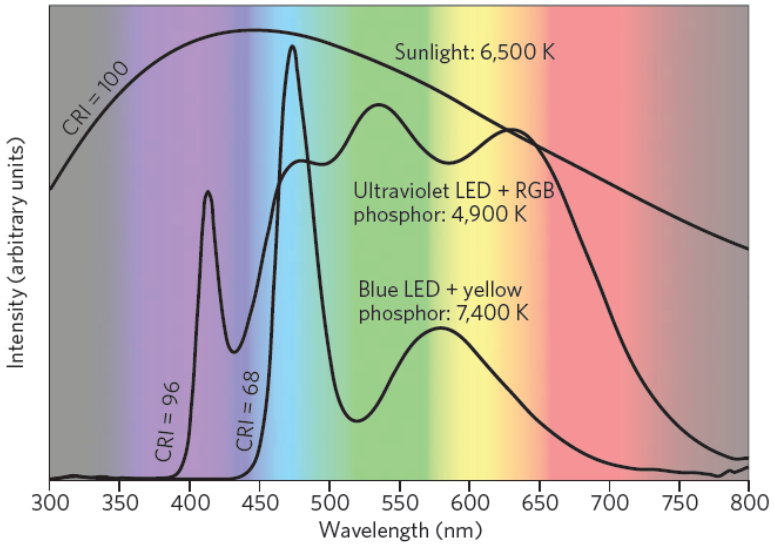

Figure 2. 14 Comparison of the ideal spectrum with two white light LED sources [55].

References

1. Faraday, M., *The Bakerian Lecture: Experimental Relations of Gold (and Other Metals) to Light.* Philosophical Transactions of the Royal Society of London, 1857. 147: p. 145-181.
2. Berry, C.R., *Effects of Crystal Surface on the Optical Absorption Edge of AgBr.* Physical Review, 1967. 153(3): p. 989.
3. Brus, L., *Electronic wave functions in semiconductor clusters: experiment and theory.* The Journal of Physical Chemistry, 1986. 90(12): p. 2555-2560.
4. Steigerwald, M.L., A.P. Alivisatos, J.M. Gibson, T.D. Harris, R. Kortan, A.J. Muller, A.M. Thayer, T.M. Duncan, D.C. Douglass, and L.E. Brus, *Surface Derivatization and Isolation of Semiconductor Cluster Molecules.* Journal of the American Chemical Society, 1988. 110(10): p. 3046-3050.
5. Brennan, J.G., T. Siegrist, P.J. Carroll, S.M. Stuczynski, L.E. Brus, and M.L. Steigerwald, *The preparation of large semiconductor clusters via the pyrolysis of a molecular precursor.* Journal of the American Chemical Society, 1989. 111(11): p. 4141-4143.
6. Saleh, B.E.A. and M.C. Teich, *Fundamentals of Photonics*. second ed. 2007: John Wiley & Sons, Inc.
7. Kortshagen, U., *Nonthermal plasma synthesis of semiconductor nanocrystals.* Journal of Physics D: Applied Physics, 2009. 42(11): p. 113001.
8. Reimann, S.M. and M. Manninen, *Electronic structure of quantum dots.* Reviews of Modern Physics, 2002. 74(4): p. 1283.
9. van der Wiel, W.G., S. De Franceschi, J.M. Elzerman, T. Fujisawa, S. Tarucha, and L.P. Kouwenhoven, *Electron transport through double quantum dots.* Reviews of Modern Physics, 2002. 75(1): p. 1.
10. Stangl, J., Hol, yacute, V., and G. Bauer, *Structural properties of self-organized semiconductor nanostructures.* Reviews of Modern Physics, 2004. 76(3): p. 725.
11. Petroff, P.M. and S.P. DenBaars, *MBE and MOCVD growth and properties of self-assembling quantum dot arrays in III-V semiconductor structures.* Superlattices and Microstructures, 1994. 15(1): p. 15-15.
12. Klimov, V.I., *Nanocrystal quantum dots*. Vol. 2nd ed. 2010: Taylor & Francis, Inc.
13. Alivisatos, A.P., *Semiconductor clusters, nanocrystals, and quantum dots.* Science, 1996. 271(5251): p. 933-937.
14. Michalet, X., F.F. Pinaud, L.A. Bentolila, J.M. Tsay, S. Doose, J.J. Li, G. Sundaresan, A.M. Wu, S.S. Gambhir, and S. Weiss, *Quantum dots for live cells, in vivo imaging, and diagnostics.* Science, 2005. 307(5709): p. 538-544.
15. Reiss, P., M. Protière, and L. Li, *Core/Shell Semiconductor Nanocrystals.* Small, 2009. 5(2): p. 154-168.
16. de Mello, D., aacute, and Celso, *Formation of nanoscale spatially indirect excitons: Evolution of the type-II optical character of CdTe/CdSe heteronanocrystals.* Physical Review B. 81(16): p. 165303.
17. Tytus, M. and et al., *Differences between photoluminescence spectra of type-I and type-II quantum dots.* Journal of Physics: Conference Series, 2008. 104(1): p. 012011.
18. Piryatinski, A., S.A. Ivanov, S. Tretiak, and V.I. Klimov, *Effect of Quantum and Dielectric Confinement on the Excitonâ^'Exciton Interaction Energy in Type II Core/Shell Semiconductor Nanocrystals.* Nano Letters, 2006. 7(1): p. 108-115.
19. Lamer, V.K. and R.H. Dinegar, *Theory, Production and Mechanism of Formation of Monodispersed Hydrosols.* Journal of the American Chemical Society, 1950. 72(11): p. 4847-4854.

20. Majumder, S., I.T. Bae, and M.M. Maye, *Investigating the role of polytypism in the growth of multi-shell CdSe/CdZnS quantum dots.* Journal of Materials Chemistry C, 2014. 2(23): p. 4659-4666.
21. Brus, L., *Quantum crystallites and nonlinear optics.* Applied Physics A: Materials Science & Processing, 1991. 53(6): p. 465-474.
22. Stubbs, K.S., *"Photo-physics and applications of colloidal quantum dots"*, 2010, PhD Thesis.
23. Klimov, V.I., *Spectral and dynamical properties of multilexcitons in semiconductor nanocrystals.* Annual Review of Physical Chemistry, 2007. 58: p. 635-673.
24. Berry, C.R., *Structure and Optical Absorption of AgI Microcrystals.* Physical Review, 1967. 161(3): p. 848.
25. Irimpan, L., V.P.N. Nampoori, and P. Radhakrishnan, *Visible luminescence mechanism in nano ZnO under weak confinement regime.* Journal of applied physics, 2008. 104(11): p. 113112.
26. Peng, X.G., *Mechanisms for the shape-control and shape-evolution of colloidal semiconductor nanocrystals.* Advanced Materials, 2003. 15(5): p. 459-463.
27. Efros, A.L. and A.L. Efros, *Interband Absorption of Light in a Semiconductor Sphere.* Soviet Physics Semiconductors-Ussr, 1982. 16(7): p. 772-775.
28. Brus, L.E., *A Simple-Model for the Ionization-Potential, Electron-Affinity, and Aqueous Redox Potentials of Small Semiconductor Crystallites.* Journal of Chemical Physics, 1983. 79(11): p. 5566-5571.
29. Efros, A.L., *Luminescence Polarization of Cdse Microcrystals.* Physical Review B, 1992. 46(12): p. 7448-7458.
30. Murray, C.B., D.J. Norris, and M.G. Bawendi, *Synthesis and characterization of nearly monodisperse CdE (E = sulfur, selenium, tellurium) semiconductor nanocrystallites.* Journal of the American Chemical Society, 1993. 115(19): p. 8706-8715.
31. Efros, A.L. and A.V. Rodina, *Band-Edge Absorption and Luminescence of Nonspherical Nanometer-Size Crystals.* Physical Review B, 1993. 47(15): p. 10005-10007.
32. Calcott, P.D.J., K.J. Nash, L.T. Canham, M.J. Kane, and D. Brumhead, *The Luminescence Mechanism of Porous Silicon.* Microcrystalline Semiconductors : Materials Science & Devices, 1993. 283: p. 143-148.
33. Takagahara, T., *Effects of Dielectric Confinement and Electron-Hole Exchange Interaction on Excitonic States in Semiconductor Quantum Dots.* Physical Review B, 1993. 47(8): p. 4569-4585.
34. Nomura, S., Y. Segawa, and T. Kobayashi, *Confined Excitons in a Semiconductor Quantum-Dot in a Magnetic-Field.* Physical Review B, 1994. 49(19): p. 13571-13582.
35. Chamarro, M., C. Gourdon, P. Lavallard, and A.I. Ekimov, *Enhancement of Exciton Exchange Interaction by Quantum Confinement in Cdse Nanocrystals.* Japanese Journal of Applied Physics Part 2-Letters, 1994. 34: p. 12-14.
36. Nirmal, M., D.J. Norris, M. Kuno, M.G. Bawendi, A.L. Efros, and M. Rosen, *Observation of the Dark Exciton in Cdse Quantum Dots.* Physical Review Letters, 1995. 75(20): p. 3728-3731.
37. Klimov, V.I., *Nanocrystal Quantum Dots, Second Edition*. Laser and Optical Science and Technology. 2010: CRC PRESS-TAYLOR & FRANCIS GROUP.
38. Nanda, J., S.A. Ivanov, H. Htoon, I. Bezel, A. Piryatinski, S. Tretiak, and V.I. Klimov, *Absorption cross sections and Auger recombination lifetimes in inverted core-shell nanocrystals: Implications for lasing performance.* Journal of Applied Physics, 2006. 99(3).
39. Frantsuzov, P.A. and R.A. Marcus, *Explanation of quantum dot blinking without the long-lived trap hypothesis.* Physical Review B, 2005. 72(15).
40. Califano, M. and F.M. Gomez-Campos, *Universal Trapping Mechanism in Semiconductor Nanocrystals.* Nano Letters, 2013. 13(5): p. 2047-2052.

41. Califano, M., *Origins of Photoluminescence Decay Kinetics in CdTe Colloidal Quantum Dots.* Acs Nano, 2015. 9(3): p. 2960-2967.
42. Kamat, P.V., *Quantum Dot Solar Cells. The Next Big Thing in Photovoltaics.* Journal of Physical Chemistry Letters, 2013. 4(6): p. 908-918.
43. Kim, S., S.H. Im, and S.W. Kim, *Performance of light-emitting-diode based on quantum dots.* Nanoscale, 2013. 5(12): p. 5205-5214.
44. Thakar, R., Y.C. Chen, and P.T. Snee, *Efficient emission from core/(doped) shell nanoparticles: Applications for chemical sensing.* Nano Letters, 2007. 7(11): p. 3429-3432.
45. Prins, F., M. Buscema, J.S. Seldenthuis, S. Etaki, G. Buchs, M. Barkelid, V. Zwiller, Y.N. Gao, A.J. Houtepen, L.D.A. Siebbeles, and H.S.J. van der Zant, *Fast and Efficient Photodetection in Nanoscale Quantum-Dot Junctions.* Nano Letters, 2012. 12(11): p. 5740-5743.
46. Dang, C., J. Lee, C. Breen, J.S. Steckel, S. Coe-Sullivan, and A. Nurmikko, *Red, green and blue lasing enabled by single-exciton gain in colloidal quantum dot films.* Nature Nanotechnology, 2012. 7(5): p. 335-339.
47. Shockley, W. and H.J. Queisser, *Detailed Balance Limit of Efficiency of P-N Junction Solar Cells.* Journal of Applied Physics, 1961. 32(3): p. 510-&.
48. Zhao, J., A.H. Wang, and M.A. Green, *24.5% efficiency PERT silicon solar cells on SEH MCZ substrates and cell performance on other SEH CZ and FZ substrates.* Solar Energy Materials and Solar Cells, 2001. 66(1-4): p. 27-36.
49. Green, M.A., K. Emery, Y. Hishikawa, W. Warta, and E.D. Dunlop, *Solar cell efficiency tables (version 43).* Progress in Photovoltaics, 2014. 22(1): p. 1-9.
50. Soer, W.V., K.; Shchekin, O., *The Road to 250 lm/W.* Philips Lumileds, 2014.
51. Lighting, O. *LED ACADEMY*. http://www.ledacademy.net/.
52. Smet, P., A. Parmentier, and D. Poelman, *Selecting Conversion Phosphors for White Light-Emitting Diodes.* Journal of the Electrochemical Society, 2011. 158(6): p. R37-R54.
53. Nizamoglu, E., *Warm-white light-emitting diodes integrated with colloidal quantum dots for high luminous efficacy and color rendering.* Optics letters. 35(20): p. 3372.
54. Oh, J.R., S.H. Cho, J.H. Oh, Y.K. Kim, Y.H. Lee, W. Kim, and Y.R. Do, *The realization of a whole palette of colors in a green gap by monochromatic phosphor-converted light-emitting diodes.* Optics Express, 2011. 19(5): p. 4188-4198.
55. Pimputkar, S., J.S. Speck, S.P. DenBaars, and S. Nakamura, *Prospects for LED lighting.* Nat Photon, 2009. 3(4): p. 180-182.
56. Phillips, J.M., M.E. Coltrin, M.H. Crawford, A.J. Fischer, M.R. Krames, R. Mueller-Mach, G.O. Mueller, Y. Ohno, L.E.S. Rohwer, J.A. Simmons, and J.Y. Tsao, *Research challenges to ultra-efficient inorganic solid-state lighting.* Laser & Photonics Reviews, 2007. 1(4): p. 307-333.
57. McCluney, W.R., *Introduction to Radiometry and Photometry* 1994 ARTECH HOUSE, INC. .
58. Gorrotxategi, P., M. Consonni, and A. Gasse, *Optical efficiency characterization of LED phosphors using a double integrating sphere system.* Journal of Solid State Lighting, 2015. 2(1): p. 1.
59 Wang, J. and M. Isshiki, Wide-Bandgap II–VI Semiconductors: Growth and Properties, in Springer Handbook of Electronic and Photonic Materials, S. Kasap and P. Capper, Editors. 2007, Springer US. p. 325-342.
60 Datta, S., T. Saha-Dasgupta, and D.D. Sarma, Wannier function study of the relative stability of zinc-blende and wurtzite structures in the CdX (X = S, Se, Te) series. Journal of Physics-Condensed Matter, 2008. 20(44).
61 Capek, R.K., I. Moreels, K. Lambert, D. De Muynck, Q. Zhao, A. Vantomme, F. Vanhaecke, and Z. Hens, Optical Properties of Zincblende Cadmium Selenide Quantum Dots. Journal of Physical Chemistry C, 2010. 114(14): p. 6371-6376.

Chapter 3. Experiments.

3.1. Introduction

This chapter will describe the optical spectroscopy techniques used to characterise the quantum dots. Optical spectroscopy has the advantage of being a non-destructive technique, and does not require physical contact with the quantum dots under study.

3.2. Absorption spectroscopy

Steady state absorption spectroscopy refers to the technique that measures the absorbance spectrum, that is the light absorbed as a function of wavelength, due to its interaction with the material.

An ideal instrument has a light source that emits with equal intensity at all wavelengths, a monochromator that splits the beam into its constituent wavelengths, and a detector that responds to all wavelengths. The basic principle is illustrated schematically in Figure 3. 1 below.

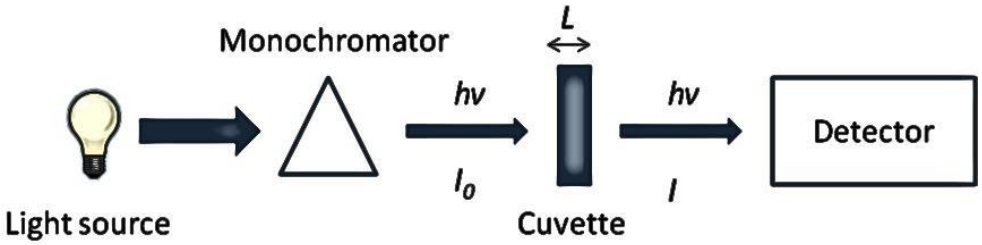

Figure 3. 1 Principle of an absorption experiment.

The intensity of the beam, before the sample, is defined as I_0. The intensity of the beam after sample is defined as I.

When I_0 = I the sample does not absorb light at that wavelength. If $I_0 > I$ there is absorption of the light in the sample. The amount of light absorbed is usually described either by the absorbance $A = log\frac{I_0}{I}$,or the transmittance, $T = \frac{I}{I_o}$.

In this work a LAMBDA 1050 WB UV/Vis/NIR Spectrophotometer, shown in Figure 3. 2, was used to obtain absorbance spectra. Its operation is described in detail below.

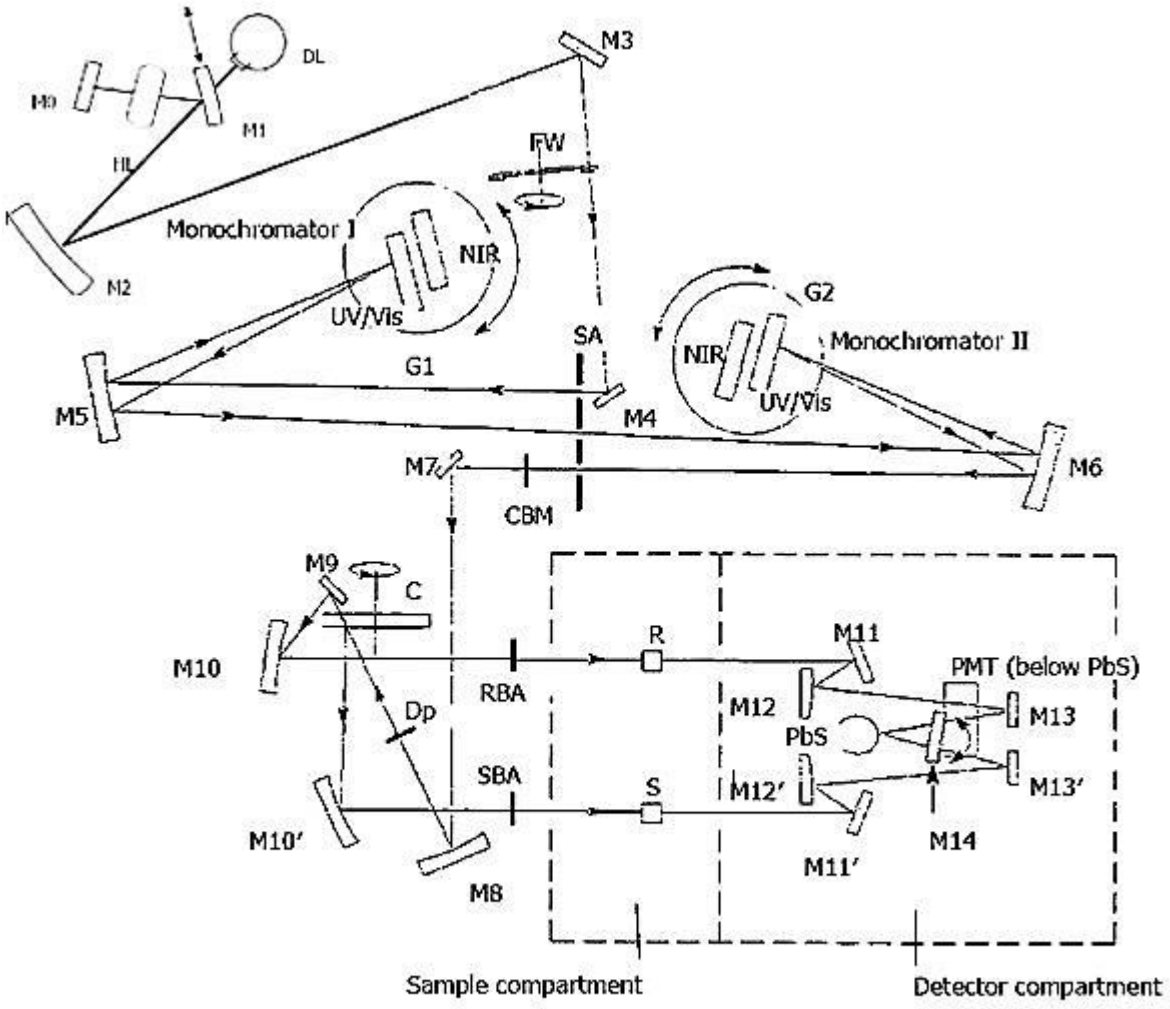

Figure 3. 2 The optical layout of the Lambda 1050 spectrometer (Modified from [1])

The system has two excitation sources, a deuterium lamp, (DL) for the UV range and halogen lamp (HL) for the near-infrared (NIR) and visible (Vis) ranges.

The mirror M0 increases the intensity of the light from the halogen lamp which is reflected by mirror M1 to mirror M2. At the same time it blocks the radiation from the deuterium lamp. For operation in the NIR range, the mirror M1 is raised to allow the radiation from the deuterium lamp to mirror M2. The source change is automatic. The radiation from the corresponding lamp is reflected from mirror M2 to mirror M3 through an optical filter on the filter-wheel assembly (FW) to mirror M4. The FW is controlled by a stepping motor that is synchronized with the monochromators. The filters are selected depending on the wavelength range; an optical filter is located in the beam path to pre-filter the radiation directed to mirror M4. From this mirror, the beam is redirected through the entrance slit of Monochromator I. All the slits are located on a slit assembly (SA).

The beam is collected at mirror M5 and directed to grating G1. The beam will hit either the UV/Vis grating or the NIR grating, depending upon the wavelength range selected. (The grating monochromator has 1440 Lines/mm UV/Vis blazed at 240 nm and 360 Lines/mm NIR blazed at 1100 nm).

The beam is dispersed into its spectrum by the grating and a range from this spectrum is selected by the rotational position of the grating. The selected segment of the spectrum is directed to mirror M5 and through the exit slit. The exit slits restricts the selected segment of the spectrum to a near monochromatic beam.

This beam is directed to Monochromator II. The beam from M5 is reflected to mirror M6 and directed to the appropriate grating G2 (UV/Vis grating or the NIR grating). Then the beam is reflected back to mirror M6 and directed through the exit slit to mirror M7. The rotational position of both grating G1 and G2 are synchronized. The beam emerging the exit slits has high spectral purity with low stray radiation content.

The slits widths are automatically changed by the software during the scanning to maintain constant energy at the detectors.

A common beam mask (CBM) is mounted between the slit assembly (SA) and mirror M7. The mask restricts the cross section of the beam. The beam is directed from mirror M7 via mirror M8 to a depolarizing filter (DP), which is optional, and then to the chopper assembly (C). As the chopper rotates, a mirror segment, a window segment and two dark segments are brought into the beam in turn.

The reference beam (R) is created when the window segment enters the beam, the beam passes through to mirror M9 and is directed to mirror M10. The sample beam (S) is when mirror segment enters the beam; the reflected beam is directed via mirror M10' to the sample path beam. The two dark segments are used to create the dark signal, when a dark segment is in the beam path, no radiation is detected.

There are internal attenuators for the sample beam (SBA) and the reference beam (RBA). The possible values are 0%, 0.1%, 1% and 100% transmittance.

The alternated beam from the reference and sample are directed to the correct detector by using mirrors M11, M12, M13, and M11', M12', M13'.The software controls the detectors changeover and is fixed by the wavelength ranges.

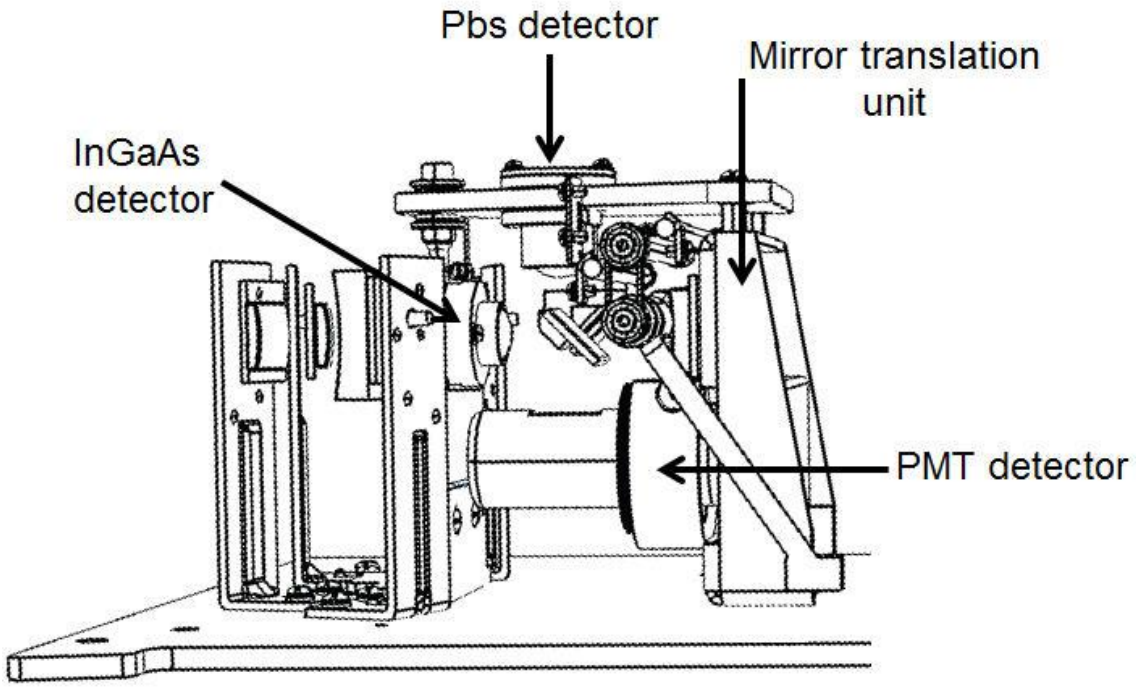

Figure 3. 3 The three Detector Module (Modifed form [2])

The detector compartment is based on a module with three detectors, a photomultiplier tube (PMT) detector for the UV/Vis range (175–860 nm), and for the NIR a wideband InGaAs detector (860–2500 nm) and a lead sulfide (PbS) detector (860–3300 nm). This is shown in Figure 3. 3

The LAMBDA 1050 WB UV/Vis/NIR Spectrophotometer is controlled by the software UV WinLab [3] and the instrument is calibrated via this software, as well.

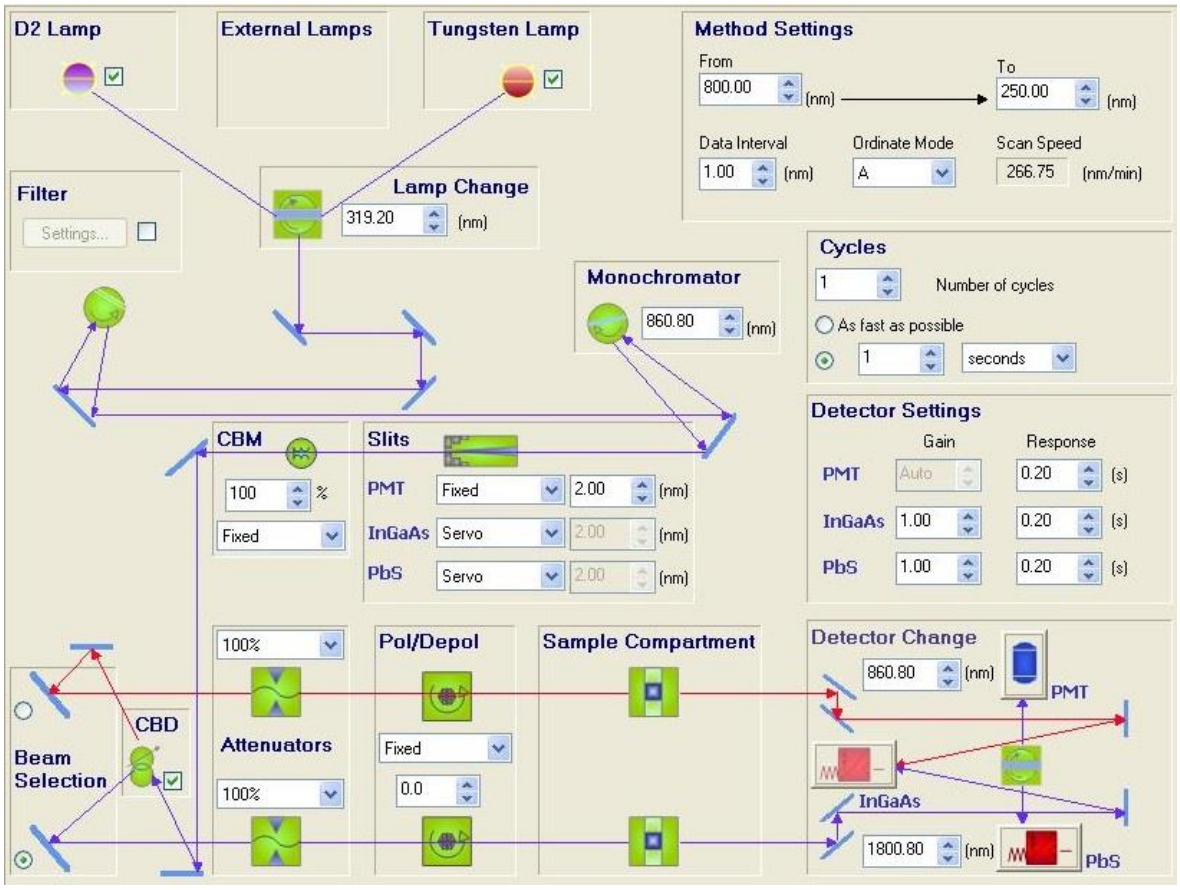

Figure 3. 4 The data collection display, where the setup of the lamp sources, detectors and scanned region are selected (taken from [3])

The data collection screen is shown in Figure 3. 4. This screen allows the experimental parameters to be changed: excitation sources (deuterium and/or halogen-tungsten or an external lamp), filters (predetermined by the wavelength range), monochromator, slits, common beam mask (CBM) which reduces the cross-section, beam selection (change the path of the beam to fit different accessories), common beam depolarizer (CBD), rear and front beam attenuators, depolarizer and polarizer, wavelength range, cycles and detector settings.

3.3. Fluorescence spectroscopy

Emission spectroscopy is a complementary technique to absorption spectroscopy; this technique reveals the energy spectra of the electronic transitions from an excited state to the ground state, while absorption spectroscopy reveals the transitions from the ground state to an excited state. In this work emission, also known as photoluminescence (PL) or fluorescence spectroscopy, provides information about the band gap, exciton binding energies and quantum dot sizes.

When an electron is in an excited state, it can release the energy it had gained from excitation through emission of a photon, and thus go to the ground state. This effect is called fluorescence and for QDs typically occurs on the time scale of 10's of nanoseconds [4]. The energy of the emission is typically less than that of absorption. *i.e* the fluorescence typically occurs at lower energies or longer wavelengths.

The spectrofluorometer Fluorolog-3 model FL3-22iHR from Horiba Jobin Yvon was used in this work and (see in Figure 3. 5)

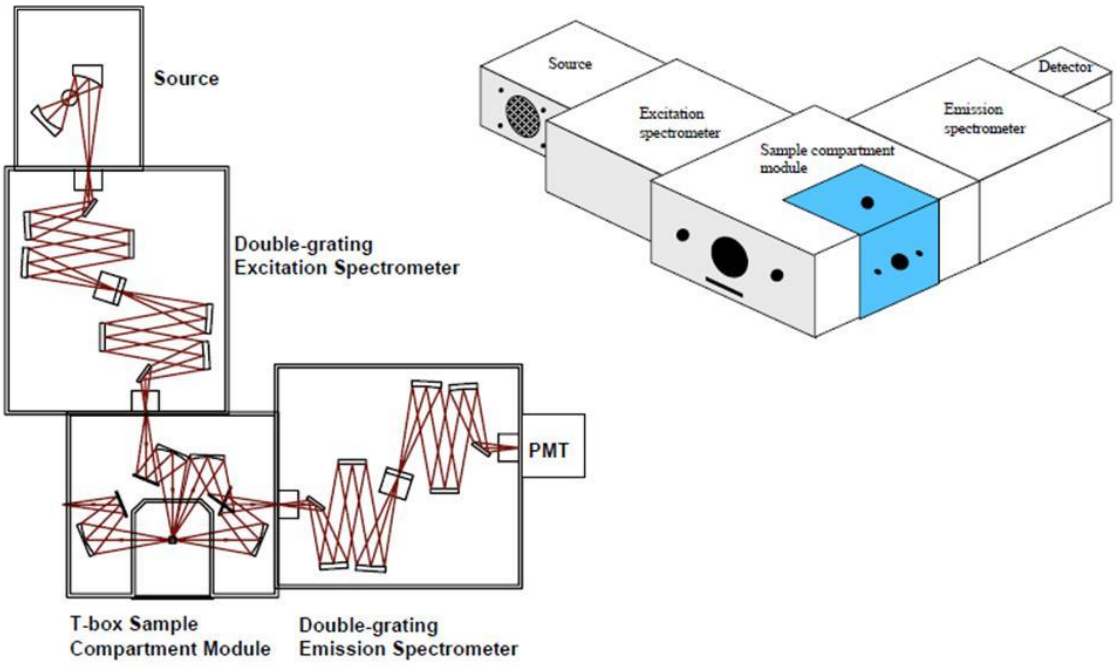

Figure 3. 5 The Fluorolog 3-22iHR (modified from[5])

The optical system consists of a 450W xenon lamp as an excitation source: the lamp is cooled by air and mounted in a vertical position. The mirror in front the lamp increases the intensity of the lamp and then the light is collected and directed by a mirror through a slit to the excitation spectrometer. This enables the excitation wavelength to range from 220 nm to 600 nm (via a double grating monochromator with 1200 lines/mm and blazed at 330 nm).

The spectrum after the exit slit of the double grating corresponds to a near monochromatic radiation beam with high spectral purity and extremely low stray radiation content. The beam is directed to the T-box or sample compartment. The light from the sample can be collected and directed in two different ways: standard right-angle emission or front-face emission.

The beam from the sample is directed to the emission spectrometer through slits, the double grating emission spectrometer range is from 290nm to 850nm (the double grating monochromator has 1200 lines/mm and is blazed at 500 nm). After the emission spectrometer, the light is directed through the slits to the R928P PMT, which is cooled by water. All the slits are controlled and calibrated by software.

The F-3018 integrating sphere accessory was fixed in the T-box, during the measurement of PL quantum yield. In section 3.5, the method used for measuring quantum yield is described in some detail because it proved experimentally challenging to obtain reliable and repeatable results for our samples, and considerable effort was needed to identify the sources of experimental error.

3.4. Fluorescence lifetime measurements

Time correlated single photon counting (TCSPC) is a well-known and frequently used technique for fluorescence lifetime measurement. It is also used for measurements of photon migration, optical time domain reflectometry and time of flight measurements (TOF)[6].

The TCSPC system is based on the detection of single photons and measuring the time intervals between each photon detected. TCSPC is a statistical method which requires a great number of events (detected photons). The detected photons are accumulated in channels according to arrival time. Each channel represents the probability that a photon is detected within certain time interval. The principle of the TCSPC is shown in Figure 3. 6.

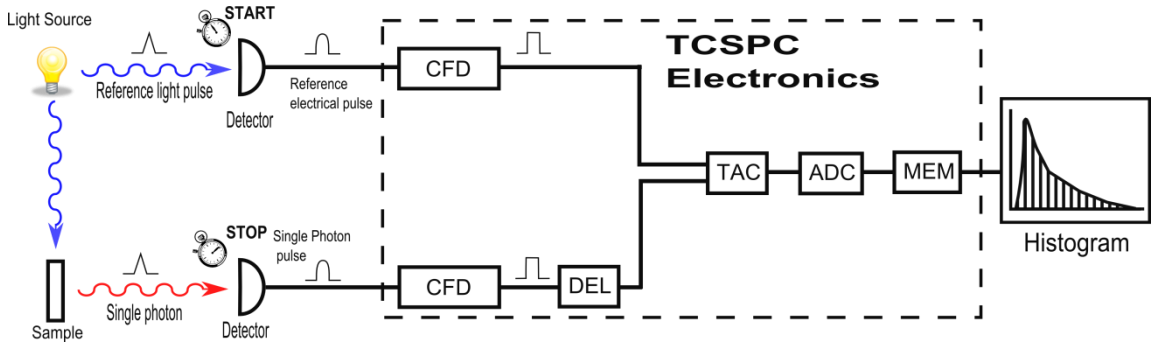

Figure 3. 6 The principle of the TCSPC system.(modified from [7])

The TCSPC electronics can be compared to a stopwatch with a start and stop signals. The stopwatch is started by the reference electrical pulse (start) and stopped by the single photon pulse (stop).The time recorded for one “start-stop” sequence is represented by a stack base memory allocation; this memory is divided in channels that form the histogram. The histogram represents fluorescence intensity or number of counts (y-axis) versus time or channels (x-axis). The process of recording a single “start-stop” depends on the repetition rate of the light source, detectors and the TCSPC electronics.

The TCSPC electronics are shown in Figure 3. 7, the main modules are: Constant Fraction Discriminators (CFD), electrical delays (DEL), Time-to-Amplitude Converter (TAC), Analogue to Digital Converter (ADC) and digital memory (MEM).

The Constant Fraction Discriminators (CFD) select peaks that are higher than a threshold value, the peaks are chosen by setting the zero crossing, which is an offsetting level adjustment of the timing jitter introduced by amplitude jitter of the detector pulses. The output is a pulse with a standard height and shape.

The Time-to-Amplitude (TAC) measures the time interval between the start and stop input pulses. The output is an analogue pulse which ramps up to am amplitude which depends on the stop signal.

The Analogue to Digital Converter (ADC) transforms the height of an analogue pulse to a height of a digital pulse, this digital pulse is a discrete value saved in a bin or channels. The width and number of the bins sets the full time range.

3.4.1. System description

The TCSPC experiment used in this work was built by Stuart Stubbs, Thomas Badcock and me and is shown in Figure 3. 7.

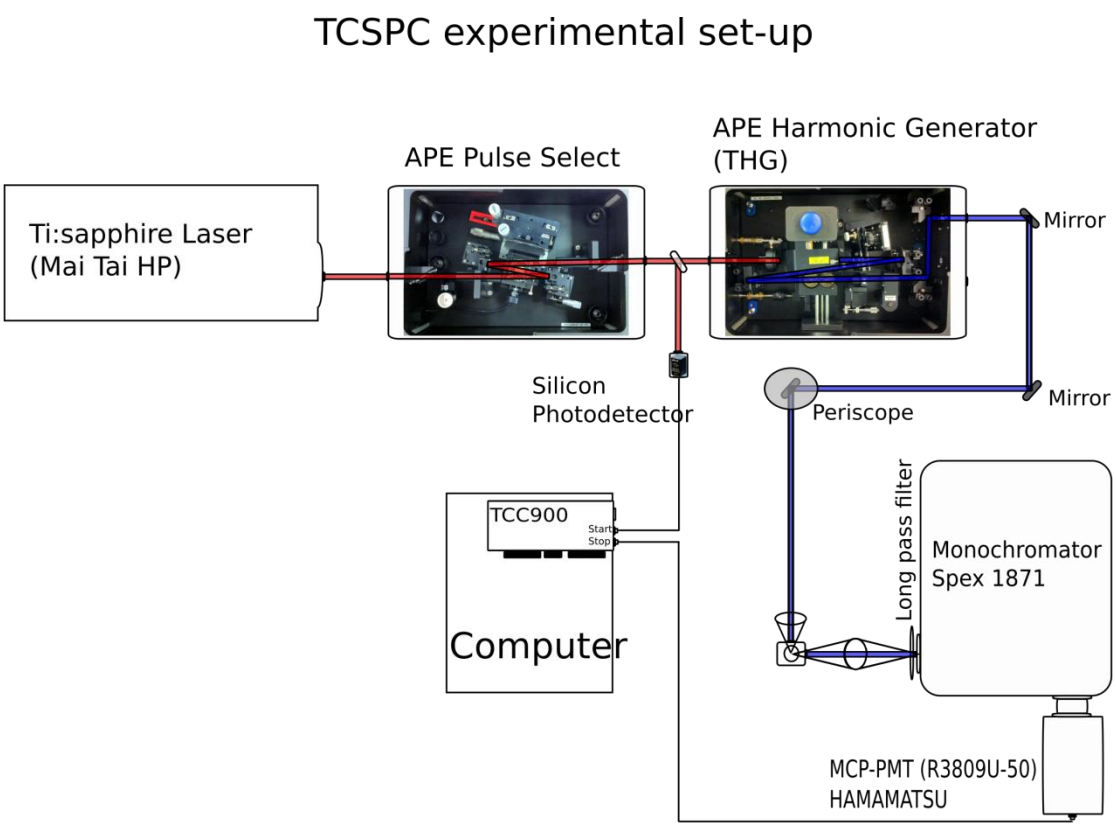

Figure 3. 7 TCSPC experimental set-up.

The excitation source is a Spectra Physics Mai Tai High Performance (HP) mode-locked Ti:Sapphire femtosecond laser. This system has a repetition rate of 80 MHz, a range of tuning from 690 nm to 1020 nm, a pulse width <100 fs and a maximum average power of 2.5 W at 800nm. The Mai Tai laser is pumped with 15 W power at 532 nm by a CW Nd:YVO_4 laser.

The laser beam is directed to the APE Pulse Select [8],which decreases the repetition rate from 80 MHz to 8 MHz or 4 MHz. The Pulse Select is a module that contains two main parts: an electronic driver and optical module. In the optical module there is a Bragg-cell that allows us to select single pulses from the laser beam with the help of the acousto-

optical effect. The electronic driver gives a modulated RF signal for the Bragg-cell with a carrier frequency equal to five times the repetition frequency of the laser and an output power up to 17.5 W. When the beam passes through the crystal and the acoustic wave is inside the crystal, the crystal acts like an optical grating, the pulse train is deflected to the first diffraction order. These pulses are used in the experiment and the zero order pulses are blocked with a blade.

The output beam from the Pulse Select is directed to the APE Harmonic Generator and the EOT Silicon Photodetector (ET-2000) though a beam splitter. The Photodetector sends a signal to the TCC900 (Edinburgh Instruments) that is the TCSPC electronics. The signal from the photodetector acts as the “start” for the system.

The APE Harmonic generator (Third Harmonic Generator THG) is designed to triple or double the optical frequency. The beam from the Pulse Select is focussed to the doubling crystal (SHG X-tal) [9] by a mirror. Here the frequency is doubled by the nonlinear optical interaction in the crystal; with the phase-matching condition fulfilled by angle tuning the crystal. The generated beam and fundamental beams passes through a compensator block, which corrects for the difference in angle of refraction introduced between the two beams by the difference in refractive index at the fundamental and second harmonic wavelengths. Both beams are focussed into the THG crystal where the frequency is tripled if needed.

After the THG crystal, the beams are collimated by a curved mirror and a dichroic mirror separates the THG beam, the SHG beam and the depleted fundamental. The THG or SHG are selected by steering mirrors and sent to the output.

The output beam from the harmonic generator is directed to the sample holder, through two mirrors, and a periscope; it is focused with a microscope lens (Olympus DPlan 10x,NA=0.25) for experiments for which high fluxes are required. The light emitted by the

sample is collected by lenses and sent to the monochromator (Spex 1871) through a band pass filter, which blocks the residual scattered laser light.

The monochromator (Spex 1871) is controlled by the HORIBA Jobin Yvon SynerJY™ software. The light from monochromator is directed to the detector. The photoluminescence peak of the sample is usually chosen as the detection wavelength, however we can detect across the spectra

The detector is a microchannel plate-photo multiplier tube (MCP-PMT) from Hamamatsu (R3809U-50). This MCP-PMT has a range from 160 nm to 850 nm and uses multialkali as photocathode material. When a photon is detected by the MCPT, it sends a signal to the TCC900, which acts as the “stop” signal.

The TCC900 has two modes of operation: the “forward” and the “reverse” mode. The forward mode has the start signal as a regular event and the stop rate as a random event (since it is the probability to detect a photon in a period of time). If the photon is not detected the next start pulse works as rest and re-start. At high repetition rates (50 MHz to 100 MHz) and low detection probability, this is an inefficient use of the electronics. Therefore the reverse mode is often employed, which uses a timing delay so that the stop signal begins the timing and it end when the start signal arrives. In this mode, the electronics works at lower rate. See Figure 3. 8 for a schematic comparison of the forward and reverse mode.

In this work, the fluorescence decay was recorded in forward mode because the repetition rate of the laser was 80MHz and was divided in the pulse picker by factors of 10 times(8 MHz), 20 times(4 MHz) and 40 times(2 MHz).

The wavelength from the laser was tunable, the wavelengths used were 800 nm and 840 nm , at these wavelengths the maximum ~2.5 W power is, after decreasing the repetition rate and generating the second harmonic beam, the maximum power is ~3 mW .

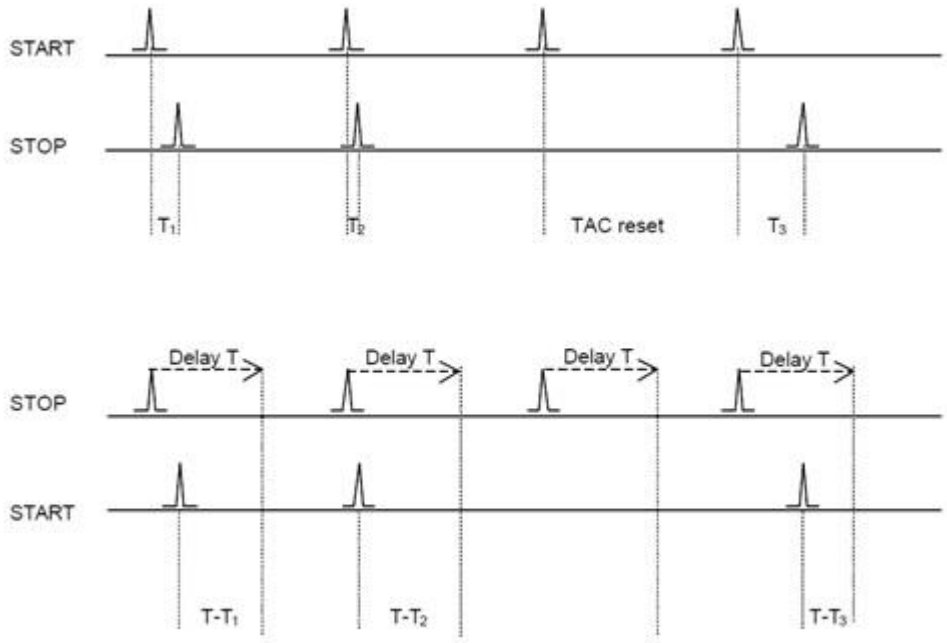

Figure 3. 8 Operations modes of the TCC900, forward (above) and reverse mode (below). (Taken from [10])

3.4.2. Calculation of the fluence, absorption cross-section and average number of photons absorbed per CQD.

The focal spot diameter was calculated using eq. (3. 1)

$$\emptyset = \frac{4}{\pi} \cdot \frac{f\lambda}{D} \cdot M^2 \quad \textbf{(3. 1)}$$

where f is the focal length of the microscope objective used to concentrate the excitation beam (17.69 mm), λ is the excitation wavelength (420 nm), D is diameter of the excitation beam (2.8 mm) and M^2 is the beam quality of the laser beam (<1.1). The focal spot diameter was thus calculated to be 0.003 mm. and the Rayleigh length, Z_R was 0.02 mm where

$$Z_R = \frac{\pi}{\lambda}\left(\frac{\phi}{2}\right)^2 \quad \textbf{(3. 2)}$$

The PL generated by the excitation beam was collected by a converging lens imaged onto the monochromator entrance slit according to (3. 2)

The focal point was calculated using eq. (3. 3)

$$\frac{1}{f} = \frac{1}{u} + \frac{1}{v} \quad \textbf{(3. 3)}$$

where u is the (object distance i.e.) distance from the excitation volume to the lens in this case (v is the image distance) i.e. is the distance from the lens to the entrance slit of the monochromator in this case, and f is the focal distance of the lens which had a value of ±12.5 cm. The total distance to from the object to the slit was 50 cm, and the lens was placed half way between them i.e a "$4f$" focusing scheme was used.

The magnification due to the lens was calculated using eq. (3. 4),

$$M = \frac{u}{v} \tag{3. 4}$$

and had a value of unity since $u = v = 2f$ for this arrangement

The extent of the excited volume sampled by the monochromator was determined by the entrance slit of the monochromator, which was set to a 1 mm throughout. Due to the $4f$ focusing a 1mm section of the excited volume was sampled by this slit width. The lens was carefully aligned by maximising the detected signal, which was assumed to correspond to when the focal point was at the centre of the sampled region. Since Z_R was small compared to the slit width, the sampled region could be described by two identical cones with apexes touching at the focal point, located in the centre of the sampled region, and a cone half-angle equal to the beam divergence half-angle. The average radius of the sample part of the excited volume is thus equal to the radius of one of these cones at a distance 0.25 mm from the focal point. The beam divergence half angle was 0.08 radians, which was calculated using eq. (3. 5).

$$beam\ divergence = tan^{-1}\left(\frac{diameter\ beam}{2\ focal\ length}\right) \tag{3. 5}$$

the average radius, $\mathrm{r}_{\mathrm{average}}$ was thus calculated using (3. 6)

$$r_{average} = 0.25 \cdot \tan(beam\ divergence) \tag{3. 6}$$

The repetition rate of the laser was 2 MHz with an average power of 5 mW, which corresponds to a pulse energy of 2.5 nJ. The average fluence during a pulse is given by the ratio between pulse energy and average area, $A_{average} = \pi \mathrm{r}^2_{average}$., and was found to

be 2 μJ/mm^2 which for excitation at a wavelength of 420 nm is equivalent to 4.3x10^{14} photon/cm^2.

The extinction coefficient at a wavelength of 410 nm for CdTe CQDs was calculated from $\epsilon_{410} = 10600(D)^3$ [11, 12] where D is the colloidal quantum dot (CQD) diameter. The extinction coefficient at 410 nm of CdTe CQDs was established by the authors of Ref [11, 12] by measuring the absorption at this wavelength for a known CQD molar concentration, C(mol L^{-1}). Extinction coefficient is then found using $A = \epsilon CL$. where A is the absorbance, $A = -log(I/I_0)$, and L is the path length of the beam through the sample. The measured absorbance spectrum found for the samples used in this study was used to scale this value to take into account that the excitation wavelength used was 420 nm.

The absorption cross section ,σ, in units of cm^2 was calculated using (3. 7) from the extinction coefficient and Avogadro's number N_A.

$$\sigma = 1000\ln(10)\frac{\epsilon}{N_A}$$

(3. 7)

The average number of photons absorbed per CQD per pulse <N> was calculated, $< N > = \sigma J$, where J is the fluence in photon/cm^2. The number of photons absorbed per pump pulse by any individual CQD is described by Poisson statistics i.e.

$$P_N = < N >^N . \frac{e^{-<N>}}{N!}$$

(3. 8)

Where P_N is the probability of a CQD absorbing N photons during a pump pulse.

3.4.3. The Instrument Response Function (IRF)

The Instrument Response Function (IRF) determines the time resolution of a TCSPC measurement. This time characterises the quality of the instrument and the effect of the instrument on the data recorded. The IRF takes into account the electronics jitter, transit time spread of the detector and the pulse duration of the light source. A lifetime measurement is the convolution of the fluorescence decay and the IRF. The detector and light source electronic jitter is typically <25 ps. The pulse width from the laser at 80 MHz is <100 fs[13].The IRF of the MCP-PMT on its own [14] at FWHM is 38.6 ps, tested by Hamamatsu Photonics K.K., Electron Tube Division. See Figure 3. 9.

The IRF can be calculated by the sum of the squares of the contributions of electronics, light sources and detector [6, 15], and for our setup is 46 ps.

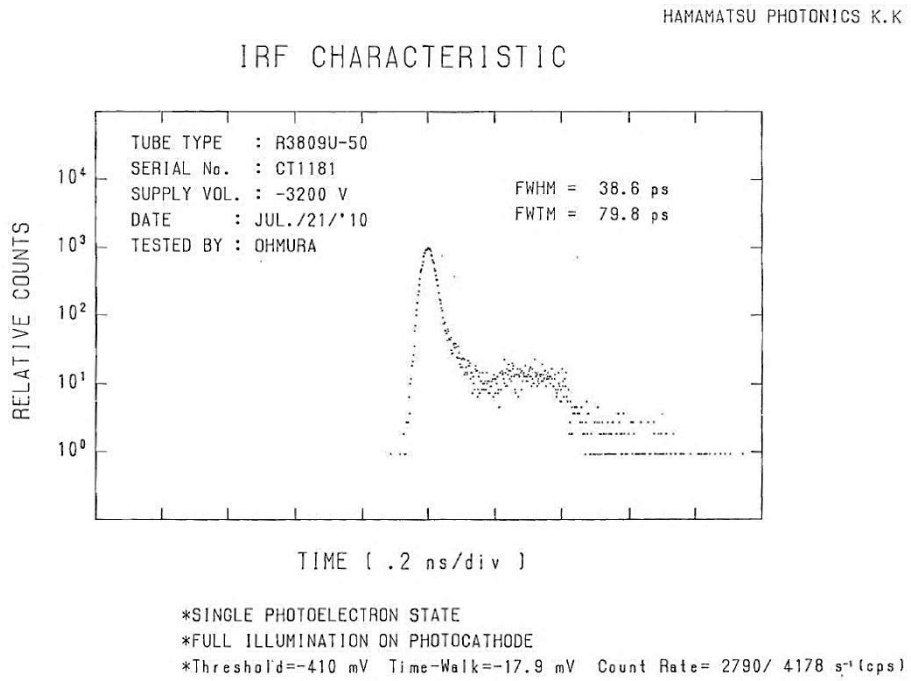

Figure 3. 9 The Instrument Response Function (IRF) of the MCP-PMT [14]

3.5. Photoluminescence quantum yield

This section describes the two methods used to record the photoluminescence quantum yield (PLQY) for the colloidal quantum dots under study. These methods are: the comparative (or relative) method and the absolute method. The PLQY expresses the proportion of excited emitters that deactivate by emitting a photon. In others words, the photoluminescence quantum yield, φ_f represents the number of emitted photons No_{em} (λ_{em}) per number of absorbed photons No_{abs} (λ_{abs}) [16]

$$\boldsymbol{\phi_f = \frac{No\ photons_{em}(\lambda_{em})}{No\ photons_{abs}(\lambda_{abs})}} \quad \textbf{(3. 9)}$$

It can also be related to the relative rates of the radiative and non-radiative pathways, which deactivate the excited states:

$$\boldsymbol{\phi_f = \frac{\kappa_r}{\kappa_r + \sum \kappa_{nr}}} \quad \textbf{(3. 10)}$$

where κ_r and κ_{nr} correspond to the rates of the radiative and non-radiative processes, respectively.

In Equation (3. 10) $\sum \kappa_{nr}$ describes the sum of the rate constants for the various processes that compete with the emission process. These processes include photochemical and dissociative processes including other, less well characterized changes that result in a return to the ground state; these processes are all non-radiative transitions.

In principle, PLQY measurement is a simple technique, but in practise it is challenging and troublesome and requires significant care and effort to obtain reliable results. .

As a result of the difficulty in measurements, there is often a discrepancy in QY values between authors. Moreover, some measurements were made more than 30 years ago and have not been confirmed with a recent method [17]. The lack of information about the procedure followed, and/or missing information about the system parameters, solvent, excitation wavelength, sample concentration and dye references, compound the difficulties in comparing experimentally obtained values to literature values

Another issue is the deficiency of application notes, technical notes and guidelines provided by instrument manufactures, and these procedures are not the most accurate available [18]

In addition PLQY measurements are sensitive to: temperature, concentration dependency (inner-filter-effect and post-filter-effect), impurity of the solvents, oxygen, bad dissolutions and photochemical instability.[19].

PLQY measurement is thus a challenging and a time consuming method, which needs lots of practice to achieve good quality and reliable results. The PLQY literature uncertainty values is commonly ±5-10%, in contrast in this work an uncertainty of ±2.5% was obtained.

This uncertainty was achieved by calibrating the system with several dyes and months of work in the lab. The cleaning process of the cuvettes proved to be a big factor in achieving reliability in the measurements.

The results achieved for the four dye standards identified as being reliable values in the literature and emitting in a similar spectral region, and with similar PLQY to the dots under study are given below in Table 3.1.

Table 3.1 Dye standards, the dyes where diluted in 99% Ethanol by Aldrich.

Dye	PLQY	PLQY literature
Rhodamine 6G by lambda Physik (LC5900)	94.9%	95% [20]
Oxazine 1 by lambda Physik (LC7250)	13.0%	14% [21]
Pyrromethene 580 by Exciton (LC5805)	90.1%	90% [22]
Pyrromethene 605 by Exciton	72.9%	74% [22]

The values of Table 3.1 were calculated using an integrating sphere using the absolute method.

3.5.1. Comparative method

The comparative or relative method was proposed by Williams *et al* [23]. This method is based on the fact the PLQY for one material is known already and can be used to quantify the QY for a different unknown sample, under the same conditions: excitation wavelength slits size, and integration time.

In this method, the number of emission photons detected is proportional to the integrated area under the corrected fluorescence spectrum.

$$\boldsymbol{F = \int_{\lambda_1}^{\lambda_2} q_p(\lambda_{ex}, \lambda_{em}) d\lambda_{em} = (hc_0)^{-1} \int_{\lambda_1}^{\lambda_2} I(\lambda_{ex}, \lambda_{em}) \cdot \lambda_{em} d\lambda_{em}}$$

(3. 11)

where F is the spectrally integrated photon flux $\mathrm{q_p}(\lambda_{\mathrm{em}})$ at the detector, $I(\lambda_{ex}, \lambda_{em})$ is the measured fluoresce spectra, and the λ_{em} and the λ_{ex} are the wavelengths of emission and excitation, respectively.

The fraction of photons absorbed, $f(\lambda_{\mathrm{ex}})$, is given by

$$\boldsymbol{f(\lambda_{ex}) = 1 - T(\lambda_{ex}) = 1 - 10^{-A(\lambda_{ex})} = 1 - 10^{-\varepsilon(\lambda_{ex}) c l}}$$

(3. 12)

where $A(\lambda_{\mathrm{ex}})$ is the absorbance, ε the molar decadic absorption coefficient, c the chromophore concentration, l the optical path length, and $T(\lambda_{\mathrm{ex}})$ the transmittance.

Hence for sample X, we can write eq.

$$\boldsymbol{\phi_x = k \frac{F_x}{f_x(\lambda_{ex})}}$$

(3. 13)

where k is a constant.

And for a standard material, for which the quantum yield is known

$$\boldsymbol{\phi_{st} = k\frac{F_{st}}{f_{st}(\lambda_{ex})}}$$

(3. 14)

Comparative measurements on solutions of sample "X" and standard "St", can then be used to estimate the ϕ of x sample by dividing the equations above to eliminate k.

$$\boldsymbol{\frac{\phi_x}{\phi_{st}} = \frac{\frac{F_x}{f_x(\lambda_{ex})}}{\frac{F_{st}}{f_{st}(\lambda_{ex})}}}$$

(3. 15)

Hence

$$\boldsymbol{\phi_x = \phi_{st}\frac{F_x}{F_{st}} \cdot \frac{f_{st}(\lambda_{ex})}{f_x(\lambda_{ex})} \cdot \frac{n_x^2}{n_{st}^2}}$$

(3. 16)

where the final term is included to take into account the fact that the PL intensities depends on the relative permittivity of the surrounding medium, $\varepsilon = n^2$. If different solvents are used for "x" and "st", then the *n*'s are the refractive indices of the solvents used for the both solutions.

The determination of the quantum yield by the comparison (or relative) method consists of the following steps:

a. Measurement of the absorption and emission spectrum of the sample.
b. Choice of suitable fluorescence quantum yield standard absorbing and emitting within a similar wavelength region as the sample.
c. Choice of the measurements conditions and measurement of the corresponding absorption and emission spectra of sample and standard and the emission spectra

of the corresponding solvents, which should be subtracted from the emission spectra of the sample and standard to remove the possible background signals.

d. Data evaluation and calculation of the relative fluorescence according with equation (3. 16)

There is an alternative procedure that uses the previous steps and adds different concentrations of the sample and standard (0/solvent blank, 20%, 40%, 60%, 80% and 100% of the sample). The integrated PL is the plotted against absorbance to yield a linear relationship with zero intercept [24]. An example of this obtained during this work is shown in Figure 3. 10.

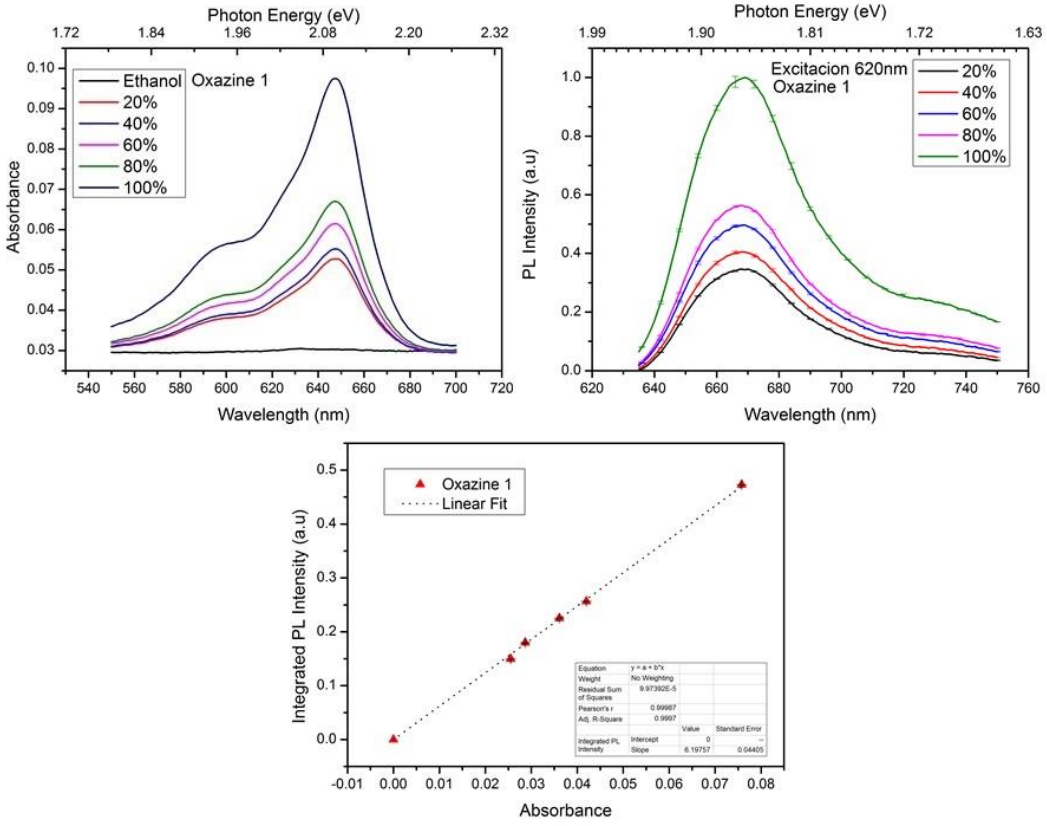

Figure 3. 10 Absorbance, PL intensity spectra and the linear plot of Oxazine 1 for five different concentrations.

The slopes of the graphs obtained (standard and sample) are proportional to the quantum yield. The PLQY value for the sample is then calculated using the equation

$$\phi_x = \phi_{st} \frac{Slope_x}{Slope_{st}} \cdot \frac{n_x^2}{n_{st}^2} \quad \textbf{(3. 17)}$$

The standards that are selected should be cross calibrated using this equation (3. 17). The match was considered valid and acceptable if the data obtained was of good quality (i.e. linear) and the experimental quantum yield matched the literature counterparts within ±10% [24].

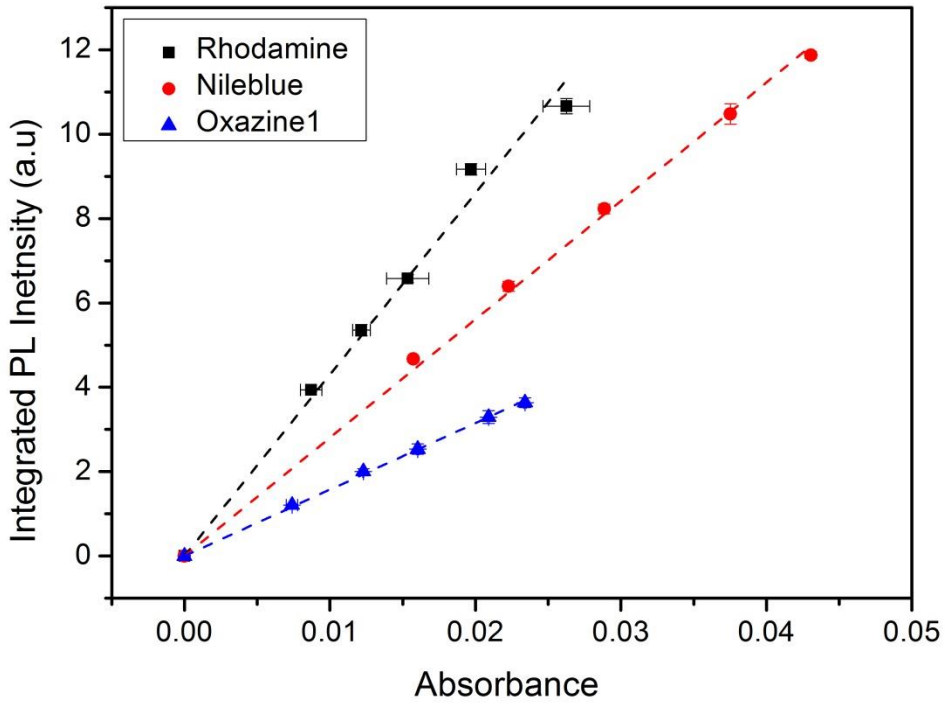

Figure 3. 11 Cross reference of three different dyes. (Rhodamine700, Nileblue and Oxazine1).

Table 3. 2 Cross reference values

Dye Standard	PLQY literature	Cross reference	Error
Oxazine 1	14% [17, 21, 25]	14%	± 0.7%
Nileblue	27% [17, 25, 26]	26%	± 1.2%
Rhodamine700	38% [27, 28]	39%	± 1.8%

Figure 3. 11 and Table 3. 2 show three dyes in ethanol, the excitation wavelength was 600nm. The values of PLQY in literature vary which is a common problem. The PLQY values for the three different dyes were calculated using the same parameters (slits, wavelength, integration time and vials)

3.5.2. The absolute method

The absolute method determines the values of $No\ photons_{em}(\lambda_{em})$ and $No\ photons_{abs}(\lambda_{abs})$ **i**n the equation (3. 9) by using an integrating sphere. In this work the F-3018 integrating sphere accessory for the Flurolog-3 was used.

An ideal integrating sphere is designed to spatially integrate radiant flux for collection of all possible emission angles from the sample; unfortunately no integrating sphere is ideal. The interior of the F-3018 has a reflecting coating, which is a material known as Spectralon. This coating material has a wide and flat reflectance of over 95% from 250 nm to 2.5 µm.The sample holder is designed for cylindrical vials [29] (diameter 8 mm and height 40 mm).

When the light passes through the excitation port and hits the sample (Figure 3. 12 shows the integrating sphere), some light is absorbed, the unabsorbed light is reflected and diffused around the sphere by the reflecting material of the sphere; and some of the reflected light is absorbed again by the sample. The baffle in the sphere located in front of the emission port prevents the exit of light which has not been diffused. The detector records the diffused light from the sample photoluminescence and excitation.

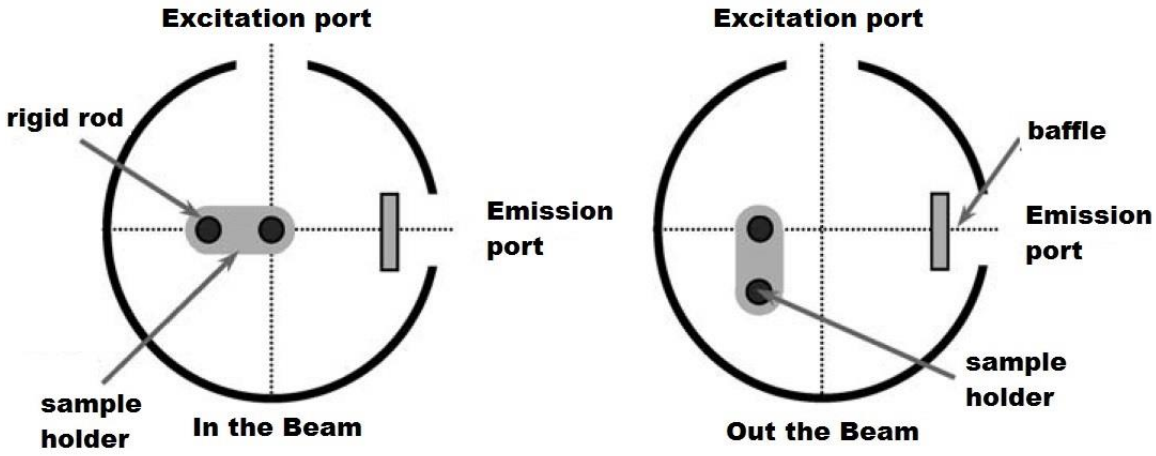

Figure 3. 12 The F-3018 at 0 and 90 degrees (in and out the beam). Modified from [30]

In this study the samples measured were recorded in the beam (0 degrees), and out of the beam (90 degrees)see Figure 3. 12. When the sample is out the beam it only absorbs diffused light. Once again the diffused light from the sample photoluminescence and excitation are detected.

The determination of the quantum yield by the absolute method consists of the following steps:

a) Measurement of the scattered light of the blank at 0 degrees at the excitation wavelength. Neutral density (ND) filters have to be used to prevent damage to the detector.
b) Measurement of emission spectra of the blank at 0 degrees using the same excitation wavelength.
c) Measurement of the scattered light and emission spectrum of the sample at 90 degrees, keeping the same setup parameters (slits, wavelength excitation, ND filters and scan range), which were used to record the scattered light and emission spectra of the blank.
d) Measurement of the absorption and emission spectrum of the sample at 0 degrees, keeping the setup parameters for the previous step.
e) Record the light intensity of the sample at the excitation wavelength when the sample is at 0 degrees using filters at the excitation and emission port and taking out the filter in the emission. Also it is important to know the background noise when the slits are closed.
f) PLQY calculator spreadsheet can be filled with data collected. The spreadsheet was provided by Horiba.

Figure 3. 13 shows an example of the data acquired with the integrating sphere for the dye rhodamine 6G, which was diluted in ethanol (99%.purity). The scattered light was recorded with a bandwidth of 1.3 nm. The excitation wavelength used was 450nm and the

scan range from 440 nm to 460 nm with a step size of 0.1 nm. The PL spectra were recorded using the same excitation wavelength and bandwidth size; the scan range was from 460 nm to 750 nm with a step size of 1 nm.

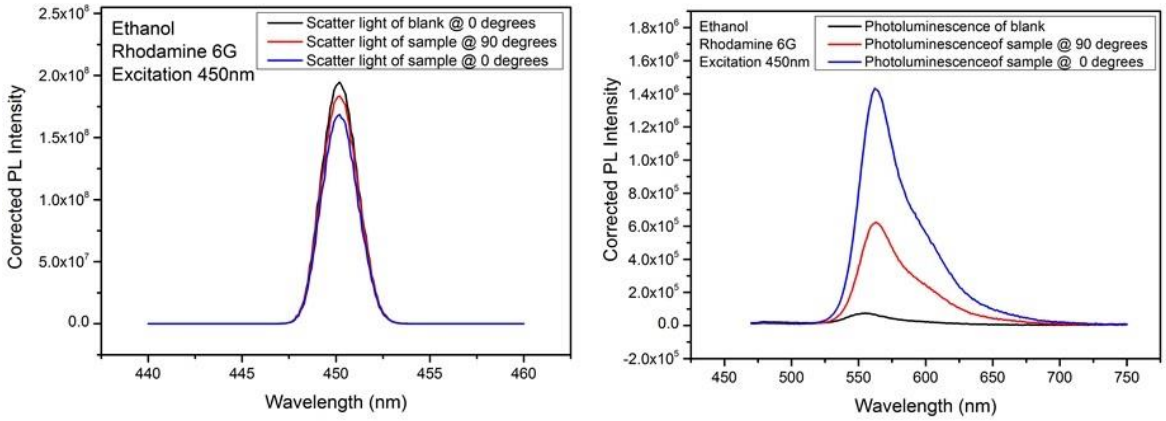

Figure 3. 13 Scatter light and photoluminescence spectra at 0 and 90 degrees for rhodamine 6g and the ethanol.

The PLQY value for rhodamine 6G in the literature is 95% [20]. This value is similar to the PLQY of 95.6% obtained using the integrating sphere for the absolute method with a sample absorbance of 0.05.

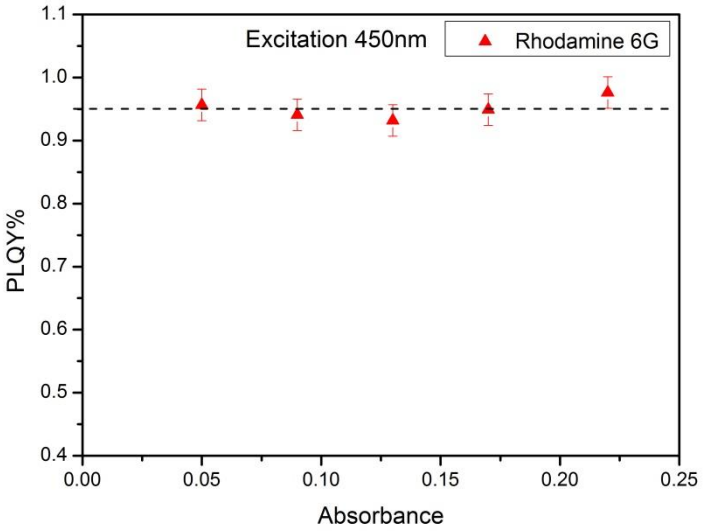

Figure 3. 14 PLQY values for 5 different concentrations of Rodamine 6G.

This method does not require a dye standard, or different concentration, however is a good practice to use different concentrations and dyes to calibrate the system.

In Figure 3. 14 PLQY values for 5 different concentrations of rhodamine 6G are shown. The recommended concentrations should be given an absorbance lower than 0.1 at the excitation wavelength and also lower than 0.1 at any wavelength longer than the excitation wavelength to avoid inner and post filter effect.

Table 3. 3 PLQY values with their respective absorbance for Rhodamine 6G.

Absorbance (a.u.)	0.05	0.09	0.13	0.17	0.22
PLQY	95.65%	94.10%	93.20%	94.90%	97.60%

The Table 3. 3 shows the PLQY for the five different concentrations. The mean of the PLQY for the five concentrations is 95.1% with an error of ±0.74%. However absorbance above 0.1 could result in a false PLQY values. The value used was the average between concentrations below 0.1. That is 94.9% with an error of ±0.8%.

An important aspect for a reliable PLQY measurement is to know the system and integrating sphere correction factors [31], usually these correction factors are given by the instrument supplier. However the integrating sphere correction factor needs to be updated periodically, because the sphere coating material may lose its reflective properties by the aging process and/or contamination.

3.6. Summary and Conclusions

Absorption and PL spectra measurements were a straightforward technique, due to the user-friendly software and system quality supplied by the manufacturers. Both instruments correct the measured spectra. The Lambda 1050 has a self-calibration routine which ensures a high accuracy in the measurements. For the Fluorolog 3 a correction factor is installed by the manufacturer and it can be updated by the user if need be.

The TCSPC system was built by Stuart Stubbs, Thomas Badcock and me. The system offers the capability to tune the excitation wavelength from 345 nm to 510 nm. And the IRF is 46 ps. This system has been optimised for an excitation wavelength of 400 nm and 420 nm.

The measurement of PLQY is a challenging procedure, which needs great care during the whole process. It is vital to plan in advance which dyes will be used as a reference for the CQD's under study, and in this work we study different dyes and CQD's using both the comparative (or relative) and absolute method.

In our experience both methods have shown similar results, the advantages and disadvantages of these methods depend more on the material under study, vials (cells), correction factors for the instrument and accessories; and also how well the ranges of concentration have been prepared.

The comparative method is simple in principle and reliable, and the use of well-known dye standards to do a cross calibration ensures the quality of PLQY values. However this method requires lots of work, planning and time. The cuvettes have to be spotless, with no fingerprints and no trace of solvents from previous sample and/or impurities. In practice this is a constant problem, the seal of the cuvette's lids can be dissolved by the solvents; also the lids keep residues of other samples. The quartz cuvettes themselves, which have a 10mm path length and were supplied by Starna Scientific Ldt, haven a small but different absorbance between each cuvette and this difference increases with age. This is

an important factor when working with five different concentrations when the maximum absorbance should be below <0.1.

In contrast the absolute method is a quick way to get PLQY values for unknown samples without a standard dye as a reference; with modern spectrofluorometers as the Fluorolog3 the PLQY measurements are accurate and fast. Despite this, the absolute method needs to be performed with care and procedures followed step-by-step to avoid problems. Another issue is the need for updated correction factors and calculation spreadsheets to get reliable values.

References

1. PerkinElmer, *High-Performance Lambda Spectrometers* Hardware Guide, 2007.
2. PerkinElmer, *Three Detector Module* User's Guide, 2007.
3. PerkinElmer, *UV WinLab Software Guide* User's Guide, 2008.
4. Lakowicz, J.R., *Principles of Fluorescence Spectroscopy, Third Edition*. 2010: Springer.
5. HORIBA, *Fluorolog-3.* Operation Manual, Part number 811014 V 3.2, 2002(Jobin Yvon Inc).
6. Edinburgh-Instruments, *Time-Correlated Single-Photon Counting.* Technical Note TN2/2012/02, 2012.
7. Becker, W., *Advanced Time-Correlated Single Photon Counting Techniques*. Chemical Physics. Vol. 81. 2005: Springer Berlin Heidelberg New York.
8. APE, P.S., *Single Pulse Selector Manual* Angewandte Physik& Electronik GmbH, 2009(Manual 125089).
9. APE, H.X., *Harmonics Generator THG Manual.* Angewandte Physik& Electronik GmbH, 2010.
10. Edinburgh-Instruments, *TCC900 Computer Module for Time Correlated Single Photon Counting.* Operating Instructions, 2002.
11. Kamal, J.S., A. Omari, K. Van Hoecke, Q. Zhao, A. Vantomme, F. Vanhaecke, R.K. Capek, and Z. Hens, *Size-Dependent Optical Properties of Zinc Blende Cadmium Telluride Quantum Dots.* Journal of Physical Chemistry C, 2012. 116(8): p. 5049-5054.
12. Yu, W.W., L.H. Qu, W.Z. Guo, and X.G. Peng, *Experimental determination of the extinction coefficient of CdTe, CdSe, and CdS nanocrystals.* Chemistry of Materials, 2003. 15(14): p. 2854-2860.
13. Spectra-Physics, *Mai Tai–Series High-Performance, Mode-Locked, Ti:Sapphire Lasers.* User's Manual, 2007.
14. Hamamatsu, P.K.K.E.T.D., *MCP-PMT (Microchannel Plate Photomultiplier Tube) R3809U-50 Final Test Sheet.* Manual, 2010.
15. Stubbs, S.K., *Photo-physics and applications of colloidal quantum dots*, in *Faculty of Engineering and Physical Sciences*2010.
16. Grabolle, M., M. Spieles, V. Lesnyak, N. Gaponik, A. Eychmuller, and U. Resch-Genger, *Determination of the Fluorescence Quantum Yield of Quantum Dots: Suitable Procedures and Achievable Uncertainties.* Analytical Chemistry, 2009. 81(15): p. 6285-6294.
17. Brouwer, A.M., *Standards for photoluminescence quantum yield measurements in solution (IUPAC Technical Report).* Pure and Applied Chemistry, 2011. 83(12): p. 2213-2228.
18. Resch-Genger, U. and K. Rurack, *Determination of the photoluminescence quantum yield of dilute dye solutions (IUPAC Technical Report).* Pure and Applied Chemistry, 2013. 85(10): p. 2005-2026.
19. Fery-Forgues, S. and D. Lavabre, *Are fluorescence quantum yields so tricky to measure? A demonstration using familiar stationery products.* Journal of Chemical Education, 1999. 76(9): p. 1260-1264.
20. Magde, D., R. Wong, and P.G. Seybold, *Fluorescence quantum yields and their relation to lifetimes of rhodamine 6G and fluorescein in nine solvents: Improved absolute standards for quantum yields.* Photochemistry and Photobiology, 2002. 75(4): p. 327-334.
21. Rurack, K. and M. Spieles, *Fluorescence Quantum Yields of a Series of Red and Near-Infrared Dyes Emitting at 600-1000 nm.* Analytical Chemistry, 2011. 83(4): p. 1232-1242.

22. Boyer, J.H., A.M. Haag, G. Sathyamoorthi, M.L. Soong, K. Thangaraj, and T.G. Pavlopoulos, *Pyrromethene-Bf2 Complexes as Laser-Dyes .2.* Heteroatom Chemistry, 1993. 4(1): p. 39-49.
23. Williams, A.T.R., S.A. Winfield, and J.N. Miller, *Relative Fluorescence Quantum Yields Using a Computer-Controlled Luminescence Spectrometer.* Analyst, 1983. 108(1290): p. 1067-1071.
24. Yvon, H.J., *A Guide to Recording Fluorescence Quantum Yields.* Manual.
25. Sens, R. and K.H. Drexhage, *Fluorescence Quantum Yield of Oxazine and Carbazine Laser-Dyes.* Journal of Luminescence, 1981. 24-5(Nov): p. 709-712.
26. Rahavendran, S.V. and H.T. Karnes, *An oxazine reagent for derivatization of carboxylic acid analytes suitable for liquid chromatographic detection using visible diode laser-induced fluorescence.* Journal of Pharmaceutical and Biomedical Analysis, 1996. 15(1): p. 83-98.
27. Ferreira, L.F.V. and S.M.B. Costa, *Fluorescence Quantum Yield Evaluation of Strongly Absorbing Dye Solutions as a Function of the Dye Concentration.* Journal of Luminescence, 1991. 48-9: p. 395-399.
28. Bachteler, G., K.H. Drexhage, J. Ardenjacob, K.T. Han, M. Kollner, R. Muller, M. Sauer, S. Seeger, and J. Wolfrum, *Sensitive Fluorescence Detection in Capillary Electrophoresis Using Laser-Diodes and Multiplex Dyes.* Journal of Luminescence, 1994. 62(3-4): p. 101-108.
29. HORIBA, J.Y.F., S), *F-3018 PLQY integrating sphere accessory.* Manual, 2008.
30. Porres, L., A. Holland, L.O. Palsson, A.P. Monkman, C. Kemp, and A. Beeby, *Absolute measurements of photoluminescence quantum yields of solutions using an integrating sphere.* Journal of Fluorescence, 2006. 16(2): p. 267-272.
31. Ltd., N., *Protocol for fluorescence quantum yield determination employed by NanocoTechnologies Ltd.* Standard for Measuring Quantum Yield, 2008.

Chapter 4. Multi-exciton and hot emission from Type II colloidal quantum dots.

4.1. Introduction

The optical properties of homogeneous CQDs are determined by the choice of material, their size and the surface passivation. However, the addition of a shell of another material around the original CQD, now known as the core, enables another means of controlling optical properties. Such 'core-shell' CQDs are heterostructures and can be divided in two main types (as illustrated in Figure 4. 1) depending on the alignment of the conduction and valence band edges of the materials the CQDs are formed [1].

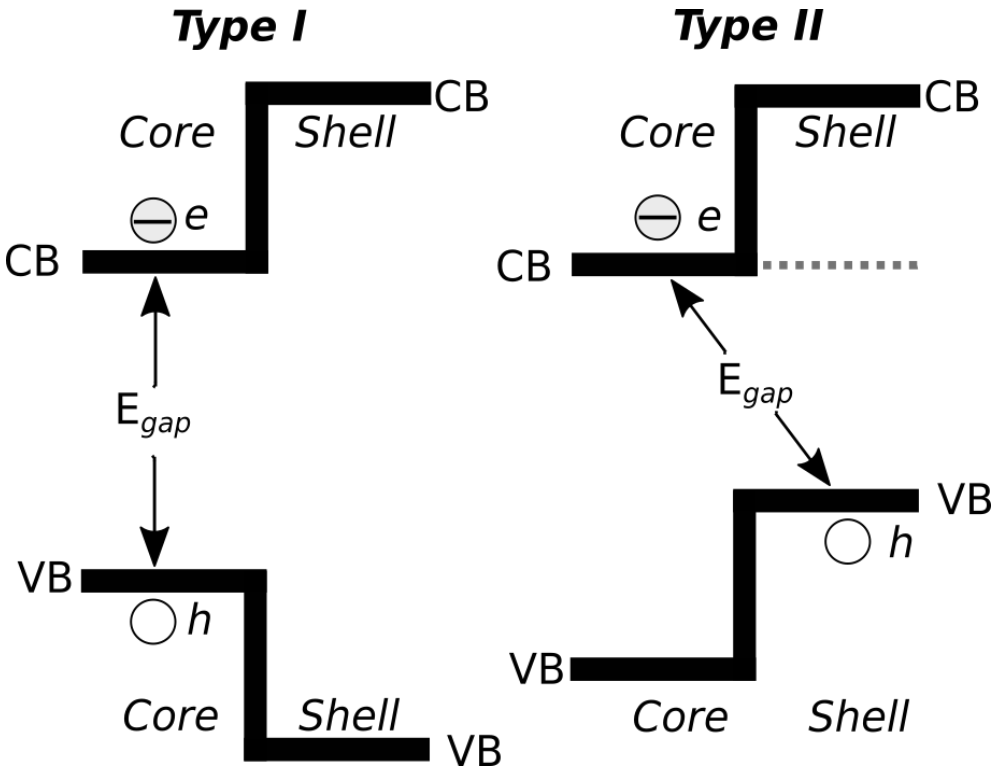

Figure 4. 1 Structure of Type I and Type I colloidal quantum dots I. For Type I both carries are in the core, and for Type II the e-h pair are localised in different part of CQDs, i.e. the core and shell)

A Type I structure is produced when the semiconductor material used to form the core has a smaller band gap than the shell material. This confines an electron and hole pair (i.e. an exciton) inside the core with the shell acting as a barrier between these charges the CQD surface. This type of structure is beneficial for emission, typically resulting in a higher PLQY than a homogeneous CQD, because it reduces the interaction of photo-generated charges with the surface states arising from incomplete passivation that enable non-radiative recombination. In contrast, in a Type II structure the alignment of the conduction and valance band edges are such that the electron and hole localise in different parts of the CQD, one in the core and the other in the shell. Recombination now occurs between the conduction band minimum and the valance band maximum of the electron and hole containing materials, respectively –see Figure 4.1. Thus, the emission wavelength can now also be tuned by control of the shell thickness as well as of the core diameter. The spatial separation of the charges results in a reduced wave-function overlap between the electron and hole (e-h), increasing exciton and multiexciton lifetimes [1]. Which are important for optical amplification and lasing. Furthermore, a type II structure has been shown to reduce the rate of hot electron cooling by 3 orders of magnitude [2], which could reduce the threshold for multiple exciton generation [3], leading to an improvement in solar cell efficiency [4].

When two excitons are present within a Type II CQD, the charge separation can also produce an imbalance between the columbic attraction (between electrons and holes) and repulsion (between the two electrons and between the two holes), resulting in an exciton-exciton (X-X) interaction energy, Δ_{xx} This interaction could be an energy increase ($\Delta_{xx}>0$) or energy reduction ($\Delta_{xx}<0$), which correspond to net repulsion or attraction, respectively. In Figure 4. 2 a schematic diagram of the two processes are shown. (For simplicity, the electric field (**E**) is between just two of the charges is shown, but in actuality all four charges interact). A net repulsive interaction increases the energy required to create a second exciton, $E_X^{(2)}$, by Δ_{xx} so that it is greater than the energy required to produce the

first, $E_X^{(1)}$, whilst a net attractive interaction reduces it by the same amount . A repulsive interaction thus blue-shifts the absorption edge of a singly excited CQD away from the emission band, reducing the threshold for optical gain. A net attraction interaction has the opposite effect, producing greater spectral overlap between the emission band and the absorption edge of singly-excited QDs and thus increasing the threshold for gain.

Thus the total energy required to produce a biexciton, E_{BX} is .

$$E_{BX} = E_X^{(1)} + E_X^{(2)} = E_X^{(1)} + \left(E_X^{(1)} + \Delta_{XX}\right) \quad \textbf{(4. 1)}$$

where Δ_{XX} is thus $\Delta_{XX} = E_{BX} - 2E_X^{(1)}$).

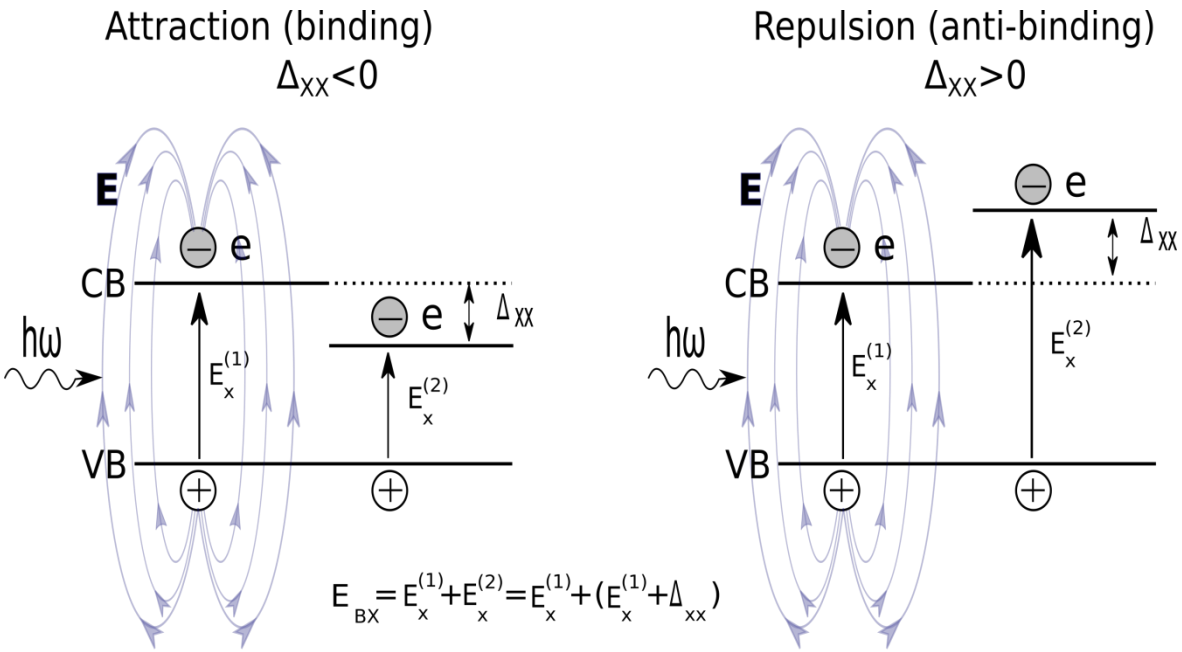

Figure 4. 2 Schematic diagram of the effects of attractive or repulsive X-X interaction energies, Δ_{XX}. In the case of net attraction the transition energy for the second exciton, $E_X^{(2)}$ is smaller than that needed to produce a single exciton, $E_X^{(1)}$, which increases the absorption at the emission wavelength. For net repulsion, however, $E_X^{(2)} > E_X^{(1)}$, which reduces the absorption at the emission wavelength).

The initial experimental work on X-X interactions in CQDs with a Type II structure was first performed by Klimov [5]. However the idea of single exciton gain [6] achieved via this effect was introduced by his group in 2004. In 2007, a theoretical study of the X-X

interactions in Type II CQDs was carried out by Klimov and collaborators, in which an analytical and numeral analysis of X-X interactions took into account the direct contribution of the Coulomb coupling between carriers and also interface polarization. This analysis indicated that the direct coulomb coupling is strongly repulsive and the interface polarization could be either repulsive or attractive depending on the relative dielectric constants of the core and shell of the CQD. However even when positive, the interface polarisation contribution was not sufficiently large to counter-balance the repulsive direct contribution and thus produce a net attractive interaction. Later that year Klimov reported a practical demonstration of optical amplification [5] from singly-excited Type II CQDs, which is only possible if the absorption band and emission band are sufficiently separated. (N.B. A biexciton fills the 2-fold degenerate conduction band edge, completely bleaching the band edge absorption that competes with emission, making optical gain possible without a spectral separation between the emission band and the absorption edge.) This was an important result because the lifetime of biexcitons is typically limited to the picosecond-timescale by efficient Auger recombination, whilst single excitons have lifetimes greater than a nanosecond. Thus, optical gain based on single excitons is much longer sustained that if it is based on biexcitons.

Klimov reported a giant interaction which was repulsive (Δ_{xx} =+106 meV) in CdS/ZnSe NCs [5], in reasonable agreement with his theoretical calculation Δ_{xx} = 91 meV, and this was observed for different emission colours. In this work, Δ_{xx} was determined by comparing the PL spectrum of the CQDs immediately after excitation to a time (2 ns later) when all biexcitons have recombined. The earlier spectrum was observed to have an additional blue-shifted component, which was attributed to biexciton emission, with the spectral shift between this feature and the PL peak at later times being equal to Δ_{xx} – see Figure 4. 3 ZnTe/CdSe type II CQDs, which emit in the near-infrared, were also studied in the same work and again a repulsive interaction energy was reported, with Δ_{xx} =+80 meV.

In the same year an extension of this work was published by the same group. [7], which supported and extended the previous results.

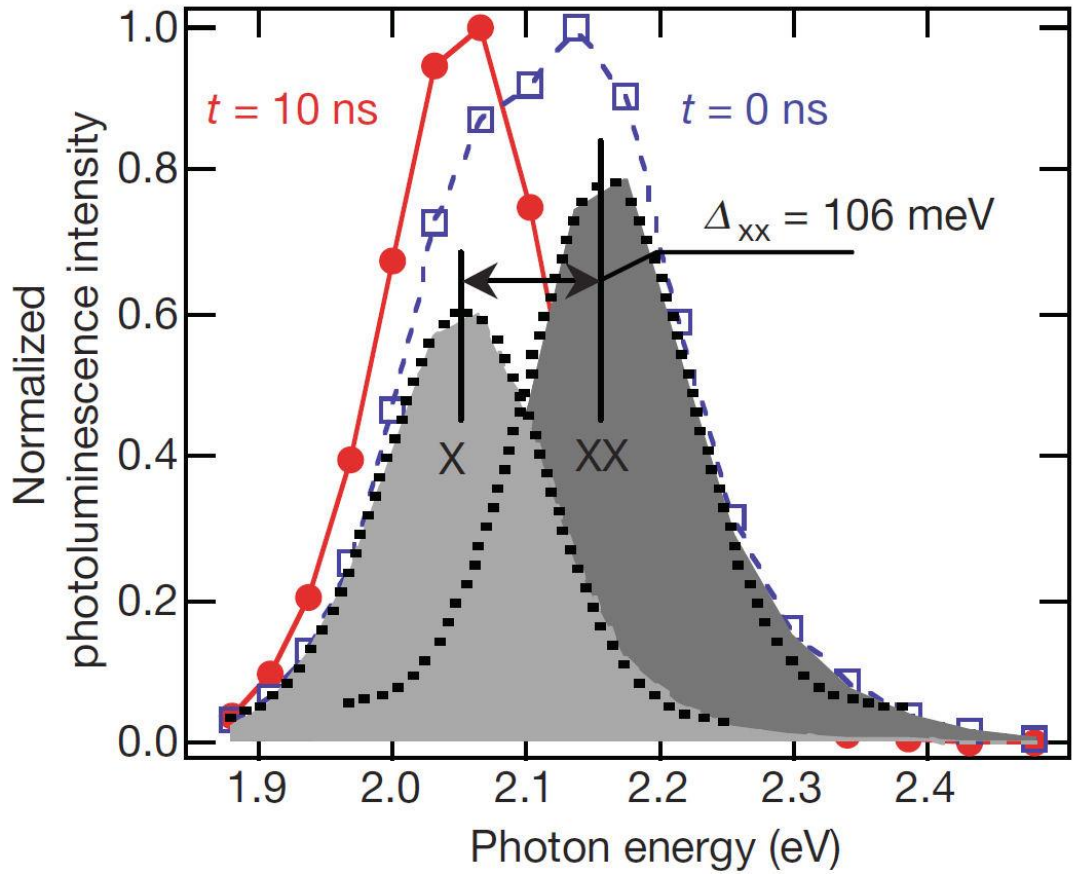

Figure 4. 3 Klimov's Transient PL experiment demonstration of repulsion interaction (anti-binding). (Taken from [5]) (single exciton in red dots and biexciton in blue squares)

Another study of multiexcitons in Type II CQDs was carried out by Oron [8] also in 2007, investigating CdTe/CdSe CQDs via quasi-cw PL spectroscopy. The properties of multiexcitons in Type I and Type II CQDs were compared, with an increase of the radiative lifetime produced by the charge separation in a Type II structure observed. The Auger recombination lifetimes also increased up to a nanoseconds time-scale for Type II, due to the reduced wave-function overlap. A net repulsive X-X interaction of up to Δ_{xx} =+30 meV was reported due to the observed blue-shift of the emission observed immediately after excitation.

In 2010, Ivanov carried out a study of Type II CdS/ZnSe CQDs [9] using time-resolved photoluminescence spectroscopy, and showed that biexcitons are significantly affected by the thickness of the shell while single-excitons showed little variation.

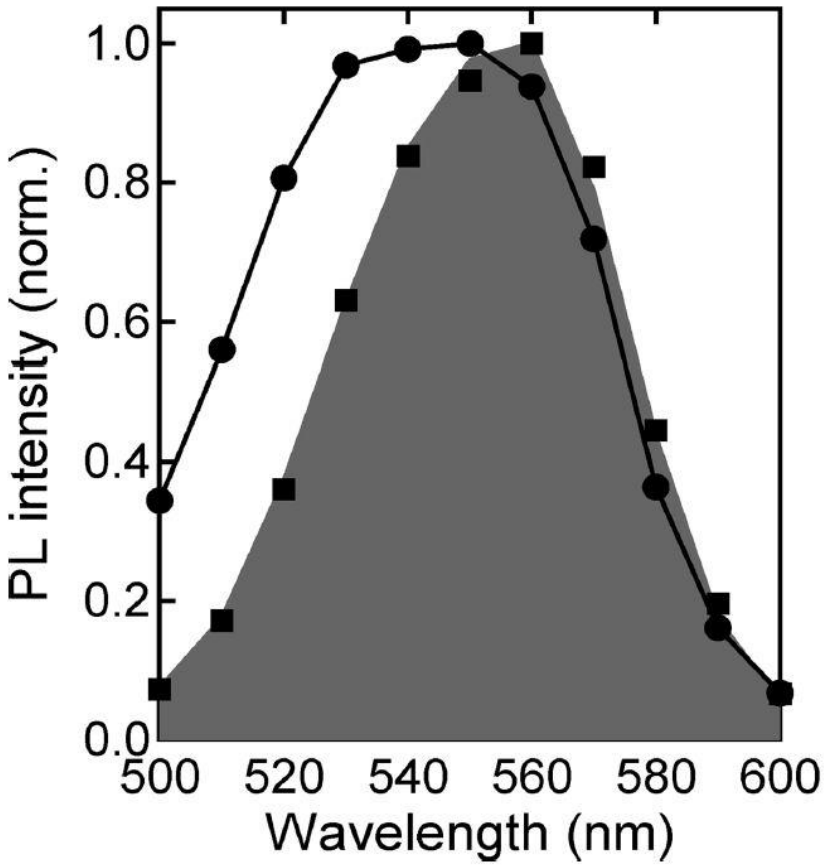

Figure 4. 4 Ivanov's transient PL experiment for CdS/ZnSe CQDs, showed a repulsion interaction (Taken from [9]) Data observed immediately after excitation are represented by the circles, with the data represented by squares corresponds to a time after biexciton recombination is complete.

The average emission lifetime was increased from 23 ns to 45 ns by increasing the thickness of the ZnSe shell, as the electron and hole increase their spatial separation as the shell increases. Exciting at high intensities produced biexcitons which had a fast, sub-nanosecond decay and at a spectral position blue-shifted with respect to that of the single exciton, which was attributed to a net coulomb repulsion between the charges in the CQDs. Figure 4. 4 shows such a spectral blue-shifting, in this case attributed to a repulsive X-X anti-binding of Δ_{xx} =+70 meV. Varying the shell thickness was found to tune

the value of Δ_{xx} extracted from the fit to the PL spectra, and the potential of this effect in optical gain applications or solar cells was discussed.[9].

In 2010 a study on charge transfer dynamics in CdTe and CdTe/CdS CQDs by Rawalekar and co-workers [10] showed an average increase in the PL lifetime as the thickness of the shell was increased, due to the charge transfer to the CdS, which also decreases the influence of the CQD surface on the hole. Also observed was an increase in the rise time of emission as the shell thickness grows, indicating that a Type II structure reduces the rate of cooling to the band edge. One year later, the same group studied charge transfer dynamics in CdTe/CdSe [11], where the lifetime was found to increase in direct proportion with the shell thickness.

In recent years, a more detailed calculation of the effects of the electron was reported by McDonald et al in 2012 [12], where a Monte Carlo method was used to calculate the exciton interactions in Type I and II CQDs. The calculations were found to agree with experimental data for CdTe/CdSe CQDs, and showed that the exciton–exciton interaction energy in this system undergoes a transition from binding ($\Delta_{xx}<0$) to anti-binding regime ($\Delta_{xx}>0$) as the shell thickness increases

4.2. Synthesis and optical characterisation of CQDs Type II

The CQDs used in this investigation were synthesised by Robert C. Page via a hot–injection method using dual source precursors [13]. The CQDs studied in this chapter are based on CdSe cores with a CdTe shell, with some of them having an extra shell of CdS. The purpose of the second shell is to passivate the CQDs since to the CdTe is vulnerable when it interacts with the oxygen in the air [14].

The CdSe cores were grown to have a zinc blende crystal structure, since this structure is isotropic and allows a uniform shell growth in all directions. The cores were synthetized at 240°C with two minutes growth time, then cooled for growing the shell. The CdTe shells were grown by the injection of Cd-oleate and trioctylphosphine telluride (TOP-Te) into the CdSe cores solution containing oleylamine as a ligand, the reaction was carried at 190°C then heated to 250°C for 30 min shell growth, depending on the desired thickness the process was repeated. The second shell of CdS was grown in similar way using Cd-oleate and TOP-S as precursors; the reaction was carried out at a temperature of 190°C which was then increased to 225°C for 30mins to grow the shell. The CdS shell grown was thin to ensure that charge carrier extraction possible for the solar cells experiments reported in Ref.[4]. The reactions to grow the CQDs were all carried out under a nitrogen atmosphere to prevent oxidation.

To confirm that the crystal structure of the CdSe, CdSe/CdTe and CdSe/CdTe/CdS CQDs was zinc blende, X-ray powder diffraction (XRD) patterns were obtained. CdS has a tendency to growth with a wurtzite crystal structure but was expected to follow the zinc blende template of the underlying CdTe. In Figure 4. 5 a) the XRD patters show a zinc blende crystal structure is present from the CdSe core, the CdTe also adopted the same crystal structure, and also for CdS shell. The diffraction peaks for CdS shell show a weak or lack of intensity, which is the result of growing a thin shell. The size and the monodispersity of the CQDs were confirmed using scanning transmission electron microscope microscopy (STEM). In Figure 4. 5b) the CdSe cores are on the top row of the

figure, and show a high monodispersity (top left); the lattice fringes observed using high magnification (top right) correspond to zinc blende crystal structure for CdSe. A size analysis for over 100 particles yielded an average diameter of 3.5 nm with a standard deviation of 0.3 nm for the CdSe cores. The corresponding values for the CdSe/CdTe CQDs were 4.9 nm and 0.8 nm and for the CdSe/CdTe/CdS were 6.6 nm and1.3 nm. The increase of standard deviation on the addition of the shells indicates a reduction of the monodispersity of the CQDs after shelling. The XRD patterns and TEM studies were performed by collaborators based in the School of Materials and the School of Chemistry, R.C Page and E A Lewis [15].

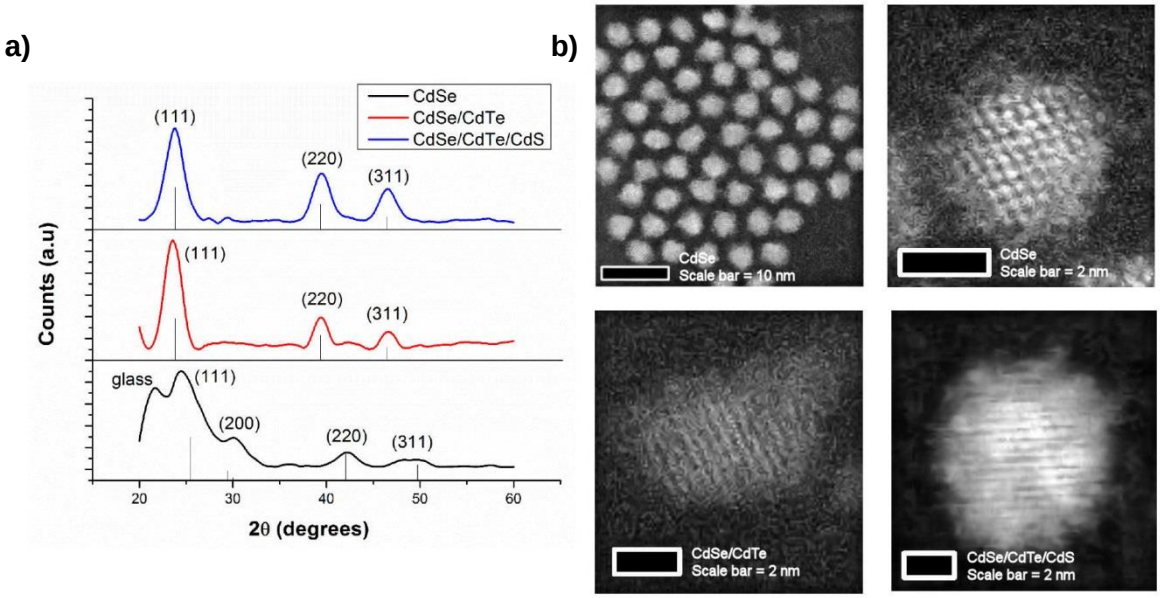

Figure 4. 5 XRD patters (a) for CdSe (black line). CdSe/CdTe (red line) and CdSe/CdTe/CdS (blue line) and STEM (b) images for CdSe (top). CdSe/CdTe (bottom left) and CdSe/CdTe/CdS (bottom right) [16]

Typical absorption and photoluminescence spectra are shown in Figure 4. 6, and are a representative of the CQDs before and after the shelling process The PL peak for the CdSe cores is at 605 nm, and undergoes a large redshift on the addition of the first shell to 660 nm, and a further but smaller redshift after the addition of the CdS shell to 675 nm. The Stokes' shift between the first absorption peak and the emission peak for the CdSe cores is 31 nm, 12 nm for the CdSe/CdTe and 10 nm for the CdSe/CdTe/CdS. In Figure 4.

6 c) the exact spectral position of the first absorption peak was found by using the second derivative of the absorbance spectrum The first absorption peak of the core shifts after growth of the shell, from 574 nm (2.16 eV) to 648 nm (1.91 eV), and after the CdS shell is added it further shifts to 665 nm (1.86 eV). Finding the position of the first absorption peak of the CdSe CQDs allows their diameter to be calculated, as described below.

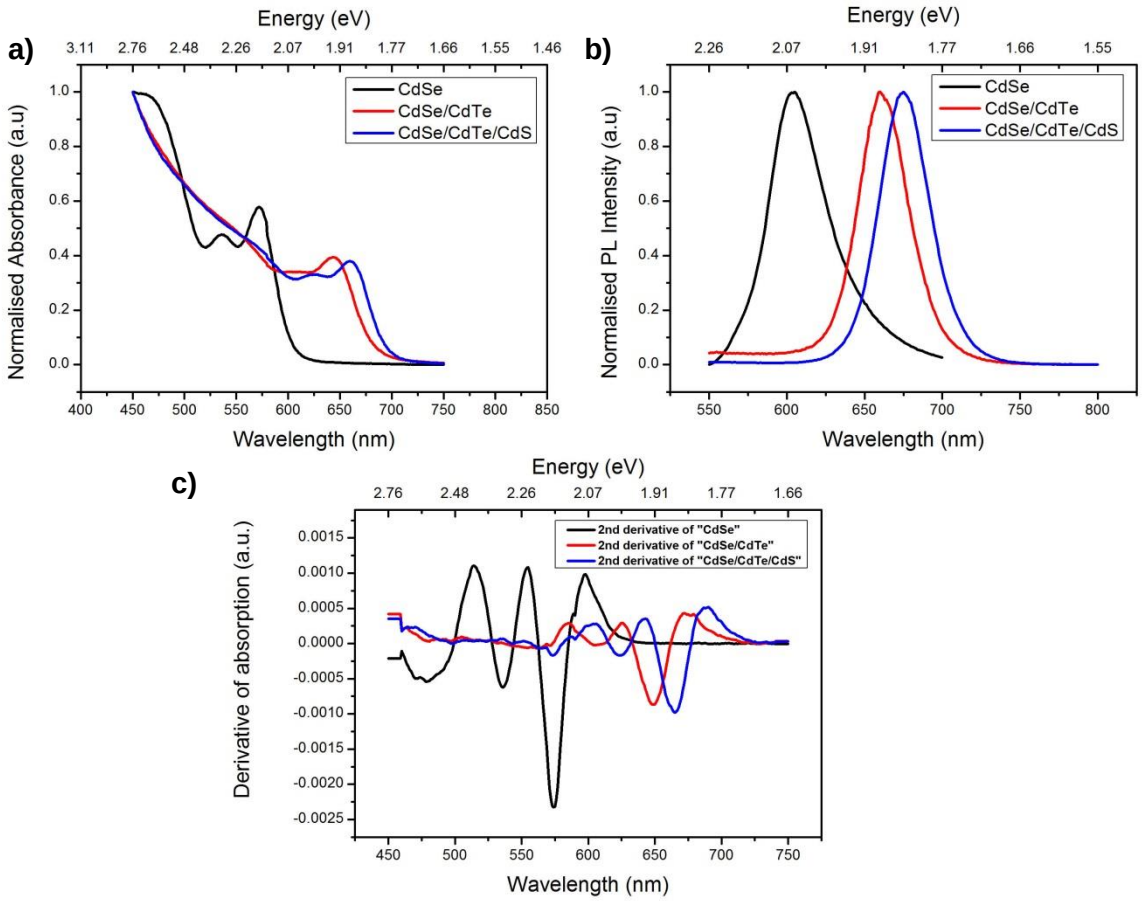

Figure 4. 6 Examples of the absorption (a) and PL (b) spectra for CdSe, CdSe/CdTe and CdSe/CdTe/CdS CQDs. c) Determination of the first absorption peak using the 2nd derivative.

To know the diameter of the core of CdSe CQD, two approaches were used. The first was by using the experimental data of Yu et al [17] and the second was by using the empirical and theoretical model by de Mello et al [18]. There is a significant discrepancy between these two approaches for first absorption peaks at short and long wavelengths. However, they are consistent over the spectral range corresponding to the samples used in this investigation.

Equation (4. 2) is from Yu et al [17] and allows the calculation of the diameter of CdSe QDs, d , from the wavelength corresponding to the first absorption peak, λ :

$$d = (9.8127\, x10^{-7})\lambda^3 - (1.7147\, x10^{-3})\lambda^2 + 1.0064\lambda - 194.84 \quad \textbf{(4. 2)}$$

and equation (4. 3) is from de Mello et al [18] and relates the band gap, E_g, to the diameter;

$$E_g(d) = 1.858 + \frac{1}{0.220d^2 + 0.008d + 0.373} \quad \textbf{(4. 3)}$$

Figure 4. 7 illustrates a) the experimental data and the fit used by Yu et al [17] and b) the data and the fit used by de Mello et al [18] and c) a comparison between Equations (4.2) and (4.3) in terms of CQD diameter and first absorption peak i.e. the absorption edge.

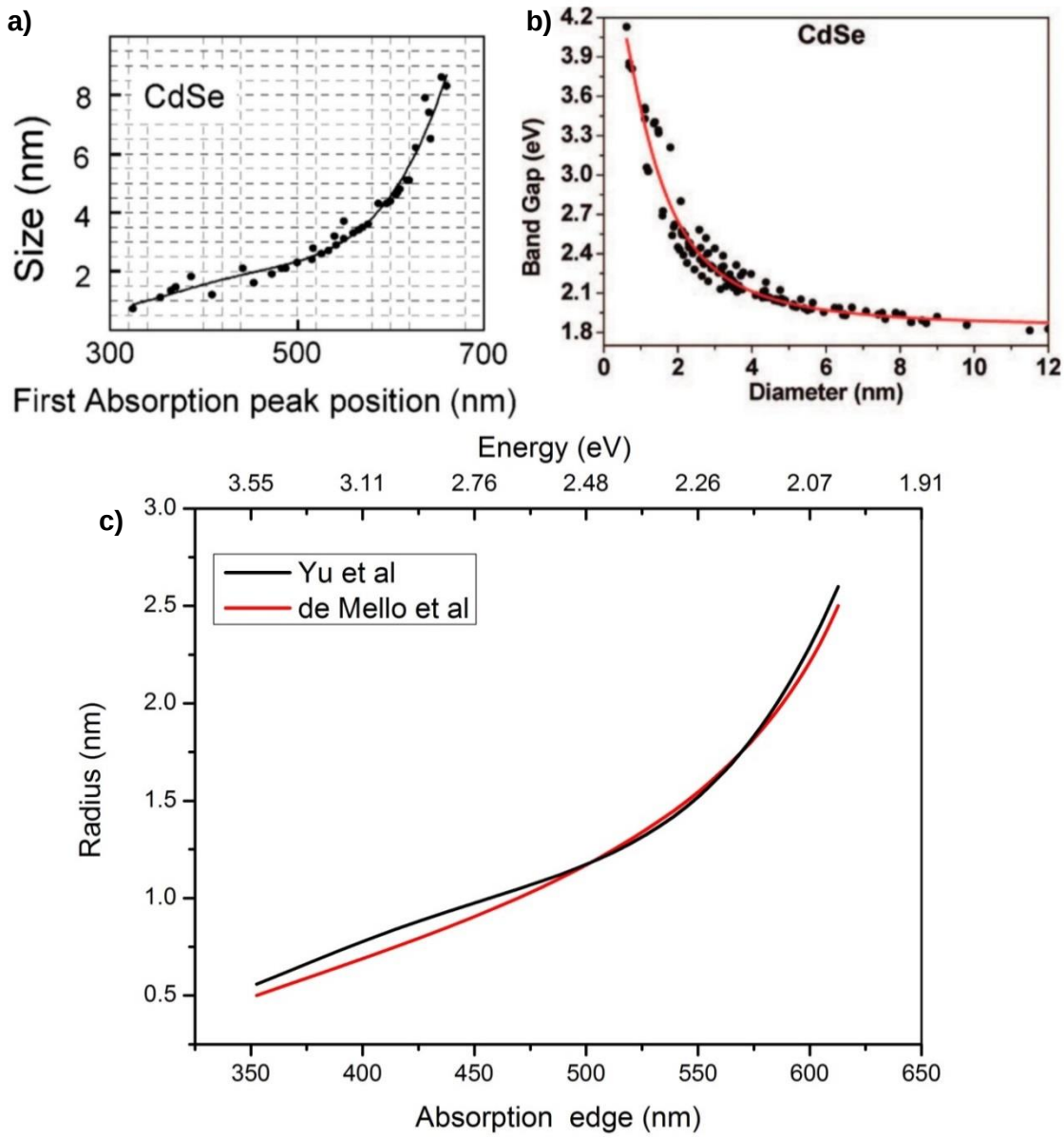

Figure 4. 7 Comparison between a) Yu et al (black line) vs b) de Mello et all (red line) diameter calculation for CdSe QD ([17, 18]). (Calculations of CdSe diameter were directly compared in c)

The comparison between the two models shows the discrepancy between the Yu and de Mello relationships between absorption edge and CQD size at the extremes of wavelength studied. The spread of data points about the fit lines shown also indicates the accuracy of these methods. de Mello claim that his model has an accuracy of 2% for 2 nm – 12 nm sizes, and the error grows 3 times for sizes smaller than 2 nm. He suggested that the reduced accuracy is due to the absorption edge being increasingly affected for smaller CQD sizes by the surface ligands and the solvents used [18]. By using these two methods

the core diameters of the CdSe CQDs in this study were calculated. To confirm the accuracy of these methods for our samples, the calculated size was also compared to the size determined by STEM for the sample shown in Figure 4.5. The Yu calculation yields 3.62 nm with an error estimation ±0.15 nm and the de Mello method gives is 3.6 nm ±0.072 nm, both of which are consistent the size determined by STEM, i.e. 3.5 nm ±0.3 nm.

Calculation of the thickness of the CdTe shell utilised a (2,6)-band effective mass approximation model for Type II CdSe/CdTe QD heterostructures by Tyrell et al [19].

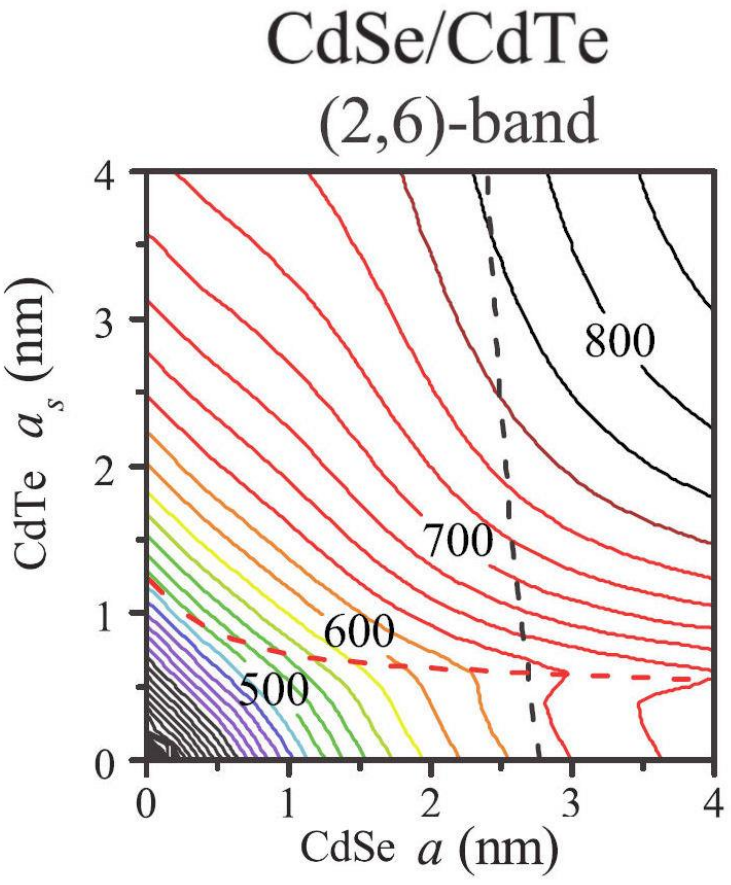

Figure 4. 8 Calculation of the CdTe shell thickness, a_s, for a CdSe core radius of *a* (Taken from [19]). The contour lines show the wavelength corresponding to the band gap for each combination of core radius and shell thickness.

Figure 4. 8 shows the band gap map used to calculate the shell thickness for a known core radius. Thus, measuring the band gap of the CdSe/CdTe CQDs enables the

thickness of the CdTe shell to be known. For example if the core radius is 1.8 nm and the PL peak is 660 nm, from Figure 4. 8 the thickness of the shell is ~1.2 nm. The total calculated diameter of the CdSe/CdTe CQD is thus 4.8nm, which is in agreement with 4.9 nm ±0.8 from the STEM images. The STEM is very time consuming and so was done just for one set of samples to confirm that the above procedure yields reliable results. As detailed above, the STEM images were also used to measure the thickness of the CdS shell for the case studied. The same growth conditions and period were used each time the CdS shell was grown and thus it is assumed that this results in approximately the same thickness of shell in each case.

Table 4. 1 Core diameters, *d*, CdTe shell thickness, t_{CdTe}, and CdS shell thickness, t_{CdS}, for the CQDs studied. The spectral position of the PL peak and the first absorbance peak are also given.

Samples	*d* (nm)	t_{CdTe} (nm)	t_{CdS} (nm)	Absorbance peak (nm)	PL Peak (nm)
CdSe/CdTe	4.17	2		656	687
CdSe/CdTe/CdS	4.17	2	0.6	670	698
CdSe/CdTe	4.17	2.2		650	663
CdSe/CdTe/CdS	4.17	2.2	0.6	672	687
CdSe	3.15			555	567
CdSe/CdTe	3.15	2.2		630	666
CdSe/CdTe/CdS	3.15	2.2	0.6	666	695
CdSe/CdTe	3.15	5		713	728
CdSe/CdTe/CdS	3.15	5	0.6	723	745
CdSe/CdTe	3.15	2		622	668
CdSe/CdTe/CdS	3.15	2	0.6	655	696
CdSe	3.15			567	590
CdSe/CdTe	3.15	2		614	630
CdSe/CdTe/CdS	3.15	2	0.6	659	664

Table 4. 1 shows the core diameters and shell thicknesses for the set of samples studied, as determined from the optical spectra by the methods described above. The CQDs can be divided into three groups based on their core diameters. The first group is based on the same core of diameter of 4.17nm and includes two different shell thickness of CdTe, with and without a final CdS passivating layer. The second group is based on a smaller CdSe core diameter of 3.15 nm with three different CdTe shell thicknesses, again with and

without a final passivating CdSe layer. The last set was a repeat of the second one, intended to show experimental reproducibility, with a similar CdSe core diameter and CdTe shell thickness to samples from the second group. It is assumed that all three groups share approximately the same CdS shell thickness, due to the identical growth conditions used to produce the final layer in each case.

To further characterise these CQDs, PLQY and PL transient measurements are presented for an example set of CQDs: the CdSe core of diameter 3.15 nm, the corresponding CdSe/CdTe CQD with shell thickness of 2 nm, with and without the CdS layer. The PLQY measurement was performed using the comparative method, which is described in Chapter 3, and the corresponding data is shown in Figure 4. 9a.

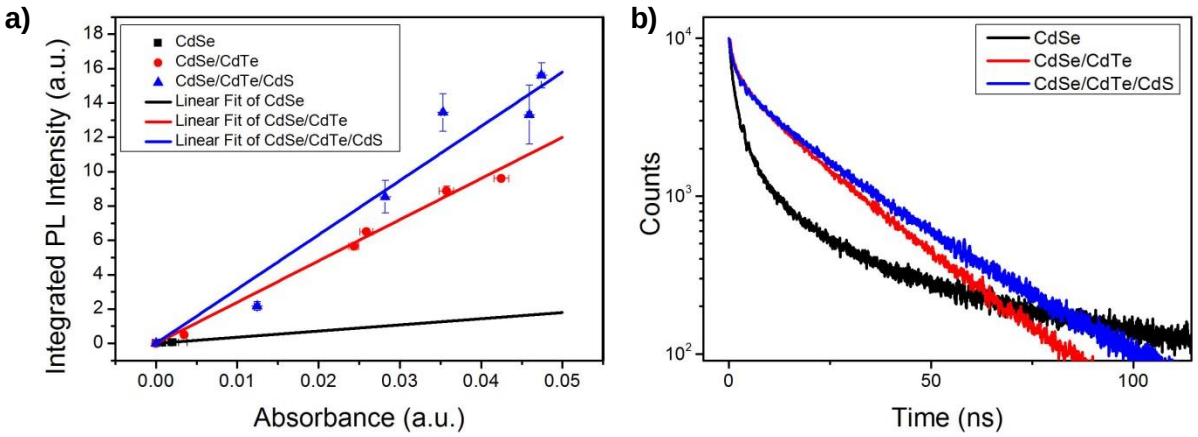

Figure 4. 9 a) CdSe, CdSe/CdTe and CdSe/CdTe/CdS CQDs slopes for the calculation of the PLQY by the comparison method and b) PL lifetimes for CdSe, CdSe/CdTe and CdSe/CdTe/CdS CQDs.(CdSe CQDs black line, CdSe/CdTe CQDs red line and CdSe/CdTe/CdS CQDs blue line)

The PLQY slopes shown in Figure 4.9a were compared to those for three different dye standards: Ozaxine1, Nileblue and Rhodamine 700. The resulting PLQY values for CdSe, CdSe/CdTe and CdSe/CdTe/CdS CQDs were 4%, 26% and 35% respectively. The PL decay transients for the same three samples are presented in Figure 4. 9 b. The CdSe cores showed a tri-exponential behaviour but for the CdSe/CdTe and CdSe/CdTe/CdS CQDs the transients could be fitted by a bi-exponential decay. However they were fitted with a tri-exponential to compare their behaviour more directly with the CdSe cores. The

PL lifetimes resulting from this tri-exponential fitting are shown in Table 4. 2. In Chapter 5 the analysis of PL decay will be discussed in detail

Table 4. 2 PL lifetimes of CdSe core base CQDs with CdTe shell and CdS shell

Samples	d (nm)	t_{CdTe} (nm)	t_{CdS} (nm)	t1 (ns)	t2 (ns)	t3 (ns)
CdSe	3.15			25.98 ±0.20	5.62 ±0.08	0.95 ±0.01
CdSe/CdTe	3.15	2		20.76 ±0.30	5.68 ±0.38	1.05 ±0.03
CdSe/CdTe/CdS	3.15	2	0.6	23.81 ±0.27	5.98 ±0.30	0.97 ±0.02

4.3. Time-resolved PL spectra measurements

The time-resolved PL (TRPL) spectra of the CdSe core-only, and CdSe/CdTe and CdSe/CdTe/CdS Type II CQDs were measured in order to determine the X-X interaction energy, following the technique pioneered by Klimov et al. The measurements were performed with the time-correlated single photon counting (TCSPC) system previously described in chapter 3, with the CQDs excited at a repetition rate of 4 MHz and at a wavelength of 400 nm. The PL decay transient was taken at different wavelengths across the spectra for a fixed accumulation time. The maximum number of counts for each wavelength was found and plotted versus wavelength. The resulting spectrum corresponds to zero delay, τ, between excitation and collection of the PL (to within the time-resolution of the system) and will be referred to as the τ_{0ns} spectrum. This spectrum will contain the contributions from any hot excitons or multi-excitons present. As discussed above, exciton cooling and biexciton recombination is complete within a nanosecond. Thus, the number of counts after a delay of τ=2 ns was found for each wavelength and used to produce a second spectrum, which will be henceforth called the τ_{2ns} spectrum. Normalised examples of these spectra obtained for the same sample are compared in Figure 4. 10. The long wavelength sides of the TRPL peaks at τ=0 ns and τ=2 ns overlap each other, but there is a significant difference on the short wavelength side, with the τ_{0ns} spectrum extending further and resulting in a blue-shift of the peak. This is the same

behaviour as noted in previous reports on other Type II CQDs, as discussed above and examples of which are shown in Figure 4. 3 and Figure 4. 4, and attributed to a repulsive X-X interaction.

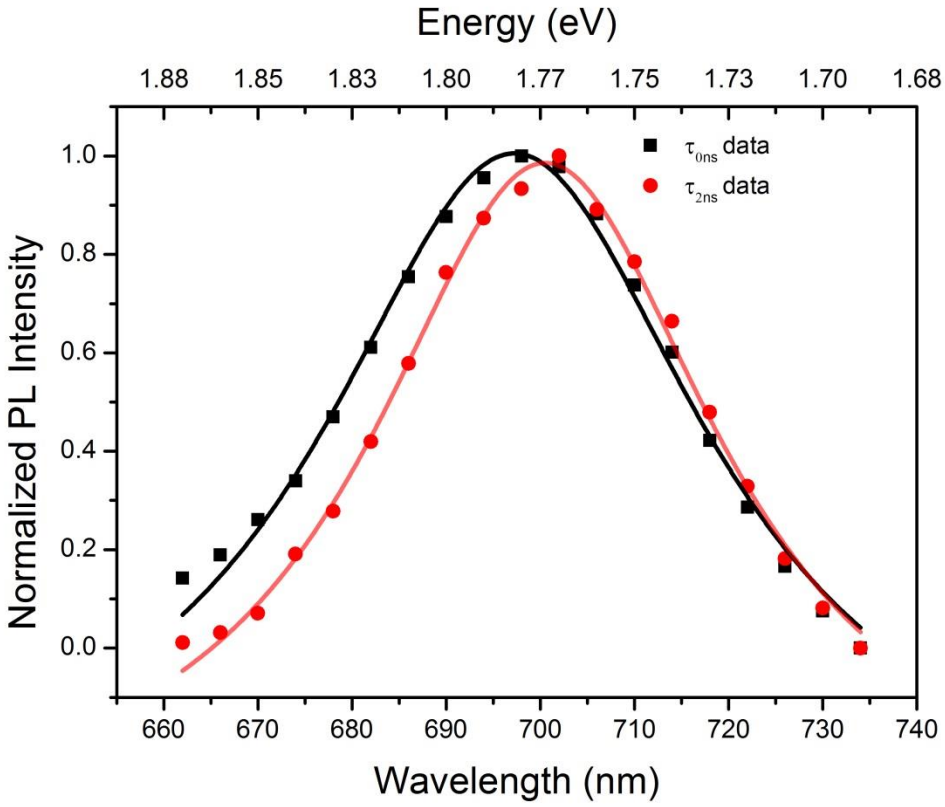

Figure 4. 10 Comparison between normalized τ_{0ns} (Black line) and τ_{2ns} (Red line) data

The TRPL spectra were thus analysed using the method pioneered by Klimov et al [5]. This is a process of deconvolution of the τ_{0ns} spectrum, using a Lorentzian peak fitting function, the form of which is given below in equation (4. 4):

$$y = y_0 + \left(\frac{2A}{\pi}\right)\left(\frac{w}{4(x - xc)^2 + w^2}\right) \quad \textbf{(4. 4)}$$

where A is the area, xc is the centre, y_0 is the offset and w the full width at half maximum (FWHM). The fitting was carried out using the peak analyser capability of OriginLab's OriginPro 8.5 software. First a single peak was fitted to the τ_{2ns} TRPL spectrum. Subsequently, the corresponding τ_{0ns} spectrum was fitted with two peaks, the position

and width of one of which were fixed to the values obtained from the fit to the τ_{2ns} spectrum. The width of the second peak was also fixed to value obtained from the fit to the τ_{2ns} spectrum, since this parameter is determined by the size distribution of the CQDs and thus will be the same for different transition energies. The other fitting free parameters were left free to vary, except for the condition that they should be greater than or equal to zero.

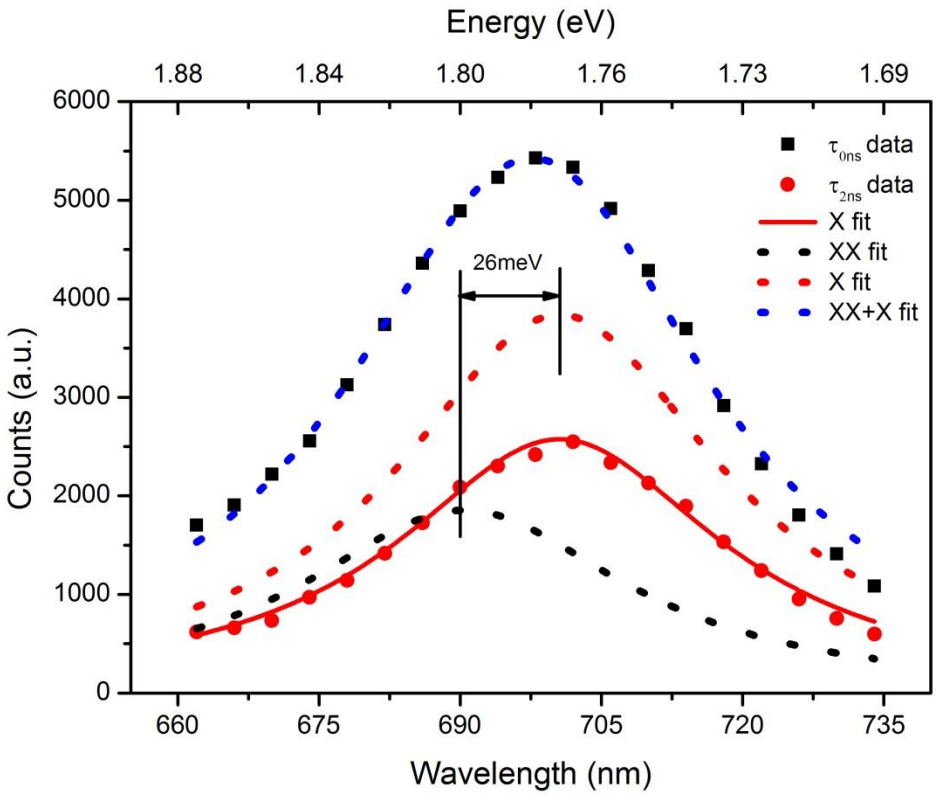

Figure 4. 11 Transient PL of CdSe/CdTe/CdS CQDs.

An example of the method used is shown in Figure 4. 11, and which corresponds to the peak analysis of a sample of CdSe/CdTe/CdS CQDs. The fit of a single Lorentzian peak to the τ_{2ns}.data, corresponding to the PL spectrum due to a single exciton and hence designated the 'X fit', yielded a value for xc and w of 700.5±0.3 nm (1.772±0.001eV) and 42 ± 3 nm, respectively. The fit of the τ_{0ns}spectrum incorporates the X fit plus a second Lorentzian peak, designated as the 'XX fit' since others have associated it with a biexciton, (the τ_{0ns}spectrum is thus described by the 'X+XX fit'), and yields a XX peak

position of 690.4 ±3.9 nm (1.798±0.01 eV). Under this analysis, the XX interaction energy is given by the energy separation of the X and XX peaks, which in this case is repulsive (i.e. blue-shifted) and has a value of +26 ±10 meV, as shown in Figure 4. 11. This Δ_{xx} value is similar to that previously reported for a sample CdSe/CdTe CQDs, although emitting at a wavelength of 800 nm [20]. Similar values have also been reported for CdTe/CSe and ZnTe/Cds Type II CQDs [20, 21].

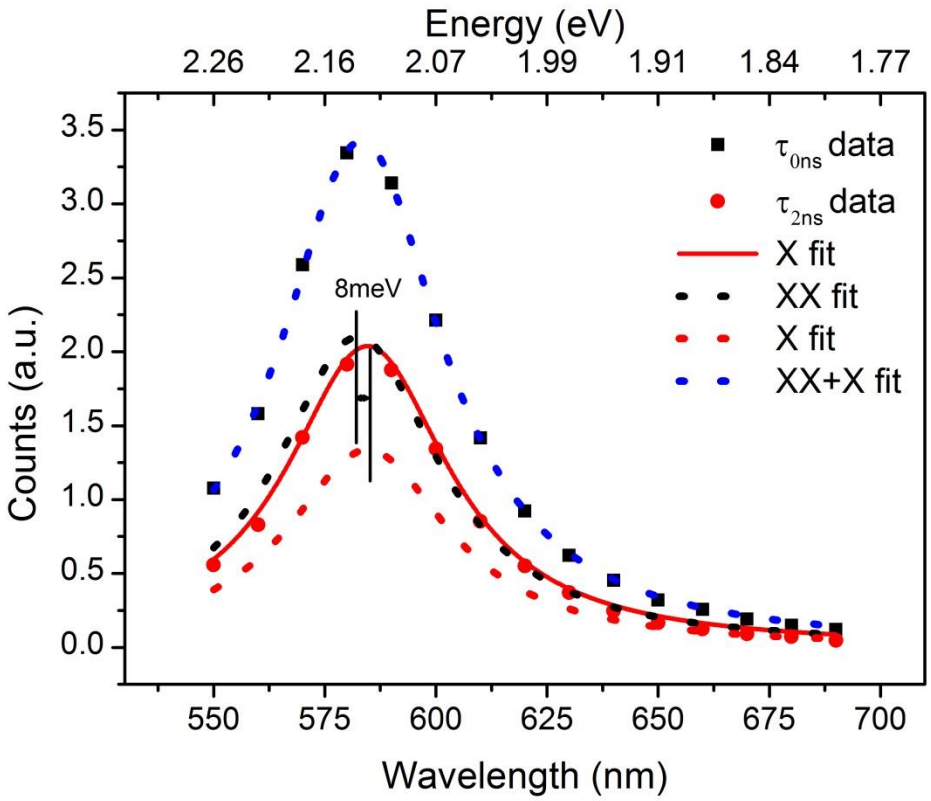

Figure 4. 12 Transient PL of CdSe cores, exciton-exciton interaction is neglected.

Figure 4. 12, corresponds to the peak analysis of a sample of CdSe core CQDs. The fit of a single Lorentzian peak to the τ_{2ns}.data, corresponding to single exciton and designated the 'X fit', yielded a value for xc and w of 584.6±0.4 nm (2.124 ±0.001eV) and 44.51 ±1.7, respectively. The fit of the τ_{0ns}, designated as the 'XX fit' yields a XX peak position of 582.4 ±3.4 nm (2.13 ±0.01 eV). The analysis XX interaction energy is given by the energy

separation of the X and XX peaks, which in this case is repulsive (i.e. blue-shifted) and has a value of +8 ±12 meV, as shown in Figure 4. 12.

However, as shown in Table 4. 3, only 3 out of the 11 samples studied produced TRPL spectra that yielded Δ_{xx} values that were significantly different from zero when analysed in this way i.e. for which the magnitude of Δ_{xx} found by this process was larger than, or at least similar in size to, the associated experimental uncertainty. The principal contribution to this uncertainty comes from the fit to the XX peak, as can be seen from the values given in Table 4.3, which was only a weak contribution to the τ_{0ns} spectrum in some cases even though an identical excitation fluence was used throughout. An example of a TRPL spectrum with a weak XX contribution is given in Figure 4.13. Here the analysis procedure yields a negative value of Δ_{xx}= -57 meV, i.e. corresponding to an attractive interaction and, as shown, a XX peak red-shifted rather than blue-shifted relative to the X peak. However, the associated experimental uncertainty in this case is nearly twice as large in this case at ±95 meV, and so no significance can be attached to this result.

Table 4. 3 Summary of the biexciton interaction energies extracted by the Klimov analysis method [5]. Those samples yielding an interaction energy significantly different from zero are shaded grey.

Samples	*d* (nm)	t_{CdTe} (nm)	t_{CdS} (nm)	Peak 0ns (nm)	Peak 2ns (nm)	Δ_{xx} (meV)
CdSe/CdTe	4.17	2.2		658 ±30	666 ±0.3	24 ±89
CdSe	3.15			573 ±3	574 ±0.1	4 ±11
CdSe/CdTe	3.15	2.2		637 ±24	665 ±0.5	84 ±74
CdSe/CdTe/CdS	3.15	2.2	0.6	690 ±4	701 ±0.3	26 ±10
CdSe/CdTe	3.15	5		729 ±44	728.3 ±0.5	-2 ±102
CdSe/CdTe/CdS	3.15	5	0.6	748 ±67	748 ±0.5	1 ±149
CdSe/CdTe	3.15	2		654 ±32	664 ±0.6	30 ±94
CdSe/CdTe/CdS	3.15	2	0.6	699 ±155	700 ±0.3	4 ±394
CdSe	3.15			582 ±3	585 ±0.4	8 ±13
CdSe/CdTe	3.15	2		652 ±32	633 ±1.5	-57 ±95
CdSe/CdTe/CdS	3.15	2	0.6	623 ±191	658 ±2.5	106 ±611

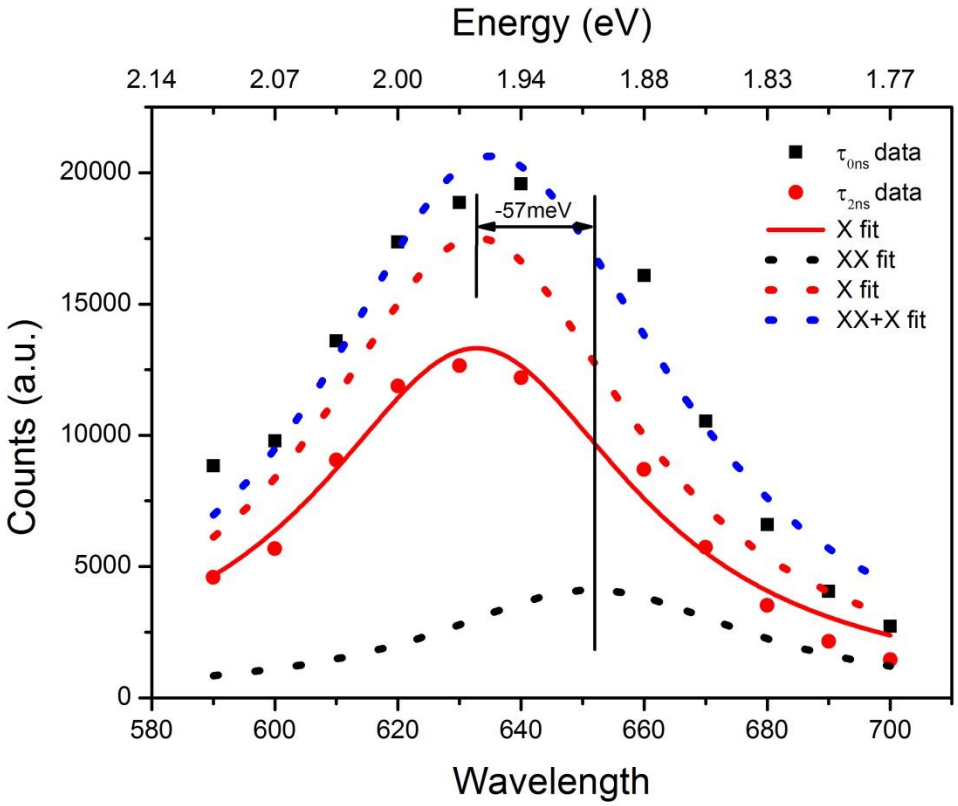

Figure 4. 13 Transient PL of CdSe/CdTe for a attraction interaction.

One possible explanation for a weak XX contribution, and thus of the observed spectra for some of the samples studied here, is that the excitation fluence used is too low to produce a significant population of biexcitons. However, this is not consistent with a significant XX contribution for some of the other samples obtained under identical excitation conditions. As described in section 3.3.1, the probability, P_2, of a CQD containing a biexciton depends on the product of excitation fluence, J, (in units of photons per cm^2 per pulse), and absorption cross-section at the pump wavelength, σ (in units of cm^2). An identical pump power was used in each case, so J is unchanged between spectra. Whilst several detailed studies have established reliable values of σ for CdSe and CdTe CQDS [17, 18, 22], no similar works exist for CdSe/CdTe Type II CQDs. However, at the pump wavelength of 400 nm, optical excitation is to a state not confined by the heterostructure and so the CQD acts as a Type I structure for the process of absorption. Moreover, at this wavelength the cross-section of CdTe and CdSe CQDs are very similar [18]. Thus a significant variation

of σ between samples is unlikely and hence does not easily explain the differences in TRPL spectra observed. Furthermore, calculations of P_2 following the method outlined in chapter 3 and using the same value of σ yield a value of ~0.6, indicating that a significant biexciton population is to be expected. Moreover, as will be discussed at length in the next section, recent experimental results obtained by other techniques and theoretical calculations cast doubt on the interpretation of any of the TRPL spectra as involving a significant XX contribution.

4.4. Discussion

In order to extend the X-X energy interaction studies ultrafast transient absorption (TA) experiments were performed initially by Stuart K Stubbs [23] and subsequently by Musa Cadirci [24], both of them students in the D. J. Binks group. Stubbs reported a large and attractive behaviour for CdSe/CdTe/CdS CQD, with Δ_{XX}=-96±7 meV. This red shift was observed right after the CQDs were-photo excited in which the contributions of high order multi-excitons and hot excitons are potentially present. In contrast, Musa Cadirci carried out the TA experiment with a delay between the pump and probe pulses of ≥500 ps, sufficient to allow all carriers to cool to the band edge and all multi-excitons to recombine, and thus created a pure population of cooled excitons. The probe pulse creates a second exciton in the pump-excited CQDs, which are exclusively monitored by the phase-sensitive detection scheme synchronised to the pump laser. Thus the X-X interaction energy for a pure population of cooled biexcitons could be found.

The results of these TA measurements by Musa Cadirci for some of the same samples as studied here using TRPL are shown in Table 4. 4. Strikingly, the TA experiment yielded only attractive energy interactions instead of repulsive, as in the TRPL measurement. These seemingly contradictory results show that the interpretation of the data produced by one or both of these techniques need to be revisited in order for these experiments to be reconciled.

Table 4. 4 Comparison of Δ_{XX} values between TRPL and TA experiments

Samples	*d* (nm)	t_{CdTe} (nm)	t_{CdS} (nm)	Δ_{xx} TRPL (meV)	Δ_{xx} TA (meV)
CdSe/CdTe	4.17	2.2		24±86	-50±0.5
CdSe	3.15			4±12	-17±2.0
CdSe/CdTe	3.15	2.2		84±75	-46.01±7.0
CdSe/CdTe/CdS	3.15	2.2	0.6	26±10	-36.1±2.2
CdSe/CdTe	3.15	5		-2±102	-34.1±1.5
CdSe/CdTe/CdS	3.15	5	0.6	1±149	-59.1±2.3
CdSe	3.15			8±13	-16.1±6.1
CdSe/CdTe/CdS	3.15	2	0.6	106±311	-60±7.2

The re-interpretation of this type of experimental data can be aided by modelling [19, 25, 26], and so, in order to understand in more detail these results, Professor Stanko Tomic at the University of Salford and his group collaborated with us to produce a model which calculates the exciton-exciton interactions energies in type II QDs. The model takes into account higher energy bands, interface polarization, the effects of spin-orbit interaction and strain between the core and the shell, and piezoelectric potential. Their model is based on a 14-band **k.p** Hamiltonian of the zinc-blend structure [25, 27].

Using the new data provided from Stanko Tomic's group, the CdTe shell thicknesses could be re-calculated. Figure 4. 14a shows the calculated position of the 1S absorption peak as a function of CdTe shell thickness for CdSe core radii of 1.5 nm and 2.0 nm, with interpolated values for the intermediate radii. Thus, measuring the position of the first absorption peak allows the thickness of the CdTe shell to be determined for a known CdSe core radius. The size of the cores was also re-calculated using de Mello et al [18]. The results of these re-calculations are given in Table 4.5 below. Moreover, the calculation of Δ_{XX} as a function of CdTe shell thickness for 1.5 nm and 2.0 nm radius CdSe core done by S. Tomic's group are shown in Figure 4. 14b. The calculated values are all negative, i.e. attractive, and of similar magnitude to the values found experimentally by TA. Hence, these theoretical calculations are consistent with the TA measurements and do not support the Δ_{XX} values found by the TRPL technique.

Table 4. 5 Updated CdSe radius cores and CdTe shell thickness calculation

Samples	r (nm)	t_{CdTe} (nm)	t_{CdS} (nm)	Absorbance peak (nm)	PL Peak (nm)
CdSe/CdTe	2	0.84		656	687
CdSe/CdTe/CdS	2	0.84	?	670	698
CdSe/CdTe	2	0.81		650	663
CdSe/CdTe/CdS	2	0.81	?	672	687
CdSe	1.6			555	567
CdSe/CdTe	1.6	0.96		630	666
CdSe/CdTe/CdS	1.6	0.96	?	666	695
CdSe/CdTe	1.6	1.74		713	728
CdSe/CdTe/CdS	1.6	1.74	?	723	745
CdSe/CdTe	1.6	0.92		622	668
CdSe/CdTe/CdS	1.6	0.92	?	655	696
CdSe	1.72			567	590
CdSe/CdTe	1.72	0.82		614	630
CdSe/CdTe/CdS	1.72	0.82	?	659	664

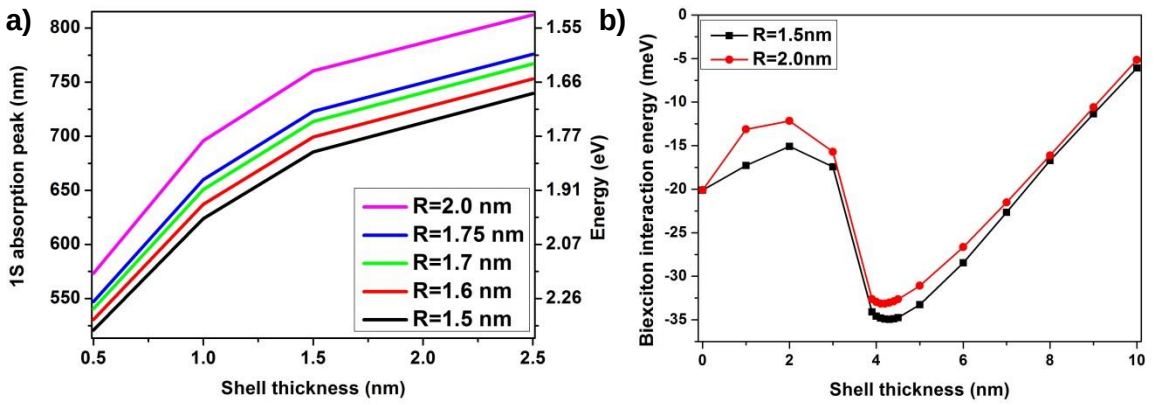

Figure 4. 14 a)Calculation of the CdTe shell thickness by the absorption peak of the CdSe core and b) Bi-exciton binding energy of CdSe/CdTe as a function of CdTe shell thickness(S.Tomic's group data).

If Δ_{XX} is attractive, in agreement with the theoretical calculations and TA measurements, and the excitation level sufficient to produce a significant biexciton population, why is not red-shifted peak observed in the τ_{0ns} spectrum and why is instead a blue-shifted peak evident, but for just a fraction of the samples studied?

The absence of a red-shifted peak can be explained by a low PLQY for biexcitons, which has been shown to range from <10% to nearly unity for 'giant' CQDs (i.e. a core surrounded by a very thick shell layer) [28]. However, the near unity PLQY values have

only reported for individual CQDs studied by single particle spectroscopy, with other CQDs in the same sample exhibiting much lower PLQY. The radiative rate constant for biexcitons should be 4 times that of single excitons since there are 4 times the number of recombination possibilities [29].Thus if for a single exciton τ_{rad} ~10 ns, as seen in Figure 4. 9, then for a biexciton the radiative lifetime should be a few ns, much longer than the 10s of ps observed in M. Cadirci's TA measurements [21]. The lack of PL features due to biexcitons is thus attributed to non-radiative Auger recombination dominating their decay.

The model of the CQDs electronic structure from the Tomic group also enabled detailed energy level calculations to be carried out. Figure 4. 15 shows the energy of the band edge transition relative that of the next highest energy transition. For a core radii of both 1.5 nm and 2.0 nm, i.e. encompassing those studied experimentally, and for a range of shell thicknesses also including those studied in the TRPL experiments, the difference in energies between these transitions varied between 20 and 35 meV. Emission from the higher level would therefore produce a PL feature blue-shifted by the same amount from the main PL, which corresponds to the band edge transition, and is thus consistent with the τ_{0ns}spectrum observed for some of our samples. The higher level would be thermally populated at room temperature but would have a great population whilst the energy of the absorbed photon in excess of the band gap is being dissipated, leading to a greater prominence of the corresponding PL feature immediately after excitation. Emission from a higher lying states has been noted before in Type I [30].The rate of energy relaxation in Type II CQDs has previously been shown [2] to vary significantly with the quality of surface passivation, which can depend on the details of sample preparation and handling and thus might explain the sample-to-sample variation observed.

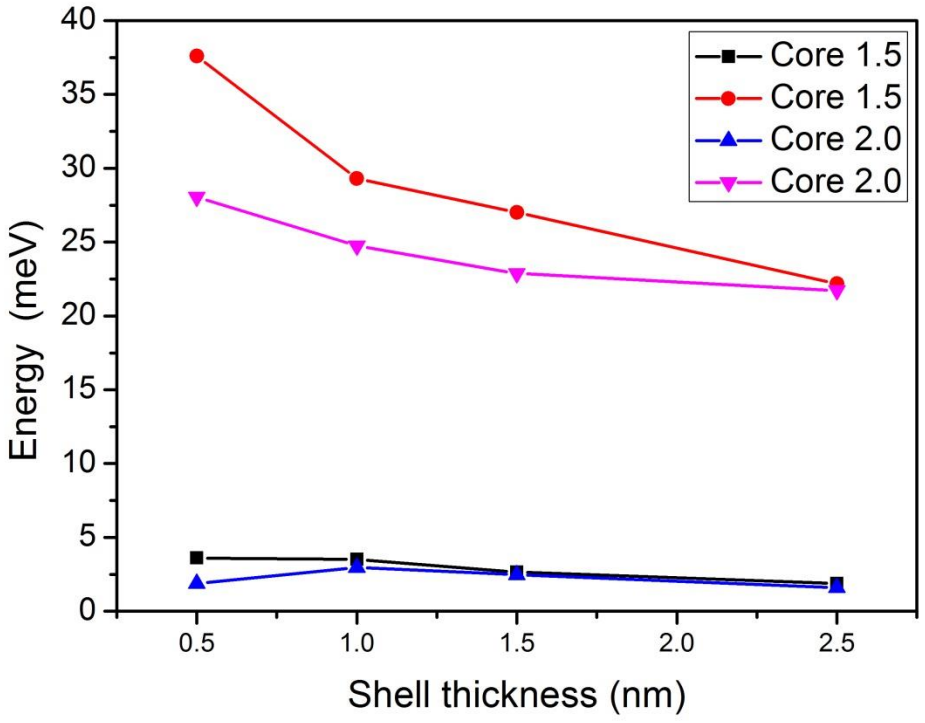

Figure 4. 15 Calculation of the next energy level from the condition band in CdSe/CdTe CQDS with core diameter of 1.5nm and 2.0 in function of the shell thickness

To confirm that the transition energy difference predicted by the calculations of the electronics structure of the CQDs is consistent with the TRPL spectra observed, the analysis of one of the spectra with a clear, additional blue-shifted peak at τ=0 ns was repeated using the energy difference as the peak shift. Figure 4. 16 shows the previous fit used to calculate Δ_{XX}, called Fit A (dotted lines) and the new fit using the energy level separation calculated by Stanko Tomic's group, this fit was called Fit B. Fit B was completed using same fixed parameters as in Fit A with one exception, the center of XX Fit B was fixed using the calculated energy difference between from the band edge transition and the next highest transition. By comparing Fit A and Fit B, it can be seen that there is not a significant change in the cumulative fit peak, i.e. the peak did not suffer a deformation by changing the centre of the XX fit. The only variation is on the amplitudes; the amplitude of X Fit for Fit B is reduced but still similar to the original amplitude fitted

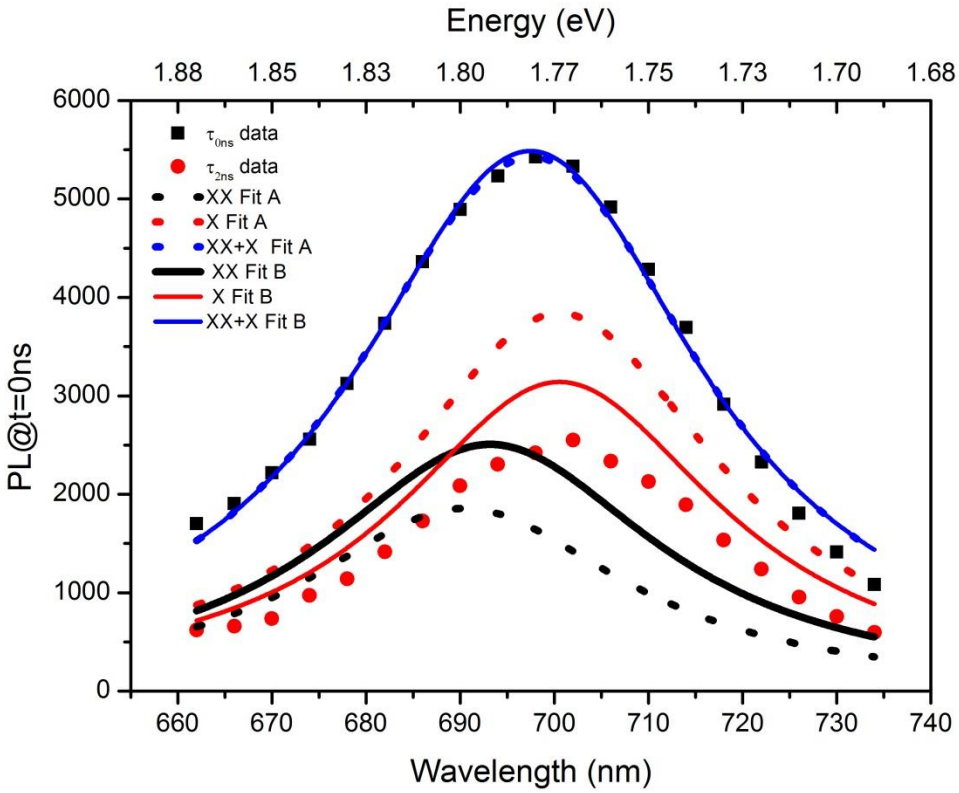

Figure 4. 16 Refit of the TRPL spectra using calculated transition energy difference

Hence, we conclude that the method of determining Δ_{XX} by analysis of TRPL spectra established over the last decade by a number of workers is not reliable, producing in our case results that are inconsistent with both theoretical calculations and ultrafast transient absorption experiments. The low PLQY for biexcitons in some samples resulting from the competition of radiative recombination with efficient non-radiative processes means that the expected spectrally-shifted PL feature corresponding to the biexciton is not evident even at excitation rates sufficiently high to produce a significant biexciton population. Moreover, emission from higher energy transitions can produce blue-shifted PL component that can easily be mis-attributed to biexcitons, making the accurate determination of Δ_{XX} by this technique even more difficult.

.

References

1. Ivanov, S.A., A. Piryatinski, J. Nanda, S. Tretiak, K.R. Zavadil, W.O. Wallace, D. Werder, and V.I. Klimov, *Type-II core/shell CdS/ZnSe nanocrystals: Synthesis, electronic structures, and spectroscopic properties.* Journal of the American Chemical Society, 2007. 129(38): p. 11708-11719.
2. Pandey, A. and P. Guyot-Sionnest, *Slow Electron Cooling in Colloidal Quantum Dots.* Science, 2008. 322(5903): p. 929-932.
3. Schaller, R.D., J.M. Pietryga, and V.I. Klimov, *Carrier multiplication in InAs nanocrystal quantum dots with an onset defined by the energy conservation limit.* Nano Letters, 2007. 7(11): p. 3469-3476.
4. McElroy, N., M. Cadirci, A. Al-Otaify, R. Page, and D.J. Binks, *Increasing Efficiency with Multiple Exciton Generation.* Quantum Dot Solar Cells, 2014. 15: p. 233-253.
5. Klimov, V.I., S.A. Ivanov, J. Nanda, M. Achermann, I. Bezel, J.A. McGuire, and A. Piryatinski, *Single-exciton optical gain in semiconductor nanocrystals.* Nature, 2007. 447(7143): p. 441-446.
6. Ivanov, S.A., J. Nanda, A. Piryatinski, M. Achermann, L.P. Balet, I.V. Bezel, P.O. Anikeeva, S. Tretiak, and V.I. Klimov, *Light amplification using inverted core/shell nanocrystals: Towards lasing in the single-exciton regime.* Journal of Physical Chemistry B, 2004. 108(30): p. 10625-10630.
7. Nanda, J., S.A. Ivanov, M. Achermann, I. Bezel, A. Piryatinski, and V.I. Klimov, *Light amplification in the single-exciton regime using exciton-exciton repulsion in type-II nanocrystal quantum dots.* Journal of Physical Chemistry C, 2007. 111(42): p. 15382-15390.
8. Oron, D., M. Kazes, and U. Banin, *Multiexcitons in type-II colloidal semiconductor quantum dots.* Physical Review B, 2007. 75(3).
9. Ivanov, S.A. and M. Achermann, *Spectral and Dynamic Properties of Excitons and Biexcitons in Type-II Semiconductor Nanocrystals.* Acs Nano, 2010. 4(10): p. 5994-6000.
10. Rawalekar, S., S. Kaniyankandy, S. Verma, and H.N. Ghosh, *Ultrafast Charge Carrier Relaxation and Charge Transfer Dynamics of CdTe/CdS Core-Shell Quantum Dots as Studied by Femtosecond Transient Absorption Spectroscopy.* Journal of Physical Chemistry C, 2010. 114(3): p. 1460-1466.
11. Rawalekar, S., S. Kaniyankandy, S. Verma, and H.N. Ghosh, *Surface-State-Mediated Charge-Transfer Dynamics in CdTe/CdSe Core-Shell Quantum Dots.* Chemphyschem, 2011. 12(9): p. 1729-1735.
12. McDonald, P.G., E.J. Tyrrell, J. Shumway, J.M. Smith, and I. Galbraith, *Tuning biexciton binding and antibinding in core/shell quantum dots.* Physical Review B, 2012. 86(12).
13. Mohamed, M.B., D. Tonti, A. Al-Salman, A. Chemseddine, and M. Chergui, *Synthesis of high quality zinc blende CdSe nanocrystals.* Journal of Physical Chemistry B, 2005. 109(21): p. 10533-10537.
14. Yu, Y., Y. Lai, X. Zheng, J.Z. Wu, Z.Y. Long, and C.S. Liang, *Synthesis of functionalized CdTe/CdS QDs for spectrofluorimetric detection of BSA.* Spectrochimica Acta Part a-Molecular and Biomolecular Spectroscopy, 2007. 68(5): p. 1356-1361.
15. Lewis, E.A., R.C. Page, D.J. Binks, T.J. Pennycook, P. O'Brien, and S.J. Haigh, *Probing the core-shell-shell structure of CdSe/CdTe/CdS type II quantum dots for solar cell applications.* Electron Microscopy and Analysis Group Conference 2013 (Emag2013), 2014. 522.

16. Page, R.C., *Synthesis of cadmium chalcogenide based quantum dots for enhanced multiple exciton generation*, in *School of Chemistry*2014, The University of Manchester.
17. Yu, W.W., L.H. Qu, W.Z. Guo, and X.G. Peng, *Experimental determination of the extinction coefficient of CdTe, CdSe, and CdS nanocrystals.* Chemistry of Materials, 2003. 15(14): p. 2854-2860.
18. de Mello Donega, C. and R. Koole, *Size Dependence of the Spontaneous Emission Rate and Absorption Cross Section of CdSe and CdTe Quantum Dots.* The Journal of Physical Chemistry C, 2009. 113(16): p. 6511-6520.
19. Tyrrell, E.J. and J.M. Smith, *Effective mass modeling of excitons in type-II quantum dot heterostructures.* Physical Review B, 2011. 84(16).
20. Deutsch, Z., A. Avidan, I. Pinkas, and D. Oron, *Energetics and dynamics of exciton-exciton interactions in compound colloidal semiconductor quantum dots.* Physical Chemistry Chemical Physics, 2011. 13(8): p. 3210-3219.
21. Avidan, A., Z. Deutsch, and D. Oron, *Interactions of bound excitons in doped core/shell quantum dot heterostructures.* Physical Review B, 2010. 82(16).
22. Kamal, J.S., A. Omari, K. Van Hoecke, Q. Zhao, A. Vantomme, F. Vanhaecke, R.K. Capek, and Z. Hens, *Size-Dependent Optical Properties of Zinc Blende Cadmium Telluride Quantum Dots.* Journal of Physical Chemistry C, 2012. 116(8): p. 5049-5054.
23. Stubbs, S.K., *Photo-physics and applications of colloidal quantum dots*, in *Faculty of Engineering and Physical Sciences*2010.
24. Cadirci, M., *Ultrafast charge dynamics in novel colloidal quantum dots*, in *Faculty of Engineering and Physical Sciences, School of Physics and Astronomy*2014, The University of Manchester.
25. Tomic, S. and N. Vukmirovic, *Symmetry reduction in multiband Hamiltonians for semiconductor quantum dots: The role of interfaces and higher energy bands.* Journal of Applied Physics, 2011. 110(5).
26. Miloszewski, J.M. and S. Tomic, *Many-Body Effects In CdSe/CdTe Coloidal Quantum Dots.* 2014 14th International Conference on Numerical Simulation of Optoelectronic Devices (NUSOD 2014), 2014: p. 1-2.
27. Miloszewski, J.M., S. Tomic, and D. Binks, *Theoretical studies of excitons in type II CdSe/CdTe quantum dots.* 4th Workshop on Theory, Modelling and Computational Methods for Semiconductors (Tmcsiv), 2014. 526.
28. Park, Y.S., A.V. Malko, J. Vela, Y. Chen, Y. Ghosh, F. Garcia-Santamaria, J.A. Hollingsworth, V.I. Klimov, and H. Htoon, *Near-Unity Quantum Yields of Biexciton Emission from CdSe/CdS Nanocrystals Measured Using Single-Particle Spectroscopy.* Physical Review Letters, 2011. 106(18).
29. McGuire, J.A., M. Sykora, J. Joo, J.M. Pietryga, and V.I. Klimov, *Apparent Versus True Carrier Multiplication Yields in Semiconductor Nanocrystals.* Nano Letters, 2010. 10(6): p. 2049-2057.
30. Moreels, I., G. Raino, R. Gomes, Z. Hens, T. Stoferle, and R.F. Mahrt, *Band-Edge Exciton Fine Structure of Small, Nearly Spherical Colloidal CdSe/ZnS Quantum Dots.* Acs Nano, 2011. 5(10): p. 8033-8039.

Chapter 5. Single-exciton recombination dynamics in Type II CQDs.

5.1. Introduction

Despite of all the studies performed in the past, still some optical properties of CQDs are under research due to the difficultly in identifying and characterising the underlying processes. Recombination is such a fundamental property, which can be divided into radiative and non-radiative processes. Radiative and non-radiative recombination characteristics are important to take into account for the design of devices, such as solar cells, lasing, light emitting devices and other applications [1]. Recombination processes can be investigated by measuring the photoluminescence lifetime and photoluminescence quantum yield (PLQY) of the CQDs.

The PLQY of CQDs is typically less than 100% which shows that non-radiative recombination processes are significant. In a simple emitting system, the radiative and non-radiative processes can be determined straightforwardly using the following relations for the PL lifetime, τ_{rad}, (see eq.(5. 1) and PLQY (see eq. (5. 2)

$$\tau_{PL} = \frac{1}{k_{rad} + k_{non-rad}} \quad \textbf{(5. 1)}$$

$$\mathrm{PLQY} = \frac{k_{rad}}{k_{rad} + k_{non-rad}} \quad \textbf{(5. 2)}$$

where k_{rad} and $k_{non-rad}$ are the rate constants for the radiative and non-radiative processes respectively. Using equations (5. 1) and (5. 2), simple relations between the

underlying radiative, $\tau_{rad} = k_{rad}^{-1}$, and non-radiative lifetimes, $\tau_{non-rad} = k_{non-rad}^{-1}$, and the experimentally observed τ_{PL} determined from the PL transients can be written down:

$$\tau_{rad} = \frac{\tau_{PL}}{PLQY}$$

$$\tau_{non-rad} = \frac{\tau_{PL}}{1 - PLQY}$$

(5. 3)

Unfortunately, it is not possible to characterise the radiative and non-radiative processes for CQDs using eq (5. 3), with the exception of CQDs with high PLQY values (near unity) for which non-radiative recombination is minimal. In contrast when the PLQY values are not near unity, non-radiative recombination becomes important and PL intermittency (also known as 'blinking') becomes significant. This is a process by which the PL is switched 'on' or 'off' within individual CQDs., and means that some CQDs within a sample do not contribute to the emission of light at a particular time [1]. However, the fraction of CQDs not emitting only affects the PLQY but not the PL decay [2, 3], invalidating equation (5.3). Another important factor is that the degree of trapping of the CQDs is different for each sample, due to the preparation and handling varying from sample to sample. Consequently this makes the reproducibility of the experiment problematic. Finally, significant non-radiative decay rates tend to produce non-exponential PL decays that cannot be characterised by a single time constant.

A typical PL decay shows a multi-exponential behaviour, requiring a tri-exponential fit to be well-described (see eq (5. 4). Using a tri-exponential fit involves up to 7 free parameters (3x τ, 3x A and y_0):

$$\tau_{PL} = y_0 + A_1 e^{-x/\tau_1} + A_2 e^{-x/\tau_2} + A_3 e^{-x/\tau_3}$$

(5. 4)

where y_0 is an offset, A_i are the amplitudes and τ_i are the time constants ($i = 1,2,3$). The tri-exponential fit might well describe the PL decay data behaviour, but in order to analyse the recombination dynamics, the radiative and non-radiative recombination processes still need to be identified from the fit. The process of separating the rates of radiative and non-radiative recombination is problematic.

In order to analyse the radiative and non-radiative rates, some authors have identified the longest time component extracted from a tri exponential fit as the radiative lifetime (e.g. [4] takes τ_3 as τ_{rad}). However, this approach is not always valid and needs detailed consideration for each case. Moreover, this methodology utilises 7 parameters that are free to vary in the fit, increasing the difficulty to robustly identify 3 separate time constants. Indeed, by comparing the total PLQY to the QY of the emitting CQDs, which was estimated by integrating the longest time constant (τ_3) component of the PL decay with respect to time and dividing by the total area under the PL decay curve, it has been established that for some QDs the longest decay component is definitely not the radiative component ($\tau_3^{-1} \neq \tau_{rad}^{-1}$).

Due to these difficulties some researchers [4] have tried a different approach, which initially tries to estimate with calculation τ_{rad} and then compare the calculation results with experimental data. However, the calculation of τ_{rad} is also very challenging. The emission from CQDs occurs from a thermally populated system of sub-levels, produced by the angular momentum fine-structure of the CQD, each of which have different lifetimes and oscillator strengths [5, 6], and the energy separation between states are in the order of several to tens of meV. These energies and therefore their thermal population depends on the size and shape of the QD [4]. This is the reason ref [4] takes the approach of empirically calculating the radiative lifetime from the integrated extinction coefficient spectrum, using

$$\tau_{rad}^{-1} = 2.88 \times 10^{-9} n^2 \langle \nu_{PL}^2 \rangle \int \varepsilon(\hat{\nu})\, d\hat{\nu} \qquad \textbf{(5. 5)}$$

where the $\hat{\nu}$ is the wavenumber and $\varepsilon(\hat{\nu})$ is the molar extinction coefficient. In practice this approach is complex, due to the troublesome calculation of the molar extinction coefficient $\varepsilon(\hat{\nu})$. The difficulty is based on the limited accuracy to which the concentration of CQDs in each sample can be determined. A typical sample of QD also contains an unknown number of ligands attached to the QD surface, and excess ligand and unreacted reagents left over from synthesis. This can be solved with washing and purification procedures, designed to remove the excess ligands however they also remove surface ligands which decrease the PLQY [6-10]. The extinction coefficient of CdSe QDs has been studied for wurtzite and zincblende structures [3, 11-13]. These results show a rough calculation of the extinction coefficient, in which for both structures the extinction coefficient increases with the particle size.

The approach presented in this chapter is based on the results of a detailed modelling of τ_{rad}^{-1} that include 14 bands, band coupling, spin-orbit interaction, strain and piezo-electric fields. The model was also used in Chapter 4, and the calculation of τ_{rad} were done by Professor Stanko Tomic and his group at the University of Salford. The model is an updated version of his previous work [14-16]. The consistencies of the calculated and observed results are assessed, and the PL transient data is re-analysed by fixing one of the lifetimes to the calculated value of τ_{rad}. This approach allows the time constants associated with non-radiative recombination to be more robustly determined which are then correlated to CQD structure.

5.2. Characterisation of CdSe core based on CQDs Type II

The synthesis and the optical characterisation of the type II CQDs based on a CdSe core with a CdTe shell and an extra shell of CdS, have been previously described in detail in section 4.2. However, a brief re-cap of the synthesis and characterisation of these CQDs is presented.

The synthesis of CQDS were done by Robert C Page [17], using a hot injection method, the CdSe core QDs have a zinc blende crystal structure; this structure is beneficial in the shelling process allowing uniform growth. These CQDs have a type II structure, in which the electron and hole (e-h) are localised in different part of the CQD [18], one in the core and the other in shell; this spatial separation of electron and hole reduces the wave-function overlap. In type II CQDs, the recombination occurs between the conduction band minimum and the valence band maximum of the electron- and hole- containing material, respectively, and by changing the alignment of the conduction and valence band edge (i.e. adjusting the core diameter and the thickness of the sell) the optical properties can be tuned.

The quality of the CQDs were evaluated with X-ray powder diffraction (XRD) patterns and scanning transmission electron microscope microscopy (STEM) studies by collaborators based in the School of Materials and the School of Chemistry, R.C Page [17] and E A Lewis [19]. The XRD patterns confirmed a zinc blende crystal structure for all the samples (CdSe, CdSe/CdTe and CdSe/CdTe/CdS); in addition the STEM images showed lattice fringes which correspond to a zinc blende structure. Also the STEM images showed a high monodispersity for the CdSe core, but this monodispersity was reduced by the shelling process. (XRD patters and STEM images are in section 4.2)

The absorption and photoluminescence (PL) spectra results are presented in Table 5. 1including PL quantum yield (PLQY) calculation by the comparative method. The radius of the CdSe core was calculated using the first absorption peak and de Mello and Koole

calculations [3]. The CdTe shell thickness was also obtained from the position of the first absorption peak using the results of calculations, done by S. Tomic's group, of the red-shift produced when a shell is grown onto a core of known diameter (see section 4.4).

Table 5. 1 Core radius, r, CdTe shell thickness, t_{CdTe}, and CdS shell thickness, t_{CdS}, for the CQDs studied. The first absorbance peak, the spectral position of the PL peak and the PLQY are also given.

Samples	r (nm)	t_{CdTe} (nm)	t_{CdS} (nm)	Absorbance peak (nm)	PL Peak (nm)	PLQY
CdSe/CdTe	2	0.84		662	682	
CdSe/CdTe/CdS	2	0.84	?	670	698	
CdSe/CdTe	2	0.81		650	663	
CdSe/CdTe/CdS	2	0.81	?	672	687	
CdSe	1.6			555	570	
CdSe/CdTe	1.6	0.96		630	676	
CdSe/CdTe/CdS	1.6	0.96	?	666	712	
CdSe/CdTe	1.6	1.74		713	729	
CdSe/CdTe/CdS	1.6	1.74	?	723	747	
CdSe/CdTe	1.6	0.92		622	669	
CdSe/CdTe/CdS	1.6	0.92	?	655	692	
CdSe	1.72			567	590	2%
CdSe/CdTe	1.72	0.82		614	630	26%
CdSe/CdTe/CdS	1.72	0.82	?	659	664	34%

The CdS shell is grown to passivate the CdTe surface, due to telluride being sensitive to air [20]. For CdTe CQDs surface hole trapping is also expected to contribute to PL decay [21] and so the CdS also acts as a barrier to the surface for holes. The CdS shell was grown under the same conditions for all samples in order to have the same thickness throughout this work, and so the CdS thickness measured previously (see last chapter) is assumed to representative of the thicknesses here.

5.3. PL decay transients measurements

The PL decay transients were measured using a time-correlated single photon counting (TCSPC) system, previously described in section 3.3. The CQDs were excited at a repetition rate of 4 MHz and at wavelength of 400 nm. The PL decay transients of the CQDs were measured at the PL peak of each sample, and the TCSPC system was setup to stop acquiring when 10 000 counts were reached. Figure 5. 1 shows a representative PL decay transients for CdSe core (black line), CdSe/CdTe (red line) and CdSe/CdTe/CdS (blue line) CQDS, all of them with a tri-exponential fit (dotted green line).

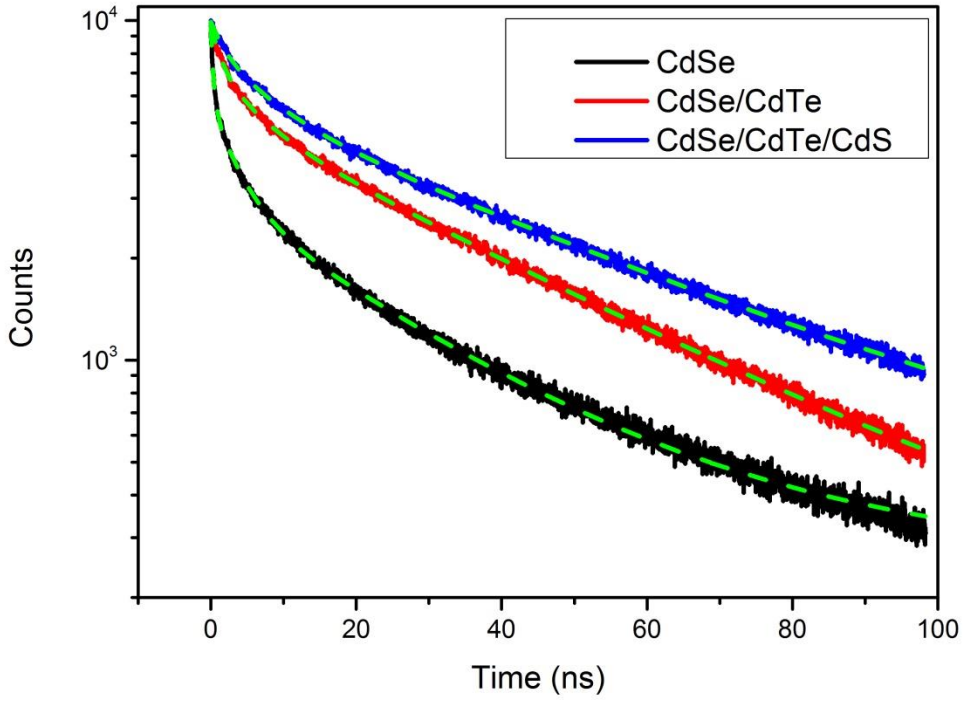

Figure 5. 1 PL decay transients with tri-exponential fit (dotted green line) for CdSe(balck line), CdSe/CdTe (red line) and C CdSe/CdTe/CdS CQDs.

The tri-exponential was fitted using equation (5. 4), where the 7 parameters were free to vary (3x τ, 3x A and y_0).The fits of the PL decay transient were analysed using a OriginLab's tri-exponential function for OriginPro 8.5 software. The data fitted for the PL decay transient were from the 0 ns (which is equivalent to the highest number of counts

10 000) to 100ns. The same data range was used for the fits performed throughout this chapter.

The values obtained from the tri-exponential fits shown in Figure 5. 1 are given in Table 5. 2. The lower bounds of the fitting were adjust to be ≥ 0 for the offset (y_0), time constants (3x τ) and amplitude (3x A). for clarity The time constants are numbered in descending order of magnitude to make easier the comparison between them i.e. the longer time constant was called τ_1 etc. The associated amplitudes were given the same number.

Table 5. 2 Result from a tri-exponential fit for CdSe, CdSe/CdTe and CdSe/CdTe/CdS CQDs. (cts = counts)

Samples	*d* (nm)	t_{CdTe} (nm)	t_{CdS} (nm)	A1 (cts)	τ_1 *(ns)*	A2 (cts)	τ_2 *(ns)*	A3 (cts)	τ_3 *(ns)*
CdSe	1.6			2728 ±10	27.86 ±0.17	2778 ±15	3.73 ±0.04	3768 ±24	0.36 ±0.005
CdSe/CdTe	1.6	1.74		5211 ±23	38.72 ±0.32	2279 ±67	1.48 ±0.04	2123 ±53	6.02 ±0.22
CdSe/CdTe/CdS	1.6	1.74	?	5533 ±39	47.12 ±0.78	2529 ±56	8.11 ±0.36	1597 ±84	2.05 ±0.10

The calculated radiative lifetimes (τ_{rad}) for different CdSe core radii and varying the shell thicknesses are shown in The Figure 5. 2. The solid back, red and blue lines correspond to 1.5nm, 2.0 nm and 2.5 nm core radius of CdSe CQDs respectively. These radiative lifetime calculations were done by collaborators from Tomic's group. And the dotted lines corresponding to core radius of 1.6 nm and 1.72 nm were interpolated values from Tomic's calculations. The interpolation was required to match the radii of the CdSe core based samples synthetized by Robert C.Page. The radiative lifetime (τ_{rad}) is found from Figure 5. 2, where τ_{rad} is a function of the shell thickness and the core radius.

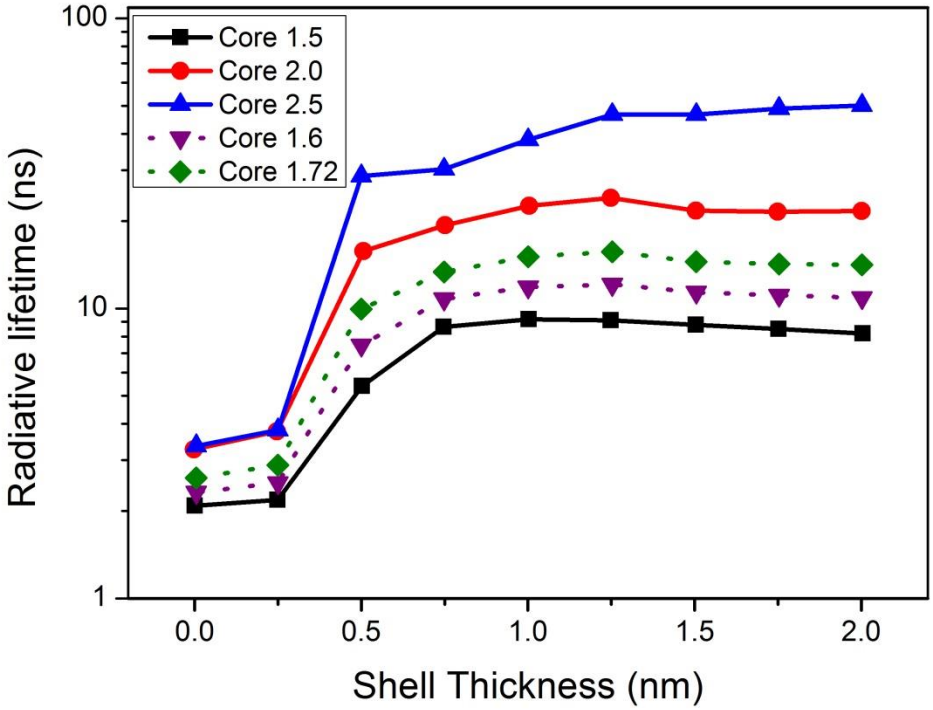

Figure 5. 2 Radiative lifetime (τ_{rad}) for CdSe/CdTe CQDs in function of the shell thickness (Modified from [22]).

Table 5. 3 The extracted radiative lifetimes τ_{rad} for different core radius and shell thicknesses

Samples	*r* (nm)	t_{CdTe} (nm)	t_{CdS} (nm)	τ_{rad} (ns)
CdSe/CdTe	2	0.84		20.5±0.37
CdSe/CdTe/CdS	2	0.84	?	20.5±0.37
CdSe/CdTe	2	0.81		20.1±0.36
CdSe/CdTe/CdS	2	0.81	?	20.1±0.36
CdSe	1.6			2.3±0.04
CdSe/CdTe	1.6	0.96		11.7±0.21
CdSe/CdTe/CdS	1.6	0.96	?	11.7±0.21
CdSe/CdTe	1.6	1.74		11.1±0.20
CdSe/CdTe/CdS	1.6	1.74	?	11.1±0.20
CdSe/CdTe	1.6	0.92		11.5±0.21
CdSe/CdTe/CdS	1.6	0.92	?	11.5±0.21
CdSe	1.72			2.6±0.05
CdSe/CdTe	1.72	0.82		13.8±0.25
CdSe/CdTe/CdS	1.72	0.82	?	13.8±0.25

The values of the τ_{rad} extracted from Figure 5. 2 are shown in Table 5. 3. These values were used for a new tri-exponential fit. The resultant time components for τ_2 and τ_3, will

be called τ_{slow} and τ_{fast} respectively, with their respective amplitudes named A_{slow} and A_{fast} .

The tri-exponential decays were re-fitted by fixing one τ constant with the extracted radiative lifetime (τ_{rad}). In Figure 5. 3 the new fit was called "Fixed τ_{rad}Fit" ,and the previous fit was renamed as "Free τ_{rad}Fit". The lower bounds of the fixed τ_{rad} fit were adjusted to be ≥ 0 for the offset (y_0), $\tau_{slow,}\tau_{fast,}$ and A_{rad}.

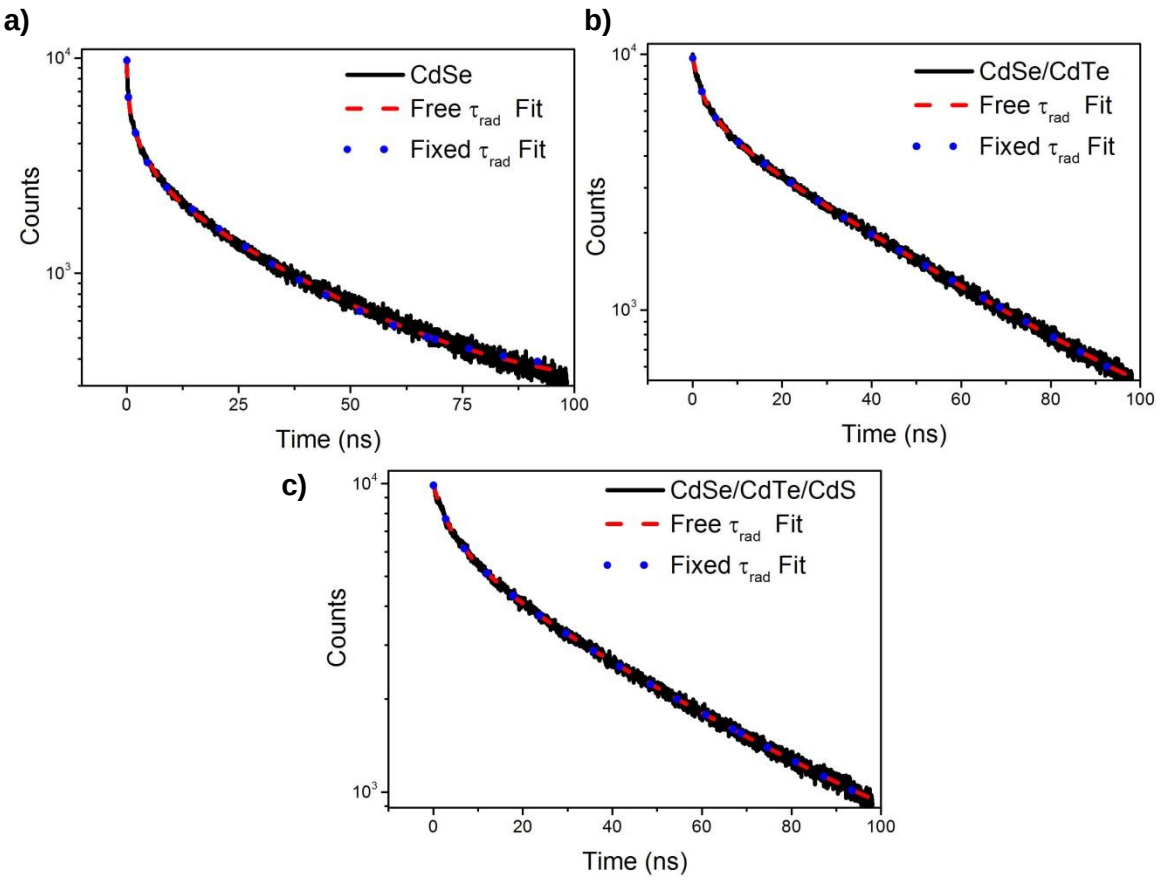

Figure 5. 3 Comparison of the tri-exponential fit between free τ_{rad} (dashed red line) and fixed (dotted blue line) τ_{rad} for a) CdSe, b) CdSe/CdTe and c) CdSe/CdTe/CdS CQDs.

Figure 5. 3 shows three PL decays - (a) CdSe , b) CdSe/CdTe and c) CdSe/CdTe/CdS - with two tri-exponential fits each (free τ_{rad}fit and fixed τ_{rad}fit). By comparing the two fits, it cn be seen that there is no apparent change between the trace of both fit, i.e. both fits describe well the behaviour of the PL decay. A detailed comparison between the time

constant resulting from each of the two fits is shown in Figure 5. 4 for three different core radiuses as function of shell thickness.

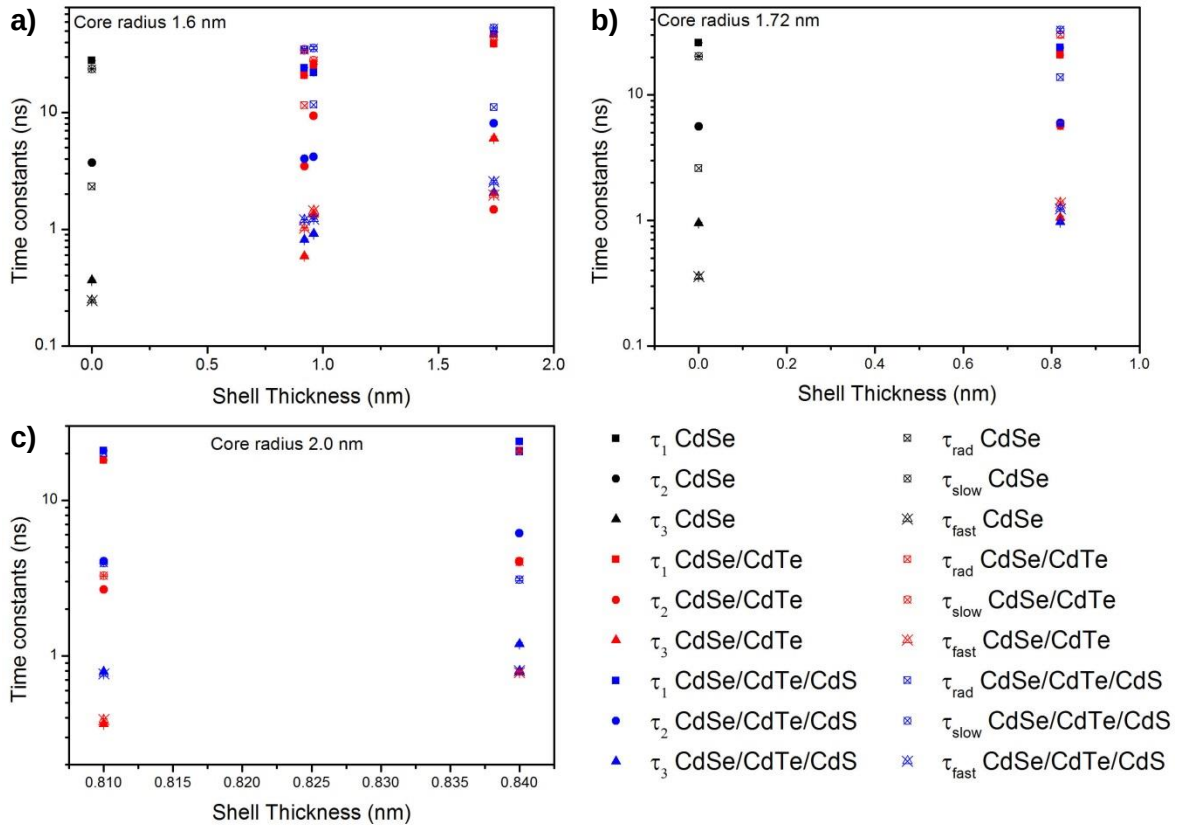

Figure 5. 4 Comparison between free τ_{rad} and fixed τ_{rad} fits for 3 different core radiuses (a)1.5 nm,b) 1.72 nm and c) 2.0 nm) in function of shell thickness. The samples are divided by colour: CdSe cores in black, CdSe/CdTe in red and CdSe/CdTe/CdS in blue. And each colour has 3 time constants associated from each fit. The fill shapes are from free τ_{rad} fit and open crossed shapes from fixed τ_{rad} fits are

In Figure 5. 4, the comparison between the filled shapes and open crossed shapes confirms that the free τ_{rad} fit and fixed τ_{rad}fit often yield different values for the time constants. The τ_{rad} for the core radius of 2.0 nm were similar to the free fit. However, τ_{rad} for the cores radius of 1.6 and 1.72 nm the values were 2 orders of magnitude greater from the free fit. This results show that choosing the largest time constant in order to determine the radiative constant (τ_{rad}) is unreliable. Therefore by fixing the extracted radiative time constant (τ_{rad}) the fitting process becomes more accurate.

5.4. Results of the non-radiative components

Non-radiative recombination is produced when the electron-hole pair recombine without releasing a photon, with the energy instead being dissipated as heat e.g. a phonon (i.e. vibration) is released. This type recombination is usually unwanted since it reduces PL, PLQY and PL lifetime of CQDs. The non-radiative process is usually associated with a charge trapping process involving defects, unsaturated bonds on the surface, or ligands attached to the surface.

As demonstrated in the previous section, knowing τ_{rad} allows the non-radiative component to be extracted more reliably from the tri-exponential fit. This component is described by τ_{slow} and τ_{fast} and the associated amplitudes. As shown in Figure 5.2, τ_{fast} is in the order of ps to a few ns, and τ_{slow} is usually several ns or 10s of ns.

The parameters describing the non-radiative component are plotted in this section as function of core size and shell thickness. Samples with core radii of 1.6 nm and 1.72 nm were treated as being sufficiently close to include in the same shell thickness graphs. The following colour labelling scheme was followed: the CdSe core plotted in black, the CdSe/CdTe plotted in red and in blue CdSe/CdTe/S. Symbols were used to distinguish between the non-radiative components, in which the diamonds are related to the slow component and the inverted triangles with the fast component. Due to the amount of data points and in some cases the overlapping points, the graphs were not merged to facilitate the view of the data points.

The non-radiative time constants are presented in Figure 5. 5 (versus shell thickness) and Figure 5. 6 (versus core radius); and their related amplitudes in Figure 5. 7 (versus shell thickness) and Figure 5. 8. (versus core radius)

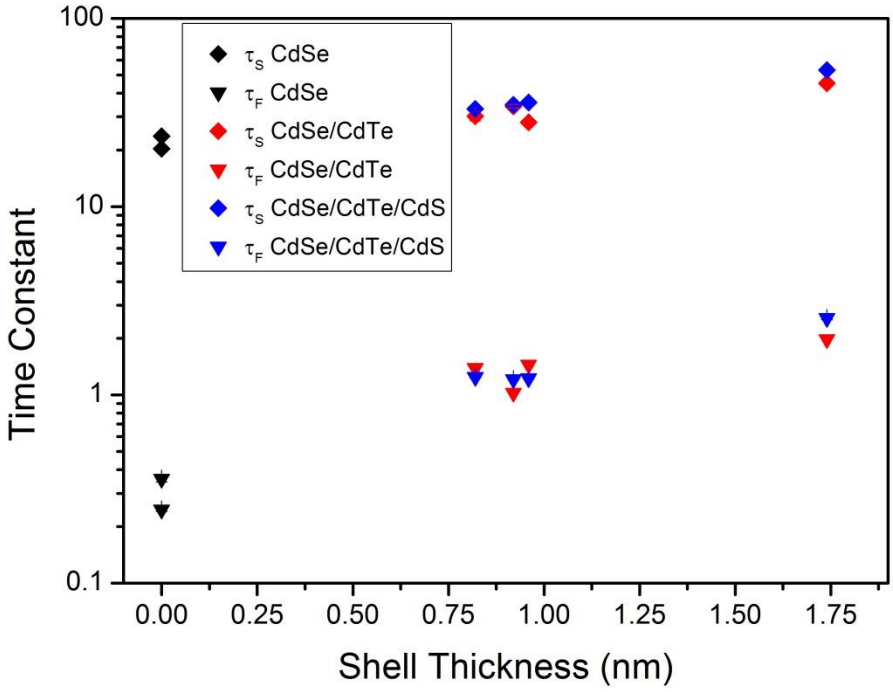

Figure 5. 5 Non-radiative time constants in fuction of shell thickness for CdSe, CdSe/CdTe and CdSe/CdTe/CdS CQDs

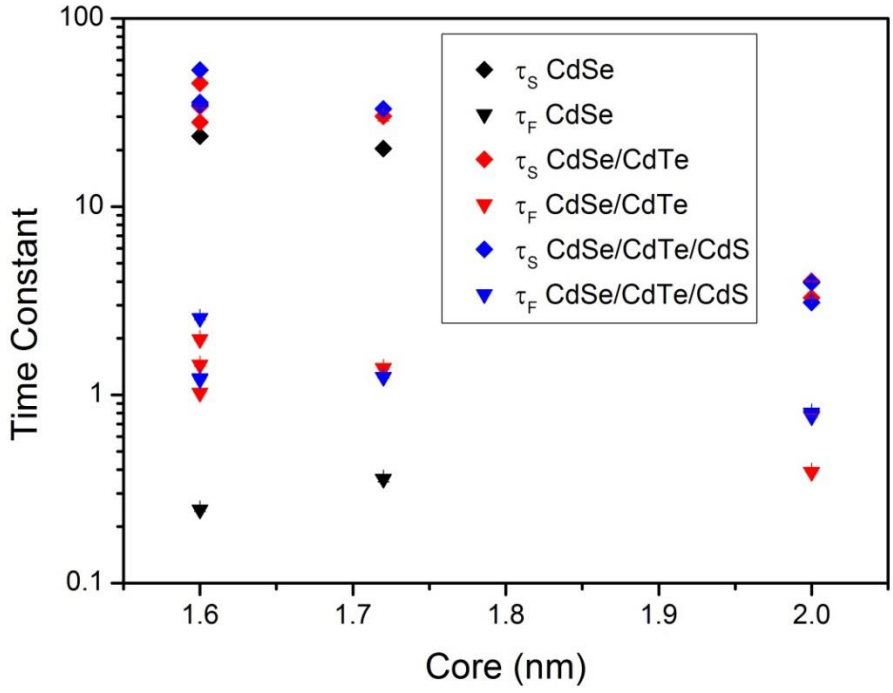

Figure 5. 6 Non-radiative time constants in fuction of core radius for CdSe, CdSe/CdTe and CdSe/CdTe/CdS CQDs

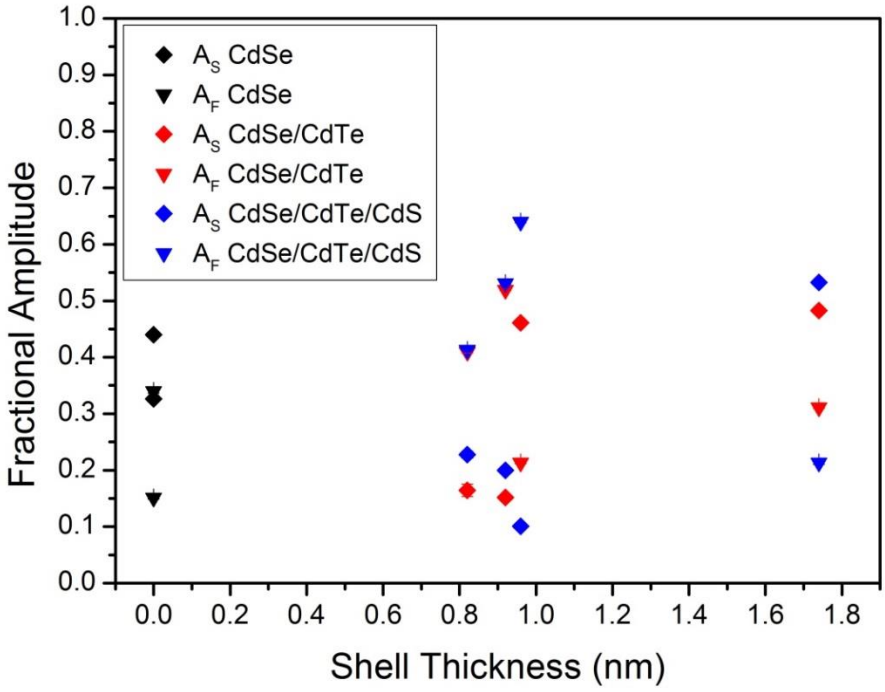

Figure 5. 7 Fractional amplitude in fuction of shell thickness for CdSe, CdSe/CdTe and CdSe/CdTe/CdS CQDs

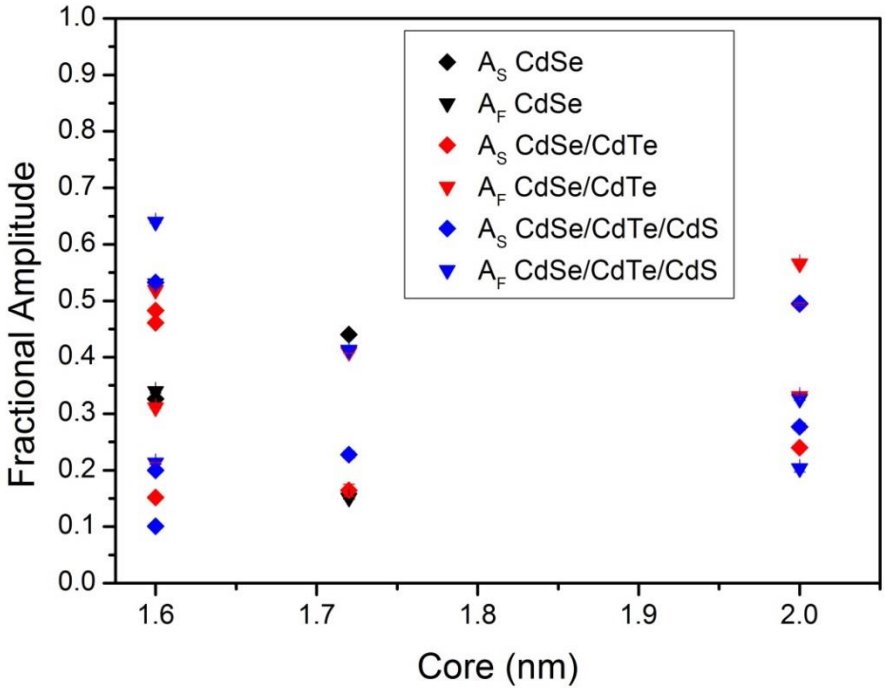

Figure 5. 8 Fractional amplitude in fuction of core radius for CdSe, CdSe/CdTe and CdSe/CdTe/CdS CQDs

Figure 5. 5 shows a clear trend for the non-radiative time constants with both τ_{slow} and τ_{fast} growing with shell thickness. The values for τ_{fast} were from tens of ps for no-shell up to few ns for the thickest shell, and for the τ_{slow} component were from 2 ns up to 6 ns.

The non-radiative time constants as a function of the core size are shown in Figure 5. 6 and reveal two main trends. The trend for the value of τ_{slow} is to reduce for an increase of core size. The values found for of τ_{fast} follow the same trend but less pronounced. The exception to this is the increase of τ_{fast} with core size for the CdSe only QDs, but since this involves only two data points care must taken in attributing much significance to this.

The fractional amplitudes of the non-radiative component as a function of the shell thickness are shown in Figure 5. 7. The fractional amplitudes of A_{slow} and A_{fast} show a random distribution. Similar distribution was also observed in Figure 5. 8 where the fractional amplitudes are as a function of the core size.

The non-radiative components showed strong trends for τ_{slow} and τ_{fast} components. .However, the lack of trend for A_{slow} and A_{fast} suggest that the fractional amplitudes are governed by the fraction of CQDs with traps that emit, which is likely to be sensitively dependent on the details of how the samples were prepared and handled.

5.5. Analysis of PL transients

The analysis of the PL transient was based on the idea of shallow trapping [4], and describes a non-radiative process , k_{nr}, with alternative paths for a fraction of the CQDs. These QDs have a trap state close to the valance band maximum, which can capture holes. From this trap state the hole can recombine non-radiatively with a conduction band electron or it can be thermally-liberated back to the valance band maximum.

This model was adapted from the one proposed by Kelley [4] in conjunction with my supervisor [23]. It is based on the postulation that there are three types of CQD in any population: trap-free, with dark traps and with bright traps.

The 'trap-free' CQDs correspond to when the recombination dynamics are completely radiative, i.e. PLQY ~100%. Values near unity have been reported for CdTe/Cl CQDs; these CQDs were passivated with chlorine ions to suppress the surface traps, showing PLQY up tp 97.2 ± 2.5% [21, 23]. The radiative process, (k_r), for the trap-free CQD is illustrated in Figure 5. 9a

CQDs with 'dark traps' do not emit any light and hence do not contribute to the PL decay transient. Studies of 'blinking' have shown that some CQDs can be completely non-radiative for periods of time longer than the duration of the experimentally observed PL lifetimes [24]. The blinking reduces the PLQY but does effect $I_{PL}(t)$ [25].

CQDs with 'bright traps' contain a shallow trap, from which charge can sometimes escape back to the band edge so that it can emit light on radiative recombination. The observed PL transient shows emission with a non-exponential form (eq. (5. 6)) which, as shown below, comes naturally out of the analysis for a shallow trap level. Trap levels have been modelled by Marco Califano, using his Auger-mediated trapping (ATM) model. The model finds that the trap level is due unsaturated bonds on the surface [26]. For CdTe CQDs the surface trap were unsaturated Te bonds which trap holes[21]. In addition, he found that the traps states are centered around two energy values $E_1 \approx E_{VBM}^{bulk} + 0.45$ eV and $E_2 \approx E_{VBM}^{bulk} + 0.05$ eV for CdTe CQDs for radii of 1.1nm and 2.3 nm [27]. Since the first

group of surface states have energies similar to the thermal energy, these traps are shallow enough to depopulate by using thermal energy.

The model of bright traps is expressed in eq. (5. 6)

$$I_{PL}(t) = A_{Trap-free}\ e^{-t/\tau_r} + A_{BT}\ f(t) \quad \textbf{(5. 6)}$$

where $I_{PL}(t)$ is the observed PL transient; the $I_{PL}(t)$ involve an exponential function $A_{Trap-free}\ e^{-t/\tau_r}$,which is the radiative process, and $A_{BT}\ f(t)$ is a non-exponential function. This non-exponential function includes the effects of the processes of trapping, with a rate constant, k_T, and detrapping, with rate constant k_D, and a non-radiative recombination process from the trap state, with rate constant k_{nr}.

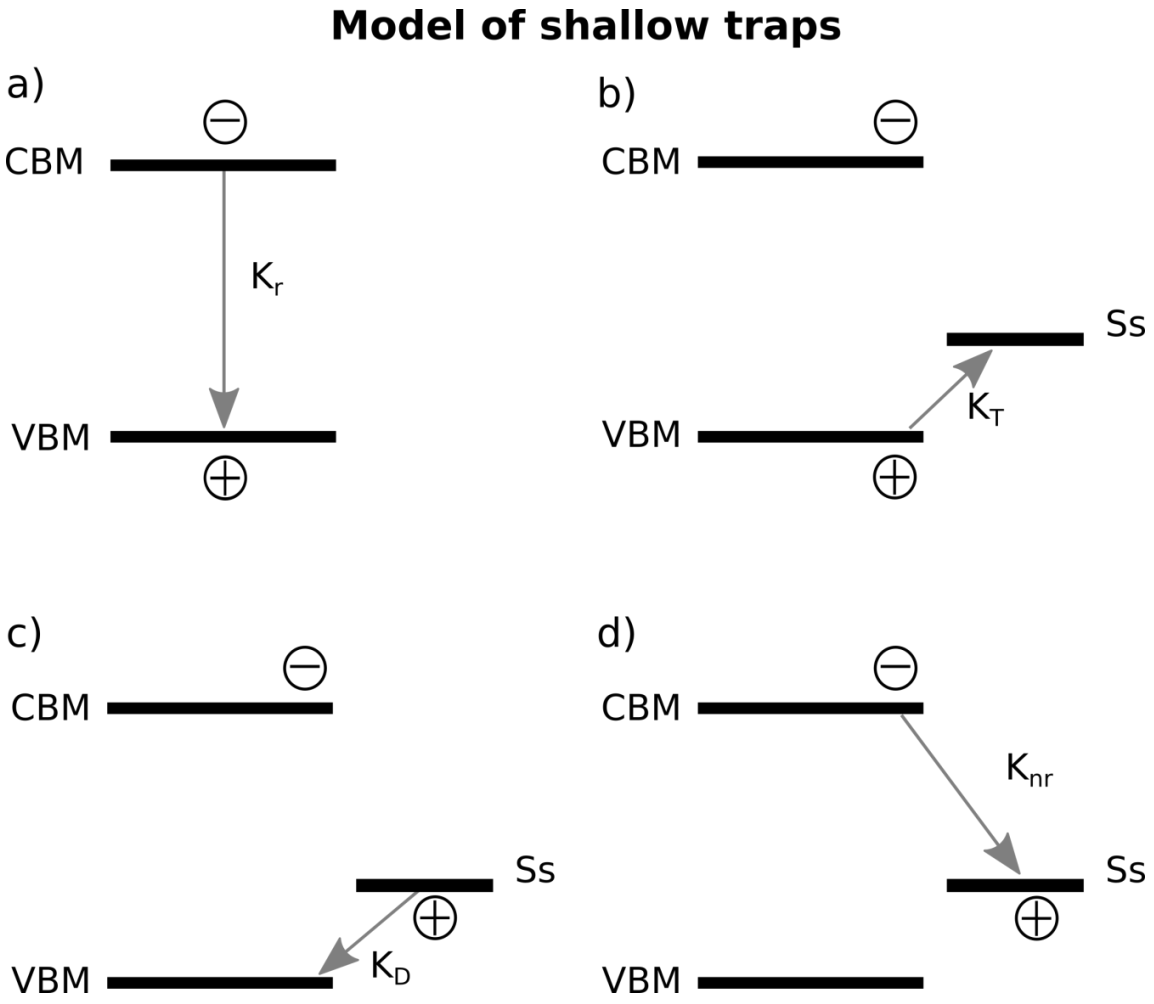

Figure 5. 9 Shallow traps model describes the possible recombination processes a) radiative process k_r, b) trapping process k_T, detrapping process k_D and d) non-radiative process k_{nr} [28].

Figure 5. 9 shows the possible processes for the model of shallow traps. This model explains the experimentally observed PL transient, which is described by eq (5. 6). There are two possible recombination processes: radiative or non-radiative. If it is radiative the valence band maximum (VBM) loses a hole by recombination(Figure 5. 9a). If the process is not radiative, the hole is trapped in a surface state (SS) and the VBM loses a hole (Figure 5. 9b). The trapping process leads to two possible process: thermal detrapping (Figure 5. 9c) or non-radiative recombination (Figure 5. 9d). In the detrapping process the VBM regains a hole, and the SS loses the hole gained during the trapping. The SS can also lose a hole during the non-radiative recombination process.

Based on the number of holes gained or lost in VBM and SS, the following rate equations can be written:

$$\dot{n} = -k_r n - k_T n + k_D n_T \tag{5. 7}$$

$$\dot{n}_T = +k_T n - k_D n_T - k_{nr} n_T \tag{5. 8}$$

where n is the number of holes in the VBM and n_T is the number of holes trapped in the SS.

The solution of these rate equations is a bi-exponential function with characteristic rates constants k_+ and k_- where

$$k_\pm = \frac{-(k_1 + k_2) \pm \sqrt{(k_1 + k_2)^2 - 4(k_1 k_2 - k_D k_T)}}{2} \tag{5. 9}$$

in which k_1 is $(k_r + k_T)$and k_2 is $(k_D + k_{nr})$. These rate constants are identified with the non-radiative components found by fitting to the PL decay transients. Thus, minus the sum of these characteristics rate constants equals the sum of the rate constants identified above. Since k_r is known from the calculation of τ_{rad} then a quantity derived from the fit to

the experimental PL decay, that is dependent only on the non-radiative rate constants can calculated

$$k_{nr} + k_D + k_T = -(k_+ + k_-) - k_r = \left(\frac{1}{\tau_{fast}} + \frac{1}{\tau_{slow}} - \frac{1}{\tau_r}\right) \quad \textbf{(5. 10)}$$

This analysis thus allows the effect of CQD structure on the total rate of the non-radiative processes to be determined experimentally, free of the influence of radiative recombination on the data.

The total non-radiative rate and the associated fractional amplitude, calculated from the sum of slow and fast amplitudes, were plotted versus shell thickness and versus core. For clarity the data points were grouped by structure of CQDs (CdSe in black, CdSe/CdTe in red and CdSe/CdTe/CdS in blue), and the figure shape indicates the type of thickness of the shell (squares for no shell, circles for medium shell values from 0.81 to 9.6 nm, and triangles for 1.74). Also the 1.6 nm and 1.72 nm core radius were merged for the shell thickness graphs.

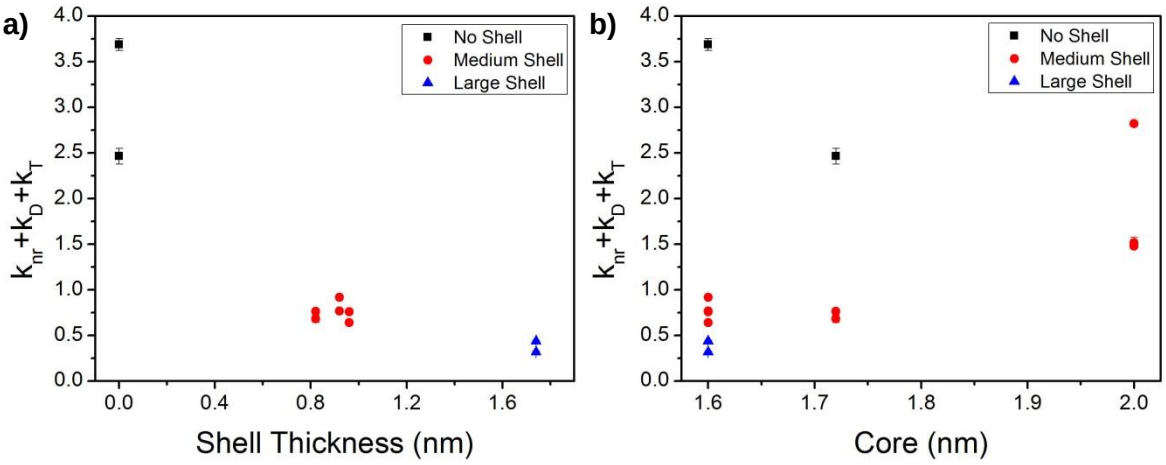

Figure 5. 10 Total rate of non-radiative process in fuction of the shell thickness (a) and (b)core size.

The calculated total rate as a function of the shell thickness is showed in Figure 5. 10a, where a strong trend is observed: the total rate is sharply decreased by the growth of shell thickness. The AMT rate depends on the wave-function overlap between electron and

hole, which decreases for thicker shells, explaining the observed behaviour. The total rate for the CdS shell is lower than the one for a single shell, which suggests the CdS shell inhibits somewhat the trapping process, but this inhibition is not dramatic.

In Figure 5. 10b there is an indication that the total rate increases for greater core size but the trend is not as clear as that with increasing shell thickness. This may be because increasing core diameter has two conflicting effects on the rate of AMT. The quantum confinement energy is reduced for larger cores, which both lowers the energy of CBM to its bulk value and also reduces the separation between adjacent levels. A lower CBM results in better confinement of the electron by the CdSe/CdTe heterojunction and thus reduced wave-function overlap which tends to lower the AMT rate. Conversely, the decreased energy level separation in the CBM better allows electrons to resonantly accept energy from the holes, which tends to increase the AMT rate. It is the interplay of these two conflicting effects that is likely preventing a clear trend form being evident.

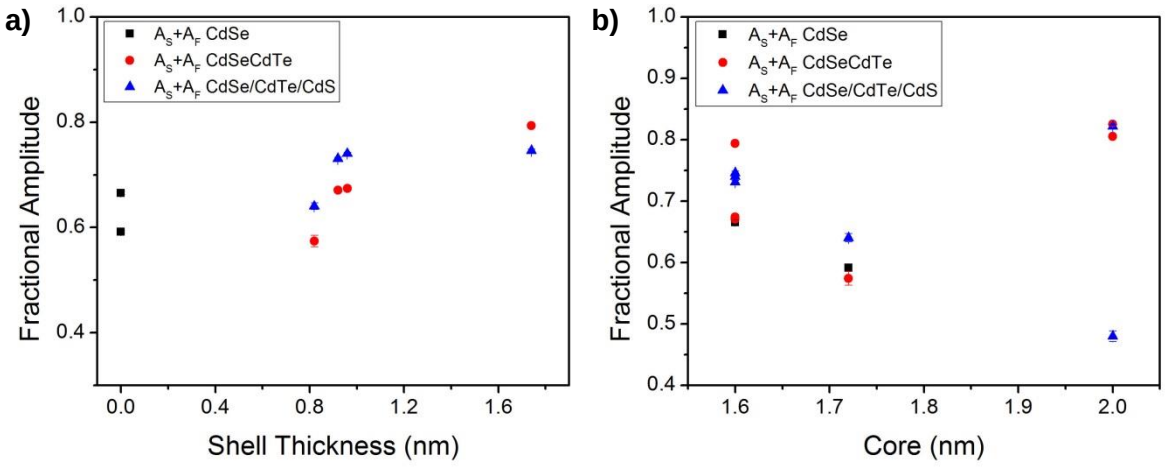

Figure 5. 11 Sum of the fractional anplituds versus shell thickness (a) and core size (b).

Figure 5. 11a shows the sum of the fractional amplitudes ($A_{Slow} + A_{Fast}$) as a function of the shell thickness, where a slight growth in the amplitudes is noticed for an increase of shell thickness. In contrast, Figure 5. 11b shows the sum of the fractional amplitudes ($A_{Slow} + A_{Fast}$) as a function of the core size, with no very clear trend with core size seen.

5.6. Discussion and summary

CQDs have the potential to be used in many applications, however this potential cannot be completely exploited due to the lack of understanding of their recombination dynamics. The analysis of single exciton recombination in CQDs from PL transient measurements is challenging, due to several factors. The recombination processes are usually dominated by non-radiative recombination, which results in low PLQY. The PL transient and PLQY can have a strong relationship, in which the PLQY is described by the ratio between the radiative lifetime and the sum of radiative and non-radiative lifetime (see eq. (5. 3)). However, this relationship separates each process (radiative and non-radiative) only for a simple system, in which the PLQY ~1.

In practise CQDs with high PLQY are not the common case, and in addition the PL often is affected by blinking. Blinking is when the CQD PL is 'on' or 'off' resulting in it contributing to the PL or not. However this does not affect the PL transient decay [24]. Another limitation is the quality and quantity of the sample. The quality is the degree of trapping of the CQDs and this varies from sample to sample. The degree of trapping is related to process of fabrication which introduces an uncertainty in the reproducibility of the CQDs. In addition to these, non-radiative recombination typically produces non-exponential PL decays.

A PL transient typically requires a tri-exponential decay function to be well-described, which involves the use involves up to 7 free parameters (3x τ, 3x A and y_0), and there is thus an accompanying difficulty in robustly separating the rates of radiative and non-radiative recombination.

To solve this difficulty of separating the rates of recombination some authors have chosen the longest time constants extracted from a tri-exponential fit to represent radiative recombination [4]. This approach however involves a drawback. Having 7 free parameters makes it difficult to robustly identify the three separate components. Furthermore when

comparing the total PLQY to the PLQY of just the emitting QDs, estimated by integrating the longest time constant (τ_3) component of the PL decay with respect to time and dividing by the total area under the PL decay curve, it has been established that for some QDs the longest decay component is not the radiative component ($\tau_3^{-1} \neq \tau_{rad}^{-1}$).

Due to the number of complexities, some researchers [4] have tried a different approach, in which a comparison between the experimental data and a calculation of τ_{rad} from extinction coefficient data is done. This approach also involves some challenges. The predicament is to accurately measure the molar extinction coefficient because the concentration of CQD samples is hard to determine with precision. A typical sample of QDs also contains an unknown number of ligands attached to the QD surfaces, and excess ligand and unreacted reagents left over for the synthesis process. Washing and purification procedures, designed to remove the excess ligands also remove surface ligands which decrease the PLQY [6-10].

The approach followed in this work to analyse the recombination process was based on the use of a calculated radiative lifetime to decrease the number of free parameters in the tri-exponential fit. The radiative lifetime was calculated by S. Tomic's group, the detailed modelling of τ_{rad} included 14 bands, band coupling, spin-orbit interaction, strain and piezo-electric field. In order to confirm that the calculated τ_{rad} was adequate, a comparison between the free τ_{rad} and the calculated τ_{rad} tri-exponential fit was done (see Figure 5. 3). Both types of fit describe the PL transients well yet yield significantly different time constants, showing that the free τ_{rad} fit is not a robust way of determining the time constants.

The time constants were extracted from the calculated τ_{rad} fit, in which the non-radiative component of the decay is described by τ_{slow} and τ_{fast} with their respective amplitudes (A_{slow} and A_{fast}). These time components and their amplitudes were analysed by core size and shell thickness; the time constant attributed to τ_{fast} ranged from a few ps to a

few ns, and τ_{slow} ranged between 2 ns and 6 ns. The time constant grew as a function of the shell thickness (see Figure 5. 5), and decreased fas aunction of the core size (Figure 5. 6). The amplitudes A_{slow} and A_{fast} did not present a strong trend which suggest that the amplitudes are governed by the population of trapping CQDs.

A rate equation analysis of recombination was done in order to understand the underlying process. The analysis was based on the idea of shallow traps; a shallow trap is is a surface state produced by unsaturated bonds. This shallow trap can be populated and depopulated by the hole, and the depopulation is due to the thermal energy in the system.

The proposed model considers three types of CQD in any population. Firstly, a 'trap-free' CQD in which recombination is completely radiative. PLQY ~100% has been reported recently [21, 23] showing that this type of CQD can exist. CQDs with a 'dark trap' do not emit. It has been established that some CQDs can be completely non-radiative for periods of time longer than the duration of the experimentally observed PL lifetimes [24]. This 'blinking' reduces the PLQY but it does not contribute to observed PL transient [25]. The 'bright traps' CQDs contain shallow traps, but can still emit after liberation of the hole. The observed PL transients show emission decays that are non-exponential in form. consistent with a shallow trap level. Trap levels have been calculated by AMT modelling, with the trap level due to unsaturated bonds on the surface [26] [21]. The traps states are calculated to be around two energy values $E_1 \approx E_{VBM}^{bulk} + 0.45$ eV and $E_2 \approx E_{VBM}^{bulk} + 0.05$ eV for CdTe CQDs with radii of 1.1 and 2.3nm [27]. Thus these surface states have energies similar to the thermal energy, consistent with shallow traps depopulated using the thermal energy.

References

1. Cordones, A.A. and S.R. Leone, *Mechanisms for charge trapping in single semiconductor nanocrystals probed by fluorescence blinking.* Chemical Society Reviews, 2013. 42(8): p. 3209-3221.
2. Kim, J.Y., O. Voznyy, D. Zhitomirsky, and E.H. Sargent, *25th Anniversary Article: Colloidal Quantum Dot Materials and Devices: A Quarter-Century of Advances.* Advanced Materials, 2013. 25(36): p. 4986-5010.
3. de Mello Donega, C. and R. Koole, *Size Dependence of the Spontaneous Emission Rate and Absorption Cross Section of CdSe and CdTe Quantum Dots.* The Journal of Physical Chemistry C, 2009. 113(16): p. 6511-6520.
4. Gong, K., Y.H. Zeng, and D.F. Kelley, *Extinction Coefficients, Oscillator Strengths, and Radiative Lifetimes of CdSe, CdTe, and CdTe/CdSe Nanocrystals.* Journal of Physical Chemistry C, 2013. 117(39): p. 20268-20279.
5. Efros, A.L., M. Rosen, M. Kuno, M. Nirmal, D.J. Norris, and M. Bawendi, *Band-edge exciton in quantum dots of semiconductors with a degenerate valence band: Dark and bright exciton states.* Physical Review B, 1996. 54(7): p. 4843-4856.
6. Moreels, I., G. Raino, R. Gomes, Z. Hens, T. Stoferle, and R.F. Mahrt, *Band-Edge Exciton Fine Structure of Small, Nearly Spherical Colloidal CdSe/ZnS Quantum Dots.* Acs Nano, 2011. 5(10): p. 8033-8039.
7. Qu, L.H. and X.G. Peng, *Control of photoluminescence properties of CdSe nanocrystals in growth.* Journal of the American Chemical Society, 2002. 124(9): p. 2049-2055.
8. Kilina, S., K.A. Velizhanin, S. Ivanov, O.V. Prezhdo, and S. Tretiak, *Surface Ligands Increase Photoexcitation Relaxation Rates in CdSe Quantum Dots.* Acs Nano, 2012. 6(7): p. 6515-6524.
9. Guyot-Sionnest, P., B. Wehrenberg, and D. Yu, *Intraband relaxation in CdSe nanocrystals and the strong influence of the surface ligands.* Journal of Chemical Physics, 2005. 123(7).
10. Bullen, C. and P. Mulvaney, *The effects of chemisorption on the luminescence of CdSe quantum dots.* Langmuir, 2006. 22(7): p. 3007-3013.
11. Jasieniak, J., L. Smith, J. van Embden, P. Mulvaney, and M. Califano, *Re-examination of the Size-Dependent Absorption Properties of CdSe Quantum Dots.* Journal of Physical Chemistry C, 2009. 113(45): p. 19468-19474.
12. Capek, R.K., I. Moreels, K. Lambert, D. De Muynck, Q. Zhao, A. Vantomme, F. Vanhaecke, and Z. Hens, *Optical Properties of Zincblende Cadmium Selenide Quantum Dots.* Journal of Physical Chemistry C, 2010. 114(14): p. 6371-6376.
13. Kamal, J.S., A. Omari, K. Van Hoecke, Q. Zhao, A. Vantomme, F. Vanhaecke, R.K. Capek, and Z. Hens, *Size-Dependent Optical Properties of Zinc Blende Cadmium Telluride Quantum Dots.* Journal of Physical Chemistry C, 2012. 116(8): p. 5049-5054.
14. Miloszewski, J.M., S. Tomic, and D. Binks, *Theoretical studies of excitons in type II CdSe/CdTe quantum dots.* 4th Workshop on Theory, Modelling and Computational Methods for Semiconductors (Tmcsiv), 2014. 526.
15. Miloszewski, J.M. and S. Tomic, *Many-Body Effects In CdSe/CdTe Coloidal Quantum Dots.* 2014 14th International Conference on Numerical Simulation of Optoelectronic Devices (NUSOD 2014), 2014: p. 1-2.
16. Tomic, S. and N. Vukmirovic, *Symmetry reduction in multiband Hamiltonians for semiconductor quantum dots: The role of interfaces and higher energy bands.* Journal of Applied Physics, 2011. 110(5).
17. Page, R.C., *Synthesis of cadmium chalcogenide based quantum dots for enhanced multiple exciton generation*, in *School of Chemistry*2014, The University of Manchester.

18. Kim, S., B. Fisher, H.Y. Eisler, and M.G. Bawendi, *Novel type-II quantum dots: CDTE/CDSE(core/shell) and CDSE/ZNTE(core/shell) heterostructures.* Abstracts of Papers of the American Chemical Society, 2002. 224: p. U443-U443.
19. Lewis, E.A., R.C. Page, D.J. Binks, T.J. Pennycook, P. O'Brien, and S.J. Haigh, *Probing the core-shell-shell structure of CdSe/CdTe/CdS type II quantum dots for solar cell applications.* Electron Microscopy and Analysis Group Conference 2013 (Emag2013), 2014. 522.
20. Yu, Y., Y. Lai, X. Zheng, J.Z. Wu, Z.Y. Long, and C.S. Liang, *Synthesis of functionalized CdTe/CdS QDs for spectrofluorimetric detection of BSA.* Spectrochimica Acta Part a-Molecular and Biomolecular Spectroscopy, 2007. 68(5): p. 1356-1361.
21. Espinobarro-Velazquez, D., M.A. Leontiadou, R.C. Page, M. Califano, P. O'Brien, and D.J. Binks, *Effect of Chloride Passivation on Recombination Dynamics in CdTe Colloidal Quantum Dots.* Chemphyschem, 2015: p. n/a-n/a.
22. Tomic, S., *Effect of electron correlations on the exciton dynamics in type II CdSe/CdTe core/shell QDs for MEG solar cells*, 2015, IOP: QD Day 2015 one day quantum dot meeting.
23. Page, R.C., Espinobarro-Velazquez, D., Leontiadou, M. A., Smith, C., Lewis, E. A., Haigh, S. J., Li, C., Radtke, H., Pengpad, A., Bondino, F., Magnano, E., Pis, I., Flavell, Wendy. R., O'Brien, P. and Binks, D. J., *Near-Unity Quantum Yields from Chloride Treated CdTe Colloidal Quantum Dots.* Small, 2014.
24. Galland, C., Y. Ghosh, A. Steinbruck, M. Sykora, J.A. Hollingsworth, V.I. Klimov, and H. Htoon, *Two types of luminescence blinking revealed by spectroelectrochemistry of single quantum dots.* Nature, 2011. 479(7372): p. 203-U75.
25. Galland, C., Y. Ghosh, A. Steinbruck, J.A. Hollingsworth, H. Htoon, and V.I. Klimov, *Lifetime blinking in nonblinking nanocrystal quantum dots.* Nature Communications, 2012. 3.
26. Califano, M. and F.M. Gomez-Campos, *Universal Trapping Mechanism in Semiconductor Nanocrystals.* Nano Letters, 2013. 13(5): p. 2047-2052.
27. Califano, M., *Origins of Photoluminescence Decay Kinetics in CdTe Colloidal Quantum Dots.* Acs Nano, 2015. 9(3): p. 2960-2967.
28. Binks, D., *Model of shallow traps analysis* 2015, Photon Science Institute - University of Manchester.

Chapter 6. Photoluminescence of chloride-treated CdTe CQDs.

6.1. Introduction

As discussed earlier Colloidal Quantum Dots (CQDs) are generating a lot of interest due to their low fabrication cost, a band gap tuneable via the quantum size effect, and a number of possible applications such as energy harvesting in solar photovoltaics, and lighting devices [1-3]. However the efficiency of these devices is compromised when the CQDs have many surface traps, which are associated with non-radiative recombination. Photoluminescence (PL), photoluminescence quantum yield (PLQY) and PL lifetime measurements have a strong dependency on the radiative and non-radiative recombination processes, and can be used to investigate their relative and absolute rates.

Trap states are produced by dangling bonds on the surface of the CQDs [4]. In previous reports [5-7] these surface traps have been reduced by passivating the surface with long-chain alkyl and aliphatic ligands. Both methods present complications. The first one is steric hindrance resulting in partial passivation, this mean that some traps remain due to the size of the passivating molecules preventing access to some dangling bonds. The second problem is that the ligand acts as a barrier for the electrons to be extracted or injected, reducing the efficiency of the optoelectronic devices [8, 9].

Recently the use of halide passivation has been shown to be an effective way to reduce traps without affecting the charge mobility; Chuang achieved a record efficiency of 8.55% for a CQD-based solar cell using this method [10]. Passivation with compact halide ions reaches hard-to-access inter-cation sites; this reduces the number of trap states and improves photovoltaic device efficiency [11]. Also halide passivation has been shown to improve photostability and photoluminescence (PLQY). Until now chloride passivated CQDs PLQY

values have been up to 60% [12]. CQDs with chlorine passivation have also shown improved air stability, a particular advantage for heavier chalcogenides (Se and Te).[13].

Chloride passivation can be achieved using different methods and in the literature there are three prevailing techniques: molecular chlorine [13], alkylchlorosilanes [4, 9, 14] and ionic metal chloride salts [1, 15]. The most common passivated CQDs have been Pb(S or Se) and Cd(S or Se). Bae reported molecular chlorine passivation of PbTe which was ineffective due to the instability of the CQDs to decomposition and precipitation [13]. Chloride ion passivation of CdTe has been only studied by Zanella [9]. He used propyltrichlorosilane for the passivation and reported an improvement in the photocurrent in CQD films. However Zanella's work lacks PL lifetime and PLQY studies which are the key for understanding the charge dynamics, due to their strong dependence on the radiative and non-radiative recombination processes. Furthermore the Zanella passivation process used propyltrichlorosilane rather than chloride ions.

The study of cadmium chloride passivation of different CdTe CQDs sizes is presented in this chapter. The results of cadmium chloride passivation are the significant reduction of surface traps leading to almost unity PLQY, and improved stability to air exposure.

Figure 6.1 Colloidal Quantum Dots grown by C.R. Page (taken by Page)

6.2. Synthesis and structural characterisation of CdTe

The Colloidal quantum dots studied were grown by R.C. Page. His synthesis of CdTe CQDs were based on the method reported by Wang [5]. Cadmium oxide (CdO), 1-tetradecylphosphonic acid (TDA) and 1-octadecene (ODE) are loaded and mixed in a three-neck flask. The mixture is heated to 315°C and then cooled to 290°C for the fast injection of Te precursor. The precursor is a solution of Te dissolved in trioctylphosphine (TOP) and heated at 210°C then this solution is diluted with ODE. After the precursor is injected the flask is cooled to 270°C to grow the nanocrystals. Depending on the times of growth the CQD sizes varies; the CQDs used have diameters from 3.2 nm to 4.9 nm, which corresponds to growing times from 30 s to 6 mins. All the reaction was carried under nitrogen (N). Page treated the surface of these CdTe CQDs with chloride ions by injecting $CdCl_2$ in oleylamine containing tetradecylphosphonic acid (TDPA) into a solution with CdTe CQDs in toluene. This reaction was continued for 15 min at 60°C. [16].

In Figure 6.2a the absorption and the photoluminescence spectra of the CdTe CQDs show a peak shift of few nm between the untreated and treated samples. The spectra were normalized to show the peak fit This peak shift depends on the chloride reaction time.. Figure 6.2b shows the X-ray powder diffraction (XRD) patterns and confirms CdTe with a zinc blende crystal structure for both untreated and chloride treated CQDs. This demonstrates the chloride treatment did not change the crystal structure of the CQDs. Figure 6.2c and Figure 6.2d show the high angle annular dark field (HAADF) scanning transmission electron microscope (STEM) images for the CQDs before and after chloride treatment respectively. From the images the CQD sizes look similar after chloride treatment and in both cases the shape of CQDs are roughly spherical. The average diameter is 4.6 nm ±0.7 nm for untreated and 4.5 nm ±0.8 nm for treated. The XRD and TEM studies were performed by collaborators based in the School of Materials and the School of Chemistry.

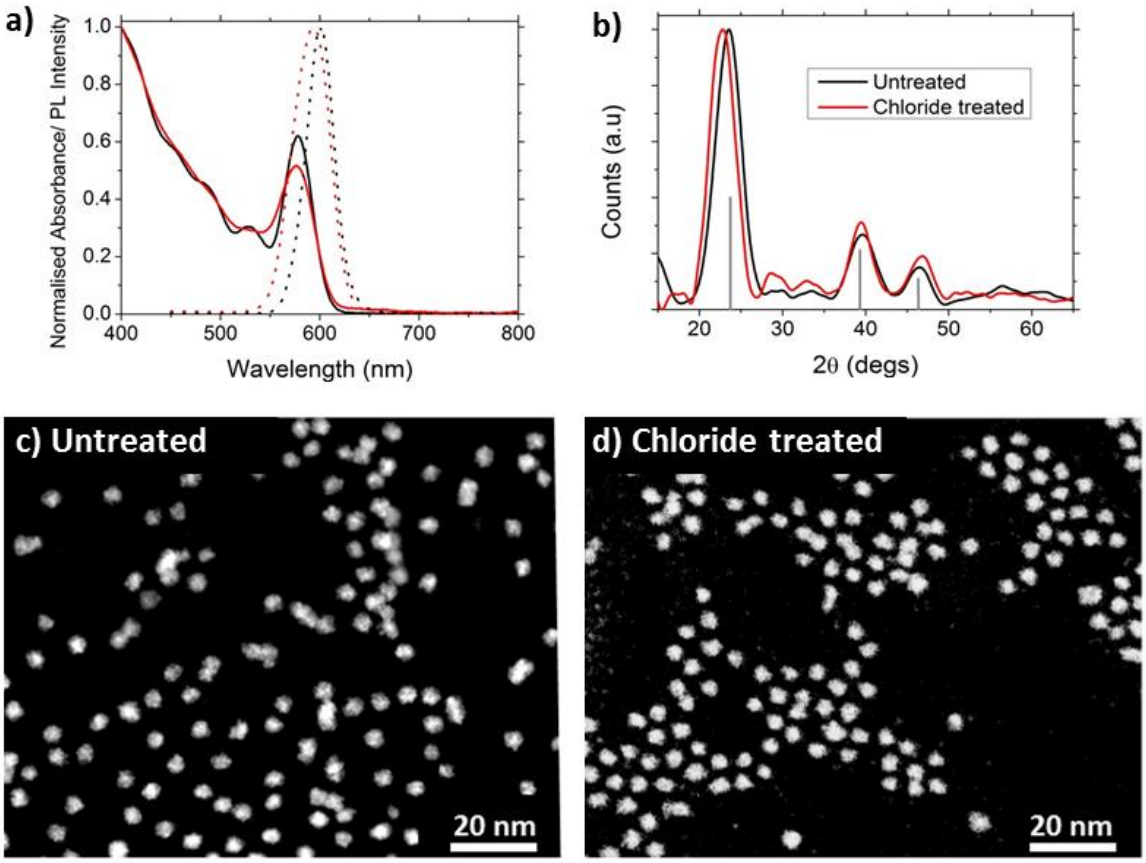

Figure 6.2 CdTe CQDs before and after chloride treated. (Taken from [16]). a) Absorption (solid lines))and Photoluminescence spectra (dotted line), the untreated is black and after chloride treated is red. b) X-ray diffraction photoelectron spectroscopy (XRD) patterns. c) High angle annular dark field (HAADF) scanning transmission electron microscope (STEM) after treatment. d) HAADF STEM before chloride treated

To confirm that the chloride ions were on the surface of the treated CdTe CQDs, synchrotron-excited X-ray photoelectron spectroscopy (XPS) at the 2p region for Cl and N was performed. In Figure 6.3a the Cl 2p doublet peak is shown for a chloride treated CQDs (red line), and the peak is not present for the untreated CQDs. Figure 6.3b illustrates how changing the photoelectron kinetic energy (by changing the x-ray photon energy), changes the sampling depth in XPS and this allows different regions of a CQD to be probed. For a chloride treated CdTe CQD the diameter was 4.5 nm and it was surrounded by organic ligands with a thickness of ~3.7 nm [16] as visualised in Figure 6. 5. Figure 6.3c describes how the ratio of elemental signals changes for Cl at 2p region to Cd at 3d region and of N at 1s region to Cd at 3d region for different photoelectron kinetic

energies. For the XPS experiment, the kinetic energy ranges were from 115 eV to 10000 eV, which correspond to sampling depths from 4.1 nm to 11 nm.

At a kinetic energy of 115 eV Cl and N have the highest intensity compared to Cd, indicating that Cl and N are present on the surface of the CQD. The thickness of the ligand layer is a combination of the organic ligands and some residual solvent molecules. The XPS measurements and analysis was carried out by Hanna Radtke.

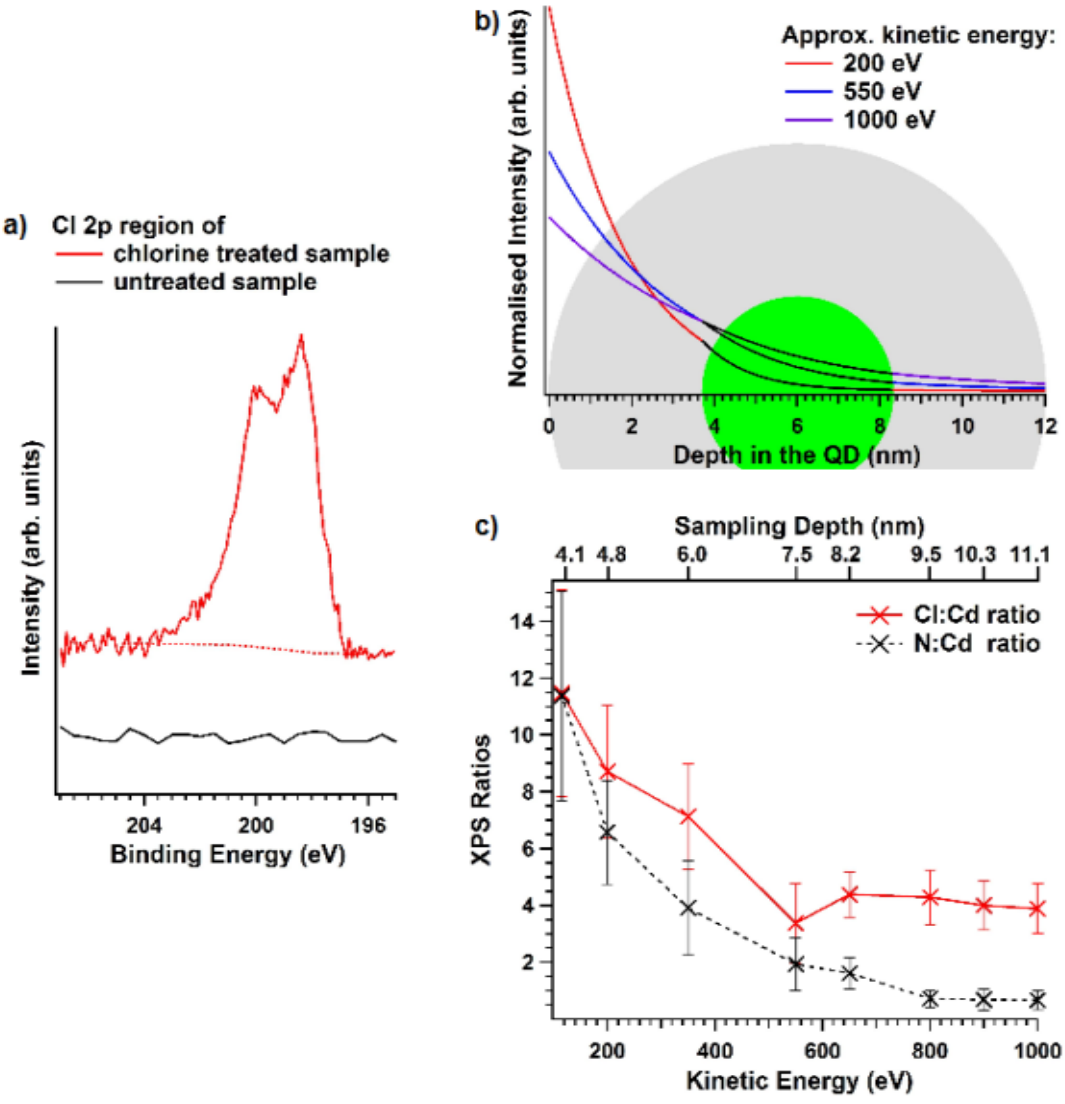

Figure 6.3 XPS studies at 2p for CdTe untreated and treated with chloride. (taken from[16]) a) Direct comparison for untreated (black line) and chloride treated (red line). b) Depth dependency at different kinetic energies and an interpretation for a spherical CQD in green bounded by an organic layer in grey. c) XPS measured ratios of Cl and N to Cd as a function of photoelectron kinetic energies and sampling depth

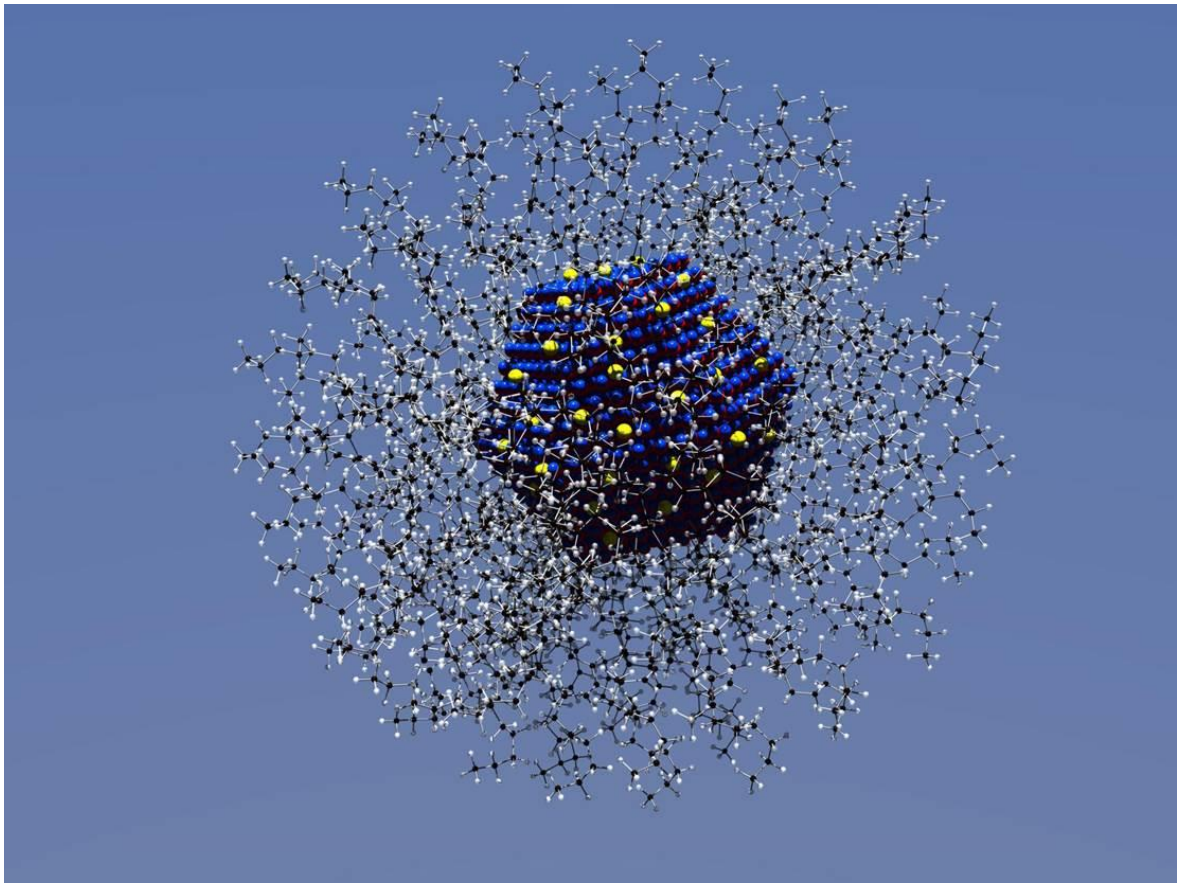

Figure 6. 4 Visualization of the atomic structure of CdTe CQD including oleylamine ligands (modelled by Chris Muryn). Chloride ions (in yellow) suppressing some surface traps of the CdTe CQD.

Figure 6. 4 shows a model of a CdTe CQD passivated by oleylamine ligands with a few chloride ions. The CQD is not fully passivated and the unsaturated bonds on the surface lead to trap states.

6.3. Effect of chloride treatment on PL

The chloride passivation method used by Page produced a substantial change in the optical properties of the CdTe CQDs. The main effect of $CdCl_2$ treatment on CdTe CQDs is an increase in photoluminescence intensity, up to 20 times for some samples (see Figure 6.6a.The absorption and PL peaks suffer a slightly shift of few nm, due to the chloride ions, however the zinc blende structure is unaltered. An example of the effect is shown in Figure 6. 5; here the shift between untreated and chloride treated is 6 nm for the absorption spectra and 9 nm for the PL spectra (see Table 6. 1). The shifts after chloride treatment are related with the amount of $CdCl_2$ and the duration of the reaction. Page found a concentration of chloride of $96Cl^-$ per nm^2 of CdTe CQD surface area, and a reaction time of 15 min at 60°C produced optimal passivation.

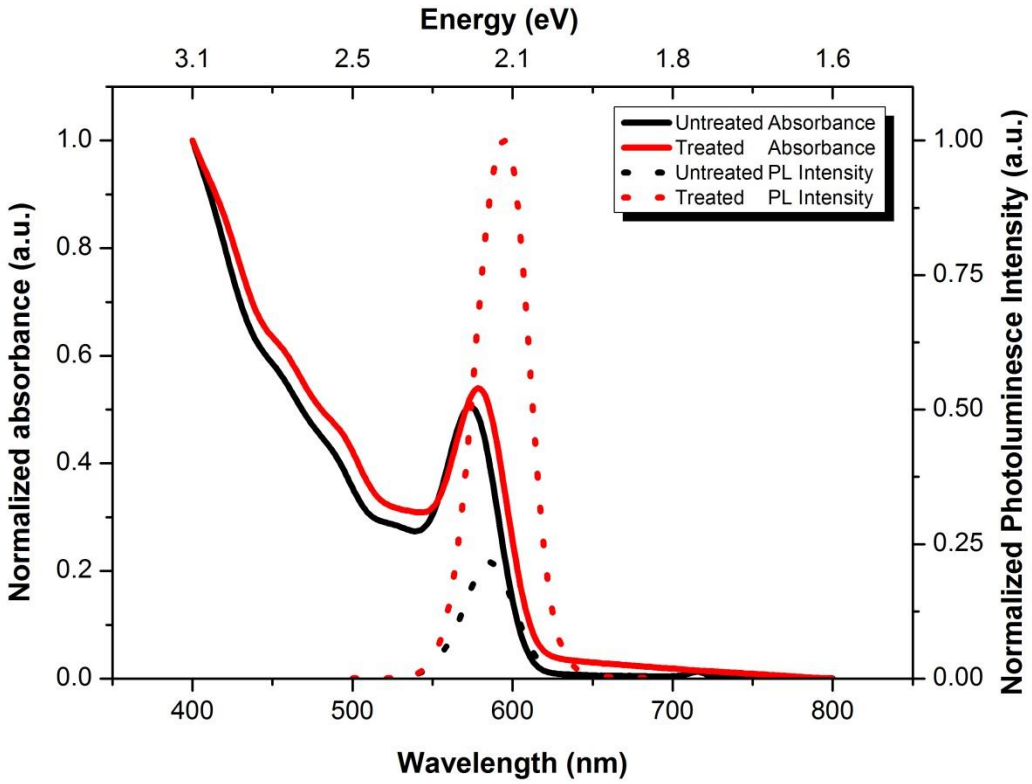

Figure 6. 5 Absorbance and PL spectra after and before chloride treatment

After the 15 min reaction, the growth layer of $CdCl_2$ on the surface of the CdTe CQDs is enough to passivate the CQDs [16]. If the layer is thicker, it may prevent electron extraction or injection. Or if the layer is thinner, the non-radiative process will predominate, affecting the performance.

Table 6. 1 CdTe CQDs diameters before and after chloride treatment showing shift in absorption and PL after chloride treatment.

CdTe CQDs diameters		Absorption peak		PL peak	
Untreated	Chloride Treated	Untreated	Chloride Treated	Untreated	Chloride Treated
3.1 nm	3.4 nm	541 nm	562 nm	557 nm	577 nm
3.2 nm	3.2 nm	548 nm	549 nm	565 nm	564 nm
3.3 nm	3.6 nm	561 nm	595 nm	572 nm	612 nm
3.4 nm	3.5 nm	567 nm	582 nm	580 nm	593 nm
3.5 nm	3.5 nm	576 nm	582 nm	586 nm	595 nm
3.7 nm	3.7 nm	603 nm	606 nm	613 nm	622 nm
3.9 nm	3.8 nm	620 nm	619 nm	631 nm	630 nm
4.8 nm	4.8 nm	668 nm	669 nm	678 nm	677 nm

Table 6. 1 shows the peaks shifts observed for a number of CQD samples of different diameter. The small diameters suffer a greater red shift in contrast as the diameter size increases the shift is reduced. On average the red shift for the absorption peak is ~9 nm and ~11 nm for the PL peak.

The diameters of the CdTe QCDs were calculated using the empirical equation (6. 1) for CdTe nanocrystals [17], where D is nm and λ (nm) is the wavelength of the first absorption peak. The error associated with the equation was estimated to be ±0.1nm, and is due to scatter of data about the empirical fit [17].

$$D = (9.8127 \times 10^{-7})\lambda^3 - (1.7147 \times 10^{-3})\lambda^2 + (1.0064)\lambda - (194.84) \quad \textbf{(6. 1)}$$

The photoluminescence quantum yield is also increased. Typical PLQY values for untreated CdTe CQDs are up to ~15% ±3%, but after treatment the PLQY increased up to 92% ± 6% (Figure 6.6b). The untreated CdTe CQDs have low PLQY which agrees with

literature values found for unshelled Cd-based CQDs [7, 18]. The PLQY of these Cd-based CQDs can be improved by growing an inorganic shell to reduce the surface defects. This is used in light emitting diodes (LED) devices [7], however the inorganic shell, which is a thick layer, acts as a barrier to charge extraction; this reduces the efficiency in photovoltaics cells [19].

By passivating CdTe CQD surface with chloride, the surface dangling bonds are reduced due to the chloride ions reaching hard-to-access inter-cation sites. The non-radiative process is related to dangling bonds therefore after being treated with chloride the CdTe CQDs the dangling bond are supressed. Transient photoluminescence spectroscopy was used to confirm that the radiative process is predominant and further investigate the effects of the chloride treatment.

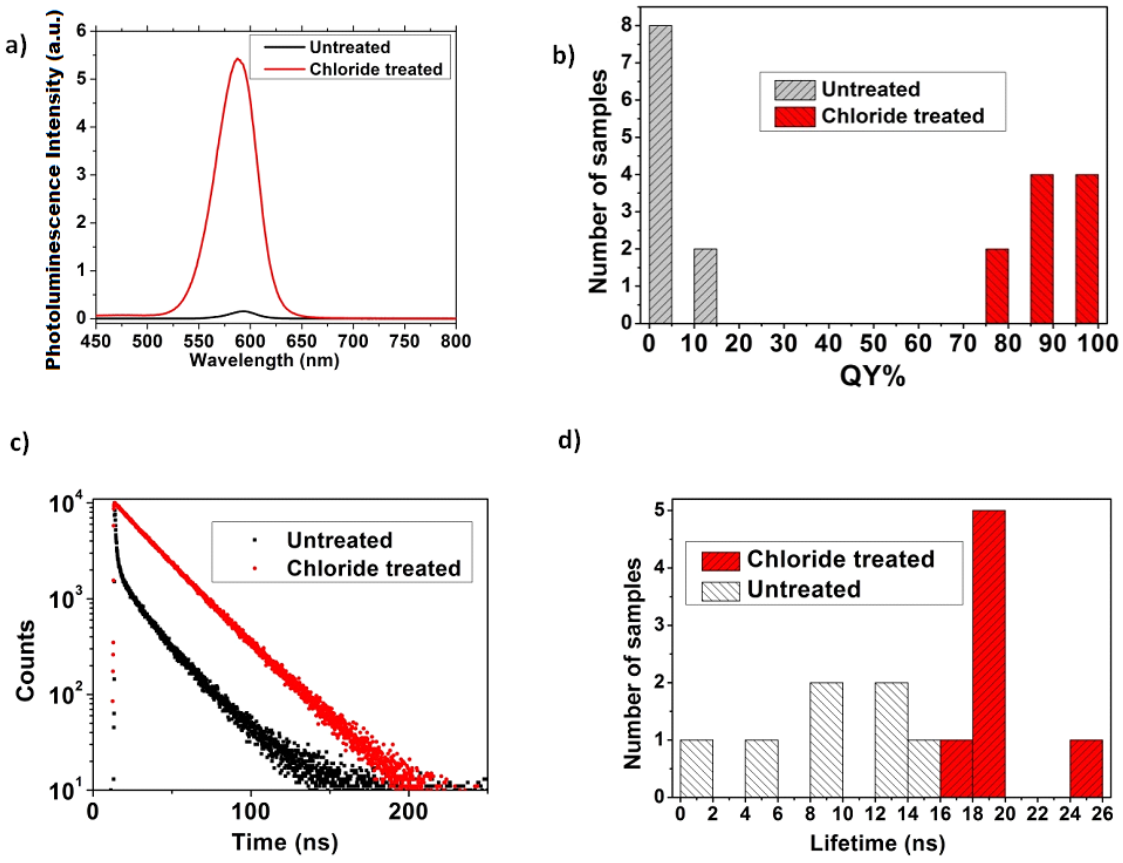

Figure 6.6 Influence of chloride on the photoluminescence of CdTe CQDs (taken from [16]) a) PL spectra of CdTe CQDs (black line) and after chloride treatment (red line), which showed an increased

PL intensity. b) The histogram show improved PLQY after chloride treatment. Untreated samples are in grey and treated samples are in red. c) PL lifetime decays, the untreated sample (black dots) shows multi-exponential decay, and after being treated (red dots) shows a mono-exponential decay. d) The PL lifetime histogram, showing the lifetime improvement after treatment.

The overall recombination rate takes into account both the radiative and non-radiative recombination processes. Where non-radiative recombination increases due to unwanted pathways caused by the presence of surface traps, PL lifetimes reduce and non-exponential decays are typically observed [20]. In Figure 6.6c the decay of untreated CdTe CQDs shows a non-exponential decay, with a lifetime of few nanoseconds. The decay is formed by radiative, and multiple non-radiative components, each component has a different amplitude and time. After the chloride treatment the CdTe CQDs showed mono-exponential decay behaviour (i.e. the radiative process is predominant) and a longer lifetime. A lifetime decay comparison between samples before and after chloride treatment is shown in Figure 6.6c. The PL lifetimes of different CdTe CQDs sizes before and after chloride treatment were plotted in a histogram showing in all cases a longer lifetime for the treated CdTe CQDs (Figure 6.6d).

The histogram compares PL lifetimes between a mono-exponential and multi-exponential decay, which is complex due to the multi-exponential decay has amplitude and time constant for each component which forms the decay, whereas a mono-exponential only has one amplitude and time constant. Equation (6. 2) describes a mono-exponential decay for the chloride treated CdTe CQDs; and equation (6. 3) describes a multi-exponential decay with three terms for the untreated CdTe CQDs:

$$I_{PL}(t) = A_r e^{-t/\tau_r} \quad \textbf{(6. 2)}$$

where A_r is amplitude and τ_r is lifetime for the radiative part

$$I_{PL}(t) = A_r e^{-t/\tau_r} + A_f e^{-t/\tau_f} + A_s e^{-t/\tau_s} \quad \textbf{(6. 3)}$$

and for the non-radiative part A_f and A_s are the amplitudes, and τ_f and τ_s are lifetimes. The non-radiative part is characterised by two processes, fast and slow rates. In section 6.4 the PL lifetimes are analysed in more detail, but for a general comparison of the PL lifetimes, the effective lifetime (τ_{eff}) parameter was used. This parameter makes possible a comparison of the multi-exponential decay (6. 3) with the mono-exponential decay (6. 2). Where effective lifetime (τ_{eff}) defined as when PL intensity drops to 37% of the initial value.

$$I = I_0 e^{-t/\tau_{PL}} \quad \textbf{(6. 4)}$$

At $t = \tau_{PL}$

$$I = I_0 e^{-\tau_{PL}/\tau_{PL}} = I_0 e^{-1} = 0.37\, I_0 \quad \textbf{(6. 5)}$$

For the untreated CdTe CQDs the PL lifetimes were calculated using the effective lifetime (τ_{eff}) and for the chloride treated CdTe CQDs a mono-exponential fitting was used.

A near unity PLQY and longer PL lifetimes with a mono-exponential decay together indicate a significantly reduced overall recombination rate. This should increase the carrier mobility of a device based on CQDs, and thus device performance. Indeed the PL lifetime has a correlation with the performance of solar cell devices [21, 22] and inorganic solar cells have showen improvement with increasing carrier lifetime [22].

6.3.1. Chloride concentration

The effect of chloride concentrations was studied by taking CdTe CQDs and passivating with three different concentrations of $CdCl_2$. All concentrations were calculated by R.C. Page as part of the synthesis procedures. The $CdCl_2$ concentration additions to CdTe CQDs were called: low, normal and high. The low chloride treated was 24 Cl^- per nm^2 of CdTe CQDs, normal 96 Cl^- per nm^2 and high 120 Cl^- per nm^2.

To compare change before and after different concentrations of chloride treatment, the optical properties were measured. In Figure 6. 7a absorption spectra before and after chloride treatment for CdTe CQDs are shown. The untreated (black line) CdTe CQDs show a absorption peak at 603 nm, which after chloride treatment undergoes a redshift for normal and high concentrations of chloride. (see Table 6. 2). The red shift is more evident in the PL spectra (Figure 6. 7b).This attributed to Cl^- ions filling electron vacancies at the band edge and thus narrowing the band gap [16]

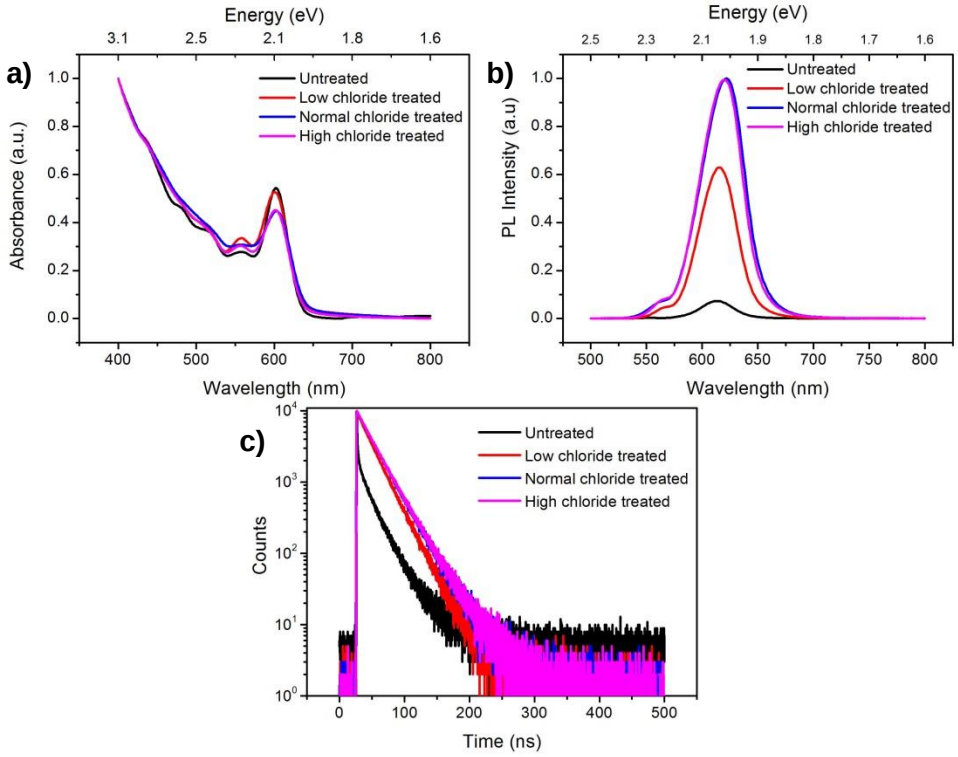

Figure 6. 7 Different concentrations of Chloride treatment for a CdTe CQDs. a) Absorption spectra before and after using different concentrations of chloride treatment. b) PL spectra before and after

using different concentrations of chloride treatment. c) PL lifetimes decays before and after using different concentrations of chloride treatment

The PL lifetime data for the untreated samples and for the samples treated with varying concentrations of Cl^- (Figure 6. 7c) show the how the decay transient changes from a multi-exponential to a mono-exponential after treatment. Comparing the chloride treated concentrations, all the PL lifetime decays are mono-exponential, but there is a small change in the slope. The low concentration shows the shortest lifetime, and the lifetime increases for the normal and high chloride treated concentrations. The PL lifetime decay differences between normal and high is almost imperceptible, with the greatest time for the high chloride treated.

Table 6. 2 Chloride concentrations for a CdTe CDQs

CdTe CQDs	Diameter	Absorption	PL peak	PLQY	PL lifetime	error
Untreated	3.7 nm	603 nm	613 nm	4%		
Low chloride treated	3.7 nm	603 nm	616 nm	77%	22.0 ns	0.5 ns
Normal chloride treated	3.7 nm	606 nm	622 nm	83%	25.0 ns	0.5 ns
High chloride treated	3.7 nm	604 nm	621 nm	70%	25.3 ns	0.5 ns

In Table 6. 2 show the optical values before and after chloride treatment with different concentrations, the diameter was calculated by using equation (6. 1) and the first absorption peak. The low and high chloride concentrations show high PLQY. However the highest PLQY was obtained by using 96 Cl^- per nm^2 of CdTe CQDs, which is the concentration of chloride used throughout this study unless otherwise stated

The chloride layer around the CdTe CQDs should not be too thick, as it may inhibit charge transfer into and from a CdTe CQD. Also the chloride layer should not be too thin due to it may not passivate all the surface traps.

The normal chloride concentration was used as standard for the CdTe CQDs due to its mono-exponential decay behaviour for the PL lifetime and high PLQY.

6.4. Recombination dynamics

The underlying dynamics of radiative and non-radiative recombination rates of the CdTe CQDs were investigated using PL Lifetime and PLQY measurement.

In section 3.4 from Chapter 3 PLQY is defined as the number of emitted photons relative to the number of absorbed photons, φ_f, and depends on the relative rates of the radiative (κ_r) and non-radiative (κ_{nr}) processes

$$\boldsymbol{\phi_f = \frac{No\ photons_{em}}{No\ photons_{abs}} = \frac{\kappa_r}{\kappa_r + \sum \kappa_{nr}}} \quad \textbf{(6. 6)}$$

where $\sum \kappa_{nr}$ is the total rate for all possible non-radiative processes [23]. The PLQY will be closer to unity if the non-radiative part is much smaller than the radiative rate, that is $\sum \kappa_{nr} < \kappa_r$.

The PL lifetime,τ is the characteristic time it takes from the excited state to return to the ground state. This is also linked to the relative rates of the radiative and non-radiative processes. [23]

$$\boldsymbol{\tau = \frac{1}{\kappa_r + \sum \kappa_{nr}}} \quad \textbf{(6. 7)}$$

The radiative rate can be found from the PLQY and PL lifetime equations (6. 6) and (6. 7) respectively;

$$\boldsymbol{\kappa_r = \frac{\phi_f}{\tau}} \quad \textbf{(6. 8)}$$

However, this analysis assumes that the PL decays mono-exponentially or sufficiently close to mono-exponentially, so that τ can reliably identified.

Experimentally however, PL decays are often significantly different from mono-exponential in form, making the determination of τ difficult.

CdTe CQDs before chloride treatment exhibit PL decays are multi-exponential and were not suitable for the above analysis. However after chloride treatment the conditions for the analysis are fulfilled, enabling extraction of the radiative rate. Figure 6. 8. shows, the PL lifetime decays of untreated and chloride treated CdTe CQDs; these decays illustrate the behaviour observed in different diameters of CdTe CQDs.

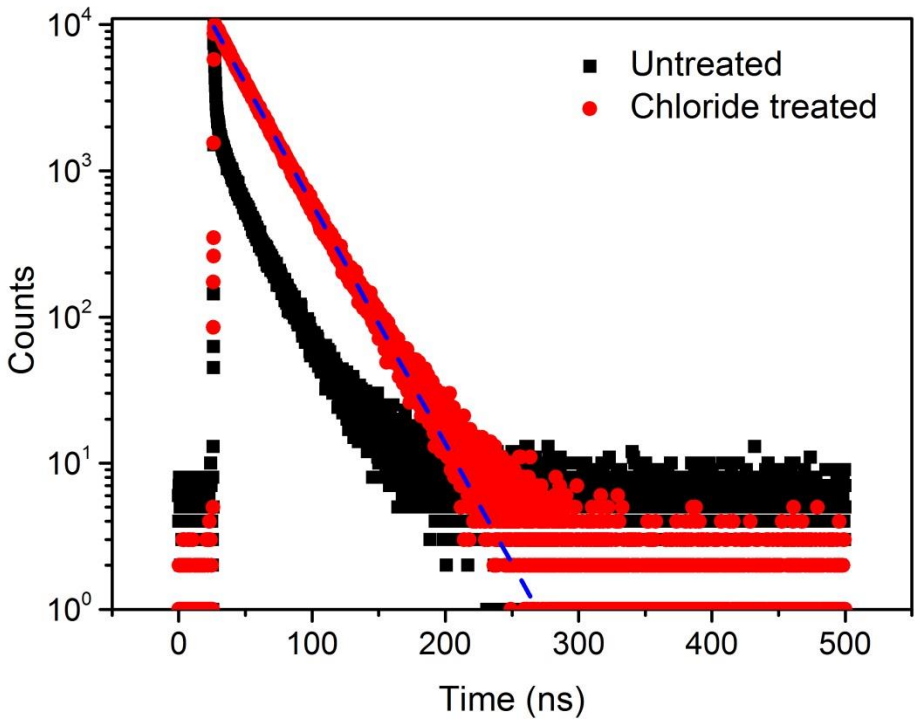

Figure 6. 8 PL lifetime decays of CdTe CQDs before and after chloride treatment. Untreated CdTe CQDs (black) show a multi-exponential decay, and a mono exponential decay for chloride treated CdTe CQDs (red).the doted blue line is to clarify the mono exponential behaviour.

The PL lifetimes decays for chloride treated CdTe CQDs show a largely mono-exponential behaviour, however for some decays the tail introduces a small deviation on fitting to a

mono-exponential function. Therefore the analysis procedure for the chloride treated CdTe CQDs was to use a mono-exponential decay only for the first decade, which corresponds to the 90% of PL intensity. For the untreated CdTe CQDs a multi-exponential was fitted, also over the first decade in order to be consistent in the method of analysis of the PL lifetimes. Table 6. 3. shows the PL lifetime values extracted by fitting a mono-exponential decay (6. 2) for the chloride treated CdTe CQDs.

Table 6. 3 PL lifetime values before and after chloride treatment for different sizes.

Chloride Treated CdTe CQDs		
Diameters	PL lifetime	error
3.4 nm	18.00 ns	± 0.07
3.6 nm	20.35 ns	± 0.04
3.5 nm	17.69 ns	± 0.05
3.7 nm	19.89 ns	± 0.06
3.5 nm	18.42 ns	± 0.09
3.7 nm	24.26 ns	± 0.10
3.8 nm	22.56 ns	± 0.05
4.8 nm	22.25 ns	± 0.07

The PLQY values calculated by the absolute method are shown in in Table 6. 4. The error of PLQY values is ±6%., which is the sum of squared errors of systematic and statistical contributions.

Table 6. 4 PLQY values before and after chloride treatment for different sizes of CdTe.

CdTe CQDs diameters		PLQY	
Untreated	Chloride Treated	Untreated	Chloride Treated
3.1 nm	3.4 nm	9%	83%
3.3 nm	3.6 nm	4%	90%
3.4 nm	3.5 nm	4%	66%
3.4 nm	3.7 nm	5%	92%
3.5 nm	3.5 nm	15%	81%
3.7 nm	3.7 nm	4%	83%
3.9 nm	3.8 nm	1%	65%
4.8 nm	4.8 nm	3%	40%

By substituting the values for PLQY and the PL lifetimes in the equation (6. 8), an estimate of the radiative rate,κ_r, was found. The radiative lifetime is just the inverse of the radiative rate constant.

$$\boldsymbol{\tau_r = \frac{1}{k_r}} \quad \textbf{(6. 9)}$$

In Figure 6. 9 the radiative lifetime (τ_r) was plotted against CQDs volume, linear fit (red line) show the linearity between the radiative life time and the volume of the CdTe CQDs, as was previously observed for CdSe QDs [24]. As the oscillator strength (f) increases linearly with size (~a), and within the strong confinement region the exciton energy (E_{ex}) scale inversely with the square of the size $E_{ex}{\sim}1/a^2$. Therefor the radiative rate is approximately the product of the energy squared and the oscillator strength ($\kappa_r{\sim}E_{ex}^2 f$), and thus scales with cubic size $\kappa_r{\sim}1/a^3$ [24]. The linearity of the radiative process with volume for CdSe QDs, agrees with the different sizes of CdTe CQDs showing linearity between the volume and radiative lifetimes. Also, in Figure 6. 9. the PL lifetime (τ_{pl}) and calculated lifetime ($\tau_{calculated}$) were plotted against the CQDs volume. The calculated lifetime ($\tau_{calculated}$) was obtained from the relationship between the recombination rate and the peak PL photon energy previously reported [25]. The values obtained of PL lifetime and calculated lifetime are comparable, while the radiative lifetime values are greater, consistent with $\tau_r \approx \tau_{PL}/PLQY$ that represent the upper limit for the radiative lifetime.

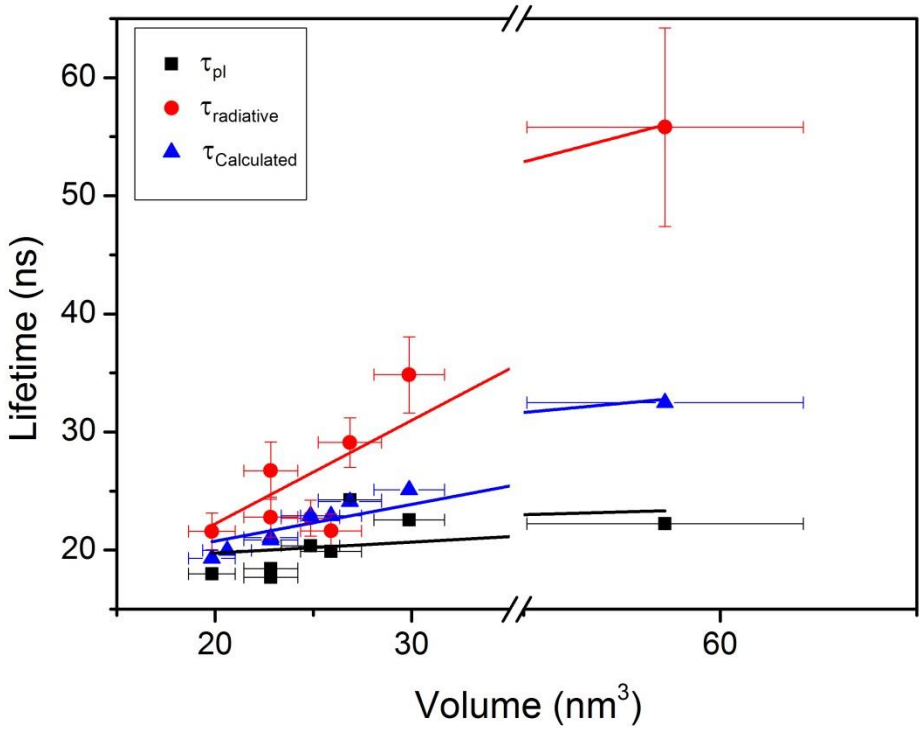

Figure 6. 9 PL lifetime (τ_{pl}), Radiative lifetime (τ_r) and calculated lifetime ($\tau_{calculated}$) as function of volume for different sizes of chloride CdTe CQDs.

The linear fit of the radiative lifetimes in Figure 6. 9 crosses within the error bar of 5 out of 8 data points. However the use of the biggest diameter of CdTe CQDs, could be inexact, since it was one of the first trial cases of chloride treatment. Even though it has a mono-exponential decay in the first decade, the PLQY is not as high as the other diameters. This prompts a reasonable doubt about why the PLQY is low. Perhaps is due to the size of the dot, and/or if the chloride treatment was insufficient or defective. Nevertheless taking out that point of the linear fitting, the linearity between the volume and radiative lifetime is still observed.

Even though the mono-exponential fitting describes well the PL decay for chloride treated CdTe CQDs, there is a deviation over the first decade indicating some degree of non-radiative recombination, consistent with the less than unity PLQY. Hence a bi-exponential decay was fitted to characterise any remanding non-radiative process (the tri-exponential

fit used for the untreated samples usually resulted in two of the time constants being made equal by the software (OriginPro 8.5)). As the radiative lifetime (τ_r) is known, the PL lifetime decay for the chloride treated CdTe CQDs was fitted now with a bi-exponential decay (6. 10), where the radiative lifetime (τ_r) is fixed in the equation (6. 10).

$$I_{PL}(t) = A_r e^{-t/\tau_r} + A_{nr} e^{-t/\tau_{nr}} \quad \textbf{(6. 10)}$$

where $A_r e^{-t/\tau_r}$ is the radiative process and $A_{nr} e^{-t/\tau_{nr}}$ is the non-radiative process.

Figure 6. 10 shows an example of the fittings for the chloride treated CdTe CQDs (red circles), the mono-exponential fit in green and the bi-exponential in red, the difference between both fits is minimal. (Nevertheless, the results of a biexponential fit for eight samples are given in Table 6. 5.)

However, caution has to be exercised when interpreting the results of this process. The software is trying to fit a decay that is very close to mono-exponential with a bi-exponential function . When the radiative lifetime (τ_r) is fixed and the non-radiative lifetime is free, the fitting program finds a value of τ_{nr} that combines with τ_r to reproduce the behaviour of a mono-exponential with a lifetime of $\tau_{PL} \approx QY\tau_r$, with values close to the PL lifetime previously extracted (Table 6. 3) with a mono-exponential fit .

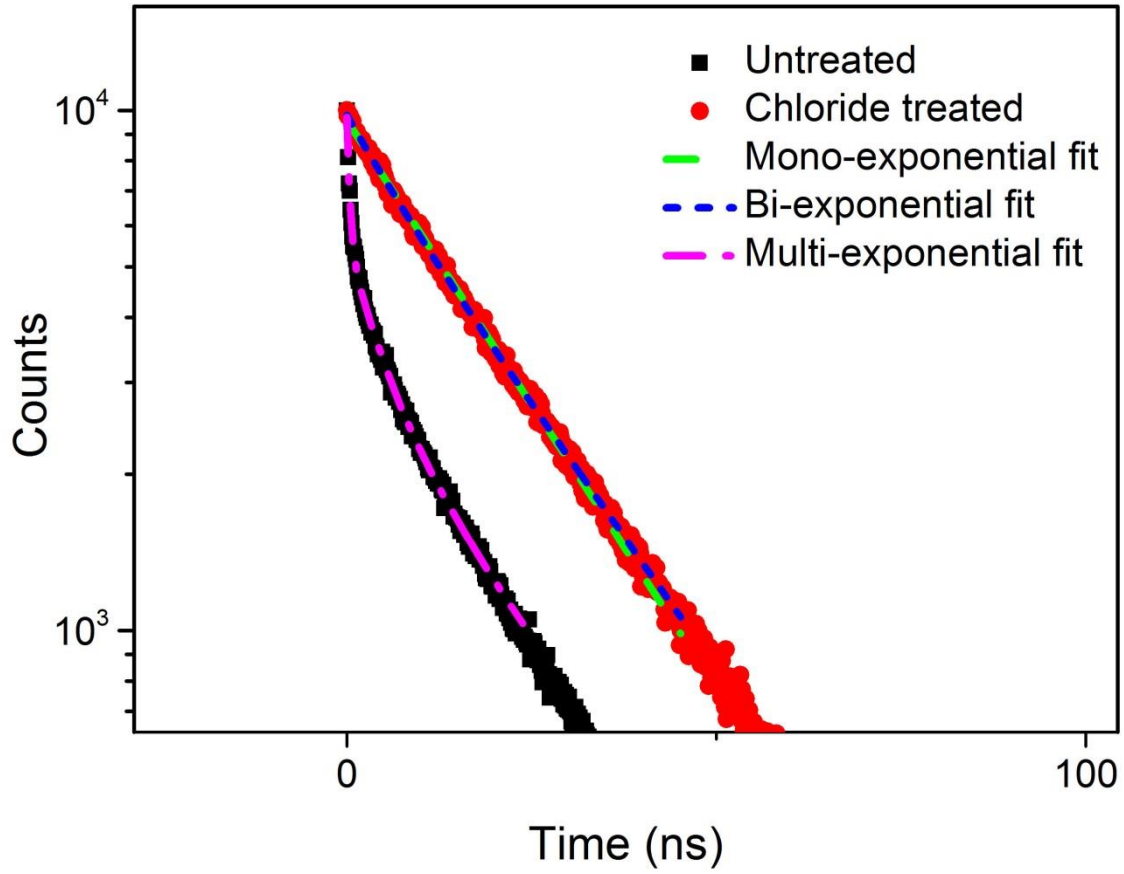

Figure 6. 10 Exponential fittings of CdTe CQQs before and after treatment. Untreated CdTe CQDs (black squares) with a multi-exponential fit (magenta dash-dots). Chloride treated CdTe CQDs (red circles) showing a mono-exponential fit (green dashes) and a bi-exponential fit (blue dashes).

Table 6. 5 Radiative and non-radiative lifetimes of chloride treated CdTe CQDs

Chloride trated CdTe CQDs								
	Radiative process				non-radiative process			
Diameter nm	Amplitude (counts)	Error ±	Time ns	Error ±	Amplitude (counts)	Error ±	Time ns	Error ns
3.4	6979.2	78.9	21.6	n/a	2476.6	70.4	8.4	0.35
3.6	7812.4	84.7	22.7	n/a	2070.4	78.2	11.8	0.40
3.5	3905.3	88.7	26.7	n/a	5903.5	81.3	12.7	0.18
3.7	8538.0	52.3	21.6	n/a	1244.6	48.4	7.4	0.50
3.5	6663.4	61.5	22.8	n/a	2678.7	55.9	7.8	0.28
3.7	5844.6	244.4	29.1	n/a	4117.6	237.8	19.7	0.52
3.8	3183.2	102.9	34.8	n/a	6594.6	95.5	17.5	0.23
4.8	1686.1	45.1	55.8	n/a	8086.9	39.2	17.7	0.14

A similar approach is used to know the non-radiative process for the untreated CdTe CQDs, as both the untreated and chloride treated share the radiative lifetime (τ_r).

However, this analysis is much more reliable because the transients for the untreated samples are far from mono-exponential. The PL lifetimes for untreated CdTe CQDs are fitted with a multi-exponential (6. 3), where the radiative part ($A_r e^{-t/\tau_r}$) is known and $A_f e^{-t/\tau_f} + A_s e^{-t/\tau_s}$ is the non-radiative part with fast and slow components. Figure 6. 10 shows an example of the multi-exponential decay fitting for the untreated CdTe CQDs (magenta dash-dots).

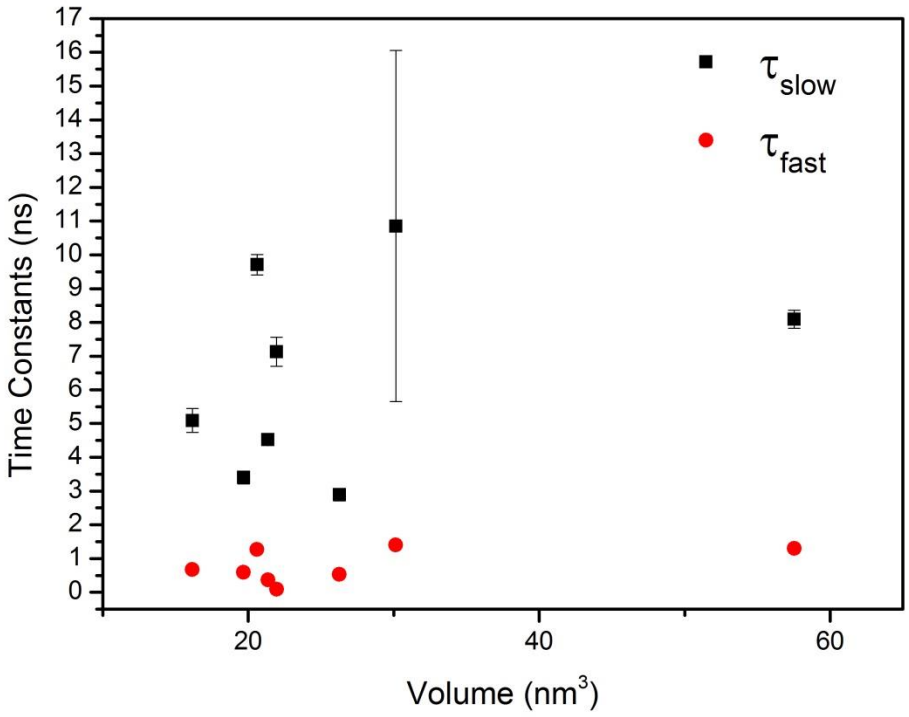

Figure 6. 11 Fast and slow time constants of the non-radiative process for the untreated CdTe CQDs.

Figure 6. 11 show the fast and slow time constants of the non-radiative process for different untreated CdTe CQD sizes. The fast lifetime constant (red) last no more than a couple of nanoseconds, and for the slow lifetime constant (black squares) does not show a pattern or a relationship with the fast lifetime constant, and the time constant varies from a couple of ns up to an order of magnitude greater . However the error bars for one CdTe CQDs are significant, which suggest a fitting artefact.

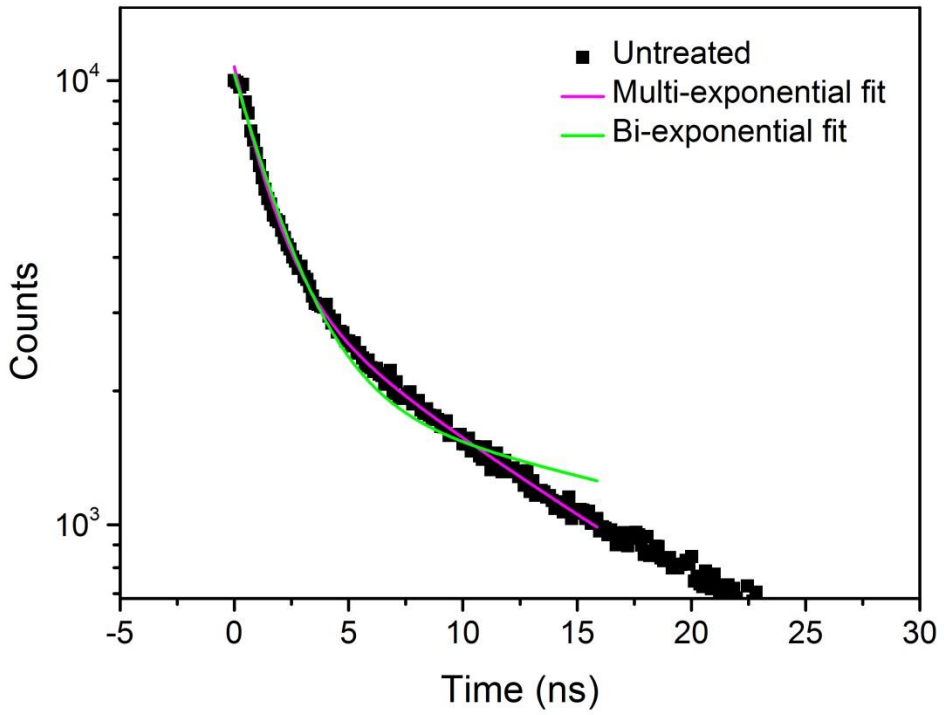

Figure 6. 12 PL lifetime decay of untreated CdTe CQDs, fitted by multi-exponential and bi-exponential decay.

Figure 6. 12 correspond to the PL lifetime decay of the untreated CdTe CQDs, whose error bars were significant in Figure 6. 11. By using a multi-exponential fit (magenta), the error was substantial, but the fit followed the PL lifetime decay. By using a bi-exponential fit (green) the decay is less well described with a variation on the fit tail.

Comparing the radiative and non-radiative components of lifetime for different sizes of CdTe CQDs (see Figure 6. 9 and Figure 6. 11); There is a relation between volume of CdTe CQDs and radiative lifetime; and this relation is not observed for the fast or slow component of the non-radiative lifetime., which means that both processes are independent. In other words, the analysis procedure has successfully separated the radiative and non-radiative recombination dynamics.

A power dependency study was done by varying the energy of the excitation pump and recording the PL decays at the emission peak of the CdTe CQDs. Figure 6. 13 shows the

radiative lifetime (τ_r) of the chloride treated CdTe CQDs, the PL decays were mono-exponential and maintained a mono-exponential behaviour as the pump power was reduce by neutral density filters. The PL lifetime decays are shown in Figure 6. 13a. PLQY value; and the lifetimes values extracted from the mono-exponential fitting were substituted in equations (6. 8) and (6. 9). The radiative lifetimes (black dots) are shown in Figure 6. 13b. Also the non-radiative part was analysed, by fitting a bi-exponential decay and using the radiative lifetimes. In this way the non-radiative process was included. However, fitting a bi-exponential may generate artefacts as discussed earlier.

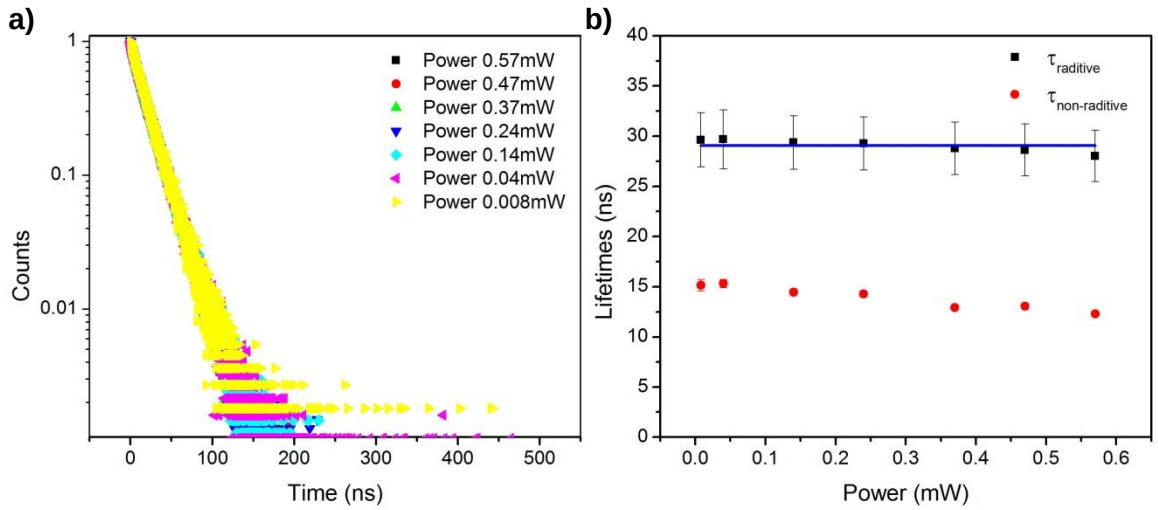

Figure 6. 13 Power dependency at PL peak of CdTe CQDs a) PL life time decays varying the excitation power at the PL peak. b) Radiative and non-radiative lifetimes

The radiative lifetimes (τ_r) in Figure 6. 13 has a linear fitting with a fixed slope to zero, which shows the changes by pumping energy. This study confirms that the radiative lifetime (τ_r) has no dependency on the excitation power. A gradual decline in the non-radiative lifetime with greater pump power energy is evident, suggesting a pump- induced increase in non-radiative recombination due to photo-damage of the CQD surface

6.5. Effect of air exposure

The untreated and chloride treated CdTe CQDs were exposed to air with the purpose of measuring their stability to oxidation. It is known that CdTe CQDs are vulnerable to oxygen, leading to luminescence quenching[26]. However using molecular chlorine to passivate the CdTe CQDs reduces the degradation caused by oxygen. [13]

The study of air exposure started immediately after the CdTe CQDs were grown, diluted with dry toluene and transferred to the cuvettes in a glovebox under a nitrogen atmosphere. The optical properties (absorbance, PL, PLQY and PL lifetime) of the CdTe CQDs before air exposure were measured; this data was called 0 hours. Then the cuvette caps were removed and the optical properties were measured again over a number of hours.

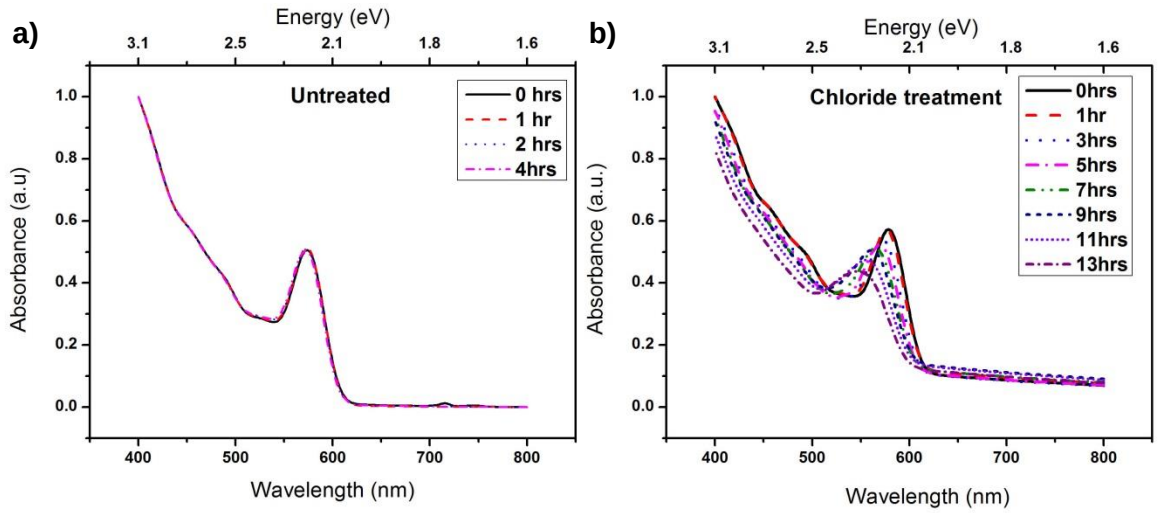

Figure 6. 14 Absorption spectra of CdTe CQDs before and after air exposure. The study for the untreated CdTe CQDs (a) lasted 4 hours exposed to the atmosphere, and for the treated CdTe CQDs with chloride ions (b) lasted 13 hours.

The absorption spectra for the treated CdTe CDQs shown in Figure 6. 14b, exhibited a blue-shift, which increased with further air exposure. In contrast for the untreated CdTe CDQs (Figure 6. 14a) no shift is observed after air exposure. The total blue shift, using the second derivative of the first absorption peak in the spectra, was 14 nm after 13 hours of

air exposure. This indicates the red shift observed during the passivation of CdTe CQDs with $CdCl_2$ starts to reverse when the CdTe CQDs have been air exposed.

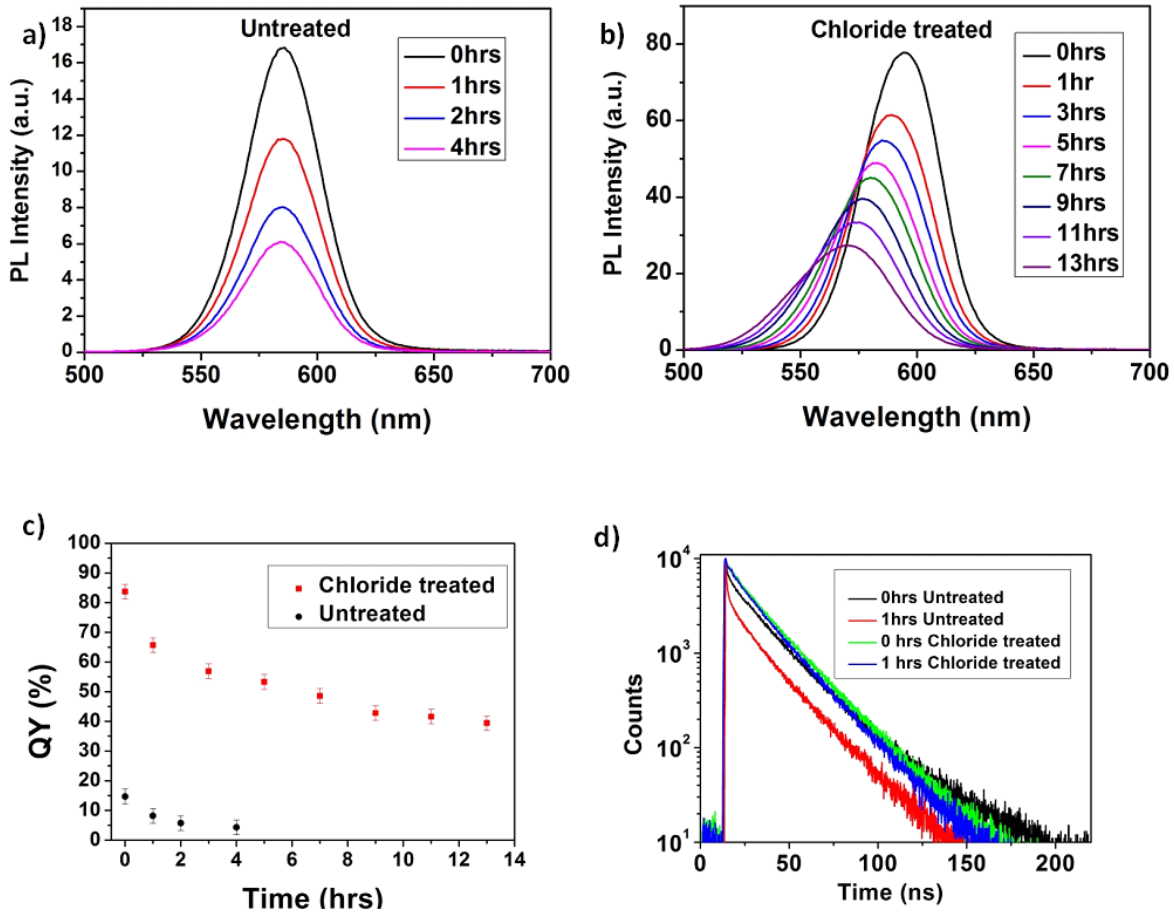

Figure 6. 15 The air exposure effects on CdTe CQDs. (taken form [16]) PL spectra of CdTe CQDs exposed to air: a) before treatment and b) after treatment. c) PLQY degradation due to air exposure vs time, black dots un treated and red dot treated. d) PL lifetime decays of untreated and treated before and after air exposure. (Black line untreated before air exposure, green line after 1 hour air exposure, red line before air exposure and blue line after 1 hour air exposure).

Figure 6. 15a shows PL spectra for the untreated CdTe CQDs. After the first hour of air exposure the PL intensity decreased by 35%, and the total reduction after 4 hours is around 70%. For the treated CdTe CQDs the PL spectra is shown in Figure 6. 15b. The PL intensity was reduced after 1 hour by 20%, and after 13 hours the PL intensity was reduced by 70%. After the first hour of exposure the treated CdTe CQDs start a process of blue shifting and moderate PL quenching. However this shift was not present for the untreated CdTe CQD. The red shift observed follow passivation is due to chloride ions filling electron vacancies at the band edge, narrowing the band gap [16]. The blue shift absorbed during air exposure suggests that oxidation reverses this process. The PL peak

of treated CdTe CQDs before air exposure was 595 nm and 571 nm after air exposure. For the untreated CdTe CQDs the peak was constant at 586 nm. Taking the untreated CdTe CQDs PL peak as a reference for the shifts, a 9 nm red shift is observed after chloride passivation, and a 15 nm blue shift occurs after 13 hours of air exposure. However, after 13 hours, the PL intensity is still higher than the untreated sample immediately after synthesis.

PLQY values on air exposure are shown in Figure 6. 15c. For untreated CdTe CQDs before air exposure, PLQY was 15%, which decreased to 5% after 4 hours of air exposure. For the treated CdTe CQDs the starting PLQY is 80% before air exposure, and after 13 hours of air exposure the PLQY was still close to 50%. The air exposure deterioration of the CdTe CQDs is greater for untreated than treated. After many months under nitrogen the treated CdTe CQDs, exhibit PLQY values unchanged from values immediately after synthesis.

Figure 6. 15d shows the PL lifetime decays of the untreated and treated CdTe CQDs before air exposure and after 1 hour of air exposure. The treated CdTe CQDs before air exposure show a mono-exponential decay and after air exposure the decay is still mono-exponential with a similar lifetime, which indicates that the radiative process is still dominating. For the untreated CdTe CQDs the decay before air exposure show a multi-exponential decay with a short lifetime and after air exposure the decay is a multi-exponential with a noticeable drop at the beginning, and a shorter lifetime.

The lifetime decays for the untreated CdTe CQDs after number of hours of air exposure are shown in Figure 6. 16a. The multi-exponential decays from 2 and 4 hours exposure times have a similar trend as the decay from 1 hour air exposure. The only change is a faster drop at the initial times, which reduces the PL lifetime and suggests a greater number of traps.

The CdTe CQDs treated with chloride were air exposed for a period of 13 hours. However there are only four decays plotted in Figure 6. 16b, for clarity. The four decays behave as mono-exponentials before and after air exposure, the only difference is a slightly increase in the decay rate which reduces the PL lifetime. The mono exponential PL decay indicates radiative recombination still dominates. This is evidence that the chloride treatment applied to the CdTe CQDs has passivated the surface by removing the majority of surface traps. After the maximum time of air exposure, the PL decay still have a strong mono-exponential behaviour, which suggest that the surface trap are not increasing in a large number by air exposure.

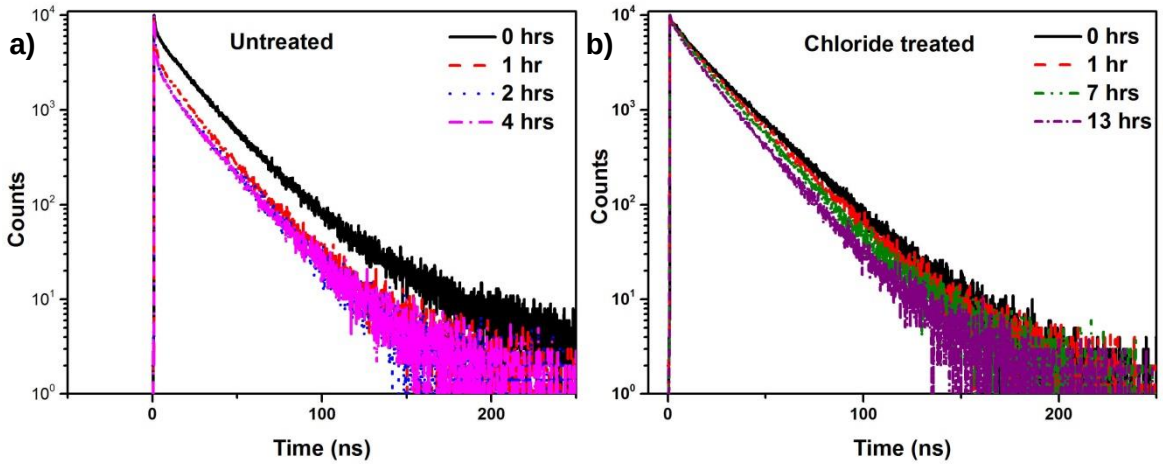

Figure 6. 16 PL lifetime decay comparison of untreated and treated CdTe CQDs before and after air exposure. a) shows a untreated CdTe CQDs before (black line) and after (dot lines) air exposure for a maximum period of 4 hours. b) shows a chloride treated CdTe CQDs before (black line) and after (dot lines) air exposure for four different times, the maximum air exposure was 13 hours.

The recombination dynamics during air exposure were studied by extracting the radiative lifetime of chloride treated CdTe CQDs, using equations (6. 8) and (6. 9) at 0 time (no air exposure). As the radiative lifetime does not change and is known, the PL lifetime decays were fitted with a multi-exponential decay (6. 3)with a fixed value of τ_r found from the 0 hour transient, to better identify the non-radiative components (τ_{Slow}.and τ_{fast}).The approach was to use a global fit over the first decade for both untreated and chloride treated CdTe CQDs. The non-radiative lifetimes values (τ_{Slow}.and τ_{fast}) in the multi-

exponential decay (6. 3) were shared between all the transients, but the amplitudes A_i for $i = r, f, s$) were free to vary.

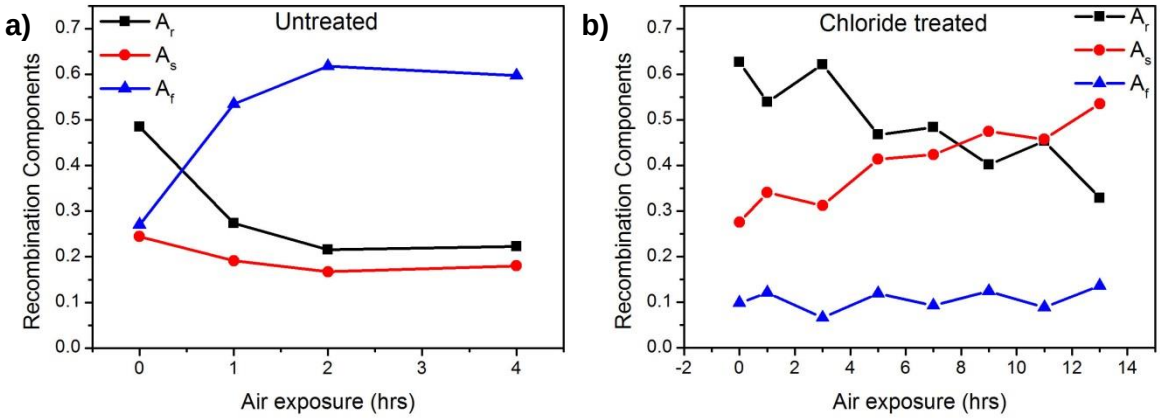

Figure 6. 17 Comparison of the change of radiative and non-radiative process during air exposure. a) untreated CdTe CQDs exposed to air for a period of 4 hours. b) chloride treated CdTe CQDs exposed to air for 13 hours. (black squares are the radiative part, red circles are the slow component and blue triangles are the fast component.)

Figure 6. 17 shows the fractional contribution of the amplitudes. As expected for the chloride treated CdTe CQDs the radiative part decreases and the non-radiative components increase as the oxidation process continues. As for the untreated samples, the radiative part quickly decreases, and non- radiative slow component remains largely unchanged. The non- radiative fast component has a quick increase.

In summary, the chloride treatment on the surface of the CdTe CQDs produced a resistance against oxidation. After a prolonged period of exposure the PL peak suffers a blue shift however the PL intensity is still high and more intense than an untreated CdTe CQD without air exposure. Also the PLQY values for the treated CdTe CQDs show a good stability after the exposure. For treated CdTe CQDs PLQY ~50% after 13 hours of air exposure compared to 15% PLQY for the untreated before air exposure. The PL lifetime decays for the chloride treated CdTe CQDs show a mono-exponential decay before and after air exposure which is linked to radiative recombination dominating.

6.6. Spectral dependence of recombination

The spectral analysis was done on chloride treated CdTe CQDs by taking PL lifetime across the spectra. The experiment was set up to stop the acquisition after a certain time period instead of reaching a certain number of counts. The period of time for the acquisition was set to the time taken for the number of counts to reach 10 000 at the PL peak of the chloride treated CdTe CQDs. After determining the acquisition time the PL spectra was divided into 10nm spectral step.

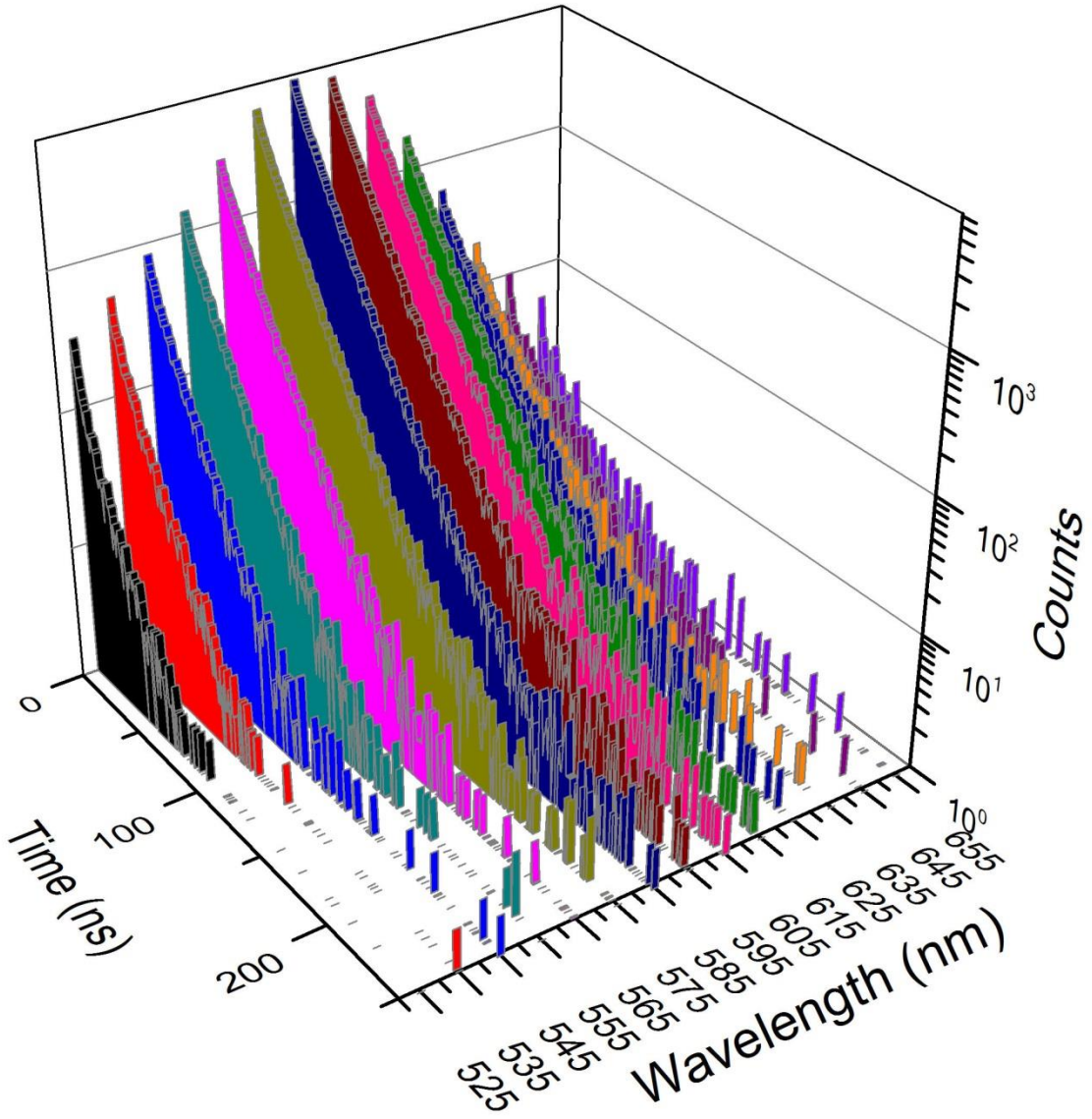

Figure 6. 18 PL lifetimes across the spectra.

A 3D representation of the spectrally resolved PL decay is shown in Figure 6. 18, where the z axis is the number counts, taken in a fixed period of time. The y axis is the time in nanoseconds and the x axis is the wavelength, which also correspond to different sizes of CdTe CQDs within the overall size distribution in the sample. The excitation wavelength was at 420 nm

The transient PL lifetimes decays were taken at different pump pulse energies, and the maximum number of counts for each wavelength was plotted versus wavelength. The spectra were fitted with a Lorentz peak function; this reconstructs the PL spectra from the PL decays. Figure 6. 19 show the Lorentz fitting at different pump pulse energies, and Table 6. 6 shows how the peak wavelength resulting from this fit varied with average pump power.

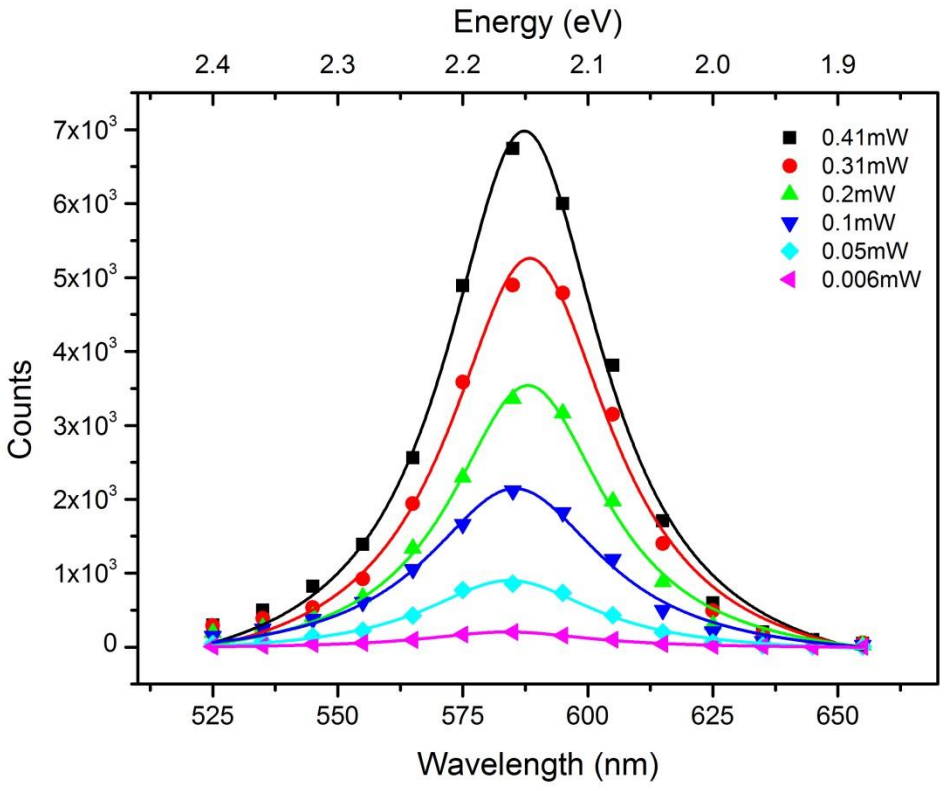

Figure 6. 19 Transient PL at different pump power.

A weak trend to longer wavelength with increased pump power was observed. This redshift is about ~10meV, similar to the binding energy for biexcitons reported for type I CQDs [27] which would form only at high powers. Table 6. 6 shows the PL peak found by fitting a Lorentz function at different pump energies, the mean peak varying the power pump was 586.33 nm with an error of ±2.06 nm. At the highest pump power the average number of photons absorbed per CQD,<N>, was 0.61, which corresponds to a probability of producing biexcitons of 45%. However biexcitons undergo Auger recombination, which is not radiative and has lifetime that is around 2 orders of magnitude shorter than that radiative recombination i.e.in picoseconds regime. Biexcitons are thus unlikely to be responsible for observed redshift despite being produced in significant number at the highest pump power. This shift is instead likely to be related to the experimental error introduced by the step size of the measurements, and not an effect of biexciton binding energies which should affect the PL spectrum.

Table 6. 6 Lorentz PL peaks fit versus pump energy

Pump energy	Lorentz PL peak fit	Error
0.41 mW	587 nm	± 0.7 nm
0.31 mW	589 nm	± 0.8 nm
0.2 mW	588 nm	± 0.7 nm
0.1 mW	586 nm	± 0.8 nm
0.05 mW	584 nm	± 0.9 nm
0.006 mW	584 nm	± 0.7 nm

The radiative process was analysed using the PL lifetime decays across the spectra and assuming PLQY is constant. Each wavelength was taken to correspond to a different diameter of CQD within the overall size distribution of the sample By substituting the values in equations (6. 8) and (6. 9) the radiative lifetime was thus obtained for different diameters of the chloride treated CdTe CQDs. This was done for the wavelengths across the spectra different pump pulse energies. The radiative lifetime was plotted versus volume of the CdTe CQDs in Figure 6. 20. The first two (525 nm and 535 nm) and last two (645 nm and 655 nm) wavelengths were removed for all the pump powers because the data was too noisy for a reliable fit. On the left bottom of the Figure 6. 20 shows only the

radiative lifetimes for a pump pulse power of 0.41 mW with a strong linearity across different volume sizes.

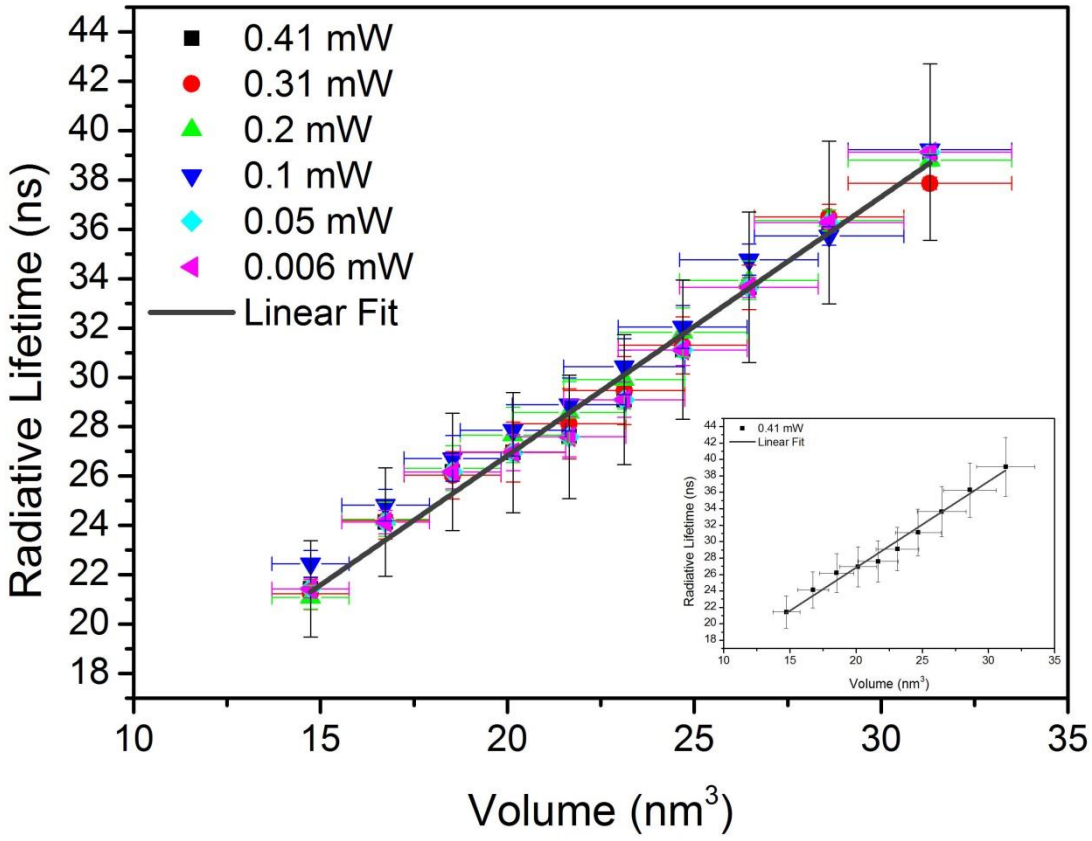

Figure 6. 20 The radiative lifetimes across the spectra at different pump powers. On the left bottom the radiative lifetime only for a pump power of 0.41mW, showing a linear fit.

Nanocrystals of copper indium sulphide (CIS) have shown different radiative lifetime behaviour across the spectra [28], with the decays on the red and blue side of the spectra corresponding to different recombination processes. On the blue side, the lifetime decay is short and on the red side, the lifetime decay is long. The short lifetimes are explained by a direct recombination from the conduction band to valence band (relaxation). The long lifetimes are explained by a radiative traps recombination pathway, from the conduction band to a surface traps and then to the valence band. This is in contrast to the radiative lifetimes across the spectra in Figure 6. 20, where the variation in lifetime decays across the spectra can be explained solely by a change in the volume of the CdTe CQDs. The

radiative lifetimes across the spectra show a linear dependency on volume of the CdTe QCDs, for all levels of pump power excitation used, indicating that traps are not being formed by high pump powers, as has been reported [29].

6.7. Summary and Discussion

The hot injection method used for the synthesis of CQDs is inexpensive in comparison with the molecular beam epitaxy and similar methods used to produce other QDs. Unfortunately the optical properties of many CQDs, including CdTe CQDs are not ideal immediately after synthesis, with low PLQY due to significant non-radiative recombination. However the optical properties of CdTe CQDs can be dramatically improved by passivating their surface with chloride ions. This process does not change the zinc blend crystal structure of the CdTe CQDs as shown by STEM and XRD measurement .Moreover XPS has been used to demonstrate that the chloride is on the surface of the CdTe CQDs rather than being incorporated into the volume of the nanocrystal.

In this chapter the improvement in the optical properties of CdTe CQDs produced by the chloride treatment has been characterised in detail: PL increased up to 20 times after treatment; PLQY values before treatment were below 15% and after treatment the values were near to unity for some CdTe CDQs, and the PL decay showed a multi-exponential behaviour before treatment and a longer mono-exponential behaviour after treatment. The optical improvement was shown to have a direct relation with the amount of chloride used during the passivation process. Too little chloride during the reaction might not remove all the surface traps and an excess of chloride could lead to a thick layer forming which would inhibit carrier injection and extraction.

The red shifts after the chloride passivation in absorption and PL emission are related with the quantity of chloride used and the reaction time. This red shift has been shown to be due to the reduction of the CQD surface by the negative chloride ions, which fills vacant valance band edge states and thus narrow the bandgap [16].

The amount of chloride used during treatment also affects the PLQY and PL lifetime. For lower and higher chloride concentrations, the PLQY values are inferior to the PLQY values obtained with the normal concentration of chloride (96 Cl^- per nm^2 of CdTe CQDs).

For the PL Lifetime decays, the chloride concentrations affect the slope of the decay, with higher concentrations of chloride increasing the lifetime of the decay.

The chloride treatment also protects the CdTe CQDs against the air exposure; the optical properties of untreated CdTe CQDs after air exposure decrease in the first hour, leading to an optical quenching after few hours. The chloride treated CdTe CQDs are more resistant against the effects oxygen: the optical properties decrease at a slower rate than for the untreated CQDs with the PL decay remaining mono-exponential and PLQY values keeping above 50%.This suggests that the chloride ions are protection sites of the surface of the CdTe CQDS which would otherwise be subject to oxidation.

In order to understand the recombination dynamics of the CdTe CQDs, the radiative and non-radiative processes were analysed by assuming the radiative rate (κ_r) is predominant ($\kappa_r > \kappa_{nr}$) and ($\kappa_{nr} \cong 0$) the non-radiative is minimal for treated samples. As the PL decay for the chloride treated CdTe CQDs shows a mono-exponential behaviour, the radiative lifetimes are extracted by fitting a mono-exponential to know (τ_{PL}). The procedure was to use the first decade of the PL decay for both: treated and untreated sample.

The effect of PL intermittency often called ‘blinking’, was considered in the analysis. PL intermittency can results from trapping of charge on CQD surfaces sites that are not well-passivated [30, 31], it determines the number of CdTe CQDs that contribute to the PL, reducing the PLQY but the PL lifetime itself is unaffected since this is influenced only by those CQDs that emit light. The trapping of hot exciton directly to a surface site, missing out the band edge [32], also reduces the PLQY whilst leaving the rate of the band edge recombination unaffected. Hence the “real” radiative lifetime lies between the PL lifetime, τ_{PL}, and $\tau_r \approx \tau_{PL}/PLQY$, where τ_r is a more accurate estimate when the value of PLQY is near unity.

The radiative lifetime (τ_r) values found are between 20 ns and 55 ns. In previous studies values between 20ns and 40ns have been reported for similar sizes [25, 33].However these studies used the PL lifetime instead of radiative lifetime $\tau_r \approx \tau_{PL}/PLQY$. Furthermore an empirical relation between the recombination rate and the peak PL photon energy was used to calculate an estimate of the radiative lifetime [25], which will be called the calculated lifetime ($\tau_{calculated}$) from here on. The values from ($\tau_{calculated}$) and (τ_{PL}) are similar, in contrast with $\tau_r \approx \tau_{PL}/PLQY$ values, that are longer and represent the upper limit for radiative lifetime.

The radiative lifetimes ($\tau_r \approx \tau_{PL}/PLQY$) showed a strong linearity with the volume of CdTe CQDs, this was also observed in other studies for CdSe quantum dots [24].

To investigate non-radiative recombination, the untreated CdTe CQDs were used. Their PL decay is well described by a tri-exponential, the lifetime of the radiative component (τ_r) of which can be fixed, as it is known for the treated sample. The remaining fast (τ_{fast}) and slow (τ_{slow}) time constants are associated with the non-radiative part. The time constants: (τ_{fast}) and slow (τ_{slow}) were found not to be dependant on the CdTe CQD volume. This confirms that the radiative recombination component has been isolated from the non-radiative components.

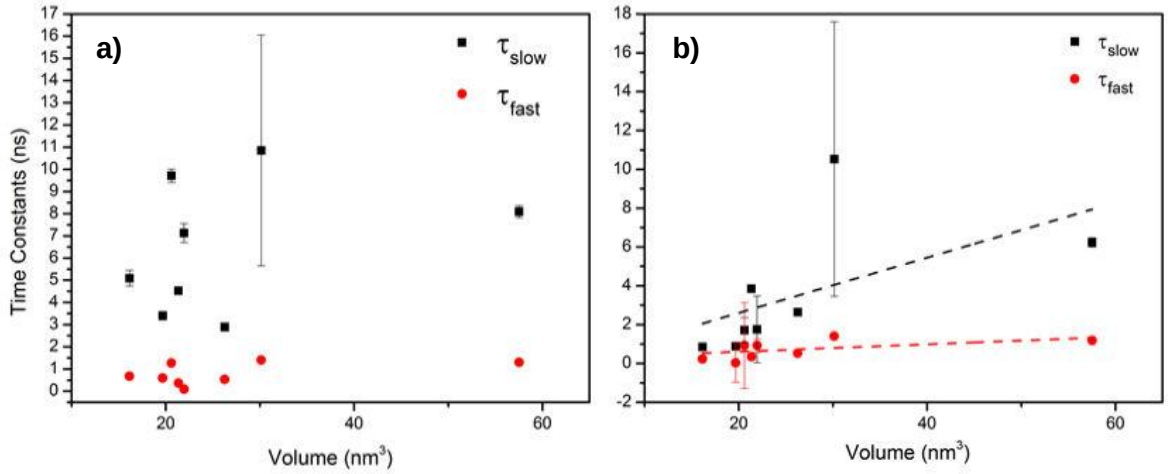

Figure 6. 21 Fast and slow time constants comparison using betweenτ_r, and τ_{PL}, for the non-radiative process of the untreated CdTe CQD. On the left a) τ_r, and b). τ_{PL} on the right.

In Figure 6. 21.a) shows the values found of τ_{slow} and τ_{fasr} from radiative lifetime ($\tau_r \approx \tau_{PL}/PLQY$), b) show the values found of τ_{slow} and τ_{fast} from the observed life time (τ_{PL}).The resulting values of the time constants using τ_{PL} show a evident systematic variation with CdTe CQDs volume, which indicates a part of the radiative recombination is present. The use of τ_{PL} found for the untreated samples (in contrast to the treated samples) is not a reliable measurement of the radiative recombination processes because it has not been separated from the non-radiative processes.

The effect of air exposure was observed for untreated and chloride treated CdTe CQDs, as expected the optical properties were decreased for both CQDs. However the life span of the chloride treated was significantly longer than the untreated.

The absorption spectra for the untreated CdTe CQDs is not affected by the presence of oxygen, in contrast with the chloride treated CQDs, which exhibit a blue shift. This blue shift suggests that the red shift suffered during the passivation process is now somewhat reversed. The red shift during the passivation is associated with the chloride ions filling the electron vacancies at the band edge, which narrow the band gap [16]. This suggests air exposure oxidises the surface whilst chloride treatment reduces it. The PL is also affected

is similar way; for the untreated CQDs, the PL peak does not change but the intensity drop significantly in a few hours until almost complete quenching is obtained. The chloride treated CQDs present a moderate blue shift on the PL peak and a slow decrement in intensity. After several hours of air exposure the PL of the chloride treated CQDs was more intense than the untreated CQDs immediately after synthesis.

The PL lifetime was also affected by oxygen contact. For the untreated CDQs the PL decay presents a multi-exponential behaviour with a short lifetime. After 1 hour of being in contact with oxygen, there was a drop at the beginning of the decay and making the effective lifetime even shorter. In contrast, the chloride treated samples showed a mono-exponential behaviour and after being exposed to oxygen for 1 hour, the PL lifetime was still mono-exponential with an almost similar PL lifetime. Even after several hours of air exposure the PL lifetime still behaves as mono-exponential in the first decade, however there is an increase in the decay rate which reduces the effective lifetime

The analysis of the recombination dynamics after air exposure uses the radiative lifetime ($\tau_r \approx \tau_{PL}/PLQY$) before exposure, which should not be affected by changes to the surface. Knowing τ_r a multi-exponential is fit over the first decade to find τ_{slow} and τ_{fast}. The approach was to use a global fitting for all the different oxygen exposure decays, with τ_r fixed to the value obtained before exposure and the τ_{slow} and τ_{fast} values shared between each transient. In contrast, the amplitudes were free to vary. The fractional contribution of the amplitudes describes the oxidation process. For the untreated CdTe CQDs, the fractional amplitudes associated with τ_r is quickly reduced, and τ_{fast} grows fast and dominates the dynamic, whilst τ_{slow} stays almost without variation. For the chloride treated CQDs, the behaviour is opposite for the non-radiative part, the fractional amplitudes of τ_{fast} stays almost constant, and τ_{slow} grows in modest way as τ_r decreases slowly.

The recombination dynamics across the PL spectra were studied for the chloride treated CQDs, by acquiring the PL decay for a fix time. The maximum number of counts for each wavelength was plotted and fitted with a Lorentz function. The plot is the reconstruction of the PL spectra (see Figure 6. 19); this acquisition of the spectral PL transients was performed at different pump powers. The PL peak is broadly constant for the different pump pulse powers (see Table 6. 6), but the small red shift at high pump energies might suggest the formation of biexcitons [27]. However this shift is more likely related to the 10 nm spectral step size, leading in an experimental error in the determination of the peak PL wavelength. Figure 6. 22 compares examples high-pump energy transient PL spectra obtained at immediately after excitation and after 2 ns i.e. a time much longer than the biexciton lifetime. In this case the peak does not suffer any shift consistent with the redshift observed in other cases being due to experimental inaccuracy rather than being related to the formation of biexcitons.

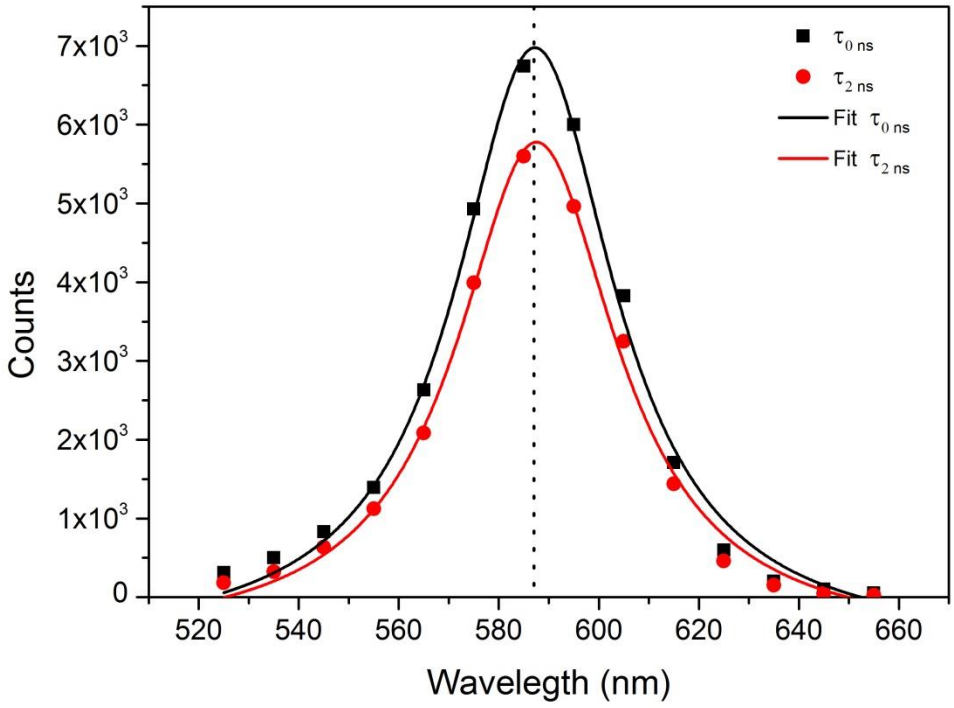

Figure 6. 22 Transient PL at high pump power energy, for 0ns and after 2ns

The analysis of the radiative process across the spectra was done by taking the PLQY as a constant across the spectra. The radiative lifetime for the different diameters of the chloride treated CdTe CQD show a strong linearity, as expected the linearity was not affected by the different pump power energies (Figure 6. 20). This linearity has a dependency on volume of the CdTe QCDs, and not for two separate recombination processes for the blue and red sides.

The contribution of the non-radiative process could be explained with the Auger-mediated trapping (AMT) model. When a photogenerated hole suffers a trapping transition to a state in the band gap, the excess of energy of the transition can be transferred non-radiatively to the electron, exciting the electron to a state above the conduction band edge. This AMT process has been used to explain the charge dynamics of CQDs experimentally observed in different materials in diverse environments [18, 34-36]. AMT times for CdTe CQDs with a radius of 2.3 nm were done by Marco Califano [36].

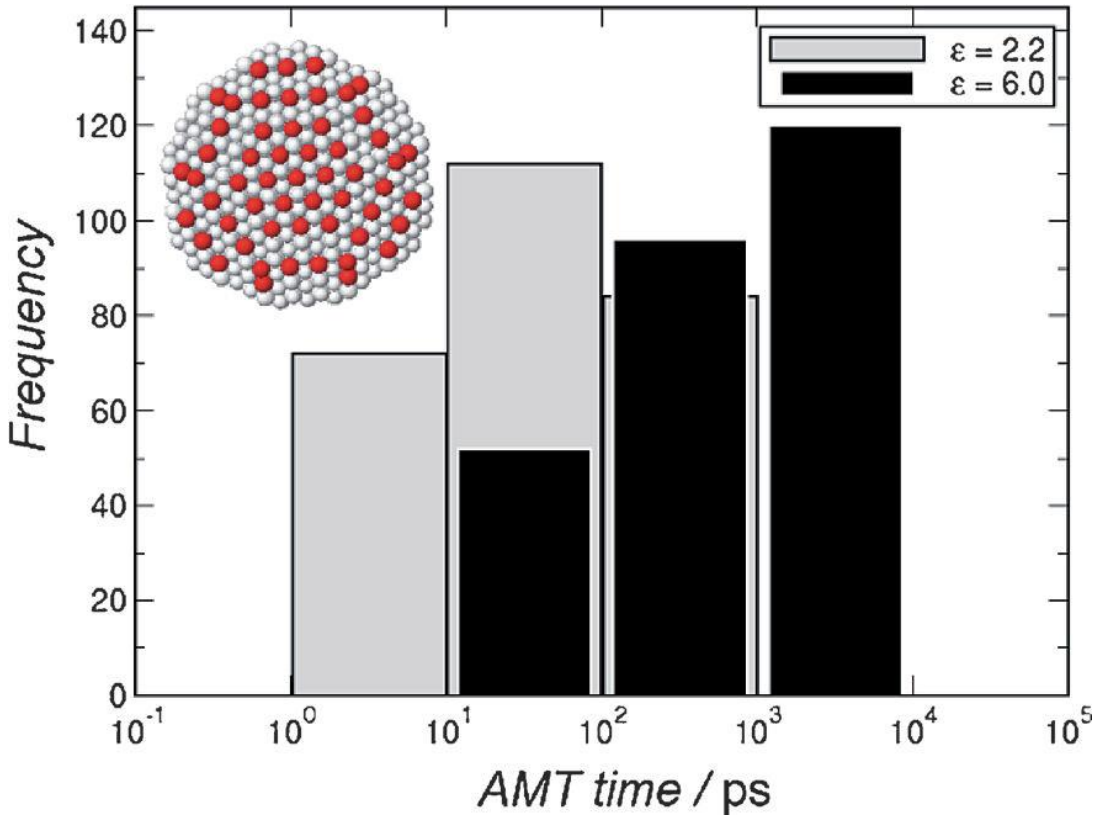

Figure 6. 23 AMT times calculated for a CdTe CQD of radius 2.3 nm for dielectric environments corresponding to the solvent used (ϵ=2.2) and to CdO (ϵ =6.0). Inset: an atomistically accurate map of

the positions of surface Te atoms with unsaturated bonds (dark spheres). Cd atoms and 4-coordinated Te atoms are displayed in white for clarity. (Taken from[36]).

The non-radiative recombination observed for the CdTe CQDs, were consistent with the calculated AMT of holes by surface dangling bonds. The calculations of the trapping times using an atomistic semiempirical pseudopotential method showed two types of hole trap for Te atoms involving either one or two dangling bonds. Each trap type produces a distribution of trapping times depending on the location of the Te atom on the CQD surface. The trapping time values directly depend on the dielectric constant of environment of the trap. The trapping times values using the dielectric constant of the toluene solvent (ϵ=2.2) are in pico-seconds. However, using the dielectric constant of CdO (ϵ=6) changes the trapping time values to the nanosecond scale. This agrees with the experimentally observed results and suggests that the oxidation process produces the observed trapping behaviour; this conclusion is supported by the increase of the non-radiative part in the observed PL decay when the sample is exposed to oxygen. In short, the oxidation process both produces traps by removing electrons from the valence band edge and also determines the time scale of non-radiative recombination by increasing the dielectric constant of the local environment. Before air air-exposure, the tetradecylphosphonic acid (used to passivate the untreated CdTe CQDs) produces a similar effect i.e. create traps by oxidation and also midifies the dielectric environment resulting in a nanosecond time scale for non-radiative recombination involving these traps.

References

1. Ip, A.H., S.M. Thon, S. Hoogland, O. Voznyy, D. Zhitomirsky, R. Debnath, L. Levina, L.R. Rollny, G.H. Carey, A. Fischer, K.W. Kemp, I.J. Kramer, Z.J. Ning, A.J. Labelle, K.W. Chou, A. Amassian, and E.H. Sargent, *Hybrid passivated colloidal quantum dot solids.* Nature Nanotechnology, 2012. 7(9): p. 577-582.
2. Shirasaki, Y., G.J. Supran, M.G. Bawendi, and V. Bulovic, *Emergence of colloidal quantum-dot light-emitting technologies.* Nature Photonics, 2013. 7(1): p. 13-23.
3. Sargent, E.H., *Colloidal quantum dot solar cells.* Nature Photonics, 2012. 6(3): p. 133-135.
4. Owen, J.S., J. Park, P.E. Trudeau, and A.P. Alivisatos, *Reaction chemistry and ligand exchange at cadmium-selenide nanocrystal surfaces.* Journal of the American Chemical Society, 2008. 130(37): p. 12279-+.
5. Wang, J., Y.T. Long, Y.L. Zhang, X.H. Zhong, and L.Y. Zhu, *Preparation of Highly Luminescent CdTe/CdS Core/Shell Quantum Dots.* Chemphyschem, 2009. 10(4): p. 680-685.
6. Greytak, A.B., P.M. Allen, W.H. Liu, J. Zhao, E.R. Young, Z. Popovic, B.J. Walker, D.G. Nocera, and M.G. Bawendi, *Alternating layer addition approach to CdSe/CdS core/shell quantum dots with near-unity quantum yield and high on-time fractions.* Chemical Science, 2012. 3(6): p. 2028-2034.
7. Saha, A., K.V. Chellappan, K.S. Narayan, J. Ghatak, R. Datta, and R. Viswanatha, *Near-Unity Quantum Yield in Semiconducting Nanostructures: Structural Understanding Leading to Energy Efficient Applications.* Journal of Physical Chemistry Letters, 2013. 4(20): p. 3544-3549.
8. Tyrrell, E.J. and J.M. Smith, *Effective mass modeling of excitons in type-II quantum dot heterostructures (vol 84, 165328, 2011).* Physical Review B, 2012. 86(23).
9. Zanella, M., L. Maserati, M.P. Leal, M. Prato, R. Lavieville, M. Povia, R. Krahne, and L. Manna, *Atomic Ligand Passivation of Colloidal Nanocrystal Films via their Reaction with Propyltrichlorosilane.* Chemistry of Materials, 2013. 25(8): p. 1423-1429.
10. Chuang, C.H.M., P.R. Brown, V. Bulovic, and M.G. Bawendi, *Improved performance and stability in quantum dot solar cells through band alignment engineering.* Nature Materials, 2014. 13(8): p. 796-801.
11. Katsiev, K., A.H. Ip, A. Fischer, I. Tanabe, X. Zhang, A.R. Kirmani, O. Voznyy, L.R. Rollny, K.W. Chou, S.M. Thon, G.H. Carey, X. Cui, A. Amassian, P. Dowben, E.H. Sargent, and O.M. Bakr, *The Complete In-Gap Electronic Structure of Colloidal Quantum Dot Solids and Its Correlation with Electronic Transport and Photovoltaic Performance.* Advanced Materials, 2014. 26(6): p. 937-942.
12. Zhang, J.B., J.B. Gao, E.M. Miller, J.M. Luther, and M.C. Beard, *Diffusion-Controlled Synthesis of PbS and PbSe Quantum Dots with in Situ Halide Passivation for Quantum Dot Solar Cells.* Acs Nano, 2014. 8(1): p. 614-622.
13. Bae, W.K., J. Joo, L.A. Padilha, J. Won, D.C. Lee, Q.L. Lin, W.K. Koh, H.M. Luo, V.I. Klimov, and J.M. Pietryga, *Highly Effective Surface Passivation of PbSe Quantum Dots through Reaction with Molecular Chlorine.* Journal of the American Chemical Society, 2012. 134(49): p. 20160-20168.
14. Anderson, N.C. and J.S. Owen, *Soluble, Chloride-Terminated CdSe Nanocrystals: Ligand Exchange Monitored by H-1 and P-31 NMR Spectroscopy.* Chemistry of Materials, 2013. 25(1): p. 69-76.
15. Tang, J., K.W. Kemp, S. Hoogland, K.S. Jeong, H. Liu, L. Levina, M. Furukawa, X.H. Wang, R. Debnath, D.K. Cha, K.W. Chou, A. Fischer, A. Amassian, J.B. Asbury, and E.H. Sargent, *Colloidal-quantum-dot photovoltaics using atomic-ligand passivation.* Nature Materials, 2011. 10(10): p. 765-771.

16. Page, R.C., Espinobarro-Velazquez, D., Leontiadou, M. A., Smith, C., Lewis, E. A., Haigh, S. J., Li, C., Radtke, H., Pengpad, A., Bondino, F., Magnano, E., Pis, I., Flavell, Wendy. R., O'Brien, P. and Binks, D. J., *Near-Unity Quantum Yields from Chloride Treated CdTe Colloidal Quantum Dots.* Small, 2014.
17. Yu, W.W., L.H. Qu, W.Z. Guo, and X.G. Peng, *Experimental determination of the extinction coefficient of CdTe, CdSe, and CdS nanocrystals.* Chemistry of Materials, 2003. 15(14): p. 2854-2860.
18. Gomez-Campos, F.M. and M. Califano, *Hole Surface Trapping in CdSe Nanocrystals: Dynamics, Rate Fluctuations, and Implications for Blinking.* Nano Letters, 2012. 12(9): p. 4508-4517.
19. McElroy, N., R.C. Page, D. Espinbarro-Valazquez, E. Lewis, S. Haigh, P. O'Brien, and D.J. Binks, *Comparison of solar cells sensitised by CdTe/CdSe and CdSe/CdTe core/shell colloidal quantum dots with and without a CdS outer layer.* Thin Solid Films, 2014. 560: p. 65-70.
20. Sher, P.H., J.M. Smith, P.A. Dalgarno, R.J. Warburton, X. Chen, P.J. Dobson, S.M. Daniels, N.L. Pickett, and P. O'Brien, *Power law carrier dynamics in semiconductor nanocrystals at nanosecond timescales.* Applied Physics Letters, 2008. 92(10).
21. Ohnesorge, B., R. Weigand, G. Bacher, A. Forchel, W. Riedl, and F.H. Karg, *Minority-carrier lifetime and efficiency of Cu(In,Ga)Se-2 solar cells.* Applied Physics Letters, 1998. 73(9): p. 1224-1226.
22. Rath, A.K., M. Bernechea, L. Martinez, F.P.G. de Arquer, J. Osmond, and G. Konstantatos, *Solution-processed inorganic bulk nano-heterojunctions and their application to solar cells.* Nature Photonics, 2012. 6(8): p. 529-534.
23. Lakowicz, J.R., *Principles of Fluorescence Spectroscopy, Third Edition*. 2010: Springer.
24. Javier, A., D. Magana, T. Jennings, and G.F. Strouse, *Nanosecond exciton recombination dynamics in colloidal CdSe quantum dots under ambient conditions.* Applied Physics Letters, 2003. 83(7): p. 1423-1425.
25. de Mello Donega, C. and R. Koole, *Size Dependence of the Spontaneous Emission Rate and Absorption Cross Section of CdSe and CdTe Quantum Dots.* The Journal of Physical Chemistry C, 2009. 113(16): p. 6511-6520.
26. Amelia, M., C. Lincheneau, S. Silvi, and A. Credi, *Electrochemical properties of CdSe and CdTe quantum dots.* Chemical Society Reviews, 2012. 41(17): p. 5728-43.
27. Klimov, V.I., *Spectral and dynamical properties of multilexcitons in semiconductor nanocrystals.* Annual Review of Physical Chemistry, 2007. 58: p. 635-673.
28. Li, L.A., A. Pandey, D.J. Werder, B.P. Khanal, J.M. Pietryga, and V.I. Klimov, *Efficient Synthesis of Highly Luminescent Copper Indium Sulfide-Based Core/Shell Nanocrystals with Surprisingly Long-Lived Emission.* Journal of the American Chemical Society, 2011. 133(5): p. 1176-1179.
29. Cadirci, M., S.K. Stubbs, S.M. Fairclough, E.J. Tyrrell, A.A. Watt, J.M. Smith, and D.J. Binks, *Ultrafast exciton dynamics in Type II ZnTe-ZnSe colloidal quantum dots.* Physical Chemistry Chemical Physics, 2012. 14(39): p. 13638-45.
30. Schmidt, R., C. Krasselt, C. Gohler, and C. von Borczyskowski, *The Fluorescence Intermittency for Quantum Dots Is Not Power-Law Distributed: A Luminescence Intensity Resolved Approach.* Acs Nano, 2014. 8(4): p. 3506-3521.
31. Galland, C., Y. Ghosh, A. Steinbruck, M. Sykora, J.A. Hollingsworth, V.I. Klimov, and H. Htoon, *Two types of luminescence blinking revealed by spectroelectrochemistry of single quantum dots.* Nature, 2011. 479(7372): p. 203-U75.
32. Kambhampati, P., *Hot Exciton Relaxation Dynamics in Semiconductor Quantum Dots: Radiationless Transitions on the Nanoscale.* Journal of Physical Chemistry C, 2011. 115(45): p. 22089-22109.

33. van Driel, A.F., G. Allan, C. Delerue, P. Lodahl, W.L. Vos, and D. Vanmaekelbergh, *Frequency-dependent spontaneous emission rate from CdSe and CdTe nanocrystals: Influence of dark states.* Physical Review Letters, 2005. 95(23).
34. Zhu, H.M., Y. Yang, K. Hyeon-Deuk, M. Califano, N.H. Song, Y.W. Wang, W.Q. Zhang, O.V. Prezhdo, and T.Q. Lian, *Auger-Assisted Electron Transfer from Photoexcited Semiconductor Quantum Dots.* Nano Letters, 2014. 14(3): p. 1263-1269.
35. Califano, M. and F.M. Gomez-Campos, *Universal Trapping Mechanism in Semiconductor Nanocrystals.* Nano Letters, 2013. 13(5): p. 2047-2052.
36. Espinobarro-Velazquez, D., M.A. Leontiadou, R.C. Page, M. Califano, P. O'Brien, and D.J. Binks, *Effect of Chloride Passivation on Recombination Dynamics in CdTe Colloidal Quantum Dots.* Chemphyschem, 2015: p. n/a-n/a.

Chapter 7. Conclusions and further work.

7.1. Conclusions

An investigation of the exciton-exciton interaction energy, Δ_{XX}, in type II CQDs using an established technique based on time-resolved photoluminesence (TRPL) spectroscopy indicated that the overall interaction was in some cases repulsive, consistent with other reports on similar Type II CQDs using the same method, but in the majority of cases was not well-resolved. However, other measurements of the exciton-exciton interaction on the same samples but using an alternative technique, ultrafast transient absorption (TA), showed that the overall interaction was clearly attractive. Further, theoretical calculations of Δ_{XX} were consistent with TA data in both magnitude and sign i.e. corresponded to an overall attraction interaction. These findings were reconciled in the following way. Biexciton PLQY has been reported as near as unity [1], but only for selected individual CQDs, not for ensembles. The low average PLQY for biexcitons in macroscopic samples results from the competition of radiative recombination with efficient non-radiative processes, and means that the expected spectrally-shifted PL feature corresponding to the biexciton is not evident even at excitation rates sufficiently high to produce a significant biexciton population. Furthermore, the blue-shifted component observed for some of our samples, and for others samples reported in the literature, can be explained by emission from higher energy states which can easily be mis-attributed to biexcitons. We thus conclude that the method of determining Δ_{XX} by analysis of TRPL spectra establish over the last decade by a number of workers is not reliable. Furthermore, we conclude that the overall interaction in these Type II CQDs is attractive rather than repulsive, making the more suitable for photovoltaic applications than for optical gain.

In the studies of single-exciton recombination dynamics in Type II CQDs, a more robust method to identify and separate the underlying processes in the recombination dynamics

was presented. The method was based on the theoretical calculation of τ_{rad}, instead of taking the largest time constant extracted from a tri-exponential fit as τ_{rad}. The observed tri-exponential recombination dynamic was also analysed in terms of the effect of shallow traps. A shallow trap is an energy level close to the valance band maximum due to a surface state formed by bonds left unsaturated during the synthesis of CQD. The numbers of shallow trap depends on different factors: excess of organic ligands, precursor, solvents, etc. This makes each sample unique. A rate equation model of the effects of shallow traps was detailed. This explained the non-exponential behaviour of the recombination dynamic as a consequence of intermediate processes of trapping prior to non-radiative recombination and of de-trapping via thermal energy. This analysis allowed the total rate of the non-radiative processes to be separated from the radiative rate in the experimental data. This revealed that the total rate of the non-radiative recombination processes decreases with increasing shell thickness, consistent with it depending on the wave-function overlap between the electron and hole. We thus concluded that non-radiative recombination in our Type II CQDs was consistent with shallow trapping and an Auger mediated trapping recombination process.

The investigation of photoluminescence of chloride-treated CdTe CQDs concluded that the process of passivation with chlorine ions enhanced the optical properties of the CdTe without affecting the zincblende crystal structure. Comparing after- and before-treatment samples showed that the PL increased up to 20 times after treatment; PLQY values before treatment were below 15% and after treatment the values were near to unity for some CQDs. The PL transient also changed from a tri-exponential to a single exponential, confirming that trapping associated with the unsaturated bonds on the surface of CQDs were supressed. The air exposure study concluded that the chloride passivation protects the CdTe CQDs somewhat from the oxidation process. The PL transient after air exposure presented a minimal change and the PLQY remained above 50%. The radiative lifetimes that now could be extracted because of the mono-exponential form of the PL decay

showed a strong linearity with the CQD volume, as expected. The non-radiative processes was also found to be affected by the dielectric constant of the environment [2]. We thus conclude that chloride passivation is a very effective method of passivating traps on the surface of CdTe CQDs

7.2. Further work

The results in chapter 6 showed that the Cl treatment described there is a very effective process for passivating CdTe CQD surfaces. Chapter 5 showed that recombination in CdSe/CdTe CQDs is dominated by non-radiative processes. In contrast to the Cl treatment of the CdTe CQDs, passivation of the CdSe/CdTe CQD surface with a further shell of CdS, whilst reducing non-radiative recombination somewhat, still leaves it as a significant recombination process.

This suggests that applying the chloride treatment to the CdSe/CdTe type II CQDs will be a more effective way of supressing the surfaces traps on the CdTe shell. In fact, the near-unity PLQY achieved for the CdTe CQDs means that this approach promises to effectively eliminate any surface related non-radiative recombination. However results from other workers [3, 4] suggest that non-radiative recombination can be only eliminated, and thus near unity PL QY reached, for core/shell CQDs if traps associated with defects at the core/shell interface are also eliminated. Fortunately, high temperature annealing of type I CQDs has been shown to effectively remove defects from the core/shell interface [3, 4]

Thus, the growth of type II CQD without interface defects or surface traps can be anticipated. Recombination in these CQDs would be purely radiative, and thus more fully controllable by selection of the size of the core and the thickness of the shell. Moreover, type II CQDs with dangling bonds completely passivated by the chloride treatments but before annealing would present an opportunity to study core/shell interface related recombination free from the competing effects of surface traps, which might otherwise obscure their effects.

Further study will facilitate the better understanding of the composition and surface chemistry of the CQDs. The crystal structure of any new CQDs will be confirmed using X-ray diffraction (XRD), before and after the addition of a shell layer or a surface passivation treatment.

The shape, quality, size-dispersion and average diameter of the CQDs will be determined using transmission electron microscopy (TEM). In previous studies, TEM images have shown that after passivation the CQDs re-arrange into a closer packed array and in some cases the QDs shrink in size. The surface chemistry of the CQDs can be analysed by using X-ray photoelectron spectroscopy (XPS). XPS provides information about elemental composition, impurities and shell thickness.

References

1. Park, Y.S., A.V. Malko, J. Vela, Y. Chen, Y. Ghosh, F. Garcia-Santamaria, J.A. Hollingsworth, V.I. Klimov, and H. Htoon, *Near-Unity Quantum Yields of Biexciton Emission from CdSe/CdS Nanocrystals Measured Using Single-Particle Spectroscopy.* Physical Review Letters, 2011. 106(18).
2. Califano, M., *Origins of Photoluminescence Decay Kinetics in CdTe Colloidal Quantum Dots.* Acs Nano, 2015. 9(3): p. 2960-2967.
3. Wang, X.Y., X.F. Ren, K. Kahen, M.A. Hahn, M. Rajeswaran, S. Maccagnano-Zacher, J. Silcox, G.E. Cragg, A.L. Efros, and T.D. Krauss, *Non-blinking semiconductor nanocrystals.* Nature, 2009. 459(7247): p. 686-689.
4. Chen, O., J. Zhao, V.P. Chauhan, J. Cui, C. Wong, D.K. Harris, H. Wei, H.-S. Han, D. Fukumura, R.K. Jain, and M.G. Bawendi, *Compact high-quality CdSe–CdS core–shell nanocrystals with narrow emission linewidths and suppressed blinking.* Nature Materials, 2013. 12(5): p. 445-451.